DESIGN AND OPTIMISATION OF THE SECTOR TRANSPORT, STORAGE AND ASSEMBLY TOOLING AND PROCEDURES OF THE NEW SMALL WHEEL FOR THE ATLAS EXPERIMENT

Peter James Sinclair

Submitted in fulfilment of the academic requirements for the degree of Master of Science in Mechanical Engineering, College of Agriculture, Engineering and Science, University of KwaZulu-Natal

Supervisor: Dr Clinton Bemont
Co-Supervisor: Dr Sahal Yacoob
Co-Supervisor: Ms Kirsty Veale

February 2016

DECLARATION

I, Peter James Sinclair declare that

1. The research reported in this dissertation, except where otherwise indicated, is my original work.

2. This dissertation has not been submitted for any degree or examination at any other university.

3. This dissertation does not contain other persons' data, pictures, graphs or other information, unless specifically acknowledged as being sourced from other persons.

4. This dissertation does not contain other persons' writing, unless specifically acknowledged as being sourced from other researchers. Where other written sources have been quoted, then:
   a. their words have been re-written but the general information attributed to them has been referenced;
   b. where their exact words have been used, their writing has been placed inside quotation marks, and referenced.

5. Where I have reproduced a publication of which I am an author, co-author or editor, I have indicated in detail which part of the publication was actually written by myself alone and have fully referenced such publications.

6. This dissertation does not contain text, graphics or tables copied and pasted from the Internet, unless specifically acknowledged, and the source being detailed in the thesis and in the References sections.

Signed_____ Date:_____
Mr Peter James Sinclair

As the candidate's supervisor I agree/do not agree to the submission of this dissertation.

Signed_____ Date:_____
Dr Clinton Bemont

As the candidate's co-supervisor I agree/do not agree to the submission of this dissertation.

Signed_____ Date:_____
Dr Sahal Yacoob

As the candidate's co-supervisor I agree/do not agree to the submission of this dissertation.

Signed_____ Date:_____
Ms Kirsty Veale

ACKNOWLEDGEMENTS

I would like to extend my deepest gratitude towards my supervisor, Dr Clinton Bemont and co-supervisors, Dr Sahal Yacoob and Ms Kirsty Veale for their continued support and guidance throughout my studies. Their enthusiasm towards my work and eagerness to assist, even at their busiest hours, are what made this dissertation possible.

A special thank you is dedicated to all who I had the privilege of working with during my research at CERN: Patrick Ponsot, for his constant guidance throughout my project, Giancarlo Spigo for his humble desire to share his infinite engineering and non-engineering knowledge and Shuvay Singh for his role as a colleague, friend and brother during and after my research at CERN. My gratitude is also extended to Raphael Vuillermet, Fabrizio Rossi, Marco Ciapetti, Hansdieter Schweiger, David Schmid and Jamie Pinnell for their eager and enthusiastic engineering advice and the productive and enjoyable working environment that they created at CERN.

I would like to thank my friends and family, especially my parents, for their encouragement, love and support throughout my studies, especially during the final months.

ABSTRACT

This report describes the design of the transport, storage and assembly tooling for the sectors of the ATLAS Experiment's New Small Wheel. This tooling is to be used during the 2018 Large Hadron Collider's shutdown, Long Shutdown 2. Comprehensive design reports following the Eurocode and CERN's unique design environment and philosophies are presented.

The NSW sector transport tool is an adaption of a previously used ATLAS EO muon transport tool, taking new sector masses, geometries and other transport restrictions into account. A safety document is provided for this tool confirming safety with regards to applied stresses in line with the Euro-code. The document also confirms lifting stability during all of the tool's intended procedures. The assembly tool allows the sTGC components to be assembled to the Micromegas chambers to create NSW sectors for the New Small Wheel. This tool also provides a platform for repairs and adjustments to be made to the NSW sectors before installation. The NSW sector assembly station is also designed in line with the Euro-code. A floor layout allocating space for transport, assembly and storage procedures in Building 191 of the Meyrin, CERN site is provided as specified by the project requirements.

An investigation confirming the validity of the finite element analysis techniques and simplifications used on the Micromegas wedges is conducted and presented. This investigation uses the results obtained from experimental thermal tests and analytical calculations of a Micromegas multiplet mock-up called the MMSW and compares them to finite element analysis results modelled to the same testing conditions. The results obtained from this investigation show that the computational results have an error of 7.6 % when compared to the attained experimental results. Consequently, because the finite element model is created in an identical manner to the one used for the Micromegas wedges, an assumption of similar errors can be applied to future simulations conducted on the Micromegas wedges, using this technique.

TABLE OF CONTENTS

LIST OF FIGURES

LIST OF TABLES

NOMENCLATURE

Abbreviations

ATLAS	-	A Toroidal LHC Apparatus
ºC	-	Degree Celsius
CAD	-	Computer Aided Drawing
CERN	-	European Organisation for Nuclear Research
cm	-	Centimetre
FEA	-	Finite Element Analysis
kg	-	Kilogram
LHC	-	Large Hadron Collider
m	-	Metre
mm	-	Millimetre
Micromegas	-	Micro mesh gaseous structure
MMSW	-	Micromegas multiplet mock-up
N	-	Newton
Nm	-	Newton-metre
NSW	-	New Small Wheel
s	-	Second
sTGC	-	Small strip Thin gap Chamber
TeV	-	Tera electron Volts
µm	-	Micrometre

Symbols

A - Area

D - Distance

E - Modulus of elasticity

F - Force

I - Moment of Inertia

L - Length

M - Moment

SF - Safety Factor

T - Temperature

w - Section Modulus

$\bar{x}$ - Centroid: x-direction

$\bar{y}$ - Centroid: y-direction

α - Co-efficient of thermal expansion

δ - Deflection

Δ - Change in:

$\sum$ - Sum of

σ_b - Bending Stress

σ_y - Yield Strength

INTRODUCTION

1.1   Research Overview

The Large Hadron Collider (LHC) of the European Organisation for Nuclear Research (CERN) is the world's largest, operational particle accelerator. The LHC first started up on the 10th of September 2008 although the design process began as early as 1984 (Jacob, 1984). Along the accelerator's 27 kilometre circumference of underground superconducting magnets, oppositely moving particles are accelerated to 0.999999991 times the speed of light (CERN, 2009). At various points along this circumference, are seven particle colliders. These colliders are designed to focus the oppositely moving particles of the LHC, resulting in particle collisions occurring at these specified locations.

The largest of these experiments, at a total mass of 7000 tonnes, is A Toroidal LHC Apparatus (ATLAS). A labelled image of a cut-away view of this detector can be observed in Figure 0-1. The experiment is situated 100 metres below ground at the main CERN site found in a small village in Switzerland called Meyrin, near the Franco-Swiss border. The detector is 44 metres long, 25 metres high and 25 metres wide (ATLAS, 2008). Along with the Compact Muon Solenoid (CMS), the ATLAS Experiment is a general purpose detectors aimed at investigating a wide range of physics, including the Higgs boson, extra dimensions and dark matter (ATLAS, 2015).
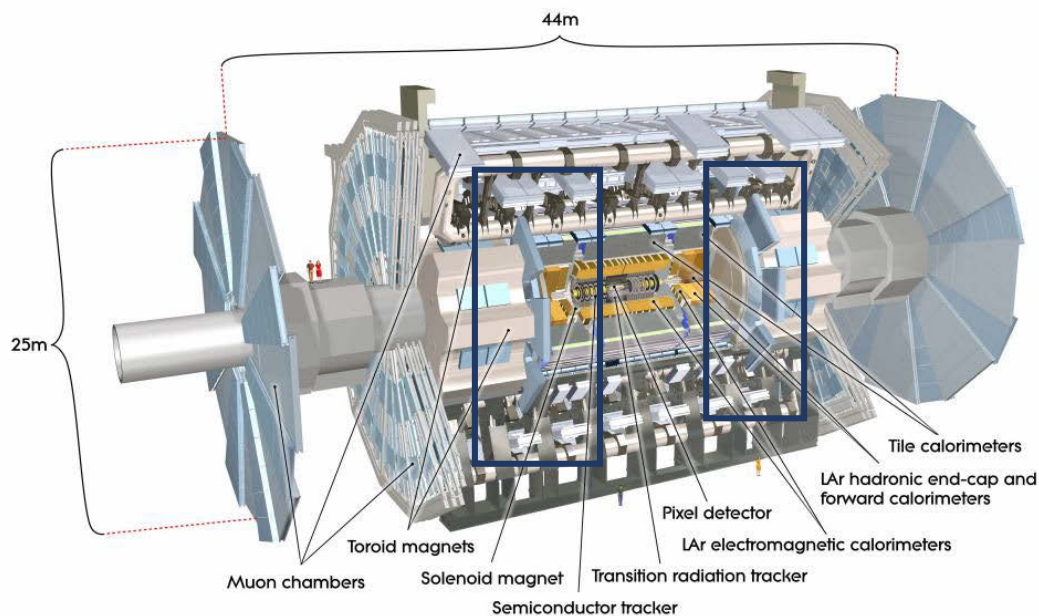
Figure 0-1. Cut-away view of the ATLAS Experiment (ATLAS, 2008).

When beams of protons collide at the ATLAS Experiment, debris is created in the form of smaller, subatomic particles such as muons, neutrinos and various bosons that soar out in all directions (ATLAS, 2008). Different detection and tracking systems of the experiment, arranged in layers around the collision point, record the paths, momentum and energy of the various particles, allowing each of these particles to be identified (ATLAS, 2008). These tracking systems can be observed in the cut-away view of the ATLAS Experiment found in Figure 0-1 and again in the quartered cross section view of the experiment in Figure 0-2.

In order for maintenance and upgrades of the LHC and its experiments to take place, the LHC shuts down for long periods of time every few years. The first significant LHC shutdown, Long Shutdown 1, began on 14 February 2013 and ended on 5 April 2015. This shutdown resulted in the energy capabilities of the LHC being increased from 4 TeV per beam to the superconducting magnet's maximum design value of 7 TeV per beam (ATLAS, 2013). The luminosity was also increased from 6×10^{33} cm^{-2}s^{-1} to 1×10^{34} cm^{-2}s^{-1} resulting in a large increase in the rate of particle collisions (ATLAS, 2013). During the next long shutdown, Long Shutdown 2, scheduled for 2018, the luminosity will further increase, exceeding 2×10^{34} cm^{-2}s^{-1} (La Rocca & Riggi, 2014). At this higher level of luminosity, the following two points regarding the muon tracking of the ATLAS Experiment are of importance:

1. The performance of the muon tracking chambers degrades with the expected increase in cavern background radiation rates. This is more prominent at the inner end cap region, which is closest to the collisions at about 7 m away (ATLAS, 2013).
2. The performance of the muon tracking chambers degrades with the expected increase of particle collisions. Fake muon triggers occur due to low energy particles, such as protons, with a similar transverse momentum. The number of fake triggers in the end cap region is eight to nine times of that in the barrel region, with about 90% of the collisions being fake (ATLAS, 2013).

In order to avoid limitations to the muon tracking systems of the ATLAS Experiment that could potentially be caused by these two issues, it has become necessary to replace the experiment's Small Wheels. The Small Wheels are the inner most end-cap stations involved in muon triggering and tracking. This can be seen as the area highlighted in blue in the cut-away view of the ATLAS Experiment in Figure 0-1 and highlighted in blue again, in the quartered cross section image of the ATLAS Experiment in Figure 0-2. The New Small Wheels (NSW) are precision tracking and

trigger detectors that are designed for much higher trigger rates, to meet the increase in LHC luminosity of Long Shutdown 2. The NSW has improved angular resolution allowing increased confirmation that the passing muons originate at the point of particle collision, reducing the number of fake muon triggers (ATLAS, 2013).
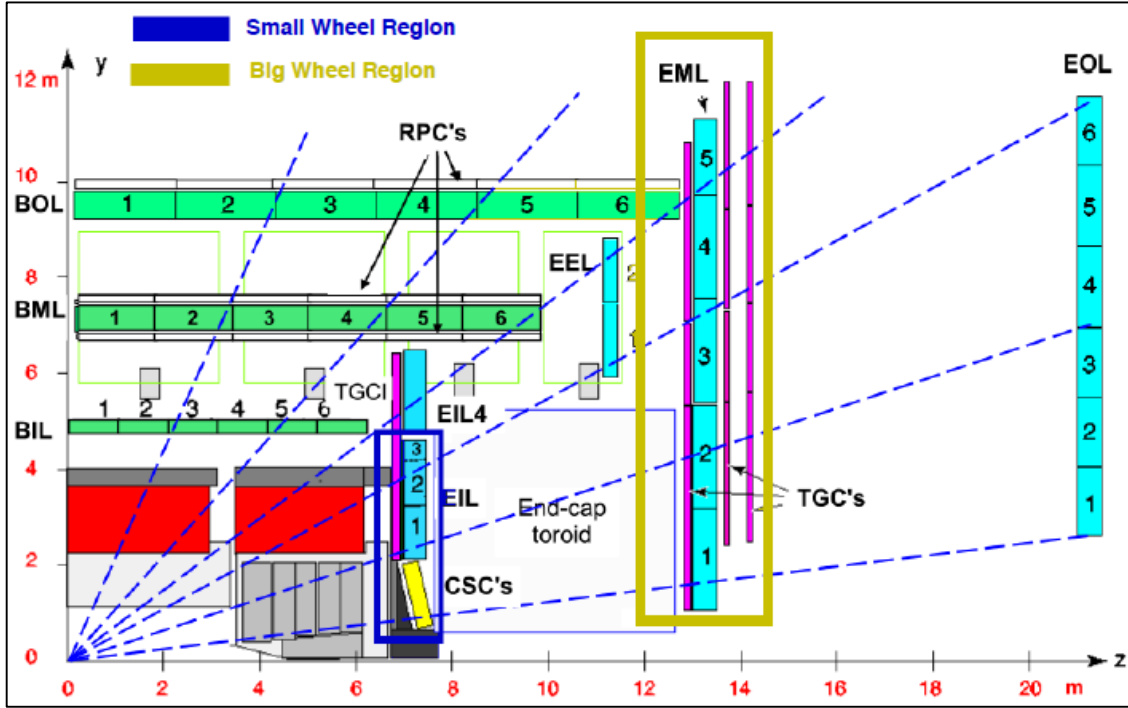
Figure 0-2. Quartered cross section of the ATLAS Experiment (ATLAS, 2013).

The NSW is a circular end-cap detector situated on either side of the ATLAS Experiment's length. Each one is made up of sixteen sectors that are shaped in a similar fashion to that of traditional pizza slices, with a flat inner edge, instead of a point. Eight of these sectors are large sectors, expected to weigh 1450 kg and eight are small sectors, expected to weigh 1100 kg, arranged in an alternating radial manner. The sectors are described in greater detail in Chapter 2.3. Due to the immense mass and delicacy of the sectors, special tooling and handling procedures are to be designed in order to assemble and transport the NSW sectors and their components, and to assemble the NSW structure. This work explores the design of the required NSW components' transport tool and the NSW sector assembly tool, used to assemble small strip Thin Gap Chambers (sTGC) to the Micro mesh gaseous structure (Micromegas) chambers to create NSW sectors. The procedures that need to be followed to complete these actions effectively and efficiently are explored and designed.

1.2   Objectives Overview

The buildings mentioned in the following objectives list can all be viewed in the map represented in Figure 0-3.

- Design mounts for the NSW sector's spacer frame (structural core) that can be used to hang Micromegas chambers and NSW sectors once assembled. The spacer frame is explained in greater detail in Chapter 2.3.

- Design a tool that can be used to transport double Micromegas chambers from Building 899 to the NSW sector assembly station situated in Building 180 or Building 191. This tool should be designed to also have the capability to transport fully assembled sectors.

- Design an assembly tool that is to be used to assemble the sTGCs to the double Micromegas chambers.

- Confirm an appropriate building and floor layout for the storage of Micromegas chambers and NSW sectors and the assembly of the NSW sectors using the assembly tool.

- Conduct testing to ensure that the computational stress analyses completed on the Micromegas wedges during these operations are accurate.
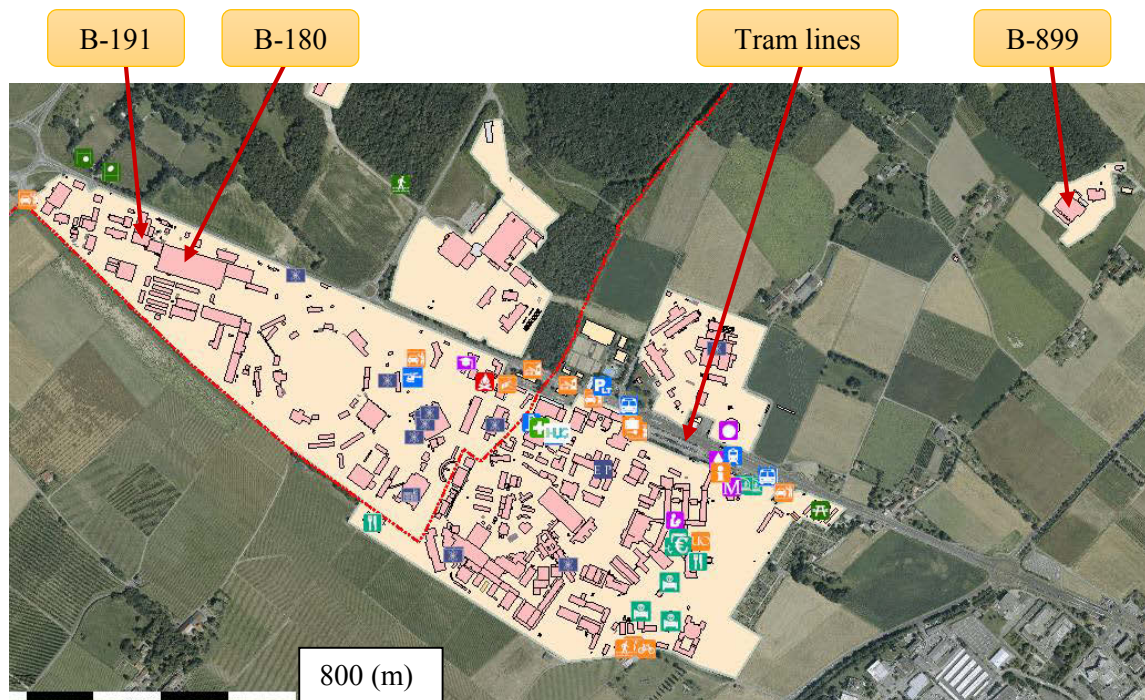
Figure 0-3. CERN, Meyrin building map (CERN, 2015).

1.3   Dissertation Outline

Chapter 2 provides an overview of the relevant improvements that are to be made to the ATLAS Experiment during Long Shutdown 2. The improvement of the physics' abilities involved in the NSW upgrade project are also discussed. Comprehensive detail is given to the structural design and materials used for the new Micromegas wedges, which are of primary concern in this work. The methodology for solving the engineering problems is discussed and analysed, including different problem solving techniques, such as analytical calculations, computational simulations and experimental analyses. All the formulae and analysis techniques relevant to this work are considered and explained. The theory involved in lifting stability analyses is investigated.

Chapter 3 provides information on the research and design methodology used to achieve the required objectives. The methodology involves explanations of the relevance of each objective and how the tasks are collectively linked.

Chapter 4 focuses on the design of the spacer frame mounts that are to be used as mounting points during the transport, storage and assembly procedures. The ergonomics issues involved in these mounts are explored and stress analyses are completed.

Chapter 5 involves the design of the Micromegas chamber's and NSW sector's transport tool. The space and size requirements are considered and met. A safety document confirming the strength of the tool is explained and completed while the stability of the tool during lifting operations is confirmed.

Chapter 6 details the storage and assembly components and procedures of the Micromegas chambers and NSW sectors. The assembly and storage structures are designed and analysed. A building floor plan used for this process is studied and recommendations are presented.

Chapter 7 provides a discussion of the designed transport, storage and assembly components and procedures. The successes and difficulties experienced in the design of these components and procedures are discussed.

Chapter 8 provides a detailed analysis of the error resulting due to the simplifications made during Micromegas computational modelling. In this analysis, the results are compared to experimental results obtained during thermal testing of a portion mock-up of a Micromegas wedge multiplet.

Chapter 9 discusses the results obtained from the experimental analysis conducted on the mock-up of the Micromegas wedge. The relevance of this investigation is discussed and other interesting and relevant discoveries made during this analysis are explored.

Chapter 10 summarises the dissertation in a final conclusion detailing all the achieved objectives. The relevance that this work has for the future of the ATLAS Experiment is stated.

CHAPTER 2 - LITERATURE REVIEW

2.1 ATLAS and Long Shutdown 2

The ATLAS Experiment is one of the leading experimental physics projects aimed at exploring the basic forces that have shaped our universe. In order to achieve new, better defined results, the project is periodically upgraded, as was the plan when the LHC was first designed (Zimmermann, 2014). A very important part of this upgrade process is the way in which the experiments track the particles once collisions have occurred. The image in Figure 2-1 displays the ATLAS Experiment with a removed end-cap calorimeter.
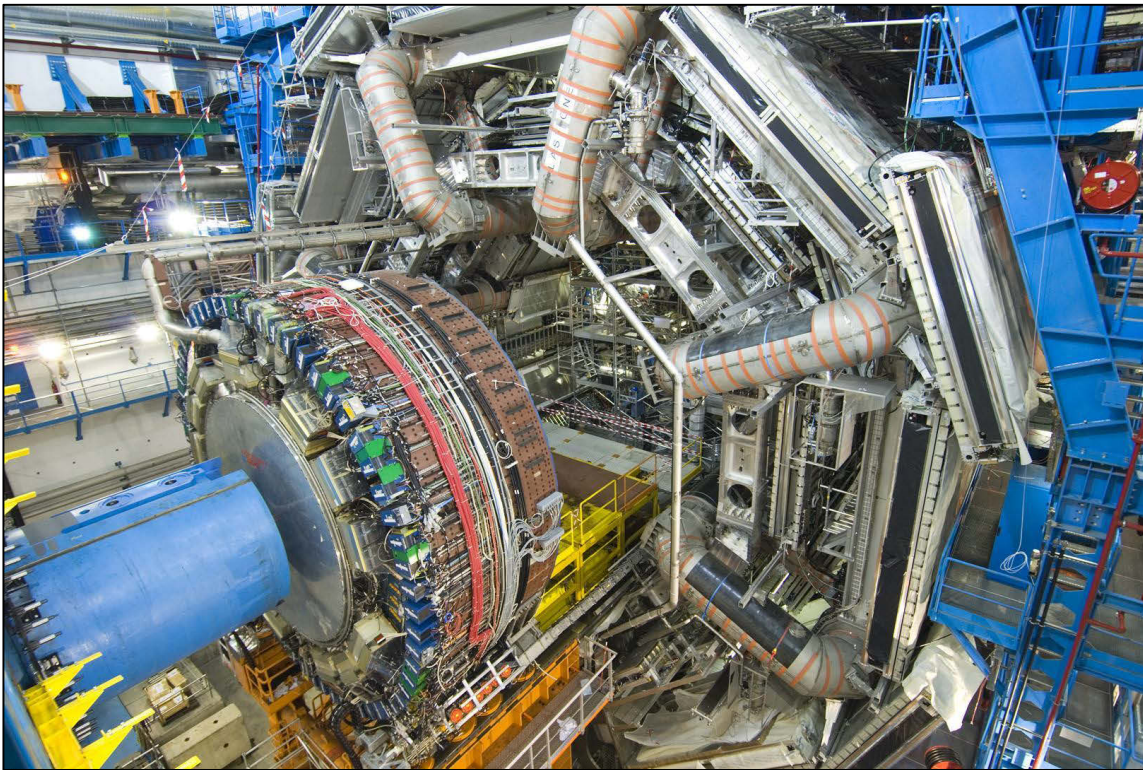
Figure 2-1. The ATLAS Experiment (ATLAS, 2007).

 In order to cope with the LHC's increasing luminosity, the ATLAS Experiment's inner most, muon tracking end cap system, known as the Small Wheel needs to be replaced. The New Small Wheel will be required to operate in a much higher background region while even more accurately reconstructing muon tracks (Zimmermann, 2014). In order to install the NSW and many other upgrades throughout the LHC, CERN have scheduled Long Shutdown 2 to take place over 18

months, starting in July 2018 (Zimmermann, 2014). In order to take full advantage of Long Shutdown 2 with regards to the NSW instalment, the ATLAS community have planned to have all designs of the structure and assembly devices completed by halfway through 2017, as can be seen in a project timeline presented in Figure 2-2. The relevant task overviews are emphasised to the right of the timeline.
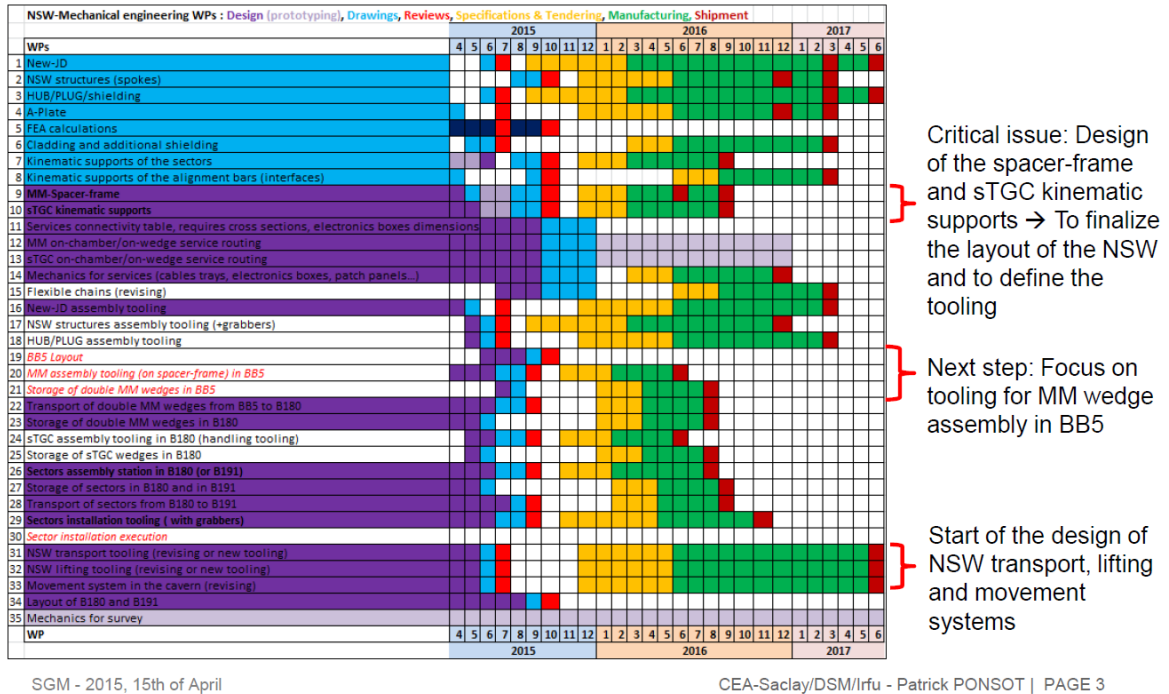
Figure 2-2. NSW project timeline (Ponsot, 2015).

2.2 Muons

Muons are negatively charged particles that possess very similar characteristics to electrons, falling in the same Lepton classification. They are, however, about 200 times the mass of electrons (Beringer, 2012). A noteworthy difference between these particles is that, unlike electrons, muons are neither stopped nor detected by ATLAS' inside detectors after the occurrence of collisions. Instead, they soar through these parts and are detected only by the outer most detector, the muon spectrometer (ATLAS, 2008).

The muon spectrometer is the outer most tracking system, consisting of three different parts. The first part is the toroidal magnets. These magnets create a magnetic field, bending the path of the negatively charged muons. The other two parts of the spectrometer are the triggers and the

trackers. The aim of the muon spectrometer is to measure the momentum of the muons passing through the detector (ATLAS, 2008). The muon tracking system is comprised of a barrel region constructed in cylindrical layers around the detector and end-cap regions called wheels, installed in planes, perpendicular to the beams (ATLAS, 2008).

2.3   Structure and Physics of New Small Wheel Sectors

The New Small Wheel is a muon tracking system intended to replace the current Small Wheel to deal with the higher luminosity upgrades of the LHC. The eight large and eight small NSW sectors are arranged in an alternating radial pattern illustrated in Figure 2-3. These sectors have mass of 1450 kg and 1100 kg respectively. Apart from their shape in the x-y plane, the large and small sectors are exactly the same and perform the same experimental operations. Figure 2-4 represents a front and rear view of the NSW so that the large and small sectors and their surrounding structures can be clearly observed.
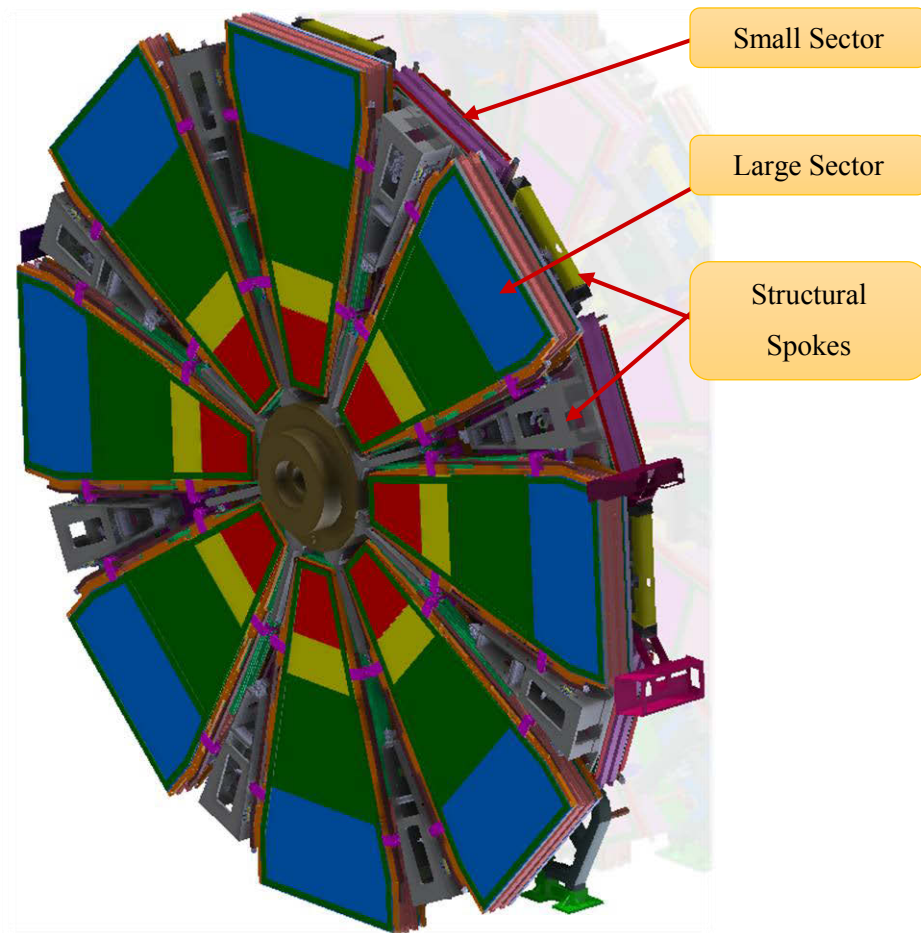
Figure 2-3. Labelled New Small Wheel (Sinclair & ATLAS, 2015).
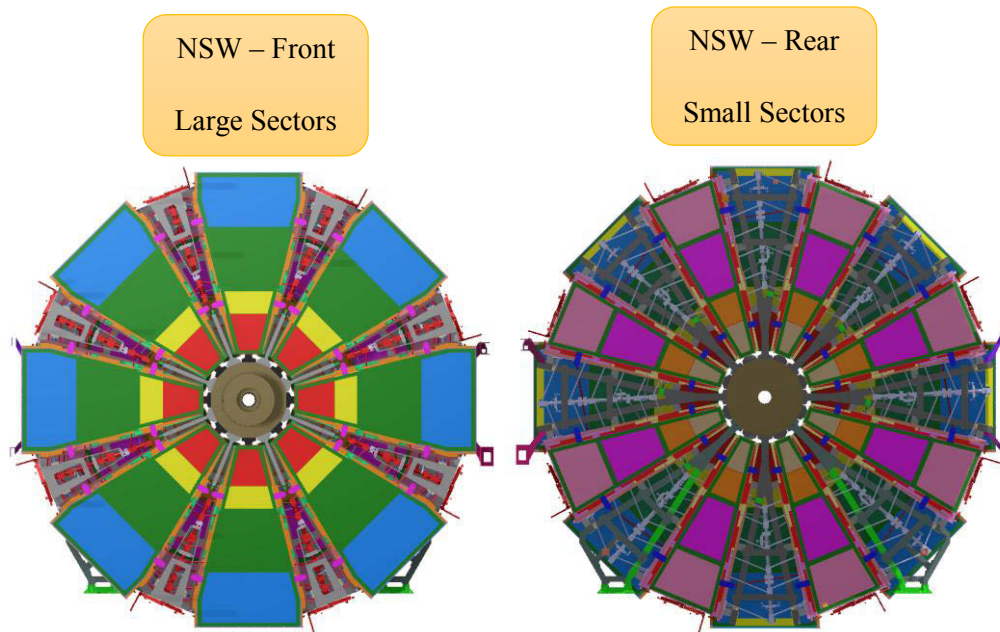
Figure 2-4. NSW front and rear views (Sinclair & ATLAS, 2015).

Figure 2-5 and Figure 2-6 are computer aided drawing (CAD) models of the large sector and the small sector respectively. The geometry differences between these two sectors can be observed.
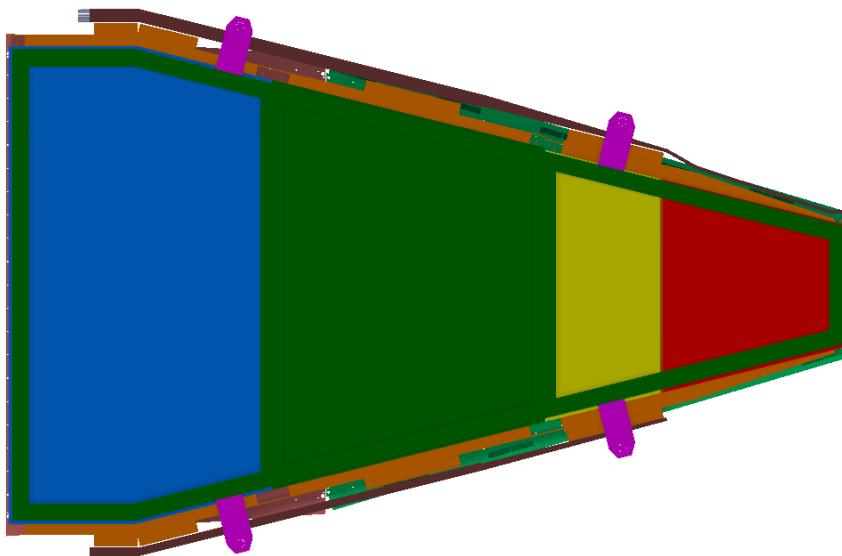
Figure 2-5. Large NSW sector (Sinclair & ATLAS, 2015).
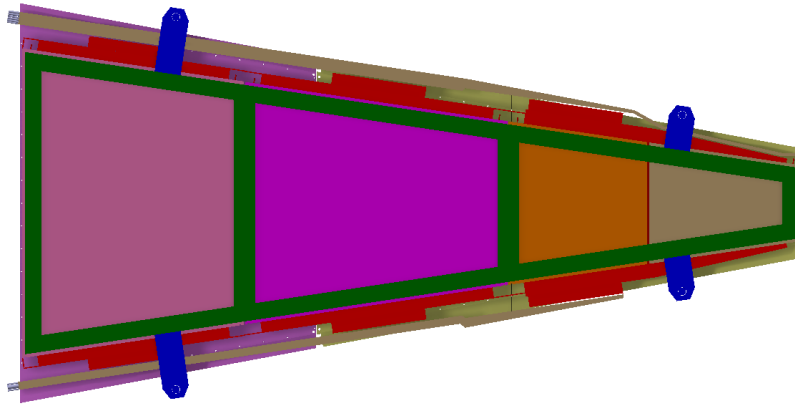
Figure 2-6. Small NSW sector (Sinclair & ATLAS, 2015).

The sectors are made up of five individual layers, called wedges, offering two different kinds of experimental physics technologies over a total thickness of 404 mm. These two different types of Muon tracking technologies are Small strip Thin Gap Chambers (sTGC) and Micro Mesh Gaseous Structures (Micromegas) (ATLAS, 2013). The global envelope in the z-direction, thickness, of the sectors as well as the intermediate dimensions of each individual technology can be seen in Figure 2-7. The two sTGCs are located at the outermost region of the sectors, sandwiched around the two Micromegas wedges which are connected to either side of an aluminium spacer frame. Once the Micromegas wedges are mounted to the spacer frame, the three layers are referred to as a double Micromegas chamber or simply, a Micromegas chamber.

The spacer frame is the 50 mm thick centre of the sector and can be identified as the central grey layer in Figure 2-7. Mechanically, the spacer frame acts as a core of the sector, giving it rigidity and stiffness due to the higher moment of inertia that accompanies the increase in thickness. It also provides a strong platform to mount the sTGCs to the double Micromegas chamber and the entire sector to the NSW structure. The spacer frame also creates a platform to mount a Micromegas chamber or, once assembled, the entire NSW sector during transportation, assembly, storage and instalment procedures.

The green layers on either side of the spacer frame in Figure 2-7 are the Micromegas wedges. These wedges are 80 mm thick and are connected to the spacer frame in many locations creating the final Micromegas chamber. This assembly, consisting of a spacer frame and two Micromegas wedges is the structure that must be transported, stored and assembled to sTGCs.

The outer most layers of the sandwich-like structure are the sTGCs. These wedges are 70 mm thick and are connected to the spacer frame by means of three kinematic mounts per wedge. The sTGCs can be identified as the blue layers in Figure 2-7. A gap of thickness 27 mm is left in between the Micromegas chamber and each sTGC.

When designing a part with so many similar components, it is important that the naming of these parts do not get confused. For this reason, ATLAS have specified that the following terminology should be used, the same naming terminology that will be followed in this thesis (ATLAS, 2013):

- Plane – A single detector gas gap with the readout structure.
- Multiplet – Assembly of n planes of a single technology in the z-direction
- Module- Assembly of m multiplets in the r-direction which constitute a single independent object
- Chamber – Assembly of two modules of a single technology in the z-direction and one or more modules in the r-direction which constitute a single independent object. A chamber might include an internal or external spacer frame between the modules in the z-direction.
- Wedge – Assembly of modules of a single technology type in the z-direction, covering a full sector in the r plane.
- Sector – 1/16th of the NSW on a side A or C, comprised of a spacer frame, two sTGCs and two Micromegas wedges.
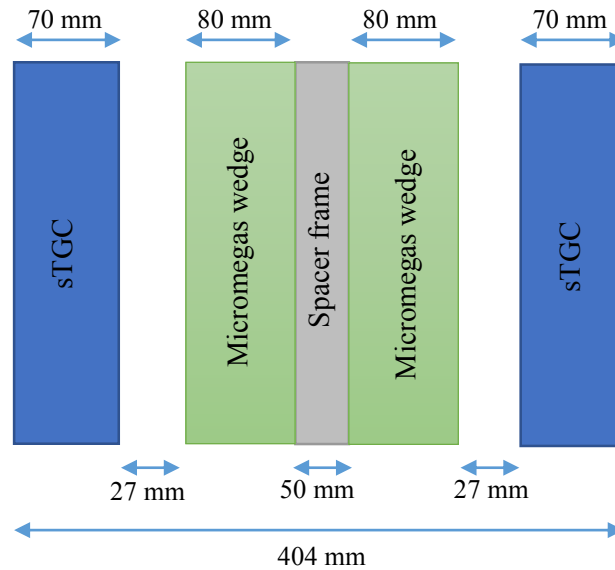
Figure 2-7. Sector global envelope in the z-direction.

2.4   Micromegas Wedges

Micromegas wedges are a new type of muon tracking detector used by ATLAS. Muon tracking detectors must meet a series of defined requirements. These requirements include very good positioning resolution independent of the particle incident angle, high efficiency tracking even at high background rates and good two track separation to reject delta rays (ATLAS, 2013).

Due to time and money constraints, a fully functional Micromegas wedge has not been created for comprehensive testing and experimentation yet. In an attempt to save money and time, ATLAS have created a smaller mock-up of a multiplet of the Micromegas wedges. This portion follows comparable proportions to the multiplet of the large Micromegas wedge represented in yellow in Figure 2-8. This mock-up has been given the name of MMSW amongst the ATLAS community and will be referred to as such in this thesis.
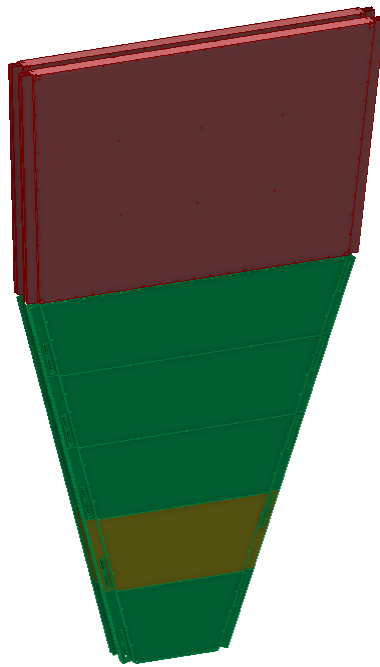
Figure 2-8. MMSW multiplet of Micromegas large sector (Sinclair & ATLAS, 2015).

The Micromegas technology is a thin, wireless, gaseous particle detector developed in the 1990's enabling the tracking of muons. The cross section and operating principle of the Micromegas detectors can be seen in Figure 2-9. Micromegas detectors consist of a planar drift electrode, a gas gap of a few millimetres thickness acting as a conversion medium and drift region and a thin

metallic mesh positioned at about 100 to 150 μm from the resistive strip, creating an amplification region. This metallic mesh is held away from the resistive strip by a series of 128 μm high pillars (ATLAS, 2013).

The high voltage potentials are chosen such that the electric field in the gaseous drift region is a few hundred volts per square centimetre and the electric field in the amplification region is about forty to fifty thousand volts per square centimetre. Charged particles travelling through the drift space ionize the gas, releasing electrons which drift towards the mesh. The mesh is transparent to about 95% of the electrons due to the electric field in the amplification region being fifty to one hundred times stronger than the electric field in the drift region. Although the electrons can take up to tens of nanoseconds to reach the micromesh, the amplification process beyond the mesh happens in a fraction of a nanosecond resulting in a fast pulse of electrons on the readout strip. It is the fast evacuation of the positive ions which makes the Micromegas technology particularly suited to operate at very high particle fluxes (ATLAS, 2013).
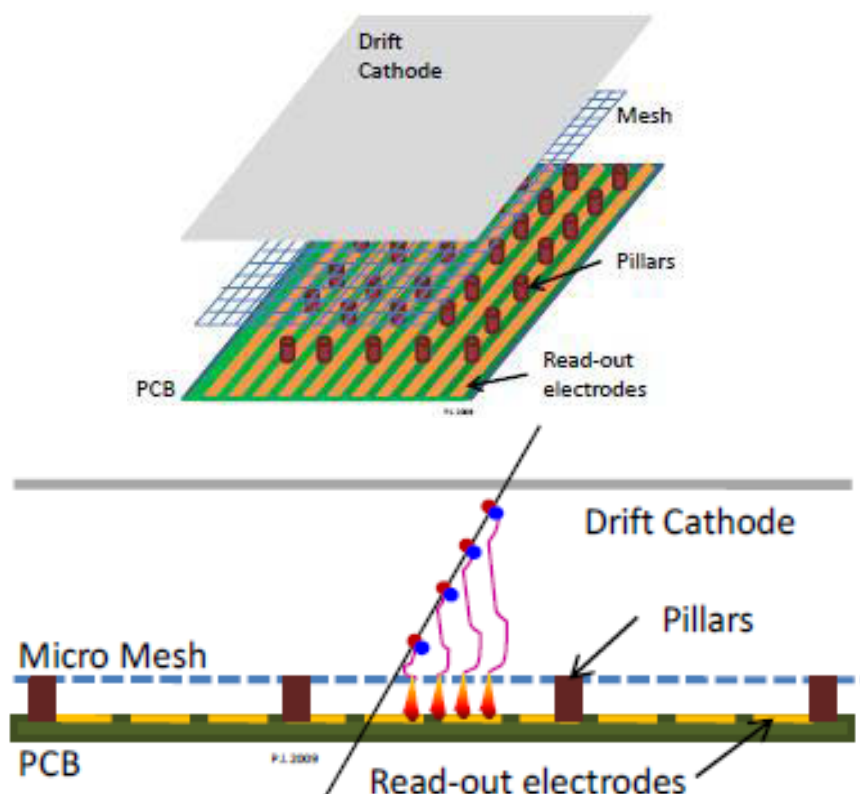
Figure 2-9. Micromegas drift region cross section (ATLAS, 2013).

The composite readout panels, contain the components responsible for delivering a signal to the readout boards enabling the tracking of the passing muons. This panel consists of a 10 mm thick aluminium honeycomb core with FR4 skins that serve as PCBs. Other than the FR4 glass reinforced epoxy sheets, the PCBs consist of layers of: copper readout strips, an insulative polyimide known as Kapton, Krempel Akaflex CDF 25 glue, carbon resistive strips and Pyralux PC 1025 mesh support pillars (Bianco, 2014). The cross section of this complex PCB describing each of the elements' thicknesses can be seen in Figure 2-10.
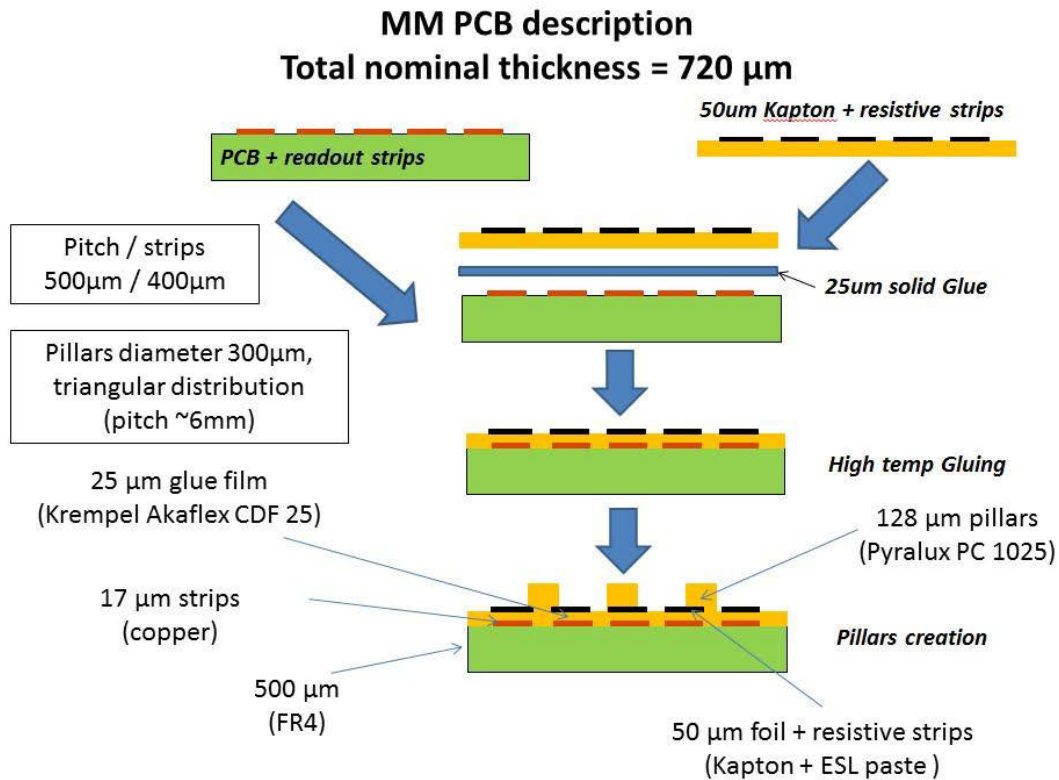
Figure 2-10. Micromegas PCB cross section (Bianco, 2014).

The aluminium honeycomb used in the MMSW and final Micromegas wedges has a cell diameter of 6.4 mm. The properties of this core structure can be seen in Table 2-1. The honeycomb thickness used is 10 mm.

Table 2-1. Material properties of core structure (Rossi, 2015).

Honeycomb type	Material	Cell size $[mm]$	Density $[kg/m^3]$	Young's Modulus $[MPa]$		
D 6.4	Aluminium	6.4	83.3	$x = 10$	$y = 10$	$z = 1000$

The PCB's used in the Micromegas structure serve two independent purposes. Their primary purpose is to provide a platform for the muon detection components. Their second function has a greater significance in this work. This function is the structural rigidity that they provide, being glued to either side of the aluminium honeycomb core. This sandwich structure gives the Micromegas their very important mechanical stiffness. The PCBs are made from FR4 which is a type of fibreglass with similar properties to that of the industrially popular, G10. The difference between these two composites is that FR4 has self-extinguishing properties, making it flame retardant, from where it got its name (Weil & Levchik, 2004). The warp to fill ratio of the fibreglass laminate used is 60 to 47, giving the fibreglass weave the style classification, 1080, according to the table found in Figure 2-11. The laminate properties for a 1080 FR4 weave can be found in the column labelled 'RO4350B' in the table in Figure 2-12, obtained from 'Rogers Corporation', the PCB suppliers for the Micromegas wedges.

Style No.	Weave	Warp Yarn Glass	Type	Filament Dia.	No.	Yarn/ inch (mm)	Fill Yarn Glass	Type	Filament Dia.	No.	Yarn/ inch (mm)	Fabric Thickness	Weight
106	plain	E	cont.	0.00023" (5 μm)	102	56 (2.2)	E	Cont.	0.00023" (5 μm)	102	56 (2.2)	0.0015" (38 μm)	0.73 oz/yd² (24.75 g/m²)
1070	plain	E	cont.	0.00023" (5 μm)	204	60 (2.4)	E	Cont.	0.00023" (5 μm)	204	35 (1.4)	0.002" (50 μm)	1.06 oz/yd² (35.94 g/m²)
1080	plain	E	cont.	0.00023" (5 μm)	204	60 (2.4)	E	Cont.	0.00023" (5 μm)	204	47 (1.9)	0.0025" (50 μm)	1.45 oz/yd² (49.16 g/m²)
2112	plain	E	cont.	0.00029" (7 μm)	204	40 (1.6)	E	Cont.	0.00029" (7 μm)	204	39 (1.5)	0.0034" (86 μm)	2.10 oz/yd² (71.20 g/m²)
2113	plain	E	cont.	0.00036" (9 μm)	130	60 (2.4)	E	Cont.	0.00036" (9 μm)	204	56 (2.2)	0.0029" (74 μm)	2.37 oz/yd² (80.36 g/m²)
2116	plain	E	cont.	0.00029" (7 μm)	204	60 (2.4)	E	Cont.	0.00029" (7 μm)	204	58 (2.3)	0.0038" (97 μm)	3.22 oz/yd² (109.18 g/m²)
7628	plain	E	cont.	0.00036" (9 μm)	408	44 (1.7)	E	Cont.	0.00036" (9 μm)	408	32 (1.3)	0.0068" (72 μm)	6.00 oz/yd² (203.43 g/m²)

Figure 2-11. Typical glass fabric styles (Groppi, et al., 1995).

Property	Typical Value RO4003C	Typical Value RO4350B	Direction	Units	Condition	Test Method
Dielectric Constant, ε, Process	3.38 ± 0.05	3.48 ± 0.05	Z	--	10 GHz/23ºC	IPC-TM-650 2.5.5.5 Clamped Stripline
[1] Dielectric Constant, ε, Design	3.55	3.66	Z	--	8 to 40 GHz	Differential Phase Length Method
Dissipation Factor tan, δ	0.0027 0.0021	0.0037 0.0031	Z	--	10 GHz/23ºC 2.5 GHz/23ºC	IPC-TM-650 2.5.5.5
Thermal Coefficient of ε,	+40	+50	Z	ppm/ºC	-50ºC to 150ºC	IPC-TM-650 2.5.5.5
Volume Resistivity	1.7 X 10¹⁰	1.2 X 10¹⁰		MΩ•cm	COND A	IPC-TM-650 2.5.17.1
Surface Resistivity	4.2 X 10⁹	5.7 X 10⁹		MΩ	COND A	IPC-TM-650 2.5.17.1
Electrical Strength	31.2 (780)	31.2 (780)	Z	KV/mm (V/mil)	0.51mm (0.020")	IPC-TM-650 2.5.6.2
Tensile Modulus	19,650 (2,850) 19,450 (2,821)	16,767 (2,432) 14,153, (2,053)	X Y	MPa (ksi)	RT	ASTM D638
Tensile Strength	139 (20.2) 100 (14.5)	203 (29.5) 130 (18.9)	X Y	MPa (ksi)	RT	ASTM D638
Flexural Strength	276 (40)	255 (37)		MPa (kpsi)		IPC-TM-650 2.4.4
Dimensional Stability	<0.3	<0.5	X,Y	mm/m (mils/inch)	after etch +E2/150ºC	IPC-TM-650 2.4.39A
Coefficient of Thermal Expansion	11 14 46	10 12 32	X Y Z	ppm/ºC	-55 to 288ºC	IPC-TM-650 2.4.41
Tg	>280	>280		ºC TMA	A	IPC-TM-650 2.4.24
Td	425	390		ºC TGA		ASTM D3850
Thermal Conductivity	0.71	0.69		W/m/ºK	80ºC	ASTM C518
Moisture Absorption	0.06	0.06		%	48 hrs immersion 0.060" sample Temperature 50ºC	ASTM D570
Density	1.79	1.86		gm/cm³	23ºC	ASTM D792
Copper Peel Strength	1.05 (6.0)	0.88 (5.0)		N/mm (pli)	after solder float 1 oz. EDC Foil	IPC-TM-650 2.4.8
Flammability	N/A	[2]V-0				UL 94
Lead-Free Process Compatible	Yes	Yes				

Figure 2-12. Glass fibre properties (Rogers, 2015).

The aluminium alloy used in the MMSW and the future Micromegas wedges is called Aluminimum 6082 T6. The chemical composition and properties of which can be found in, Table 2-2 and Table 2-3 respectively. This material is a medium to high strength aluminium alloy with very good resistance to corrosion. The alloy is well known for its structural strength and is used in high stress situations such as trusses, bridges, cranes and other support applications (Aalco, 2015).

Table 2-2. Aluminium alloy 6082 T6 – Composition (Ravikumar, et al., 2007).

Element	% Composition
Silicon (Si)	0.70 – 1.30
Magnesium (Mg)	0.60 – 1.20
Manganese (Mn)	0.40 – 1.00
Iron (Fe)	≤ 0.50
Chromium (Cr)	≤ 0.25
Zinc (Zn)	≤ 0.20
Titanium (Ti)	≤ 0.10
Copper (Cu)	≤ 0.10
Aluminium (Al)	Balance

Table 2-3. Aluminium alloy 6082 T6 – Properties (Aalco, 2015) (Haba, 2008).

Property	Value
Density	$2.70\ g/cm^3$
Thermal Expansion	$23.4\ /K$
Modulus of Elasticity	$70\ GPa$
Thermal Conductivity	$180\ W/mK$
Yield Strength	$250\ MPa$
Tensile Strength	$300\ MPa$

The glue used to bond the aluminium honeycomb to the PCBs is called Araldite®. The properties of this glue that are relevant to this work can be found in Table 2-4.

Table 2-4. Araldite® – Properties (Rossi, 2015).

Property	Value
Density	$1 \ g/cm^3$
Thermal Expansion	$15 \ /K$
Modulus of Elasticity	$1.9 \ GPa$
Thermal Conductivity	$0.13 \ W/mK$

2.5 Steel

The steel sections available from the CERN storage is an encouraged option for use in the design of engineering components at CERN. The use of this steel allows sections to be cut to length quickly and cheaply when compared to external steel suppliers. The steel available in the CERN stores is a variety of rolled sections in the Standard EN 10025, grade S235JRG2. This is a structural steel used mainly in bolted and welded engineering structures with a yield strength of 235 MPa.

2.6 Solving Engineering Problems

When solving engineering problems it is important to consider the use of the three different analysis methods. These three approaches are the analytical method, experimental method and computational method. These three methods are often used in conjunction as a way to verify the obtained results. All three approaches are used and explored in this work, creating the need of a good understanding of the procedures each one entails.

2.7 Analytical Analysis

An analytical approach to solving an engineering problem uses predefined formulae and exact engineering parameters to calculate the solution to the problem. Analytical analyses are very accurate when the examined geometry is simple and regular. When a complex geometry is analysed, however, analytical methods often become impractical and tedious, making other analysis forms more viable.

2.7.1 Bending Stress

A beam is defined as a member with a small cross sectional area when compared to its length. A bending stress is applied to a beam when a load is applied to it creating bending effects rather than twisting or axial effects. The applied bending stress in a beam can be calculated using Equation 1 or a simplified Equation 2.

$$\sigma_b = \frac{My}{I_x}$$

Equation 1

$$\sigma_b = \frac{M}{w_x}$$

Equation 2

Where: σ_b: Bending stress (Pa)
           M: Bending moment (Nm)
           y: Perpendicular distance to bending neutral axis (m)
           I_x: Second moment of area about neutral axis (m^4)
           w_x: Section modulus (m^3)

From this equation, one can observe that the bending stress in a beam is defined by the relevant bending moment created by the position and strength of applied forces. The other input to this equation is the cross sectional shape and area of the beam. It is clear that a beam with a higher cross sectional moment of inertia will experience a lower bending stress.

2.7.2 Safety Factor of a Component

The safety factor is a dimensionless quantity that tells the reader the level of safety that the component was designed to, above its yield strength. The safety factor specified for all lifting equipment, according to the Standard BS EN 13155:2003 is 2. Consequently, all components designed in this thesis must survive at least double the applied stress before yielding. The safety factor of a component can be calculated using Equation 3.

$$SF = \frac{\sigma_y}{\sigma}$$

Equation 3

Where: SF: Safety factor
           σ_y: Yield strength (Pa)
           σ: Applied stress (Pa)

From this equation, one can observe that the safety factor is a ratio of the yield strength of the components material, over the peak expected stress applied to the component. A material with a higher yield stress will increase the safety factor of the component, while decreasing the applied stress will have the same positive effect.

2.7.3 Axial Load Deflection

When an object is loaded in its axial direction, its length will change depending on the size and direction of the load. If a compressive force is applied, the object will shorten in length, while if a tensile force is applied, the object will lengthen. The amount of deflection measured can be predicted using Equation 4.

$$\delta = \frac{FL}{EA}$$

Equation 4

Where:
δ: Change in length (m)
F: Applied force (N)
L: Original length (m)
E: Modulus of elasticity (Pa)
A: Original area (m^2)

From this equation, one can see that the amount of deflection depends on the applied force, the geometry of the component and the modulus of elasticity of the material.

2.7.4 Thermal Expansion

When most materials are heated, they linearly expand, changing the shape, area and volume of the object. This expansion occurs at a linear rate that is directly proportional to its change in temperature. The change in length in a desired orientation can be calculated using Equation 5.

$$\Delta L = \alpha L_0 \Delta T$$

Equation 5

Where:
ΔL: Change in length (mm)
α: Coefficient of linear thermal expansion $(\mu m/mm)$
L_0: Original length (mm)
ΔT: Change in temperature (K)

From this equation, one can see that the change in length of the object depends on the length of the object, the change in temperature and the materials coefficient of linear thermal expansion. This coefficient is different for all materials with a higher coefficient of linear thermal expansion

resulting in a larger change in length with a change in temperature. Using this equation, one can analytically predict the change of length of a material.

2.7.5 Composite Thermal Expansion

In order to calculate the thermal expansion of a composite material with varying shape or material, the equation to find the deflection due to an axial load, Equation 3, and the equation of thermal expansion, Equation 4, can be combined. Assuming that there is no bending due to the difference in expansion of the two materials and there are no shear strains in the material, Equation 6 (Spigo, 1989) can be derived.

$$(\Delta T \times L_1 \times \alpha_1) + \left(\frac{FL_1}{E_1 A_1}\right) = (\Delta T \times L_2 \times \alpha_2) + \left(\frac{FL_2}{E_2 A_2}\right)$$

Equation 6

Where: F: Applied force (N)
L_1: Original length of material 1 (m)
L_2: Original length of material 2 (m)
E: Modulus of elasticity (Pa)
A: Original area (m^2)
α: Coefficient of linear thermal expansion ($\mu m/mm$)
ΔT: Change in temperature (K)

This equation can be used to calculate the shear force that the materials exert on each other. A compressive force is experienced by the material with the higher coefficient of thermal expansion while a tensile force is experienced by the material with the lower coefficient of thermal expansion. Once this force is calculated, an equivalent coefficient of thermal expansion of the composite material can be calculated and used to find the materials thermal expansion. In order to accurately use this equation L_1 must be equal to L_2.

2.7.6 Error Analysis

When calculating the error in results obtained, the values must be compared to values that are already known to be true, the exact value. The percentage error is calculated using Equation 7.

$$Percentage\ Error = \frac{|Approximate\ value - Exact\ value|}{Exact\ value} \times 100$$

Equation 7

The percentage error is the result of the absolute error in the approximated value divided by the exact or known value.

2.8 Experimental Analysis

Experimental analysis is the oldest investigation method and is still commonly used in biology, agriculture, engineering and many other fields. The degree of the precision and completeness of the data and information determines the efficiency of the experiment. It is important to realise that the way in which the data are collected, greatly influences the outcome of the experiment. For this reason, it is important that the researcher clearly defines the objectives of the experiment and decides on a process in which the data are to be collected, knowing all the factors that are to effect the outcome. When designing an experimental analysis it is important to define clear independent and dependent variables as well as variables that are controlled and constant. The dependent and independent variables must be easily measurable and repeatable results should be obtained (Lazic, 2004). The variables that cannot be controlled should be recorded and included in the results. This process can be observed in the diagram in Figure 2-13.
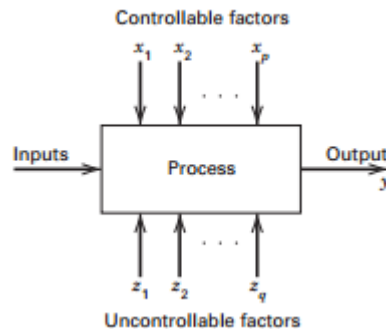
Figure 2-13. Experimental model (Montgomery, 2013).

2.9 Computational Analysis

Computational analysis is a form of investigation that uses computer hardware and software, mathematical models and numerical methods to approximate a solution to an engineering problem.

Computational analysis is accompanied by a number of advantages, the greatest being the ability to analyse some problems that are impossible to analyse using analytical or experimental methods. The results obtained from computational methods are always merely an approximation of the situation. If the analysis is done carefully, by a knowledgeable user, with a reliable software package and good computer processing power, however, computational analysis can offer a very accurate set of approximated results in lower time and cost when compared to the equivalent experimental analysis.

In order to achieve reliable results using a computational approach, the following specific analysis process needs to be followed (Pitot, 2014).

1. Beginning this process, it is essential that the problem at hand is assessed. A complete understanding of the problem and procedure to compute the problem must be gained.

2. Once an understanding of the problem is gained, the engineer must create the geometry that is to be used for the computational model. This can be done using CAD software, if possible the CAD should be created using the same software that is used for the model processing. This eliminates any chance of export and import faults. Simplifications can be made to the geometry if the designer is certain that the simplifications won't significantly skew the results.

3. Once the geometry has been created in an acceptable manner, the pre-processing of the model must be completed using pre-processing software. This processing involves creating an efficient mesh, specification of the materials and their properties and specification of the analysis boundary conditions and loads.

4. The solver that is to be used is now selected and the solution is run.

5. Once the solution has finished and there are no error messages observed, the post-processing of the results can proceed. This involves the retrieval of the results and generation of relevant, readable and understandable results.

6. The model should always be checked and the results, validated to ensure they are reliable.

The form of computational analysis used in this work is finite element analysis (FEA). FEA discretises the geometry and material properties into a series of points that can be used to analyse the model under varies loading conditions.

2.9.1 FEA Fundamentals

When a finite element analysis is done, the software discretises a user defined geometry into single points, creating simpler regions, called elements, collectively creating a mesh of the geometry. This is completed by replacing the continuous differential functions with piecewise approximations. The solver is then able to complete an approximation of the original geometry by using simple element equations at each element. Interpolation functions are able to approximate the variation of the solution between the discretised points. These elements are surrounded by nodes and can be found in either one, two or three dimensional form (Delpero, et al., 2010) (Pitot, 2014). When a mesh is created, the sizing of the elements needs to be defined. The smaller the

mesh, the closer the solution becomes to its asymptotic, perfect solution. However, with this increase in accuracy comes an increase in the computational size of the model. Mesh independence is the point where an increase in the accuracy of the mesh results in no further improvement to the solution, creating a reliable set of results (Pitot, 2014).

Finite element analysis handles complex geometries very well when compared to an analytical approach and is popular in structural and thermal problems.

2.9.2 FEA Elements

Ansys allows for one, two and three dimensional elements to be included when creating the geometry of a component in the Ansys Design Modeler. Simplifying a component's geometry to its simplest elements will decrease the complexity of the simulation and thus reduces the run time of the solution. However, if the wrong simplifications are made, the results obtained may be inaccurate.

One dimensional elements are known as beam or line elements. They are uniaxial and have two nodes, one on each side of the element. Beam elements are generally used when the structure has one dimensional properties and the cross sectional area of the geometry is insignificant when compared to its length. When creating a beam element, an infinitely thin line is produced, it is then possible to add a predefined cross section to this beam giving it a moment of inertia (ANSYS, 2013).

Two dimensional elements are known as shell or planar elements. These elements are typically used for thin structures that experience bending. Stresses are assumed to change linearly through the thickness of the material. The middle surface is assumed to have zero bending stress. It is possible to apply a composite material to a shell element, giving it the properties of a predefined composite lay-up (ANSYS, 2013).

2.10 Lifting Stability

Lifting tools and procedures play a large role in the assembly of the NSW. If the lifting operation is not done effectively, damage to property and injury is likely to occur. Lifting equipment must always be reliably connected to the crane hook by a process called slinging. Safe slinging and confirmed stability of the lifted objects is essential. To ensure this, slinging must always be carried out according to a pre-planned procedure. The suspension system must be planned according to the objects weight and shape. The location of the lifting points must be considered in order to

minimise the stresses induced in the lifted object, keep the tension in the slings at a minimum and to ensure that the lifted object will remain stable during the entire lifting procedure. The stability of a lifting system refers to whether or not the suspension arrangement allows the object to remain in its normally upright position. In general, the lower the centre of gravity is, in relation to the lifting points, the more stable the suspension arrangement will be. Objects are generally lifted in one of the two methods shown in Figure 2-14.
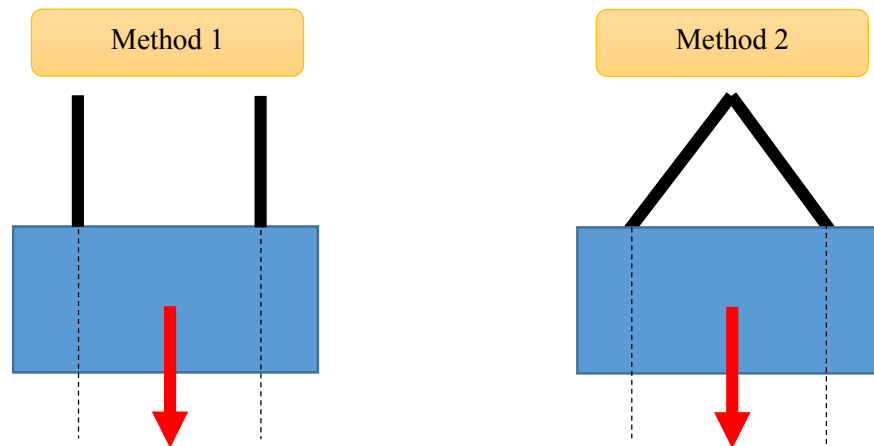
Figure 2-14. Slinging methods.

The slinging method labelled, Method 1, involves the use of two vertical slings. This method is stable for all situations where the center of gravity is between the dashed lines extending vertically from the slings. The tension in the slings depend on the position of the centre of mass of the lifted object. When the centre of mass is situated centrally between the two slings, the tension in the slings are equal. As the centre of mass moves horizontally towards either sling, however, the tension in that sling will increase until the centre of mass is directly below that sling, at which point, the complete weight of the object will be supported by that individual sling while the other sling will carry no load. If the centre of mass moves outside the region between the dashed lines, the object will rotate, keeping the centre of mass directly underneath one of the slings, regaining stability (Kaps, 2013).

The slinging method labelled, Method 2, has diagonal slings that meet at the centre. This method is more commonly used in practice due to slings being attached to the single hook of an overhead crane. The center of gravity will always readjust until it is directly below the point at which the two slings meet. If no movement or tilt is accepted during the lifting operation, then the sling

mounts must be positioned at equal horizontal distances from the centre of mass of the lifted object, resulting in a vertically aligned centre of mass and sling meeting point. If the slings are the same length, the tension in the slings will always be equal in this slinging method, however, if the slings have different lengths, the sling closer to the centre of mass will have a higher vertical force and thus a higher tension (Kaps, 2013).

CHAPTER 3 - METHODOLOGY

The process implemented for the completion of the required objectives needs to be followed in a predefined order to ensure that the effects of each decision, on other components, are considered at all times.

The first step that must be completed is a series of design concepts of all the necessary components. This allows the designer to see issues that are to arise later, at an early stage, and design all components with these complications in mind. At this stage, the designs do not need to be finalised, but all the constraints need to be considered and rough sizes and design techniques must be selected.

The transport, assembly and storage tools all rely on the design and position of the spacer frame mounts. Once all the components have been considered, the spacer frame mounts can be designed. These mounts are to be designed considering all effects they will have on future designs of the transport, storage and assembly tools. Not only do the mounts need to meet the restrictions provided by the designs of this tooling, but they also need to be compatible with other NSW assembly procedures such as the assembly of the sectors to the NSW structure. A successful stress analysis is to be performed on these mounts.

On completion of the design of the spacer frame mounts, the transport, storage and assembly tool designs can be performed. During the design of each of these three assemblies, the other two should always be considered. Components of each of these assemblies that can be designed in a way that allows them to serve more than one function is a desired outcome in order to save money and manufacturing time and resources. The three tools should be designed to minimise the floor space that they use in order to aid the design of the building layout.

Once the designs of each of the three tooling components are complete, the building floor layout plan is to be completed. This should be done in a space efficient manner and if any of the components are not compatible with the floor plan, the component should be redesigned, if possible, to accommodate the limited floor space.

Once the tooling for the various procedures has been completed, the analysis of the Micromegas wedge simulation method must be performed. In order to achieve this, a hypothesis of the comparison needs to be defined. The experimental analysis and the computational simulation must then be completed. Once the results of both analyses have been achieved, they must be compared

and an error in the computational results must be provided. This will create a platform to accurately analyse the Micromegas wedges for the various procedures.

A summary of this methodology can be observed in the flow diagram represented in Figure 3-1
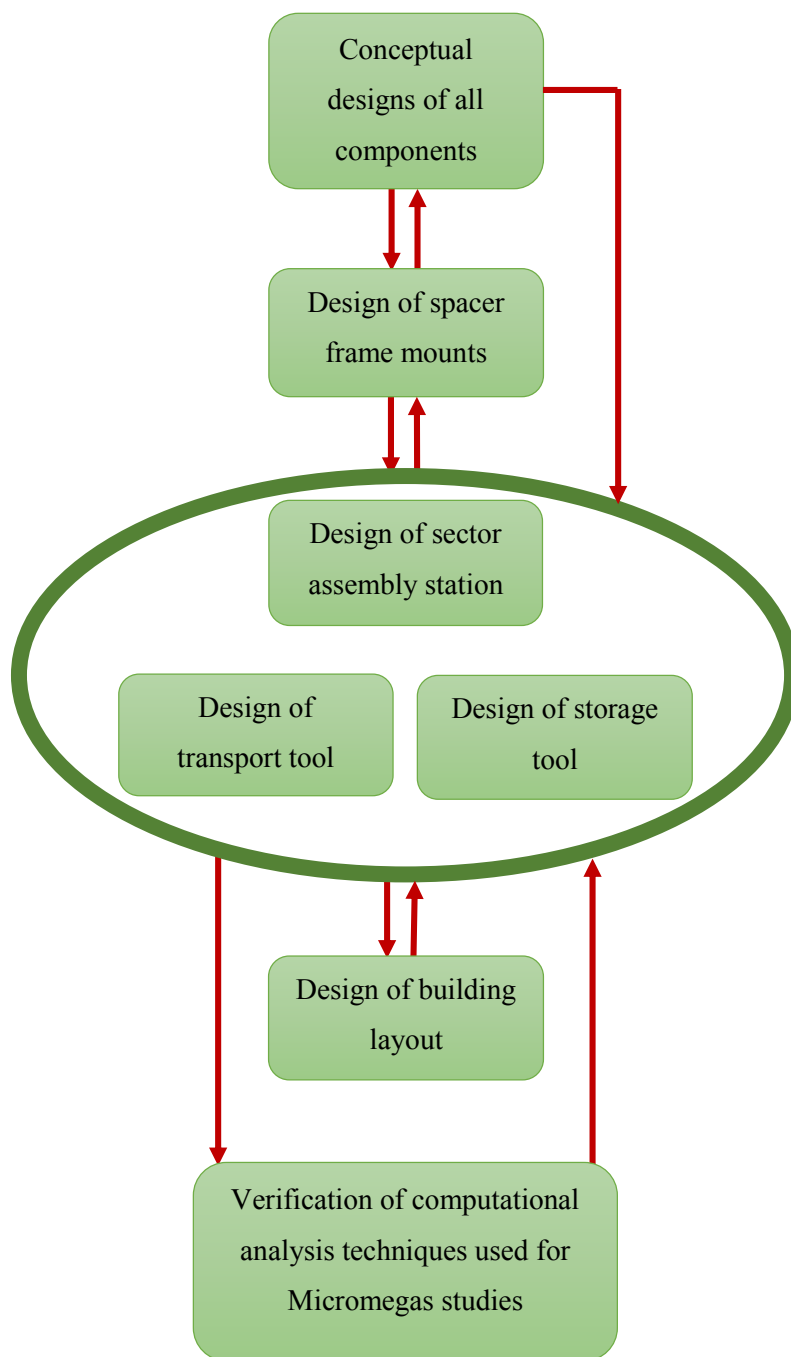
Figure 3-1. Methodology flow chart summary.

CHAPTER 4 - SPACER FRAME MOUNTS

4.1   Introduction

The Micromegas chambers, sTGCs and consequently the fully assembled NSW sectors are very delicate structures and must be manoeuvred with caution at all times. Because of their large mass of 1450 kg for the large sector and 1100 kg for the small sector, substantial stresses and deformations will occur during manipulation if they are not supported in the correct manner. In order to manipulate these components correctly, mounts have been developed that support the Micromegas chambers and the fully assembled NSW sectors in a way that minimises the stresses and deformations induced on the structure. These mounts are attached at the spacer frame and used during transport, storage and assembly of the Micromegas chambers and NSW sectors. A representation of the final designed spacer frame mount can be observed in Figure 4-1.
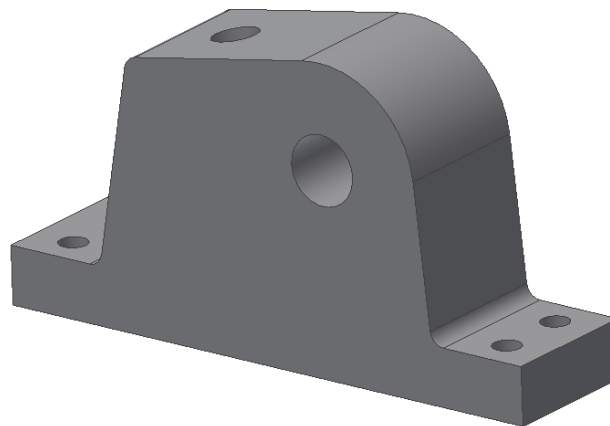
Figure 4-1. Spacer frame mount.

4.2   Design Constraints

The spacer frame mounts are required to support the NSW sectors during all manipulation procedures in a way that applies minimum stresses to the components of the Micromegas chambers. The mounts are to be attached at the spacer frame and fit within the spacer frames thickness envelope of 50 mm in order to avoid contact with the Micromegas services. The mounts must be compatible with the spacer frame connections designed by the spacer frame design team, represented in Figure 4-2. These connections are situated at predefined locations on the spacer frame that cannot easily be rearranged due to obstruction of other spacer frame components. The reliability of these placements must be considered, however, it is desirable that these mounts are

designed in a way that allows them to be used in these predefined positions. The mounts must not only be clear of all Micromegas and sTGC services but also be clear of any NSW structural members and alignment cameras when the sectors are installed to the NSW.
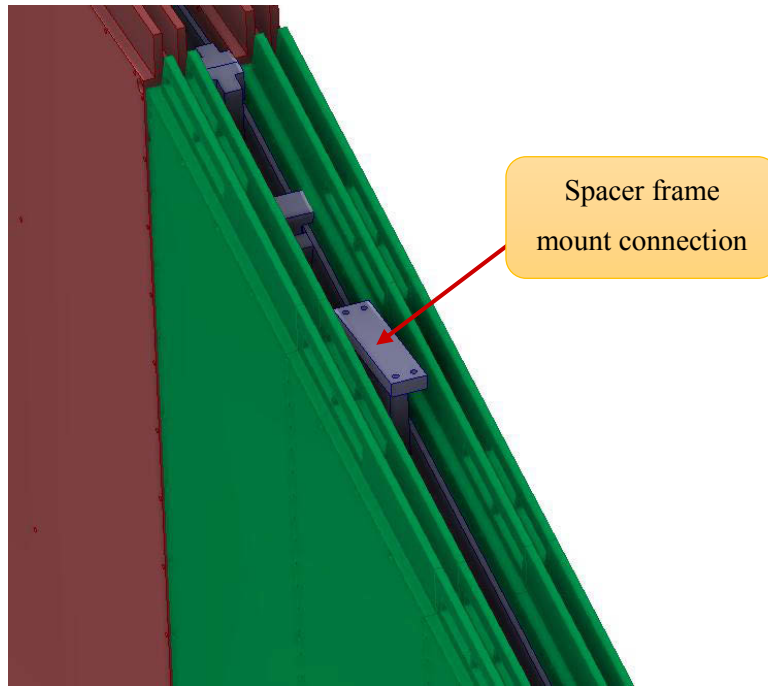
Figure 4-2. Spacer frame mount connection (Sinclair & ATLAS, 2015).

The spacer frame mounts are to be used for lifting operations and therefore must be designed to a safety factor of 2, according to the Euro-code and CERN design standards.

4.3   Final Design

The spacer frame mounts are to be used during all procedures that require the support of the Micromegas chambers and NSW sectors. In order to achieve this appropriately, the mounts were positioned and used in a way that minimises the effects of bending under the large weight of the components. All objects have a greatest resistance to bending in their orientation with the highest moment of inertia. In the case of the Micromegas chambers, sTGCs and consequently, the NSW sectors, this is when they are in the upright, vertical orientation. To accommodate this, they should always be manipulated in one of the three orientations observed in Figure 4-3.

To avoid the space and height requirements that result when the Micromegas chambers and NSW sectors are manipulated in the orientation labelled Orientation 1, in Figure 4-3, the chambers and

sectors should always be manoeuvred in the orientations labelled Orientation 2 and Orientation 3. Due to constraints during the NSW sector assembly process discussed in Chapter 6, however, the Micromegas chambers and NSW sectors are to be manipulated in the orientation labelled Orientation 3. The spacer frame mounts were therefore designed in a way in which they can be easily attached to the spacer frame and support the chamber in this manner.

| Orientation 1 | Orientation 2 | Orientation 3 |
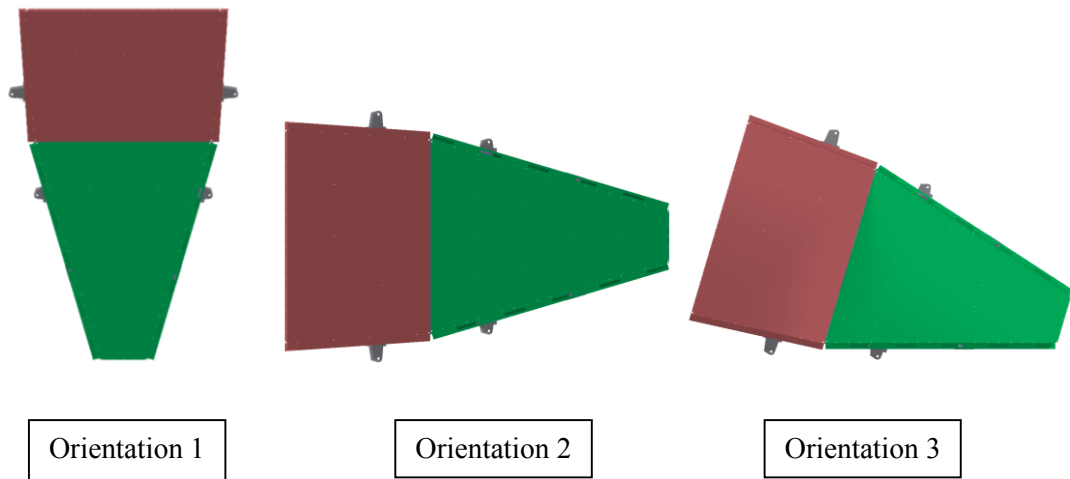
Figure 4-3. Three possible Micromegas manipulation orientations (Sinclair & ATLAS, 2015).

In order to confirm that the sectors can be safely hung by vertical slings, the centre of mass of the NSW sector were calculated to lie in between the two mounting points in the horizontal direction. The calculations of the position of the centres of mass of each of the sectors can be seen in Appendix A.1, while their positions are illustrated in the images labelled Figure A-1 and Figure A-2 in Appendix A.2. In these images, it is observed that the centre of mass of each of the sectors lies in between the mounting points confirming that the sectors can be hung in a stable manner.

When designing all engineering components, an advantage is achieved when a single part can serve many purposes. For this reason, the mounts that are to be used to mount the NSW sectors to the NSW structure (grabber mounts) and the mounts used to support the sector during the transport, assembly and storage procedures (sector support mounts) were combined into one mount with two mounting points. This not only saves time and money but also reduces the overall weight of the sector and creates more space on the spacer frame.

The image in Figure 4-4 represents the final spacer frame mount design and how it is installed to the spacer frame connection. Figure 4-5 is a labelled representation of the spacer frame mount

and the part of the spacer frame that it is mounted to. The individual mounting points for the grabber mount and the sector support mount acting perpendicular to each other is represented. It can be observed that four M10 bolts are used to achieve this connection. The bolts have a 10 mm shank through the spacer frame mount and an M10 thread that is bolted directly to the spacer frame connection.
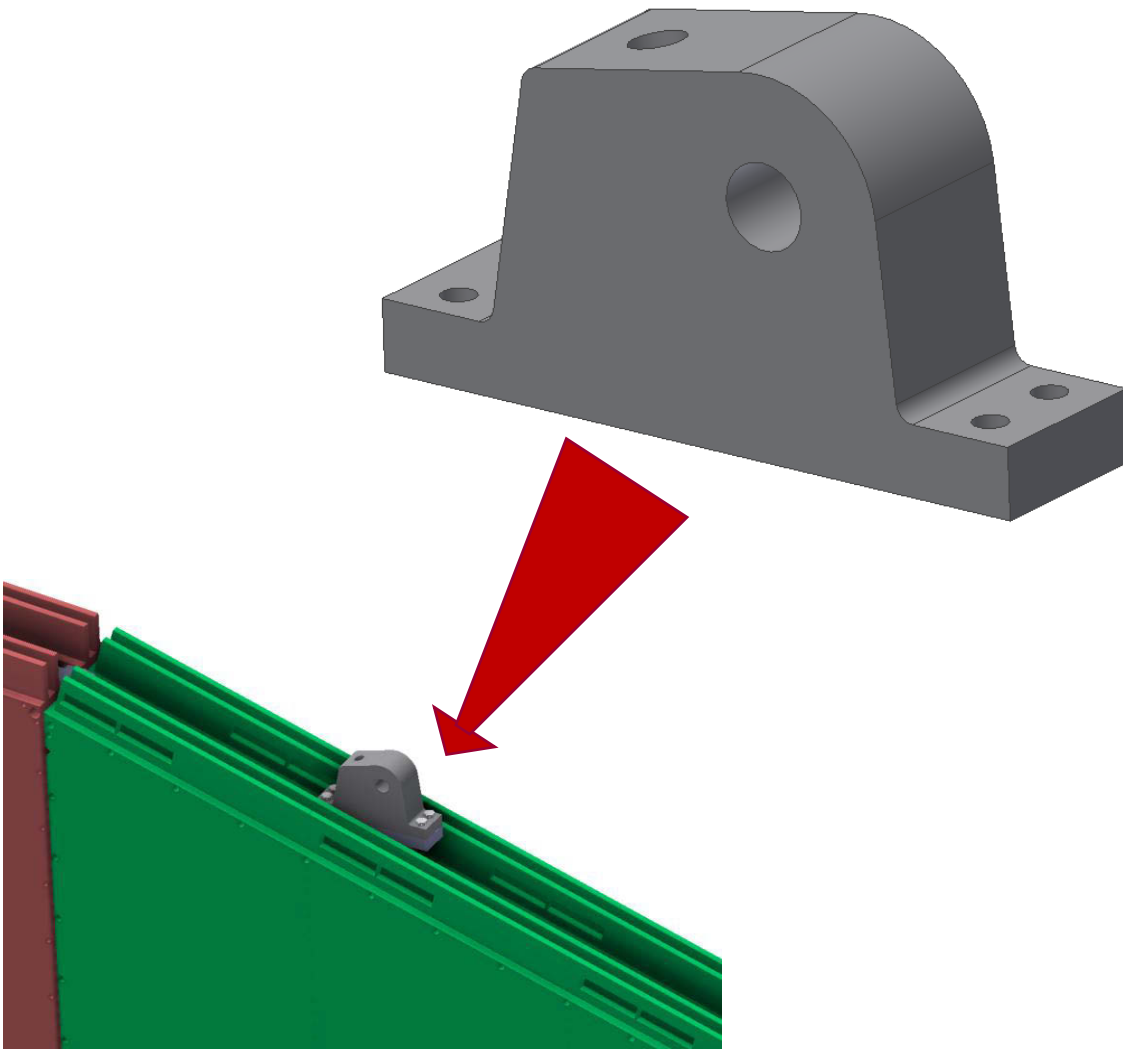
Figure 4-4. Installed spacer frame mounts (Sinclair & ATLAS, 2015).
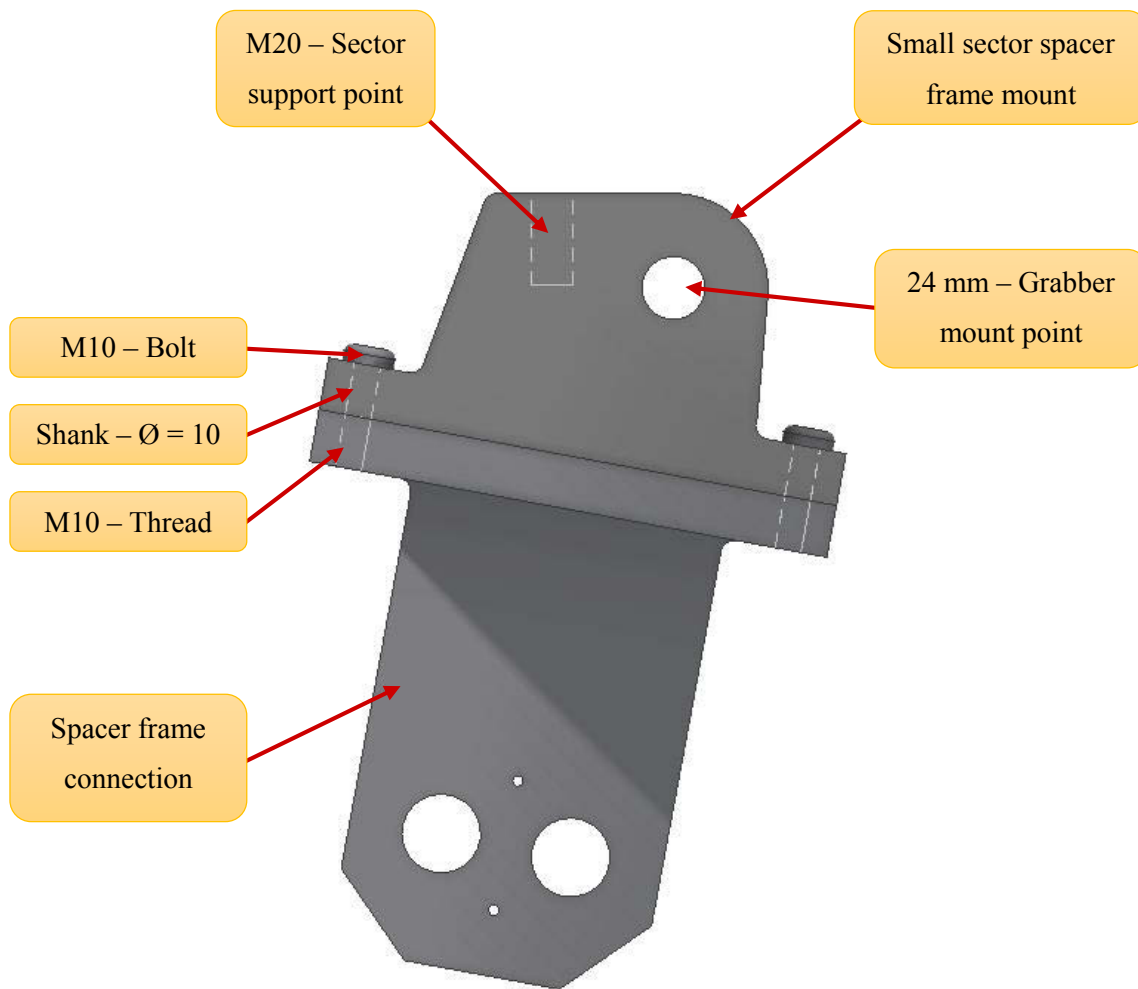
Figure 4-5. Small sector spacer frame mount (Sinclair & ATLAS, 2015).

Due to the size of the sTGC services, the mounts extend outwards, away from the spacer frames in order to avoid contact between the grabber and the sTGC services during lifting operations. The mounts are, however, not so large that they obstruct other components of the NSW assembly. For this reason, there are two different spacer frame mount designs for the large sector and one design for the small sector, creating a total of three different spacer frame mounts for the NSW sectors. The geometry design principal of each of the three mounts is equivalent, however, each experiences a difference in overall dimensions. The differences in the three spacer frame mounts can be observed in Figure 4-6.
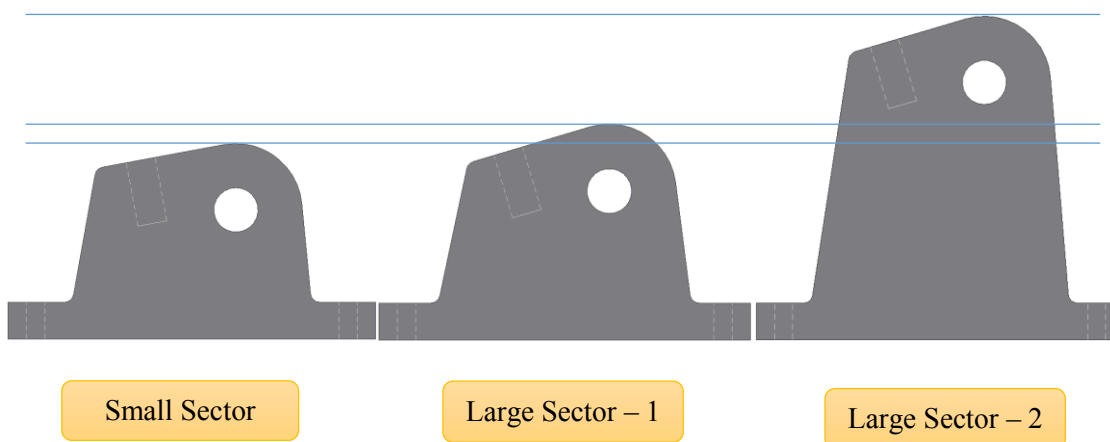
Figure 4-6. Spacer frame mounts.

It is clear from observation of Figure 4-6 that the only difference in each mount is its height. The total height of each of the spacer frame mounts can be observed in Table 4-1 while the dimensions that are common in each of the mounts can be observed in the drawing represented in Appendix B.1.

Table 4-1. Spacer frame mount heights.

Spacer frame mount	Height (mm)
Small Sector	106
Large sector – 1	116
Large sector – 2	176

The installed spacer frame mounts for the small and large sectors can be seen in the images of the fully assembled NSW in Figure 4-7 and Figure 4-8 respectively. In these images, it is clear that the spacer frame mounts do not obstruct any NSW support or alignment structures and the designs are compatible with the mount positioning provided.
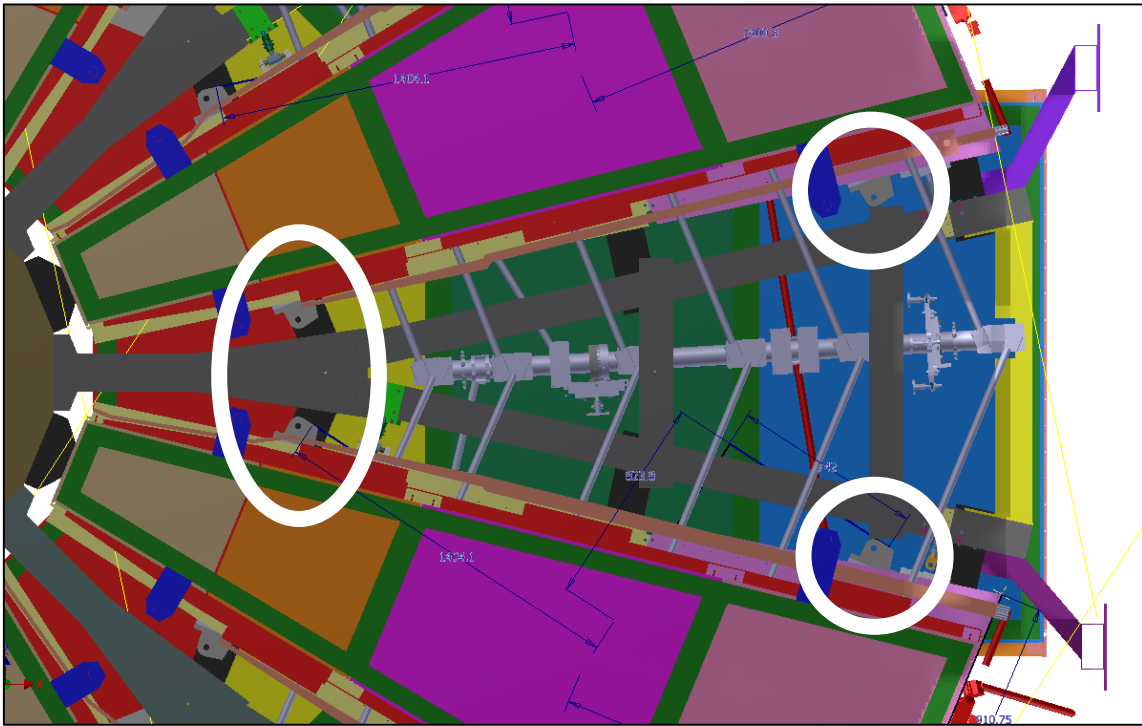
Figure 4-7. Installed small sector spacer frame mounts (Sinclair & ATLAS, 2015).
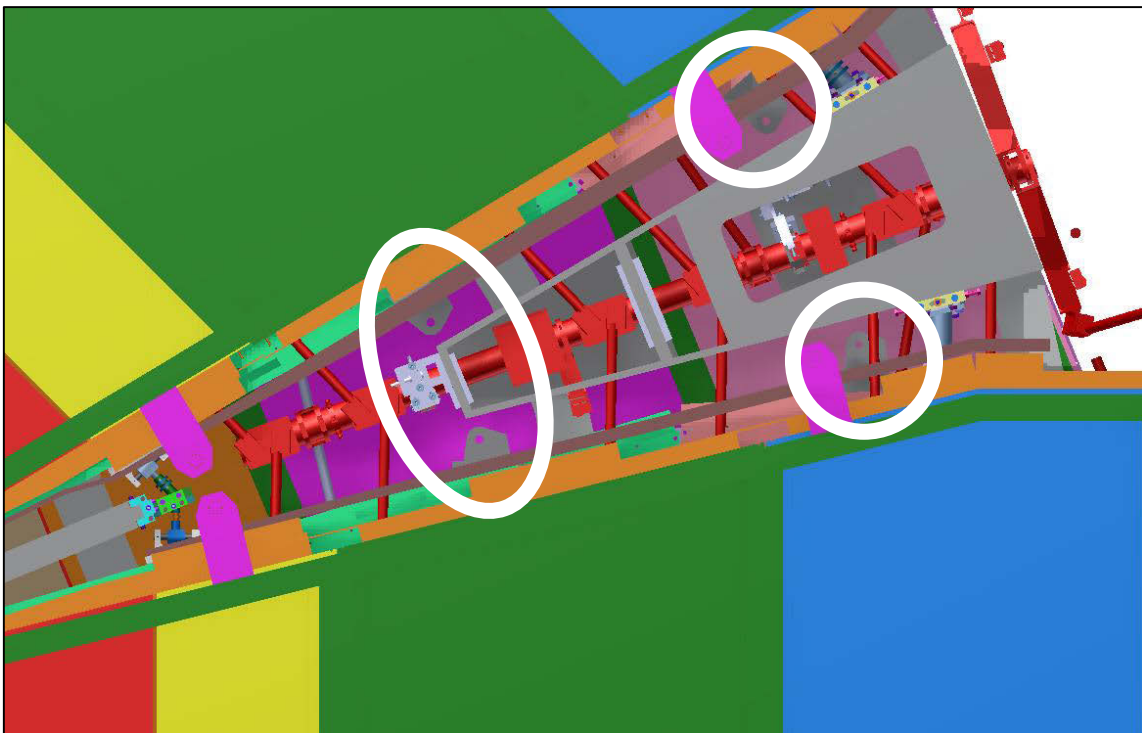
Figure 4-8. Installed large sector spacer frame mounts (Sinclair & ATLAS, 2015).

An FEA stress analysis of the spacer frame mounts subjected to the loading applied during transport, assembly and storage was completed. The conditions and constraints applied to the geometry in this analysis can be observed in Figure B-1 in Appendix B.3. The forces applied by the sector to each mount calculated in Appendix A.2 were applied to the mounts and the FEA simulation was completed for each. Detailed images of these simulations can be found in Appendix B.3 while a summary of the forces and the maximum resultant stresses for each mount can be observed in Table 4-2.

Table 4-2. Spacer frame mount stresses.

Spacer frame mount	Applied force (N)	Maximum stress (MPa)
Small Sector	7060	37.93
Large sector – 1	4293	19.30
Large sector – 2	9932	42.93

For ease of manufacture, all the mounts are to be made out of the same material. The maximum stress applied to any of the spacer frame mounts is 42.93 MPa, which is the stress that the material of the spacer frame mounts should be chosen for. A full analysis of the spacer frame mount under the loading conditions during NSW assembly should be completed by the NSW assembly tool designer, however, recommendations are made for the material to be used if only the sector support mount is used. Hot rolled S235JRG2 steel plates can be used offering a safety factor of 5.47. Aluminium Alloy 6082 – T6, which is used for many other NSW sector components, can be used offering a safety factor of 5.82. Another aluminium alloy such as 5083 – H112 with a yield strength of 190 MPa could be used, offering a minimum safety factor of 4.43. The calculations for all three safety factors can be observed in Appendix B.4.

CHAPTER 5 - TRANSPORT TOOL

5.1   Introduction

The transport tool is to be used to transport Micromegas chambers from their point of manufacture in Building 899 to the sector assembly station in Building 191. After sector assembly, the tool will then be used to store fully assembled NSW sectors. The final design of the transport tool can be observed in Figure 5-1 and Figure 5-2. In these images, the tool is being used to support and transport four large Micromegas chambers. The fundamental transport tool components have been labelled and will be referred to as such in this work.
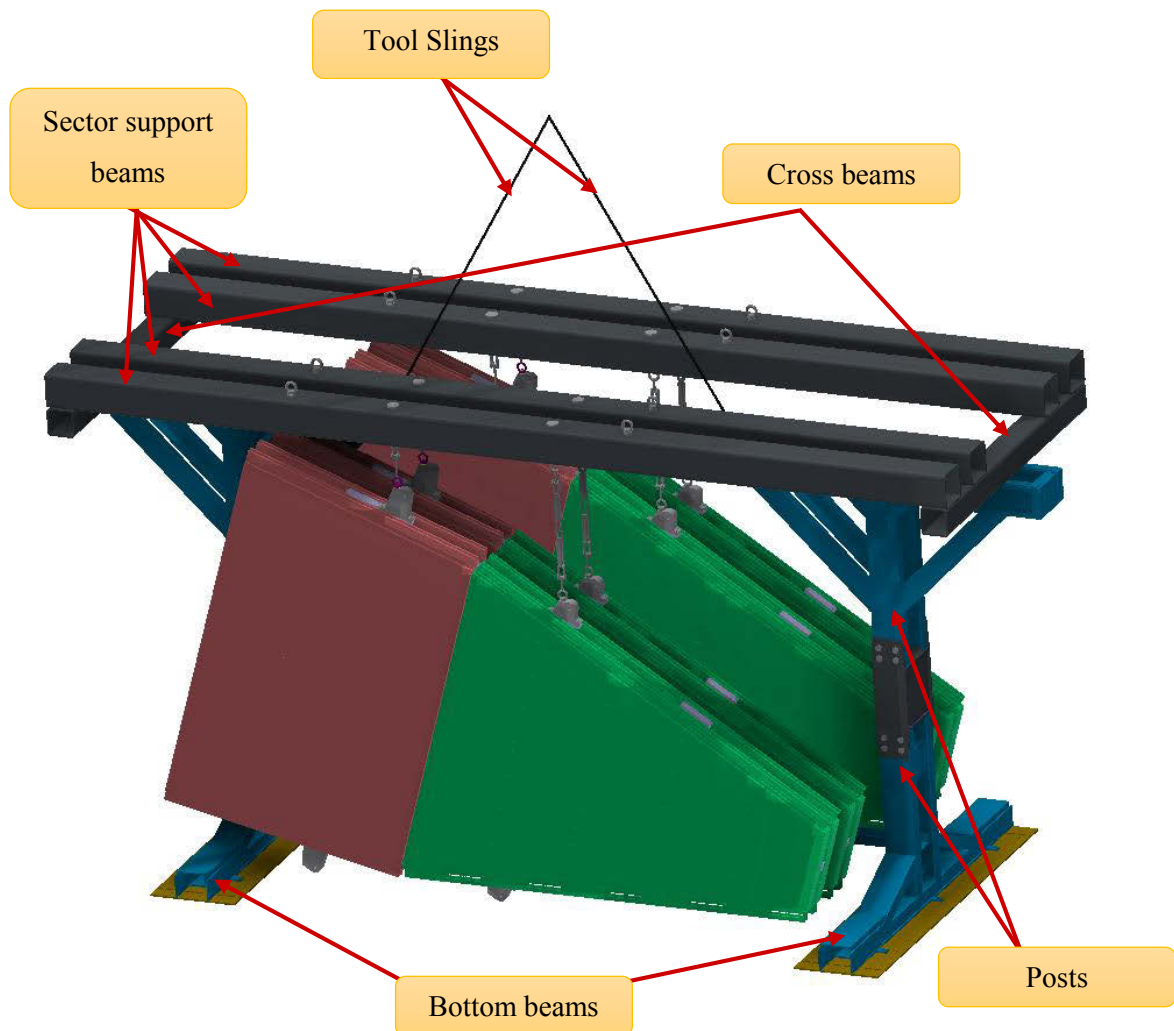
Figure 5-1. Loaded Micromegas chamber transport tool.
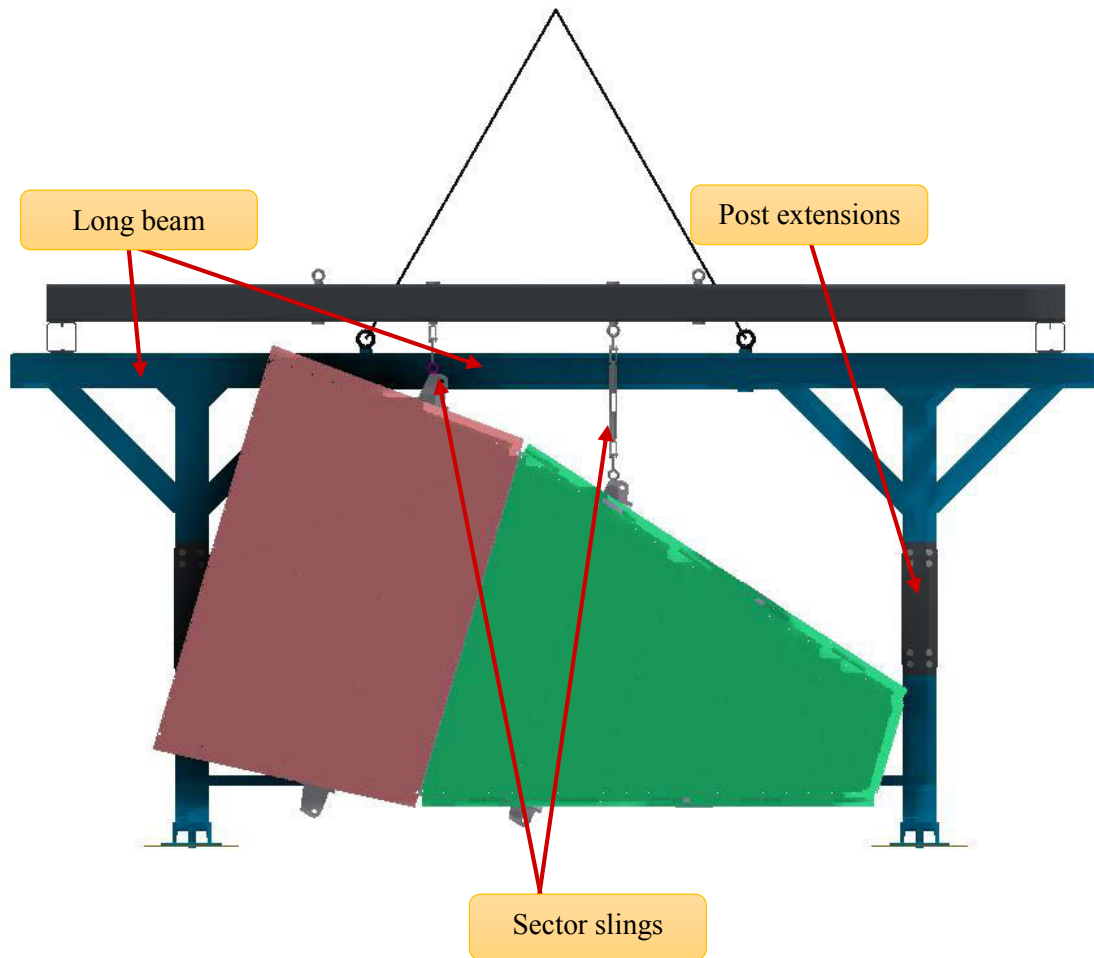
Figure 5-2. Loaded Micromegas chamber transport tool – Front view.

5.2   Design Constraints

The Micromegas chamber and NSW sector transport tool needs to be designed and manufactured in a way that meets all the design requirements and constraints confirmed by the ATLAS community, while keeping manufacturing time and cost at a minimum. The design must be in accordance with CERN design standards and regulations and follow the Eurocode. Safety documents confirming the complete safety of the transport tool must therefore be provided.

When the ATLAS Experiment was first assembled, the Endcap Outer (EO) muon chambers needed to be transported in a similar way to the Micromegas chambers. In order to transport these tracking chambers, a transport tool was designed and four were manufactured for use. This EO muon chamber transport tool is to be analysed and if possible, adapted in such a way that makes

it suitable for the transportation of the Micromegas chambers and NSW sectors. If this is not possible, a new transport tool is to be designed and manufactured, this is not a desirable situation due to time and resource restrictions.

The load requirements of the transport tool is that it should be able to carry four small or four large double Micromegas chambers estimated at 553 kg and 680 kg each, respectively, or two small or two large NSW sectors estimated to each weigh 1100 kg and 1450 kg each, respectively. Any one of the four Micromegas chambers should be able to be removed from the transport tool without the need to remove any of the other three first.

The trip from Building 899 to Building 191 runs across tram lines and consequently, beneath the tram chains running overhead. The specific rules that must be met when passing beneath the 5.5 m high tram chains follow:

1. If the object being transported is higher than 5.5 m, the tram chains must be cut and removed.
2. If the object being transported is lower than 5.5 m but higher than 4.5 m, the object must be transported when the tram chains are off to avoid high voltage electrical arcing.
3. If the object being transported is lower than 4.5 m, no special rules need to be considered and the transport can proceed freely and safely.

Another height restriction that should be met if possible, is the height of the garage door in Building 899 of 4 m. If this cannot be achieved then the transport tool, loaded with Micromegas chambers will have to be manoeuvred out of the building before loading it onto the transport trailer. This is an undesirable situation because the exposure of the Micromegas chambers to the elements should be avoided as much as possible. The weather conditions such as the hot sun or cool winds will create uneven heating and cooling on the chambers resulting in large detrimental deformations and stresses of the structure. Another option that could be considered is the alteration of the door making it high enough for the transport tool to pass under. This is again an undesirable solution because to complete these alterations, a great deal of money and resources will be used.

A full analysis on the minimum possible safe height of the transport tool and transport trailer combination should be conducted in order to transport the chambers in the most efficient way. The optimum design height that can be achieved is a height less than 4 metres while still leaving enough space for safe attachment of the Micromegas chambers and NSW sectors.

It is essential that stresses in the Micromegas chamber should be kept to a minimum during transportation. This means that an appropriate Micromegas chamber fastening method should be considered. Other precautions that may help reduce stresses on the chambers should also be considered.

The diagram in Figure 5-3 is a summary of all the design constraints that should be met by the transport tool.
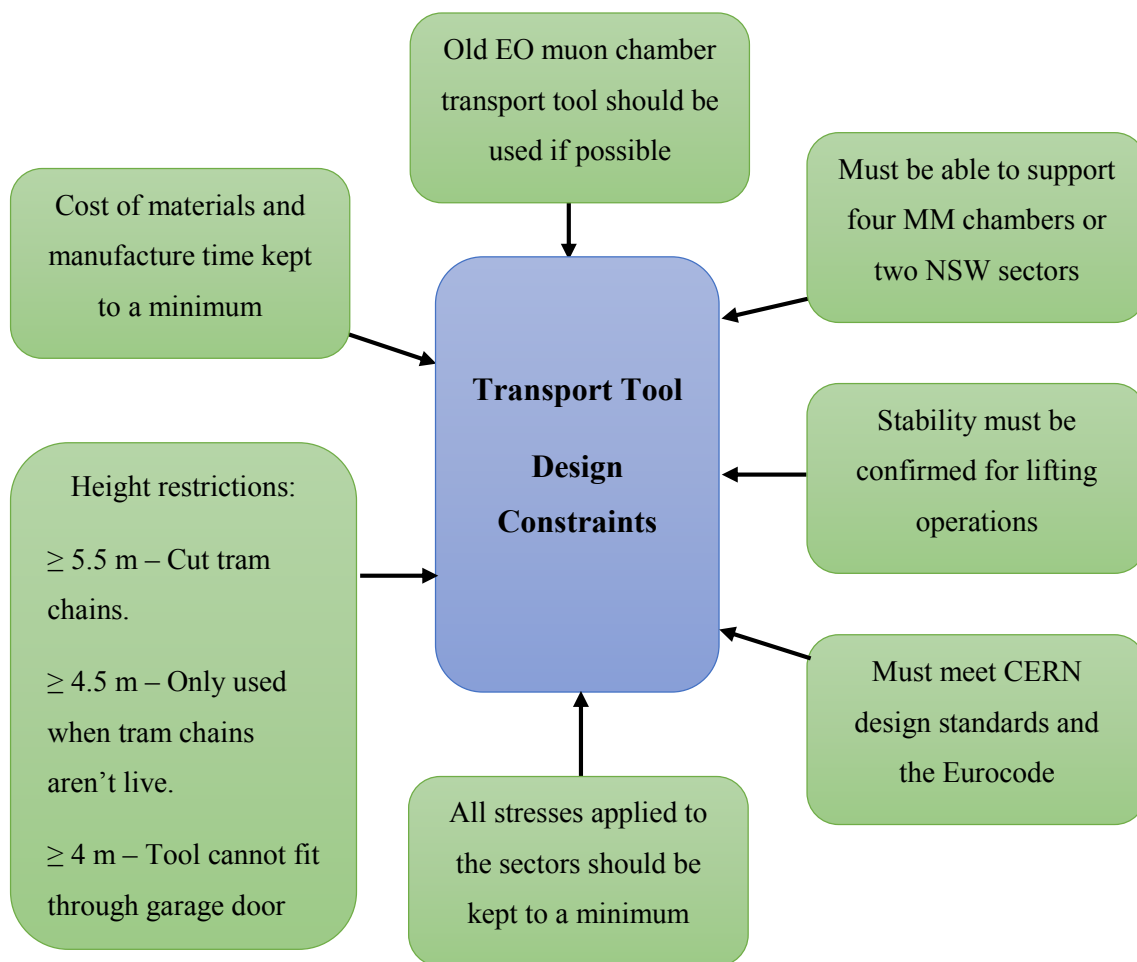
Figure 5-3. Transport tool design constraints summary.

5.3 Final Design

Keeping the design constraints previously discussed in mind, it is evident that a tool and trailer combination at a height lower than 4 m is desired and is the primary aim of the transport tool design. An adaption of the old EO muon chamber transport tool requires the least design and manufacture time and reduce money spent in the process.

After an analysis of the EO muon transport tool and the size and weight of the Micromegas chambers and NSW sectors, it was evident that modifications could be made to the transport tool in order to make it suitable for this application. The height of the tool is increased by extending the height of the upright posts. Some of the support components are also changed in order to meet the new loads applied by the large weights of the Micromegas chambers and NSW sectors. Figure 5-4 is an image of the EO muon chamber transport tool with the expected modifications represented.
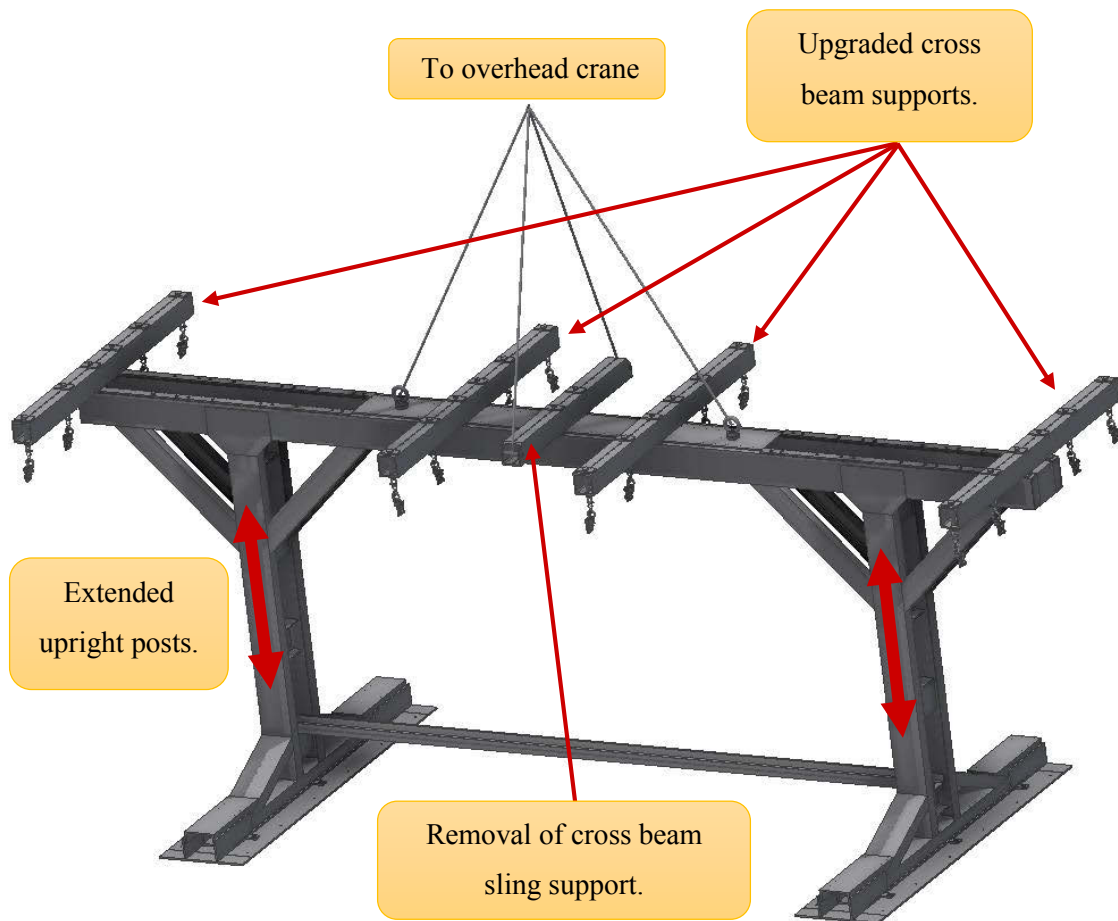
Figure 5-4. EO muon chamber transport tool (Sinclair & ATLAS, 2015).

The process that was used for the design of the modified transport tool followed a set procedure in order to ensure that the smallest, lightest and cheapest design was achieved while meeting all of the design constraints. The process is summarised in the flow chart found in Figure 5-5 while the work to follow fully describes the steps that were followed to achieve the design.
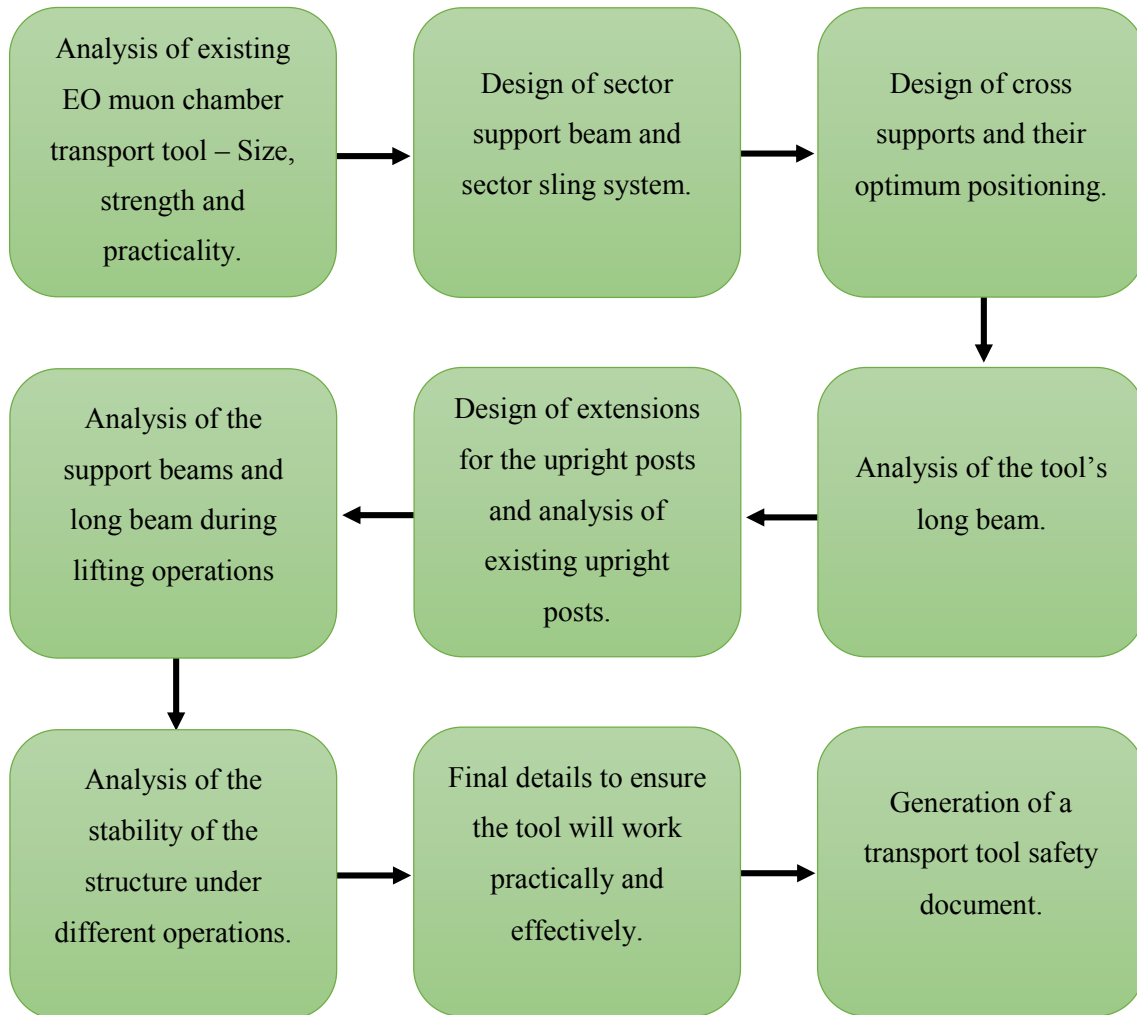
Figure 5-5. Design procedure for the transport tool.

With the primary height goal of the transport tool to be at a maximum height of 4 m above the ground during use, the height of the trailer to be used for this operation needs to be considered. The bed height of the trailer with the lowest height, meeting the load requirements applied by the fully loaded transport tool, is 900 mm. This distance is the total height from the ground to the top

of the bed of the trailer. This provided the information that the maximum height that the transport tool could be designed to was 3.1 m.

The Micromegas chambers and NSW sectors are to be hung from the transport tool by means of slings as an alternative to creating fixed fastening points for the detectors on the transport tool. This reduces the applied stresses in the Micromegas chambers and NSW sectors by removing the forces caused by a rigid connection. This also means that the Micromegas chambers are isolated from a large part of the stresses caused by vibrations during transport on the road. This is the same philosophy that was used during the design of the tooling for the EO muon chambers' transport tool.

The design procedure used for the transport tool began at the design of the support beam and connecting slings of the double Micromegas chambers. This assembly for the large and small sectors can be observed in Figure 5-6 and Figure 5-7 respectively. In the past, large support frames, mounting to the various detectors at many points have been used during transport and storage. The detector support ideology has, however, changed for the transport and storage of the Micromegas chambers and NSW sectors. A support mechanism that will stay attached to the spacer frame during transport, assembly and storage by means of vertical slings in tension will be used. These slings are mounted directly to the spacer frame in the middle of the double Micromegas chamber by means of spacer frame mounts. The support structure has a multipurpose design and is compatible with the transport, assembly and storage structures. This means that this support structure will be used for the initial Micromegas chamber storage in Building 899, the transport from Building 899 to Building 191, the sector assembly in Building 191 and ultimately, storage of the fully assembled NSW sectors before they are assembled to the NSW in Building 191.

The support structure comprises of the Micromegas chambers hanging from a square tube by means of slings. This beam, sling and Micromegas arrangement found in Figure 5-6 and Figure 5-7 will remain constant throughout the process until the sectors are ready to be assembled to the NSW. This eliminates the need for multiple support structures to be created for each stage in the NSW sector assembly and reduces the amount of times the Micromegas need to be directly handled, reducing the chance of damage occurring during any of the operations.

\
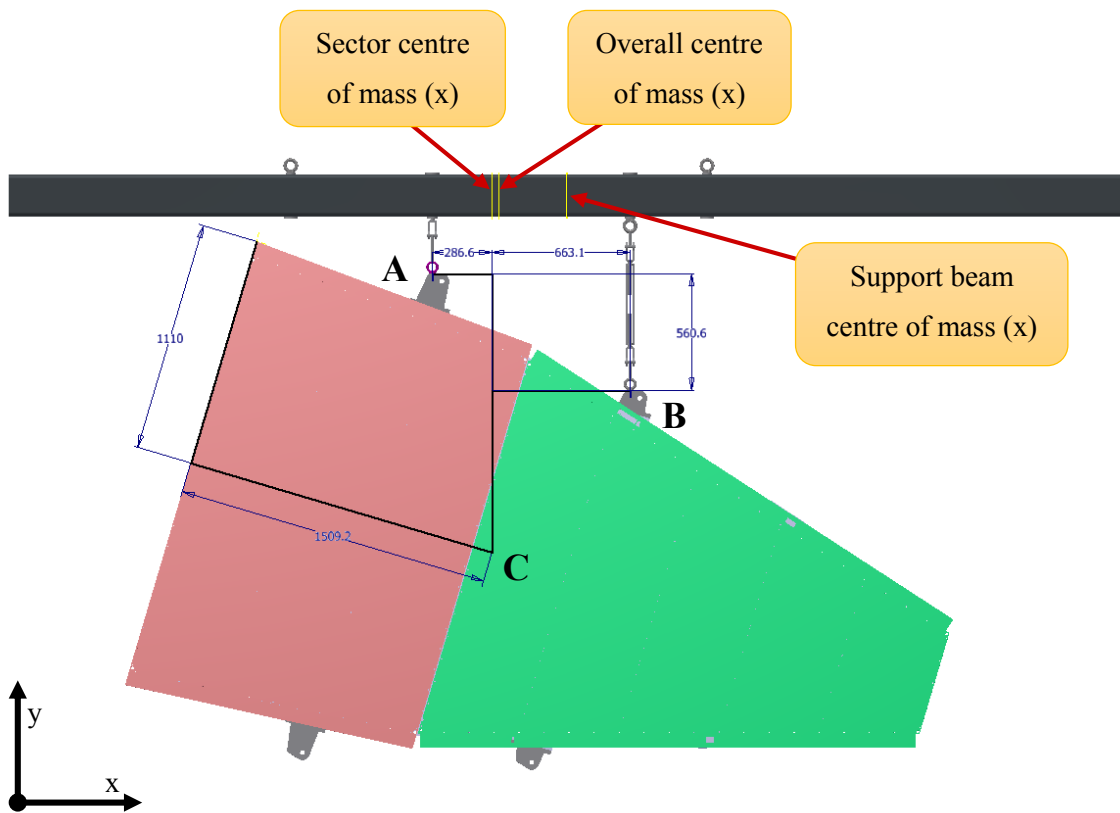
Figure 5-6. Large Micromegas chamber support.
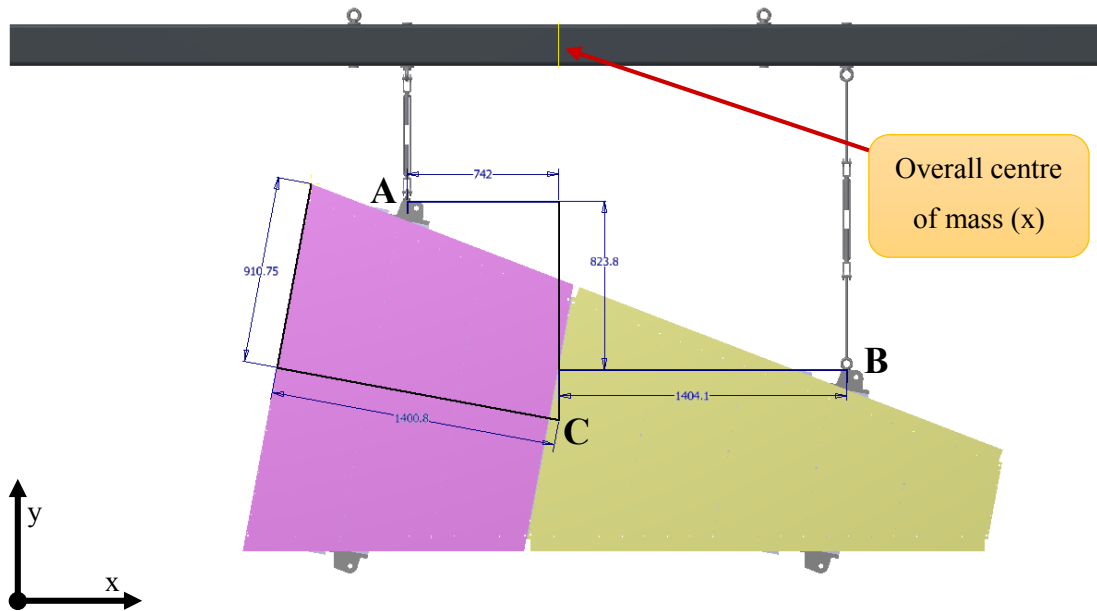
Figure 5-7. Small Micromegas chamber support.

It was desirable that the centres of mass of each of the sectors were to lie directly below the center of mass of the sector support beam. This would keep the overall center of mass of the assembly in line, relative to its x-coordinate, with the geometric center of the beam and thus of the transport tool. In order to keep the large sector from coming into contact with the bottom beam of the transport tool, it was moved slightly to the left from this ideal position, as can be observed in Figure 5-6. Due to this shift, the centre of mass of the large Micromegas chamber has been shifted 360 mm to the left of the centre of mass of the sector support beam and the transport tool. This shift creates a shift in the centre of mass of the loaded tool and creates uneven stresses in the tool which were be accounted for in the calculations that follow. The side that the sector has been shifted to, is referred to as the heavy side while the side the sector has been shifted away from, is referred to as the light side. The small sector fits on the tool above the bottom beam and therefore does not need to be shifted, allowing the centre of mass of the small sector to fall in line with the centre of mass of the sector support beam and thus, the transport tool.

In order to choose an appropriate material, length and cross sectional shape for the sector support beam, the loads applied to it by the tension in the slings caused by the weight of the sectors needed to be calculated. In order to complete this calculation, the sectors were simplified to a point load acting at each of their centre of masses. The centre of mass calculations of the large and the small sectors can be found in Appendix A.1 where an accepted assumption that the centre of mass of the sectors is at the same point as their centre of their geometry was made. When using the corner of the heavy side of the Micromegas chamber as a reference point and a local co-ordinate system with the x-axis parallel to the short length of the sector and the y-axis parallel to the long length of the sector, as viewed in the images of the large and small Micromegas chambers in Figure 5-6 and Figure 5-7 respectively, the centroid of the sectors can be found in Table 5-1.

Table 5-1. Centroids of large and small sectors.

Component	$\bar{x}$ (mm)	$\bar{y}$ (mm)
Large sector and Micromegas chamber	1110	1509.2
Small sector and Micromegas chamber	910.75	1400.8

The tension in each of the slings and thus the forces on the support beam could then be found using the balance of moments about one of the mounting points. This force calculation, completed

for the large and the small sectors can be observed in Appendix A.2. A summary of the results found for these forces can be observed in Table 5-2.

Table 5-2. Tension in slings 'a' and 'b' due to each hanging component and component weights.

Component	Fa_y (N)	Fb_y (N)	Fc_y (N)
Large NSW Sector	9932	4293	14225
Large Micromegas chamber	4658	2013	6671
Small NSW Sector	7060	3731	10791
Small Micromegas chamber	3549	1876	5425

The beams are supported by the transport tool in such a way as to allow the two inner most wedges to be removed from the transport tool by an overhead crane without removing the outer two wedges. This means that the cross supports for the support beams must be far apart enough for the length of the sector to easily fit clear inside of them when removing or adding a Micromegas wedge from above. For this reason, the lengths of the support beams are defined to have a length of 5.36 m and are supported on the transport tool at their two end points. The cross beams supporting these support beams have a width of 160 mm each. The reaction points on the sector support beams were therefore defined at 80 mm from their ends at the centre of the cross beams' width. The beam was therefore defined as 5.2 m for all stress calculations.

With the information regarding the forces applied by the sectors available, the design of the support beam could be completed. In order to determine the cross section and material required for the support beam, the applied stress due to the weight of each sector and the weight of the beam was calculated. The only significant stress applied to the support beam is a stress due to its bending moment. The bending moment for the large sector support beam and the small sector support beam was calculated using an online bending moment calculator called, Beam Calculator, provided by SkyCiv (SkyCiv, 2015). This calculator was validated using analytical calculations that represented the same results. The information provided by this calculator for the sector support beam can be observed in Appendix C.1 and Appendix C.2 for the large sector and the small sector respectively. The maximum bending moment in the large sector support beam was calculated to be 17192 Nm, while the maximum bending moment experienced by the small sector support beam was found to be significantly lower at 11372 Nm. Keeping the design of the sector support beams constant for the large and small sectors, the higher bending moment applied to the large sector

support beam was considered for the stress calculations. The maximum bending stress due to the hanging of a large sector calculated for a 200 mm by 200 mm square tube of 8 mm thickness sector support beam is 48.16 MPa. This stress creates a safety factor of 4.9 in the S235JRG2 steel square tubing used. The calculation for this applied stress and its associated safety factor can be found in the transport tool safety report found in Appendix E.1.

The bending moments resulting from the hanging of the small sector and the small and large Micromegas chambers are all less than the bending moment resulting from the hanging of the large sector as seen in Appendices C.2, C.3 and C.4. The safety factors due to bending when these components are hung are therefore higher than the 4.9 achieved for the large sector, making the design safe for all scenarios. An illustration depicting an exaggerated bending momnet experienced by the sector support beam can be observed in Figure 5-8.
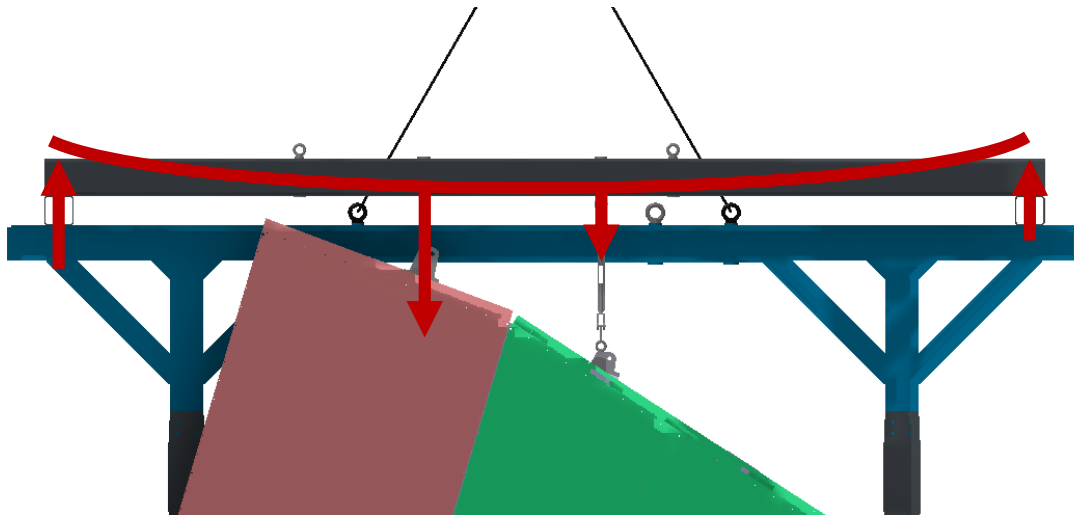
Figure 5-8. Support beam bending illustration.

Once the sector support beams were finalised, the cross beams could be designed. The highest stresses applied to the cross beams occur when two large sectors and their support beams are loaded on the transport tool. The maximum moment occurs on the heavy side, which is the left hand side cross beam when referring to Figure 5-8 because it experiences the highest force of 9226.5 N. This force can be observed as a reaction force in the free body diagram of the large sector support beam in Appendix C.1.

The beam calculator was used again to calculate the bending moment the force applied by the sector support beam exerts on the cross beam so that the bending stress could be calculated. The

results provided for the cross beam by this calculator can be observed in Appendix C.5 which shows that a maximum bending moment exerted on the cross beam is equal to 8912.3 Nm. This bending moment exerts a 40.9 MPa bending stress on the 160 mm by 160 mm square tube of thickness equal to 8 mm. This stress provides a safety factor of 5.7 in the S235JRG2 steel used. The calculation for this applied stress and its associated safety factor can be found in the transport tool safety report found in Appendix E.1. The bending moment on the cross beam resulting from the hanging of the two small sectors and the four small and four large Micromegas chambers are all less than the bending moment resulting from the hanging of the large sector as seen in Appendices C.7. The safety factors due to bending when these components are hung are therefore higher than the 5.7 achieved for the two large sectors, making the design safe for all scenarios. An illustration depicting an exaggerated bending moment in the cross beam can be observed in Figure 5-9.
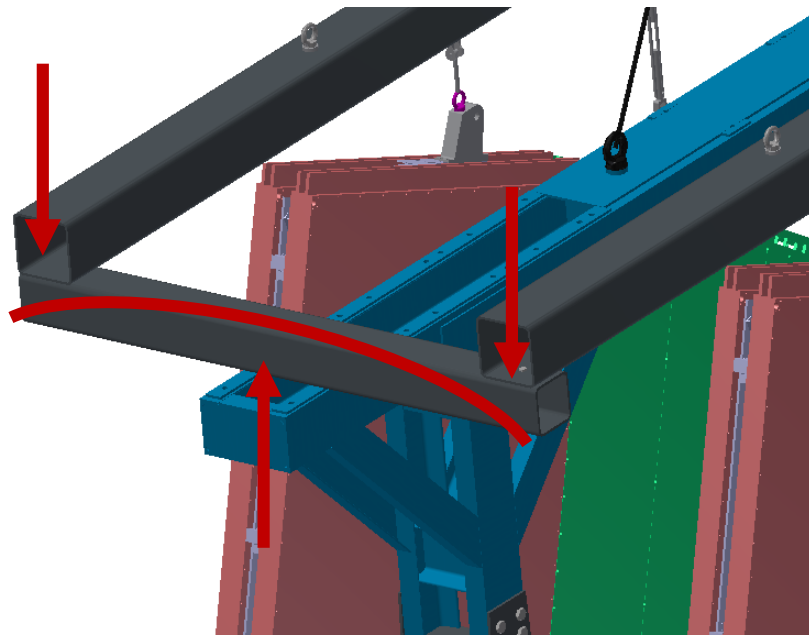
Figure 5-9. Cross beam bending illustration.

Although the case when the tool is used to carry two NSW sectors creates the largest bending moment and thus the highest stress in the cross beam, the case when the transport tool is used to carry four large Micromegas chambers results in a higher overall tool load and thus a higher load on the tool's long beam. The mass of two large NSW sectors and their support beams is 3360 kg while the mass of four large Micromegas chambers and their support beam is 3640 kg. The reason

that the bending moment is still lower in the cross beams due to the load of the four Micromegas chambers is because the load is transferred more evenly along the cross beam, creating a lower moment due to a reduced distance in the load from the fixed point. Because of this higher load, creating a higher stress in the long beam, however, the stress calculations for this component were calculated using the load of four large Micromegas.

The heavier side of the large Micromegas chamber creates a higher load to the left of the transport tool shown in Figure 5-10. This uneven loading results in the highest bending moment, when the transport tool is resting on its posts, occurring at point B, as observed in Appendix C.9. The stress induced due to this maximum bending moment was calculated in the transport tool safety document in Appendix E.1 to be 43.72 MPa resulting in a safety factor of 5.38 in the S235JRG2 steel used. The cross section of the beam at this point of the non-uniform long beam, along with the calculation of its section modulus of $w_x = 328944.68 \ mm^3$ can be observed in Appendix D.1.
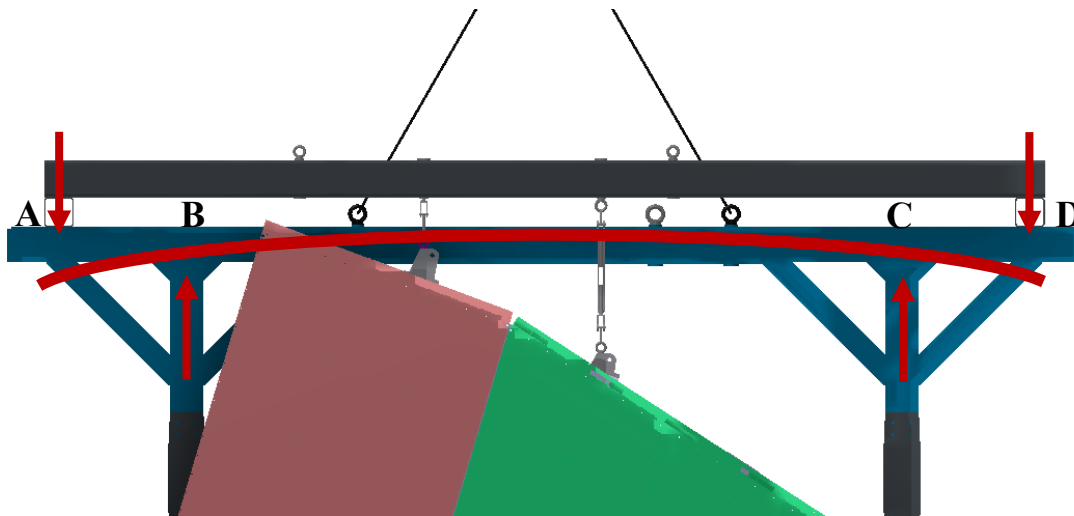
Figure 5-10. Long beam bending illustration.

The height of the transport tool is of great significance and can be negotiated by changes in the height of the upright post. The transport tool needs to be high enough to allow enough room for the sectors to hang but be low enough to fit through the garage door of Building 899 allowing a maximum tool height of just 3.1 m.

In order to extend the height of the posts they must first be cut in half. Once this is achieved, a post extension can be bolted in between the two pieces, resulting in an overall height increase of the tool. The extended post can be observed in Figure 5-11. The height of the tool has been

extended by 368 mm using this extension. This is the result of a 370 mm extension minus the 2 mm that will be lost when cutting the tool in order to fit the extension. With the inclusion of a 20 mm thick rubber platform below the tool to absorb vibrations during transport, the final tool height is calculated to be 3060 mm.
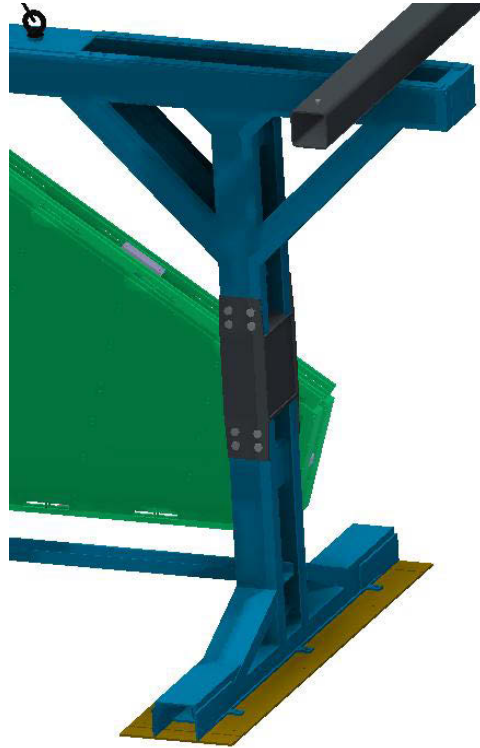
Figure 5-11. Post with fitted extension.

The post extension is made out of 10 mm and 15 mm thick S235JRG2 steel. The thick steel used allows the extension to be made quickly, allowing the components to be assembled easily without risk of deformation during welding and cutting. The safety factors due to compressive stresses on the post and the post extension due to a fully loaded tool are extremely high due to the large area of the steel used. This indicates that the structure is very safe under compressive forces. The highest stress that the post will experience, however, is due to bending when one sector and its support are loaded on only one side of the transport tool. This creates a moment at the top of the post that results in bending of the post. The moment created by a single sector is higher than the moment created by two Micromegas wedges. The moment created due to one sector is equal to 8912.3 Nm as can be observed in Appendix C.5 in the figure showing the reaction forces due to a simplified cross beam supporting a large sector. The stress that this moment creates on the post is

equal to 12.81 MPa, resulting in a safety factor of 18.35 in the S235JRG2 steel used. The section modulus in the direction of bending of this beam was calculated to be $w_x = 695555.56\ mm^3$ in Appendix D.2. The post extension has an even higher section modulus in its direction of bending of $w_x = 1094718.1\ mm^3$, calculated in Appendix D.3. As a result, the post extension only experiences a bending stress of 8.14 MPa giving it a safety factor of 28.87. The calculations for these bending stresses and safety factors can be seen in the transport tool safety report represented in Appendix E.1.

Figure 5-12 represents the way in which the post extensions fit into the gap cut in the posts. 15 mm plates are welded to the original posts for the extension to rest on. These plates evenly distribute the load from the top post to the extension and again from the extension to the bottom post. Because the extension rests on these plates, the load is distributed by a compressive force through the steel instead of a shear force in the bolts holding the extension in place. The bolts therefore experience very low stresses during normal operation and there main function is merely to hold the extension to the transport tool.
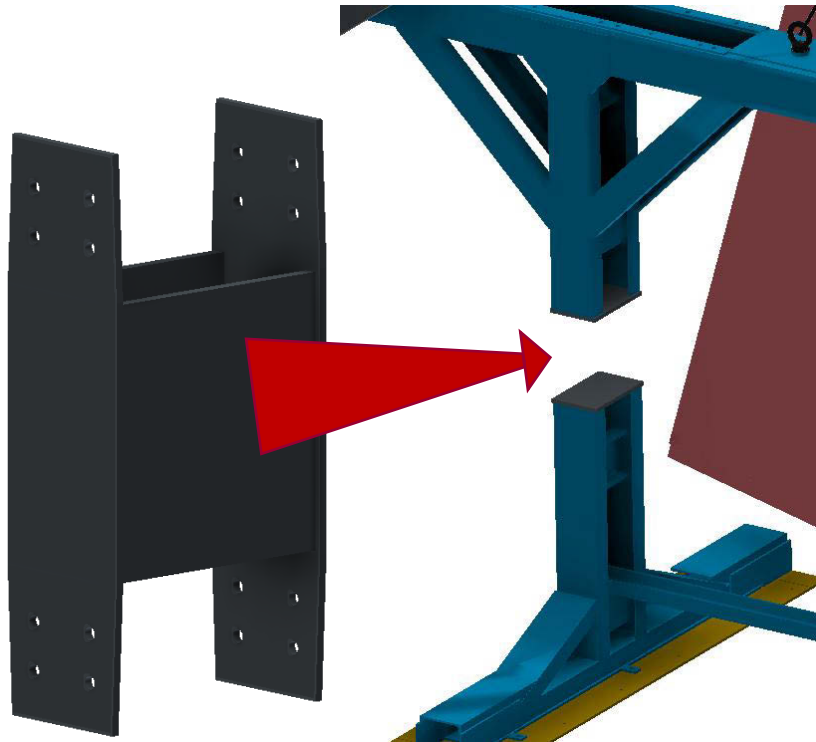
Figure 5-12. Placement of post extension.

5.3.1 Stability Analysis

The stability of the transport tool during lifting operations is of great importance in order to avoid damage caused to the Micromegas chambers if they do not stay in their specified positions. In order to achieve this stability, the point where the overhead crane meets the lifting slings needs to be directly above the lifted object's centre of gravity. A stability analysis has been completed in accordance with each components predicted mass, this however, may not be their true masses after manufacture. The components should all be weighed to confirm their final mass and centres of gravity and the slinging operation should be adjusted accordingly.

Due to the large Micromegas chamber being offset by 360 mm to the left in the image in Figure 5-13, a new centre of mass of the large Micromegas, sling and support beam assembly was calculated. The sling mounts are not to be placed symmetrically about the centre of the beam, but instead symmetrically about the new calculated centre of mass. This new centre of mass was calculated using the balance of moments about a point in the transport tool safety report in Appendix E.1. The new point, positioned centrally between the sling mounts lies 311 mm to the left of the centre point of the sector support beam. The sling mounts are positioned 2 m apart and require two 2 m slings, meeting directly above the centre of mass of the assembly to successfully lift it. The slings therefore lie at 60 degrees to the horizontal resulting in low horizontal forces and safe and secure slinging.
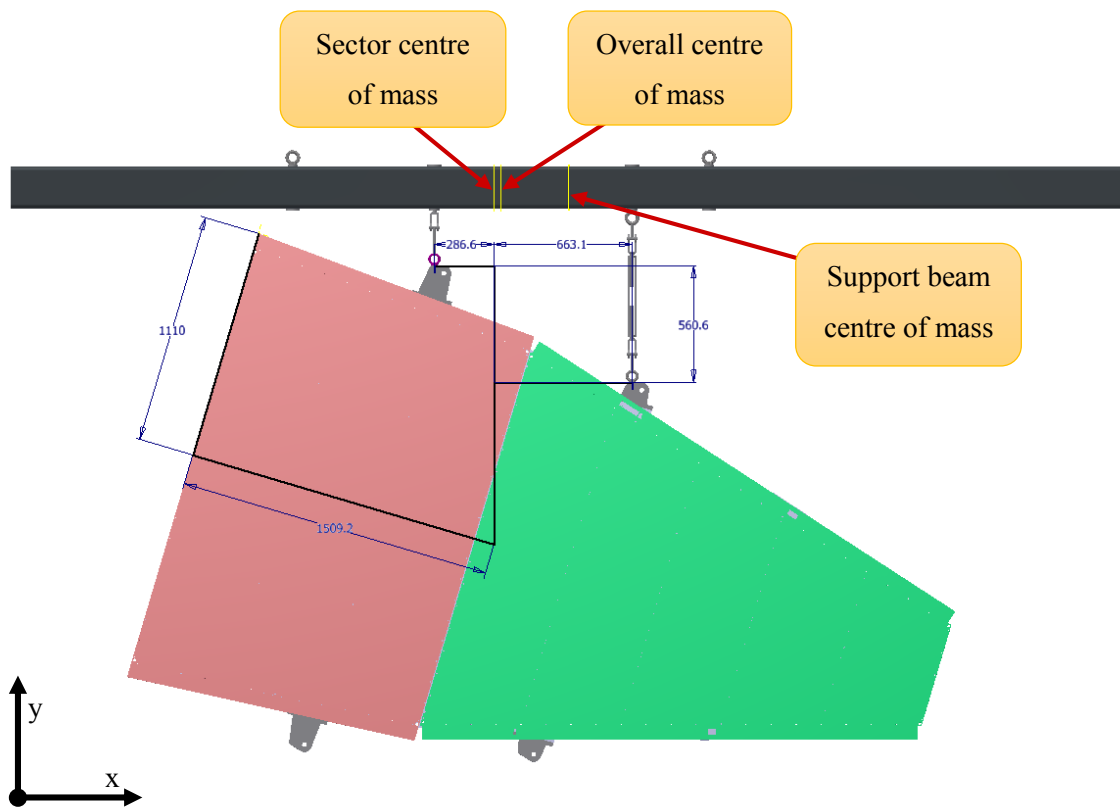
Figure 5-13. Large sector stability planes.

When lifting the large sector support beam when there is just a large Micromegas chamber attached to it, instead of a large NSW sector, the position of the centre of mass changes again. The lower mass of the Micromegas chamber has a smaller effect on the change of the centre of mass and it is therefore closer to the centre of mass of the beam. This new position is situated 42 mm to the right of the centre of mass calculated when lifting the NSW sector as calculated in the transport tool safety report in Appendix E.1. In order to use the same sling mounting points, the length of the slings should be changed to achieve this change in centre point. The diagram in Figure 5-14 is a graphical representation of this 42 mm change and shows that the new left and right slings should have lengths of 2084 mm and 2043 mm respectively. This change in length can be achieved by the use of turnbuckles incorporated in the slinging mechanism or by using different length slings.
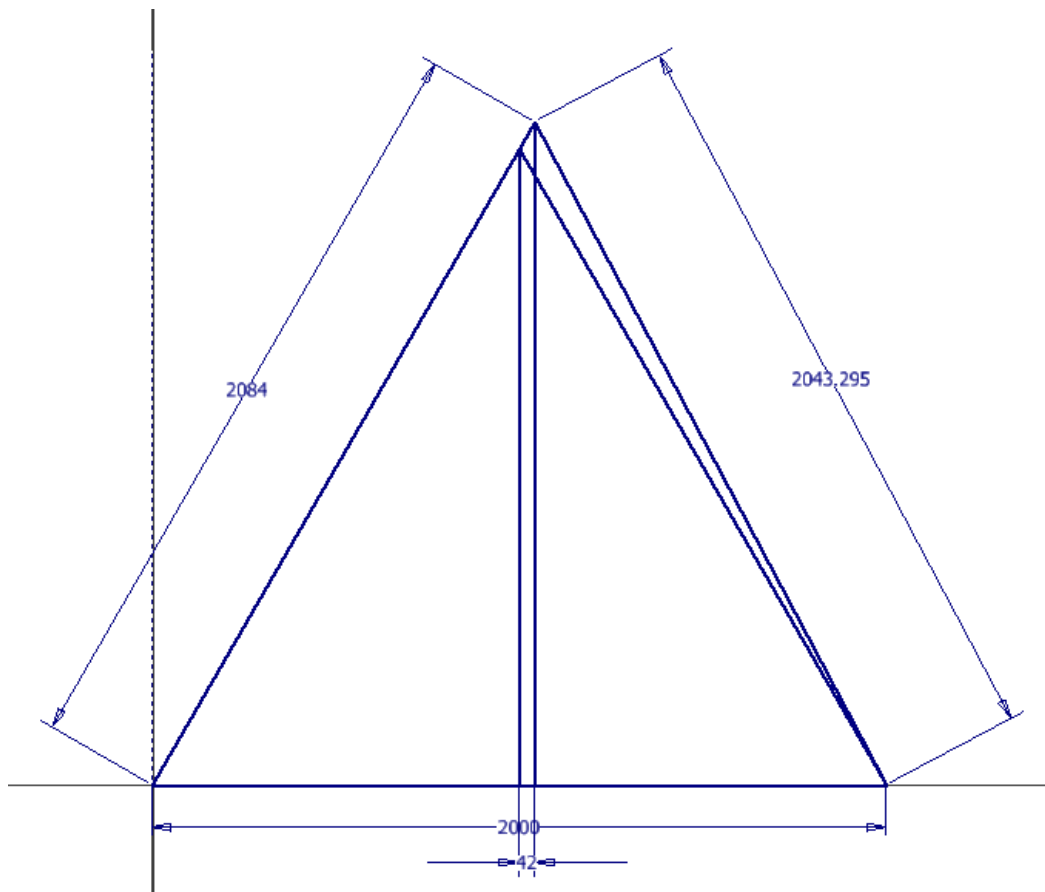
Figure 5-14. New large Micromegas chamber sling lengths.

The stress when the large NSW sectors are mounted to the sector support beam are highest due to the higher weight. The stress calculations for the beam were therefore calculated in the safety report in Appendix E.1 for this scenario using the maximum moment of 4644.1 Nm calculated in Appendix C.10. The stress in the 200 mm by 200 mm, 8 mm thick square tube is 13 MPa. This results in an 18.1 safety factor in the S235JRG2 steel used.

The centroids of the small sector and the small Micromegas chamber both lie directly in line with the centroid of the lifting beam. As a result of this, the sling hoist points for these beams lie at 1 m, symmetrically about either side of the centre of the lifting beam. This scenario creates a lower moment than that of the large sector at only 2062.8 Nm as seen in Appendix C.11, making the design suitable for the lifting of small sectors with a higher safety factor.

When loading and offloading the loaded transport tool onto the transport trailer, the entire tool needs to be lifted by slings and an overhead crane. For this reason, the points of the mounts of the transport tool slings are defined in order to ensure safe and stable lifting.

The total mass of an unloaded transport tool is equal to 1188 kg. This mass is applied symmetrically about the centre axis of the transport tool. When lifting an unloaded transport tool, the original hoisting points located symmetrically about this point can therefore be used. When four small Micromegas chambers, or two small NSW sectors are loaded on the tool, these central hoist points can be used again. This is due to the small sectors' centroids lying at the same x-position as the centroid of the transport tool.

Due to their size and shape, the centre of mass of the large Micromegas chambers are not positioned symmetrically about the centre of mass of the transport tool, at 360 mm left of the tool's center of mass. The centre of mass of the entire loaded tool is consequently shifted slightly from its original position. The original slinging technique can therefore not be used and a new slinging arrangement must be used. When the transport tool has four Micromegas chambers loaded on it, the centre of mass of the loaded tool is shifted 203 mm to the left, as calculated in the transport tool safety report in Appendix E.1. This means that new hoist points are used. The left hoist point is kept in its position, and a new hoist point was positioned at 406 mm to the left of the original right hoist point. This arrangement can be seen in Figure 5-15 where the grey eye-bolt represents the positioning of the new hoist point. Using the new hoist point allows for stable lifting of the tool loaded with four Micromegas chambers.

When the transport tool is loaded with two NSW sectors, the centre of mass of the assembly again shifts. This time, the centre of mass is shifted by 208 mm, only 5 mm more than the shift due to the four Micromegas chambers, as seen in the transport tool safety report in Appendix E.1. The shift can therefore be ignored and the large Micromegas hoist points can be used. This may result in a negligibly small tilt of the tool during lifting operations.
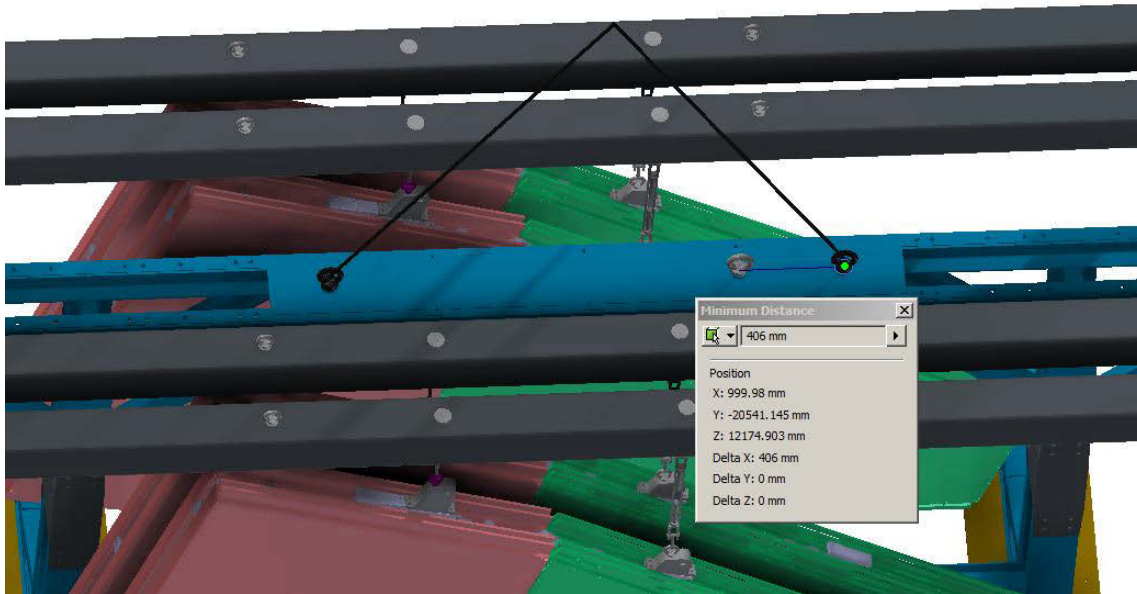
Figure 5-15. Adjusted long beam hoist point.

Once the hoisting points of the sector support beams and the long beam for the transport tool had been defined, the stresses resulting from these lifting operations could be calculated in order to ensure that the components are lifted in a safe manner.

The highest load applied to the sector support beam of the transport tool during lifting is when a large NSW sector is loaded on it. The load applied is a result of a bending moment created by the sector and the top sling mounts. The maximum moment created in the beam was calculated in Appendix C.10 to be $M = 4644.1 \, Nm$. This is significantly higher than the moment resulting from lifting of the small sector of only $M = 2062.8 \, Nm$ shown in Appendix C.11.

The stress due to the large sector is therefore calculated in the transport tool safety report in Appendix E.1 to be 8.14 MPa, resulting in a safety factor of 28.87 and a very safe beam.

The stresses in the long beam during transport tool lifting procedures were then checked. The highest load applied to the long beam of the transport tool during lifting is when four large Micromegas chambers are loaded on it. The load applied is a result of a bending moment created. The maximum moment created in the beam occurs at the right hoist point and is calculated to be $M = 38477 \, Nm$ in Appendix C.12. The section modulus at this point and the area directly around this point is equal to $w_x = 630 \times 10^3 \, mm^3$, as calculated in Appendix D.4. The stresses resulting

from these figures were calculated in the transport tool safety report in Appendix E.1 and was found to be at a maximum of 61.07 MPa creating a safety factor of 3.85 and a safe transport tool lifting procedure.

CHAPTER 6 - SECTOR STORAGE AND ASSEMBLY

6.1   Introduction

Once the Micromegas chambers and sTGCs have been transported to Building 191, they are to be stored before they are ultimately assembled to form NSW sectors using the NSW sector assembly station. The assembly station provides a platform for these components to be assembled via three kinematic mounts with high alignment precision. Due to limited factory floor space, the arrangement of the storage and assembly stations are positioned in the most space efficient way possible. All design constraints and requirements are met by the sector assembly station, which can be observed in Figure 6-1. The building layout including the sector storage area and the transport and assembly tools can be observed in the image in Figure 6-2.
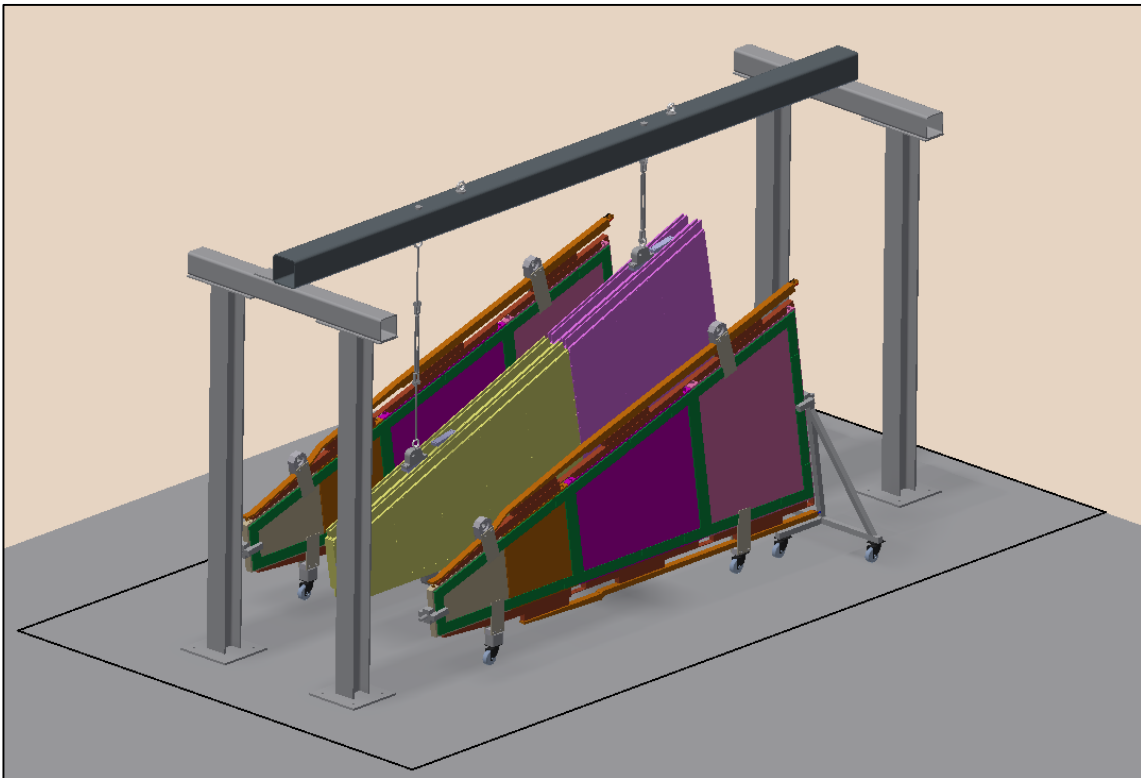
Figure 6-1. NSW sector assembly station.
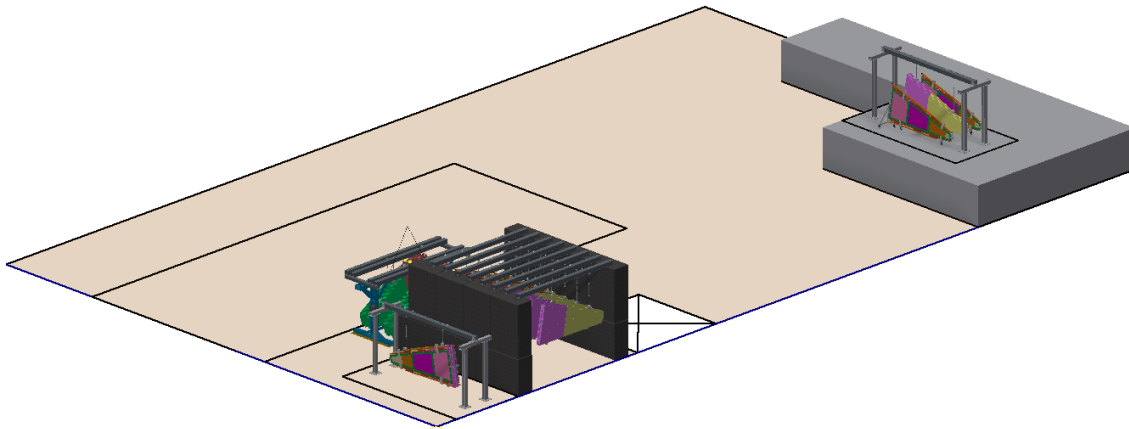
Figure 6-2. Building 191 final layout.

6.2   Design Constraints

The assembly of the Micromegas chambers and sTGCs to form NSW sectors is a critical step in the production of the ATLAS Experiment's NSW. Building 191 on the Meyrin, CERN site is the most appropriate building that can be used for the assembly and storage of the NSW sectors because it eliminates the need to transport assembled NSW sectors from their assembly station to the NSW assembly structure which is situated in Building 191. If the practicality of the storage and assembly in Building 191 is not realised, then Building 180 is to be used. This is a less desired case due to the need of additional transport of the delicate, NSW sectors from Building 180 to Building 191. Other issues may arise due to limited access to the overhead cranes in Building 180 and the clearing of space in this building to allow for additional assembly, storage and transport procedures.

A Micromegas chamber and NSW sector storage station situated in close proximity to the sector assembly station is essential in order to achieve a time efficient assembly of the NSW. The storage station not only stores the Micromegas chambers and NSW sectors, but also creates an assembly buffer between the transport of the Micromegas to the assembly station and for the NSW sectors before they are assembled to the NSW structure. The result of this is that there should never be a delay in procedures before or after the assembly of the NSW sectors that will halt their assembly.

The storage of the Micromegas chambers and NSW sectors are to be achieved in a safe and space efficient manner. The area in front of the large building entrance of Building 191, shown in Figure 6-3, must be kept clear to allow for easy building access and ther areas of the building are allocated

to other NSW assembly procedures and tools. This leaves a limited space in Building 191 available for NSW sector storage and assembly procedures. These areas can be observed in Figure 6-3.
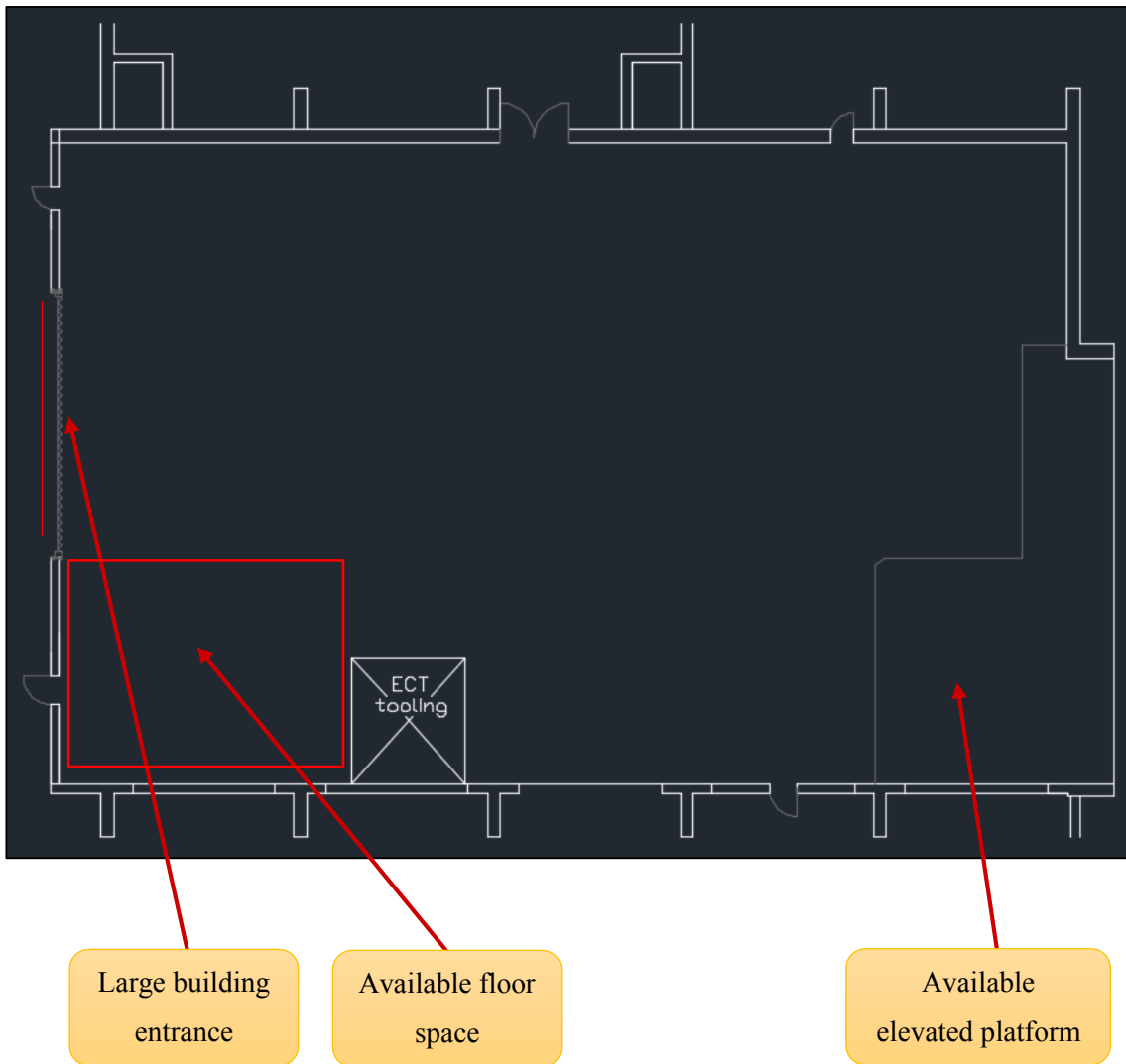
Figure 6-3. Building 191 floor plan (Sinclair & ATLAS, 2015).

The storage station is to be used to assemble the Micromegas chambers and sTGCs to create NSW sectors. The station must provide a platform which supports the Micromegas chamber while an sTGC is attached to either side using a series of three kinematic mounts for each sTGC. In order to realise this, the Micromegas chamber must be supported in the appropriate orientation in order to achieve perfect alignment between the wedges. The sTGC design team have specified that the most appropriate way to manoeuvre the sTGCs is by using a support structure that can be pushed

around on its wheels (Mikenberg, 2015). A simplified sketch of this trolley can be seen attached to a small sTGC in Figure 6-4. The design of the Micromegas chambers support structure should therefore accommodate this sTGC orientation and its trolley.
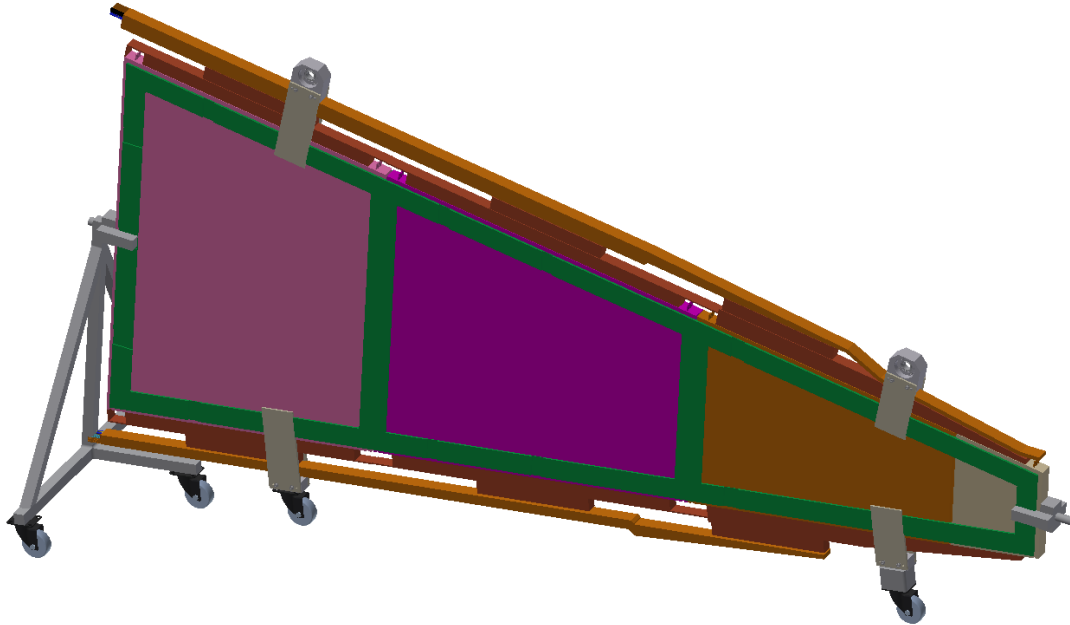
Figure 6-4. Small sTGC support stand (Sinclair & ATLAS, 2015).

6.3   Final Design

Keeping the design constraints previously discussed in mind, it was evident that a storage and assembly station situated in Building 191 was the most desired design outcome. This required a very space efficient building layout while keeping ergonomics such as pathways and accessibility in mind. In order to accurately plan the building layout of Building 191, the NSW sector assembly station was first designed in a size efficient manner.

In a continued effort to simplify the NSW sector procedures and reduce the amount of handling of the NSW sector components, the sector support beams, seen in Figure 5-6 and Figure 5-7, are again used for the NSW sector assembly station. The reuse of these components meant that only the structure, that is needed to support the sector support beams, was required to be designed in order to create the required assembly stand. The designed assembly stand can be observed in Figure 6-5 where a small Micromegas chamber is positioned, ready for assembly with two sTGCs.
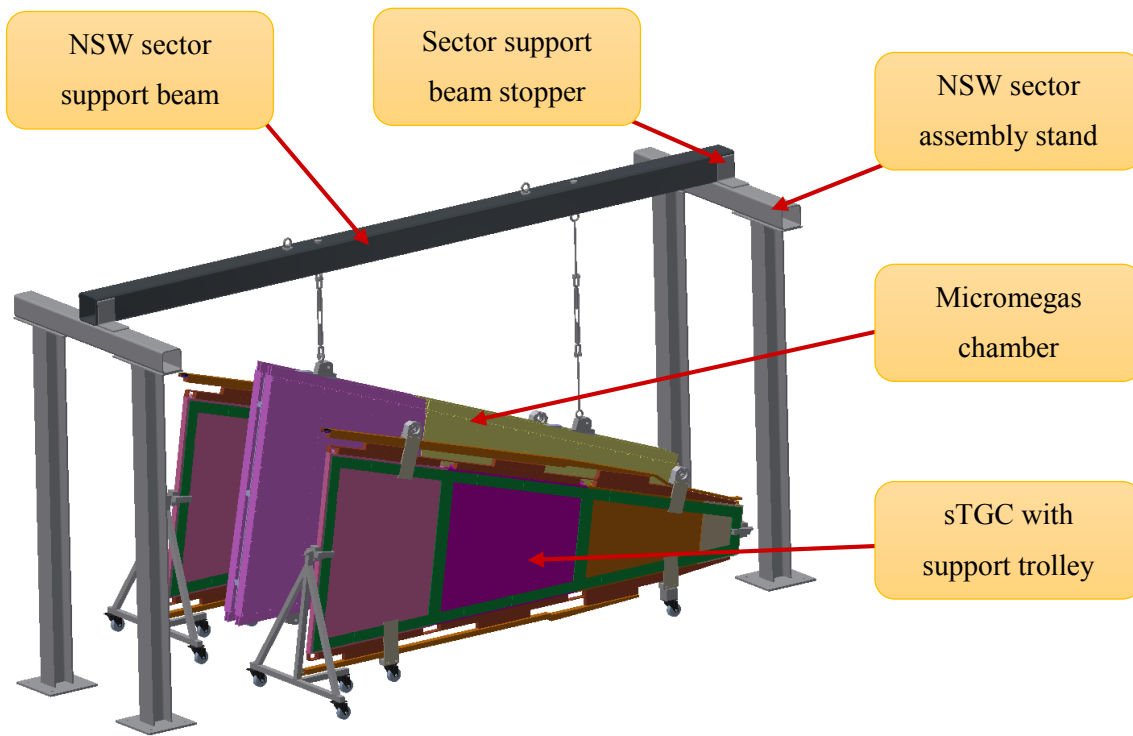
Figure 6-5. Labelled NSW sector assembly station.

The NSW sector assembly stand is made up of two stands, each consisting of two upright posts and a cross beam positioned to support the sector support beam, as seen in Figure 6-6. Each support is situated 5.2 m apart allowing the assembly stand to support the sector support beam in the same way as is done with the transport tool. This meant that no additional calculations and design considerations needed to be completed for the sector support beam to adapt it for use for the NSW sector assembly stand. The upright posts are positioned with a 1 m gap in between them allowing access to the sides of the Micromegas chambers and sTGCs during assembly.

A Micromegas alignment stopper is to be welded to the cross beam of the assembly stand. This stopper ensures that the sector support beam is positioned exactly in the middle of the cross beam and ensures that the beam lies perpendicular to the cross beam. This is essential to create a repeatable scenario for the assembly procedure. The stopper also allows for an easily accessible mounting point for the sector support beam, using a single nut and bolt. This ensures that the sector support beam will not fall if knocked, reinforcing the safety of the structure. This stopper is to be made from a 180 mm by 180 mm equal sided, S235JRG2 steel L-profile.

The stand is to be bolted to the floor by means of four bolts through each of the four 6 mm thick, S235JRG2 steel plate floor mounts, as observed in Figure 6-6. These floor mounts are welded to the upright posts which are to be manufactured using 160 mm by 160 mm HEB wide flanged S235JRG2 steel sections.
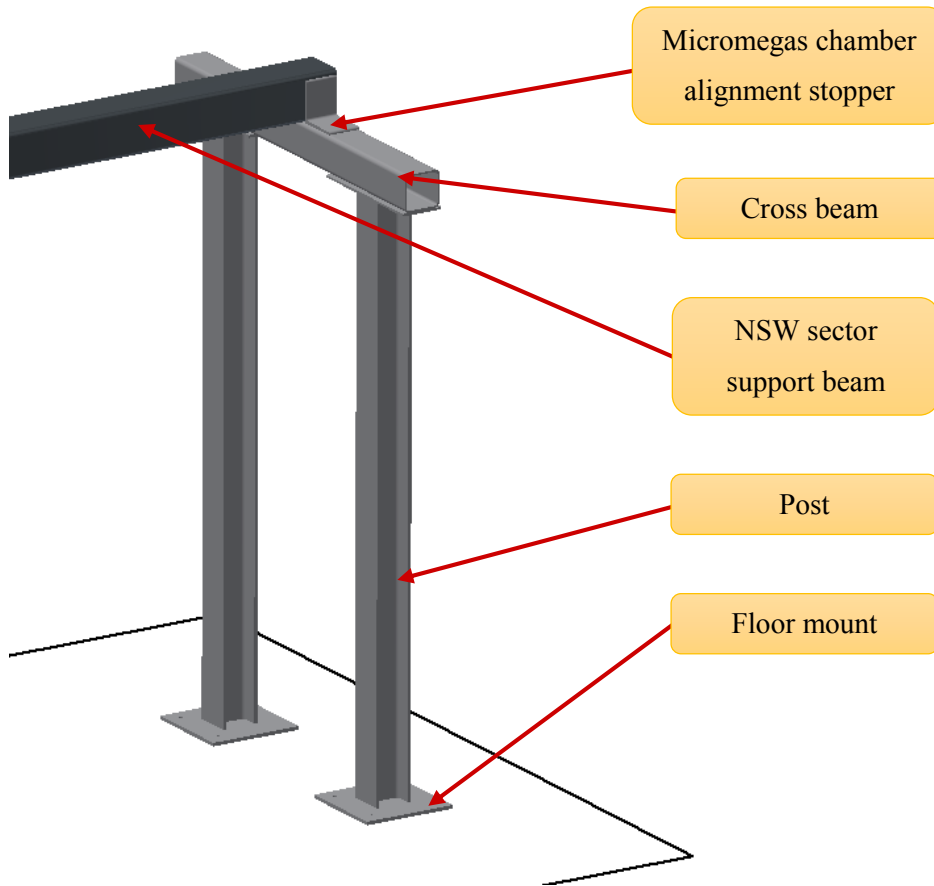
Figure 6-6. NSW sector assembly stand components.

The stresses experienced by the sector support beam were analysed during the transport tool analysis, leaving the only steel section component with a significant load in the assembly stand being the cross beams. The cross beams experience a bending load illustrated in Figure 6-7. The highest stress the cross beam experience is when it is supporting a sector support beam with the heavy side of the large NSW sector attached. This results in a downward force of 9226.5 N on the cross beam by the sector support beam, as represented in the free body diagram in Appendix F.1. This force creates a maximum bending moment of 2711.9 Nm as represented in the bending moment diagram represented in Appendix F.1. The stress induced due to this maximum bending

moment was calculated in Appendix F.2 to be 12.44 MPa resulting in a safety factor of 18.89 in the S235JRG2 steel used. This safety factor is higher than the safety factor of 2 specified for lifting equipment meaning that the design is OK. The reaction forces when the cross beam is supporting a small sector or a large or small Micromegas chamber were all calculated to be lower than the force created by the large sector. This means that a higher safety factor will result and the design is OK for all these scenarios.
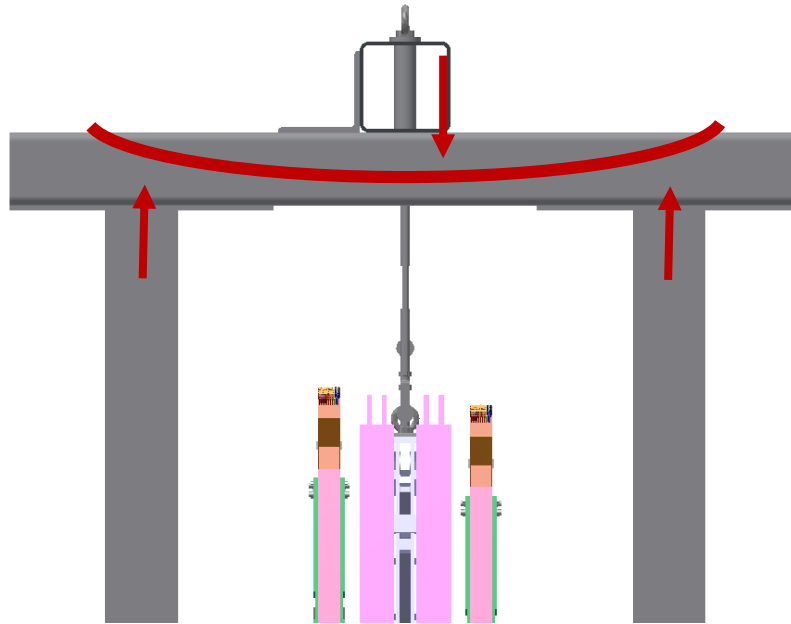
Figure 6-7. NSW sector assembly station cross beam.

The height of the Micromegas and sTGCs during the assembly process needs to be considered in order to achieve the alignment needed for the connection of the three components. In order to achieve this required height adjustment, the way in which the Micromegas chambers are attached to the sector support beam was considered. This attachment mechanism can be observed in the labelled image in Figure 6-8. All safety calculations for this support mechanism are represented in the transport tool safety document represented in Appendix E.1. It can be seen that all safety factors are above 2 when the component's rated load is used.

It can be observed in Figure 6-8, that a turnbuckle is used on the light side connection of the large sector attachment mechanism. The turnbuckle allows for height and angular adjustments to be made to the Micromegas chamber. The turnbuckle used has an adjustment range of 120 mm and

has shackles on both sides to allow for easy installation. Lifting eye bolts are used to attach the turnbuckle to the spacer frame mounts and the sector support beam.

The heavy side of the large sector, however, does not have enough clearance between the spacer frame mount and the sector support beam to fit a turnbuckle for the required adjustment. For this reason, a bolted shackle and rotating eye bolt are used in order to achieve height adjustment. This can be achieved by slightly turning the shackle, unbolting it from the sector support beam and allowing the sector to move downwards. The adjustment using this mechanism is, however, limited by the 155 mm thread length of the shackle. An adjustment of 105 mm is accepted in order to leave a safe thread length of 50 mm to keep the sector supported. Markings are to be made on the thread of the shackle to ensure that the operator does not unbolt it too much, allowing the sector to fall. A representation of the turnbuckle, shackle and rotating eye bolt used can be observed in Figure 6-9.
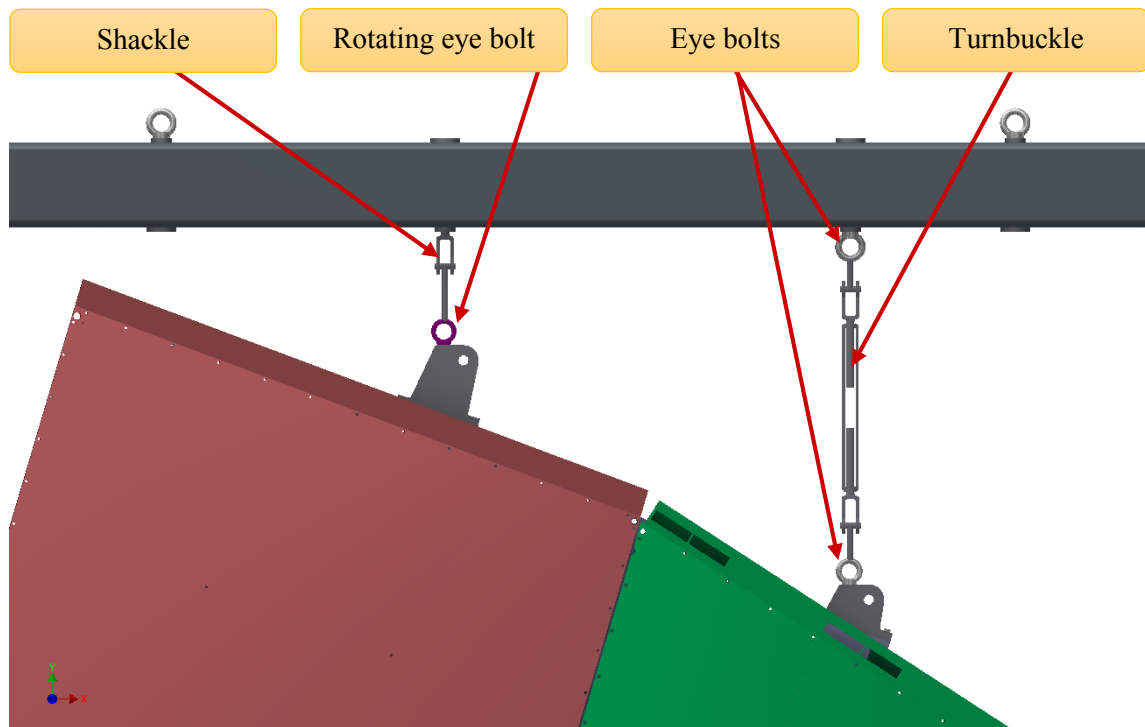
Figure 6-8. Large Micromegas chamber attachment mechanism.

Figure 6-9. Turnbuckle, shackle and rotating eye bolt (Manutan, 2015).

The height adjustment for the small sector was achieved in a similar way, however, there is enough space for a turnbuckle at both support chains, as seen in Figure 6-10. The stress calculations for the small sector adjustment components can be found in the transport tool safety report in Appendix E.1.
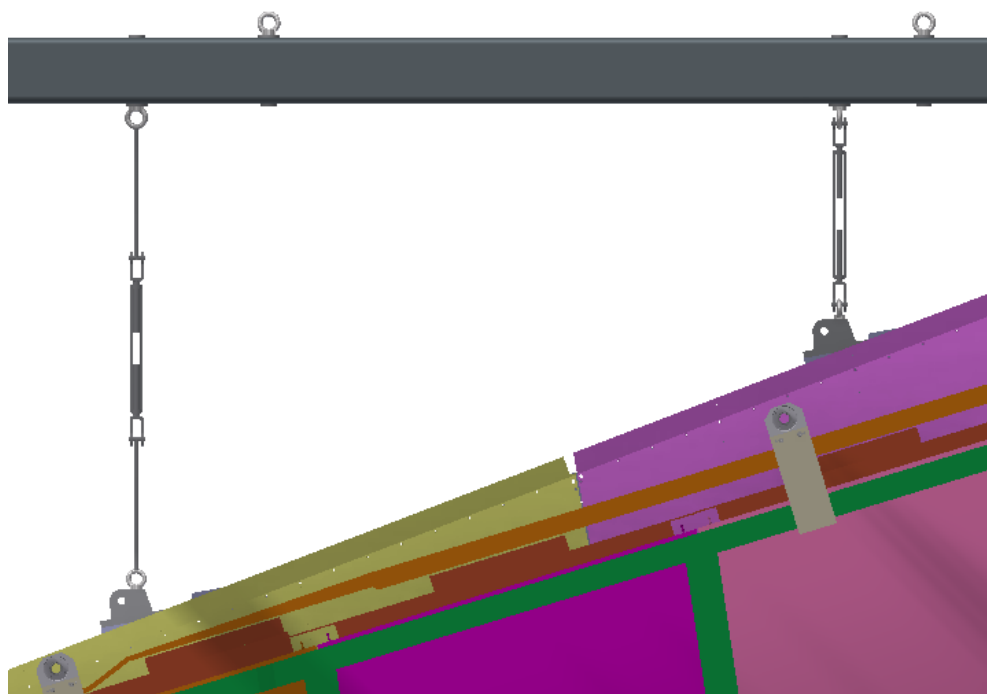
Figure 6-10. Small Micromegas chamber attachment mechanism.

The total masses and accompanying weights of all the components of the sector assembly station can be found in Table 6-1.

Table 6-1. Relevant assembly station components with their masses and weights.

Component	Mass (kg)	Weight (N)
Large Sector	1450	14224.5
Small Sector	1100	10791.0
Sector Support Beam	230	2256.3
Cross Beam	51 x 2	500.3 x 2
Post	140 x 4	1373.4 x 4
Unloaded Tool	892	8750.5
Loaded Tool (1 sector)	2342	22975.0

Once the geometry and various components of the NSW sector assembly station was finalised in the most compact manner, it became possible to plan how the structure was to fit into Building 191 in conjunction with the storage of the NSW sectors and Micromegas chambers at an independent storage station. A bird's eye view of the final layout of Building 191 can be observed in Figure 6-11.

The transport tool offload area is represented as well as an offloaded transport tool. The transport tools are designed to carry four Micromegas chambers or two NSW sectors. The four transport tools made cannot all be used at the same time resulting in at least three transport tools being available for storage of Micromegas chambers or NSW sectors. This kind of storage is beneficial because the transport tool can be moved to any unused area in the building by use of the overhead crane.

It can be observed that there are two NSW sector assembly stations positioned in Building 191. Assembly station 1 is closest to the door to Building 190 where the sTGCs will be brought from. This assembly station positioning negates the need to transport the sTGCs off the platform until they are assembled to the Micromegas chambers. A perimeter at a distance of 1 metre from the assembly tool is to be cornered off as represented by the black rectangle around the assembly station in Figure 6-11. This area is to allow for unobstructed assembly of the NSW sectors.

The second assembly stand is situated near to the storage area in Building 191. This stand is not used for assembly of NSW sectors but instead to do adjustments or repair work to any NSW sectors or Micromegas chambers that are in storage. This station, again, has a perimeter drawn around it in order to ensure work can be achieved in an unobstructed manner.
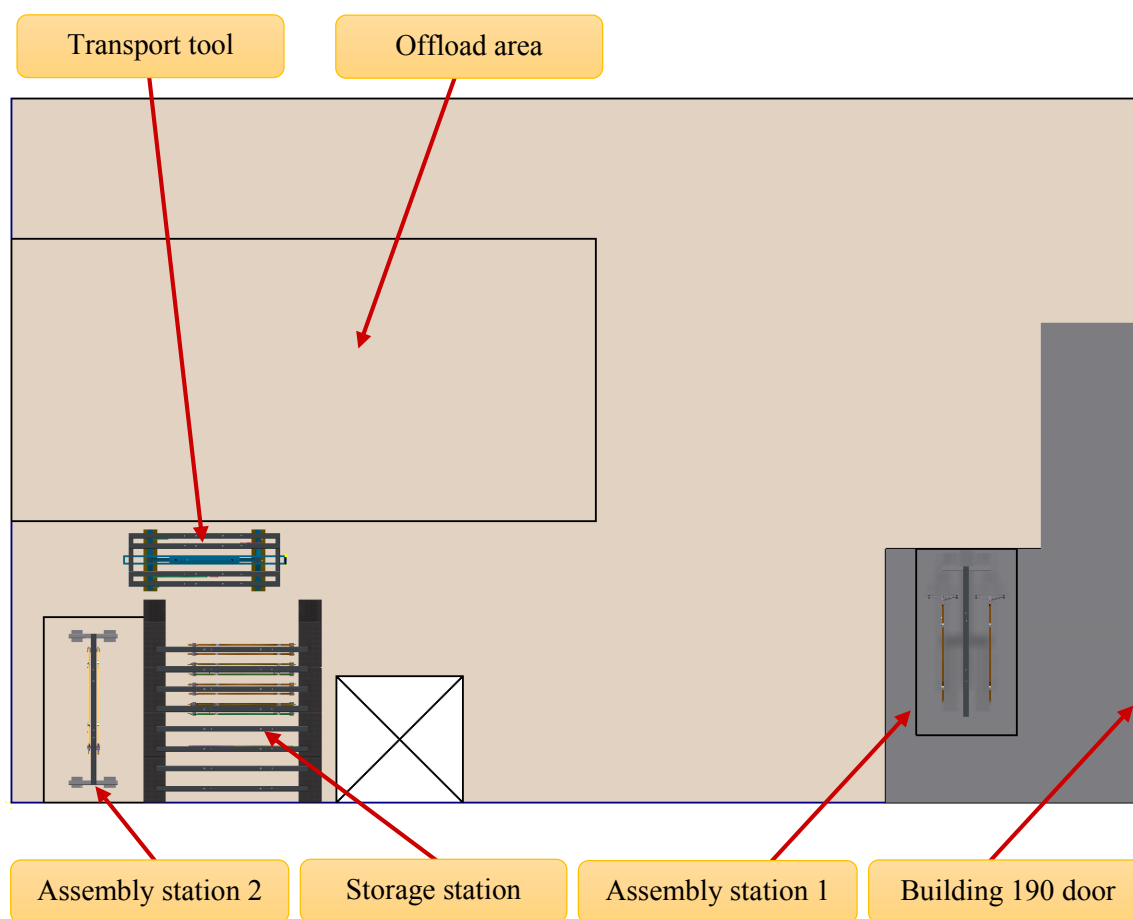
Figure 6-11. Final Building 191 layout.

The storage station seen in Figure 6-12 can fit a total of eight Micromegas chambers or NSW sectors with a gap of 300 mm between NSW sectors at their closest points. The sector support beam is again used in the storage procedures. This beam is placed on concrete blocks with the dimensions, 2400 mm x 1600 mm x 800 mm, that are readily available for this use at CERN. A total of fourteen blocks covering an area with dimensions 7200 mm x 6320 mm that fits in the allocated storage area is used. Micromegas chambers and NSW sectors can be added to or taken

away from the station by means of an overhead crane at any time without the need to move any of the others already on the storage station.
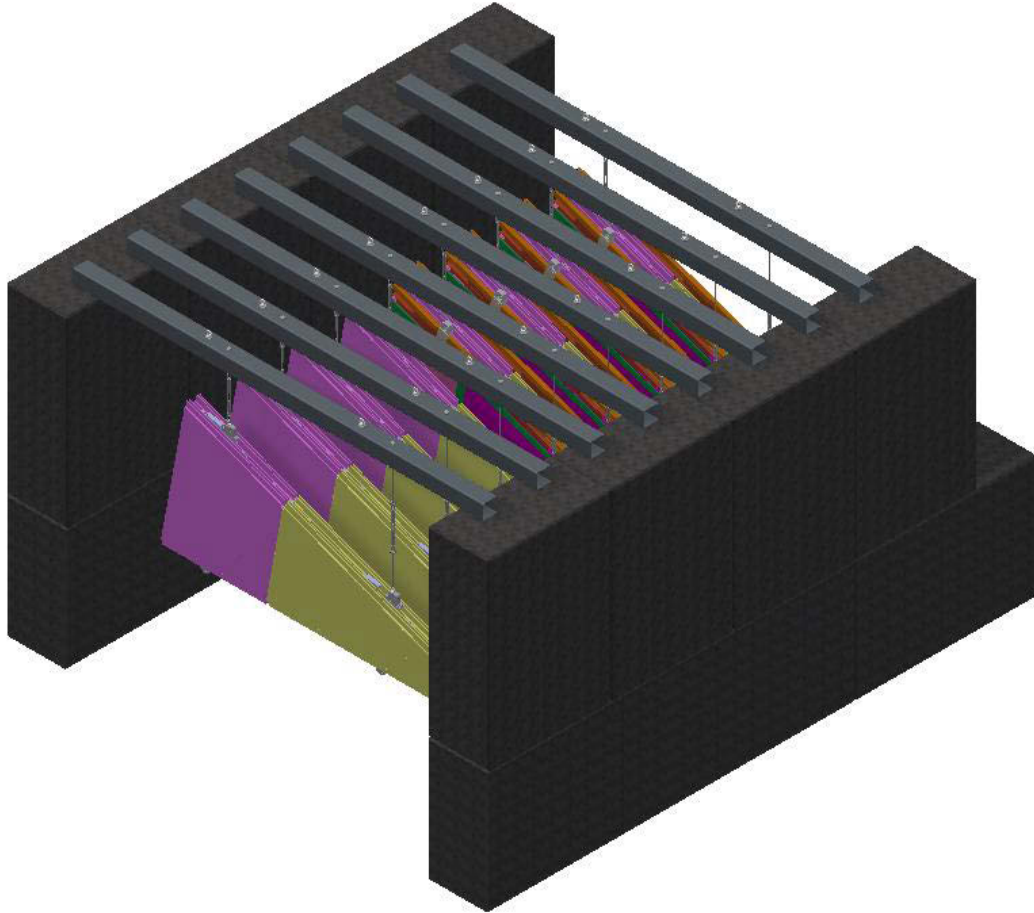
Figure 6-12. Storage station.

CHAPTER 7 - MECHANICAL DESIGN DISCUSSION

In contrast to many engineering applications, during the design process of the mechanical components, namely the spacer frame mounts and the transport and assembly tools, no significant effort was applied to the optimisation of the weight of the components used when large safety factors were achieved. In this application, there were no noteworthy mass restrictions, resulting in the tolerance of heavy structures with large safety factors. The spacer frame mounts were designed in a way that allows them to be removed from the NSW structure once the NSW sectors have been installed. This means that they do not add to the overall sector mass and their mass can be neglected in NSW mass calculations. Similarly, when the designs of the transport and assembly tools were prepared, no significant weight optimisation techniques were used. Ease of manufacture, practicality and ergonomics were favoured and creating low cost components that can be easily cut and welded was essential.

In addition, the use of bigger and thicker steel components used, opens opportunities for the assembly and transport tools to be used in future applications once the assembly of the NSW structure has been completed. By simply redesigning the length of a new post extension component for the transport tool, any realistic tool height can be achieved. With this small adjustment, the tool can be used to transport a variety of different structures.

The shift of the Micromegas chamber due to an obstruction of the bottom beam of the transport tool, creates many undesired stability complications during lifting processes. In the NSW project at CERN, many people are involved in the design, assembly and procedures involved in the assembly of the NSW in building 191. With so many people working on a project, the most simple procedure methods are always encouraged in an attempt to avoid damage occurring to any of the components due to misuse. In the case of the stability analysis, this result was not achieved. With the necessity of changed sling lengths and positions when lifting different components, it is essential that slinging instructions are followed carefully and sensibly in order to avoid the risks that are created due to unstable lifted objects.

There are, however, solutions that can result in the moving of the NSW large sector centre of gravity to a position in line with the centre of gravity of the transport tool, allowing stable lifting operations. An option to be considered is the enlargement of the door in Building 899 to allow a higher transport tool to be made. This would result in the large NSW sector hanging clear of the bottom beam that initiated in its movement away from the tools centre of mass. Another option

that may be considered is a complete redesign of the transport tool. A transport tool, carrying one sector at a time with similar design features as the assembly tool may be less space efficient, but would allow for an easier transport procedure.

Due to an ever changing design of the positions of the spacer frame mounts and the mass of the NSW sectors, a calculation code was created using a Matlab script. This code allowed the user to input the new mass of the small or large sector and the new positions of the spacer frame mounts relative to the center of gravity of the sector. The results from this calculation provide the user with the tension experienced in each of the slings, providing information on the loads on the spacer frame mounts and the sector support beam. This can be used very quickly and allowed changes in the constraints of the tools to be checked with ease.

All the calculations of the major components of the transport and assembly tools only take into account the bending moments that result from the applied loads. This is simply an estimation of the stresses occurring in the components. In reality, although they are seen as negligibly small, other stresses, including torsional, shear and axial are also induced on the tool components. The bending stresses observed from all of the calculations for the spacer frame mounts and the transport and assembly tools all have safety factors that far surpassed the safety factor of 2 required by the Standard BS EN 13155:2003 for lifting tools. This resulted in no further analysis of the stresses being necessary.

CHAPTER 8 - MICROMEGAS WEDGE ANALYSIS

8.1 Introduction

The New Small Wheel upgrade project aims at using physics and engineering technology that has never previously been used by the ATLAS Experiment. During Long Shutdown 2, the delicate new Micromegas detector technology is to be installed for the first time ever in the ATLAS Experiment. This innovation, however, is certainly accompanied by a large amount of inexperience and unfamiliarity amongst the involved physicists and engineers. For this reason, it has become essential that numerous testing and simulation analyses are conducted, allowing us to more accurately understand how the Micromegas wedges behave under various loading conditions.

The analyses conducted on the Micromegas wedges are required to prove that the wedges can withstand stresses not only during standard operation, but also during transport, assembly and storage, where they will be subject to various loads that would not be applied under standard operational conditions. In order to effectively complete the design of the transport, storage and assembly tooling, the designer should ensure that the detectors are not damaged during these operations.

In a constant struggle to optimise detector weight, while not compromising the structural integrity and operational performance of the Micromegas wedges, the design of the structural components of the Micromegas wedges and the spacer frame are constantly changing. For this reason, it is impossible to finalise the numerous, essential simulations at present. Engineers are, however, developing finite element models of the Micromegas wedges while keeping this shifting information in mind. The models use a unique technique which simplifies the structure down to its simplest components. This simplification not only allows for a quick finite element analysis solving time but also allows for quick changes to be made to the one dimensional beam element cross sections and two dimensional plane element composite panels used in these simulations of the Micromegas wedges. This is a form of adaptive design, allowing the researcher to quickly confirm the viability of structural changes when new materials or geometries are proposed. An example of a simulation completed for the Micromegas wedges during its standard operation conditions is shown in Figure 8-1.
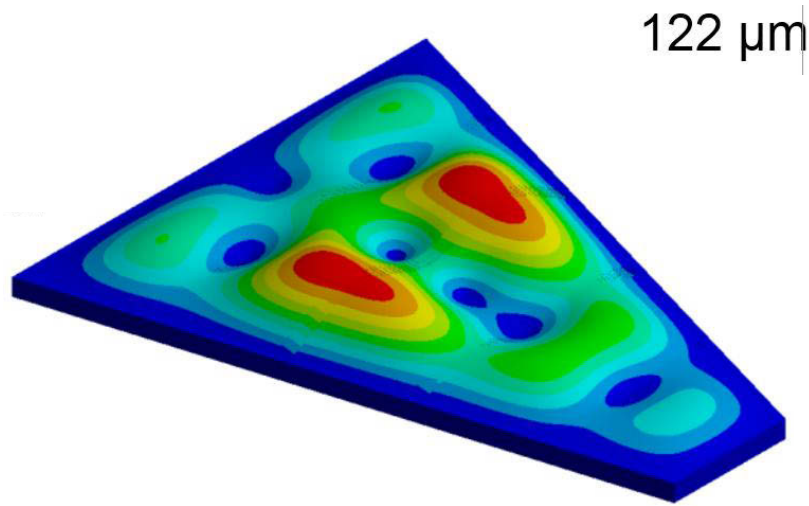
Figure 8-1. Micromegas Ansys analysis (Rossi, 2015).

Unfortunately, due to a lack of time and resources, a full scale, physical mock-up of the Micromegas wedge cannot yet be produced for full mechanical and thermal experimental testing in order to validate the results found in these unique and simplified computational simulations. This creates a great sense of uncertainty in the simulation results, not knowing if the simplifications and techniques used are acceptable. A cheaper, quicker and easier method of computational analysis validation was, for this reason, perceived. This validation method involved an experimental analysis of a much smaller mock-up of a portion of the Micromegas wedge. This portion follows comparable proportions to the multiplet of the large Micromegas wedge represented in yellow in Figure 8-2. This mock-up has been given the name of MMSW amongst the ATLAS community and will be referred to as such in this work. An image of the fully assembled MMSW can be viewed in Figure 8-3.
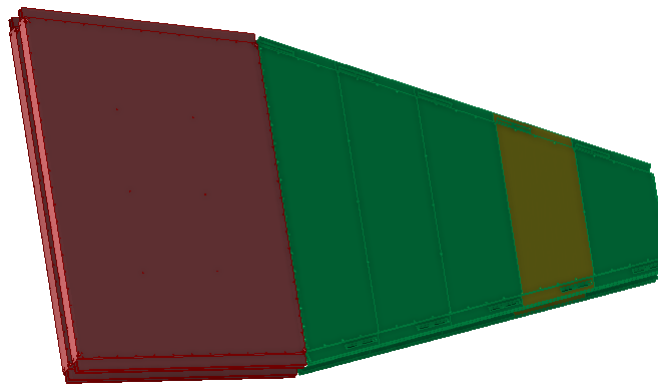
Figure 8-2. Micromegas wedge – MMSW highlighted in yellow.
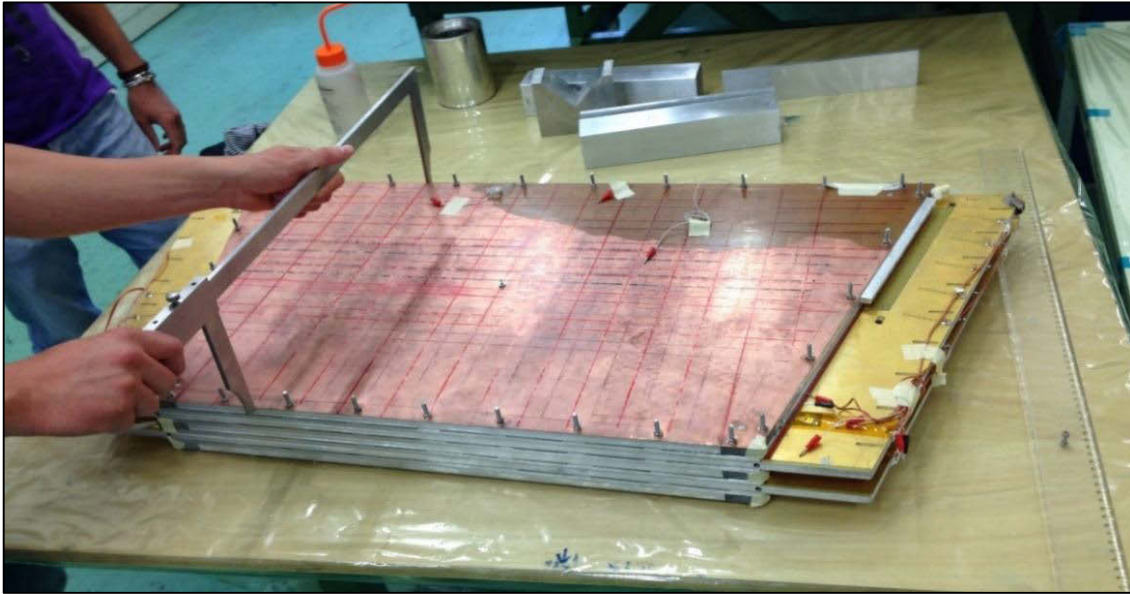
Figure 8-3. Micromegas multiplet mock-up – MMSW.

Using a smaller mock-up of just a portion of a Micromegas wedge comes with many advantages. It was considerably quicker and easier to manufacture, with reduced requirements relative to the equipment size and strength and the available laboratory space. The MMSW can be easily lifted by two people, a task that cannot be completed with the much heavier 260 kg large Micromegas wedge. The MMSW can also easily fit on mechanical testing devices for structural tests and fit in medium sized ovens for thermal testing.

A comparative analysis, using experimental and computational techniques, was conducted on this smaller mock-up in an attempt to validate the finite element analysis techniques that are to be used on the final Micromegas wedge analyses, discussed in Chapter 8.4. In order to achieve this, a finite element analysis model of the MMSW structure was created using the same model creation principles and simplification techniques that are to be used for the FEA of the final Micromegas wedges. This finite element model was then subjected to the same loading conditions as an experimental test conducted on the MMSW. The results of these two analyses were then compared by finding the error in the computational results relative to the results obtained from the experiments.

8.2   Methodology

Given both the MMSW ready for an experimental analysis and the method of finite element analysis to be used for the Micromegas wedges, the next imperative step was creating a scenario that could be constant across the two investigations. A thermal expansion experiment was selected in an attempt to minimise the chance of damage caused during experimental testing of the MMSW. A fully functional Votsch composites oven, complete with thermocouple plugs, in the temperature controlled Room 209, in Building 153 of the Meyrin CERN site, was available for use. The computational thermal load function that can be used to find the thermal expansion of a finite element model is also readily available in the Ansys workbench.

It is important to carefully analyse both the experimental and computational analysis capabilities and strengths before defining the conditions of the experiment in order to ensure that a repeatable scenario can be conducted on both platforms. A thermal expansion analysis in the y-direction due to an increase in temperature was defined. The direction of measured expansion can be observed graphically, represented by red arrows, in Figure 8-4.
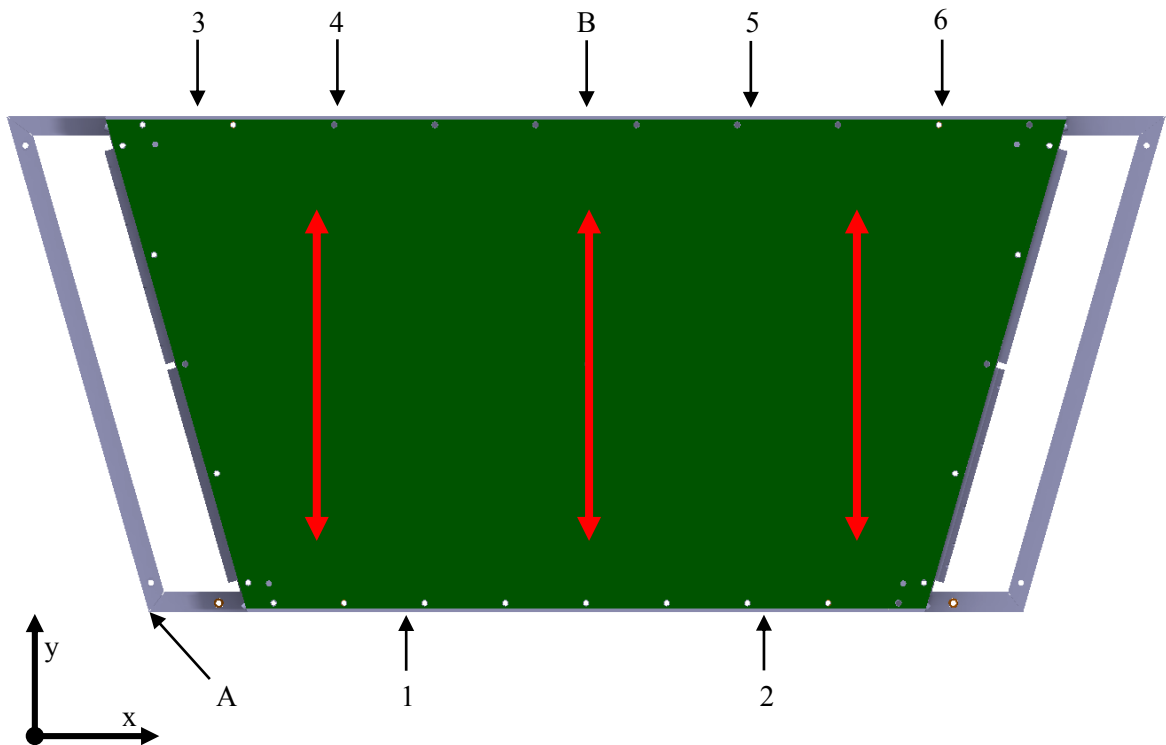
Figure 8-4. MMSW CAD model (Sinclair & ATLAS, 2015).

This expansion in the y-direction on the MMSW replicates an expansion in the r-direction on a full Micromegas wedge as can be viewed in Figure 8-5.
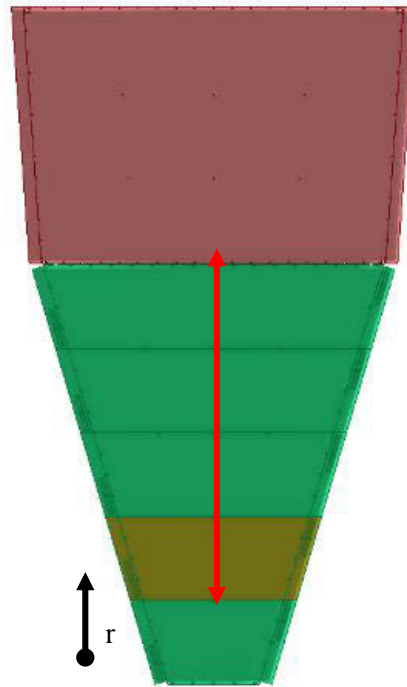
Figure 8-5. Micromegas wedge direction of thermal expansion.

In order to create a repeatable experiment, a collection of strict constraints need to be defined that will be followed by both analysis platforms. The following constraints relating to the graphical information found in the labelled CAD model in Figure 8-4 were applied to the MMSW for this analysis:

1. Fixed displacement constraints in the y-direction at point 1 and point 2. These points are situated at the following distance in the x-direction from point A:
   - Point 1: 265 mm
   - Point 2: 601 mm

   These two points are symmetrical about a vertical line running through the centre of the MMSW at 168 mm on either side of this line.

2. Free movement in the x-direction and the z-direction.

3. Y-directional displacement measurement devices at points '3', '4', '5' and '6'. The points are situated, non-symmetrically at the following distances away from point 'B' in the positive and negative x-directions:

   - Point 3: -450 mm

   - Point 4: -350 mm

   - Point 5: 300 mm

   - Point 6: 400 mm

4. A temperature change from the room temperature of 22°C, 23ºC and 24°C, to a set temperature of 50ºC.

It is important that the above defined constraints be considered and followed when conducting the finite element analysis as well as the experimental analysis to ensure that the conditions remain constant, allowing the results to also remain constant and repeatable.

Once the results have been obtained for both the experimental and computational, thermal analyses, the error of the computational analysis is calculated. The acquired experimental analysis results are considered accurate and used as the theoretical, exact value in this comparison. This is done because it is assumed that the average results obtained from the experimental analysis are a true indication of how the MMSW will behave under a changing temperature condition in reality. The results obtained from the computational analysis are taken as the approximated values with an increasing error reading as these results differ from the set of exact results obtained from the experimental analysis.

The manner in which the MMSW expands under heating will also be analysed to help gain an understanding of what behaviour should be expected from the Micromegas wedges.

In order to accurately perform this comparative process, a precise analysis method must be followed. A flow chart, represented in Figure 8-6, defines the process to be followed in order to correctly complete the analysis.

Consider both forms of analysis and define a clear set of constraints that are possible with both.	Conduct appropriate analytical calculations to acquire a reasonable approximation.	Create a reasonable hypothesis for the comparative experiment.
Conduct a finite element analysis of the mock-up using the correct simulation techniques.	Conduct an experimental analysis on the MMSW using the defined loading conditions.	Conduct experimental tests on the apparatus used to ensure it is functioning reliably.
Compare both sets of results with the calculated approximations and hypothesis.	Analyse all results, proving or disproving the validity of the FEA simulation method used.	Review errors in the data collected and conclude the analysis.

Figure 8-7. Analysis methodology.

8.3 Hypothesis

It is clear, that when exposed to a temperature increase of 27°C the MMSW will expand in all directions. The amount of thermal expansion occurring in a body depends largely on the type of materials that it is composed of. Aluminium alloys, for example, expand at almost double the rate that FR4 does. These two materials are the two principal materials composing the Micromegas wedges and consequently, the MMSW.

When broken down to its simplest form, only taking the most significant elements of the Micromegas into account, the extremity of the MMSW can be perceived as a composite panel made up of alternating layers of aluminium and FR4. If a block of this composite material of length equal to the length of the MMSW in the y-direction is defined one can perform a simple analytical calculation to determine an estimate of the thermal expansion one should expect in the comparative analyses to come. The MMSW was hypothetically sliced midway between its y-direction extremities at section labelled a-a in Figure 8-8. This section is perpendicular to the direction of measured thermal expansion and the material it cuts through was used as cross sectional areas for each layer of the hypothetical composite. A graphical representation of this simplification can be observed in Figure 8-9.
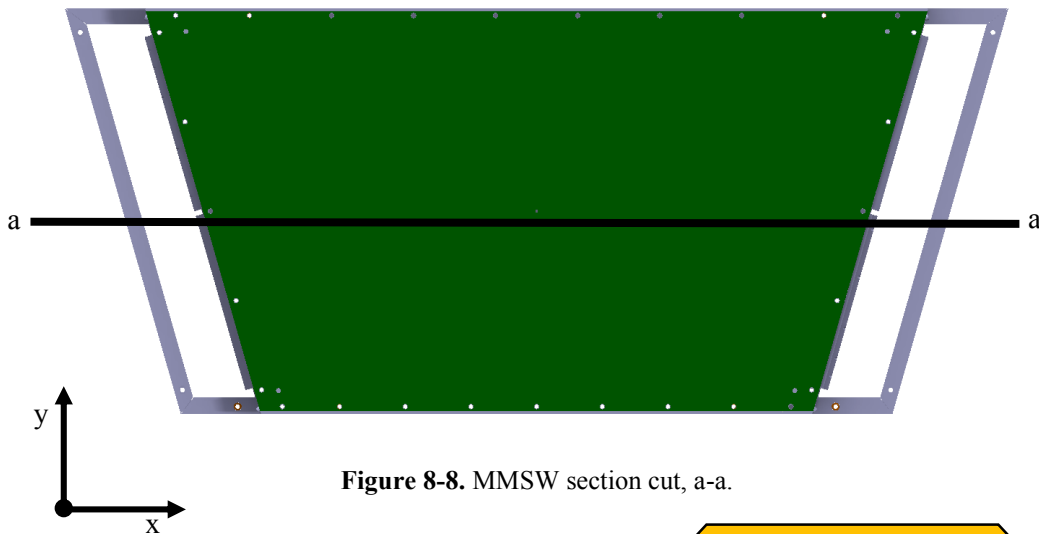
Figure 8-8. MMSW section cut, a-a.
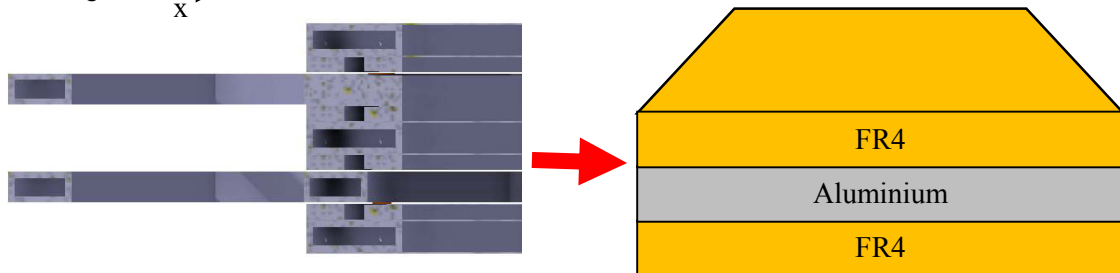
Figure 8-9. MMSW geometry simplification.

This analytical calculation which can be observed in Appendix G.1, not only takes the thermal coefficient of expansion and length in the direction of expansion of each material into account, but also the cross sectional areas and modulus of elasticity of each of the composite layers. A shear force is created in between the layers of the MMSW due to the thermal expansion of aluminium

being higher than that of FR4. This shear force results in an expansion force being applied to the FR4 and a compressive force being applied to the aluminium. In the analytical calculation, the forces applied due to the difference in thermal expansion is assumed to be completely transferred through the materials with no shear strain in each of the materials or bonding glue occurring. From the calculation, it is evident that we should expect a thermal expansion of about $\delta = 270\ \mu m$ over the length of the extremity of the MMSW in the y-direction and therefore an equivalent MMSW coefficient of thermal expansion of about $\alpha_{eq} = 20.28\ \frac{\mu m}{m \cdot °C}$ in this direction. The thermal expansion at the center of the MMSW can be calculated using the coefficient of thermal expansion of FR4 because it is the primary material in this area. This thermal expansion was calculated to be $\delta = 173\ \mu m$, significantly lower than at the extremities.

8.4   Computational Analysis

8.4.1   Introduction

The computational analysis portion of the MMSW analysis is aimed at providing a set of results, using the unique finite element analysis techniques and simplifications used for the analysis of the Micromegas wedges. These results are then compared to the experimental results that are to be explored in Chapter 8.5. The aim of this analysis is to use finite element analysis techniques to gain an understanding of the directional thermal expansion in the y-direction at the four points defined in Chapter 8.2 while applying the other appropriate system constraints as realistically as possible.

8.4.2   Procedure

The finite element analysis portion of the MMSW analysis was completed using the Ansys workbench and its static structural analysis system. This tool allows for an accurate thermal expansion approximation for a uniform change in temperature as specified in this comparative analysis. A flow chart summarising the following procedure can be viewed in Figure 8-10.

The finite element analysis technique used for the analysis of the Micromegas wedges' most unique component, is the way in which the geometry was drawn in the Ansys CAD package called Design Modeler. The geometry creation style simplified the three dimensional Micromegas wedges into mainly one and two dimensional elements, called beam elements and shell elements. In order to create a model of the MMSW that replicated the model of the Micromegas wedges, the same CAD generation technique was used.

Once the geometry had been created in the Ansys Design Modeler, the CAD and material data was imported into the Static Structural analysis system. The constraints for all the components of the MMSW assembly were then allocated. Ansys calls these constraints, connections.

The model was then discretised into a series of mesh elements. It was essential that the mesh was created satisfactorily for the given model. This was checked by visually inspecting the mesh and by using element quality checks.

Once the mesh was finalised, the structural conditions of the analysis were applied. The conditions were carefully thought out and created in the most realistic way possible. In the case of this model, the conditions consisted of displacement and rotational constraints and a thermal load.

The final step was creating the correct solution criteria to accurately analyse the model once the solver had generated a result. In the case of this experiment, the directional deformation due to the thermal expansion was presented.

Once the model had run and a result had been achieved by the solver, the results were analysed. The results were then checked against hypothesis to confirm that the model had behaved in a realistic manner.
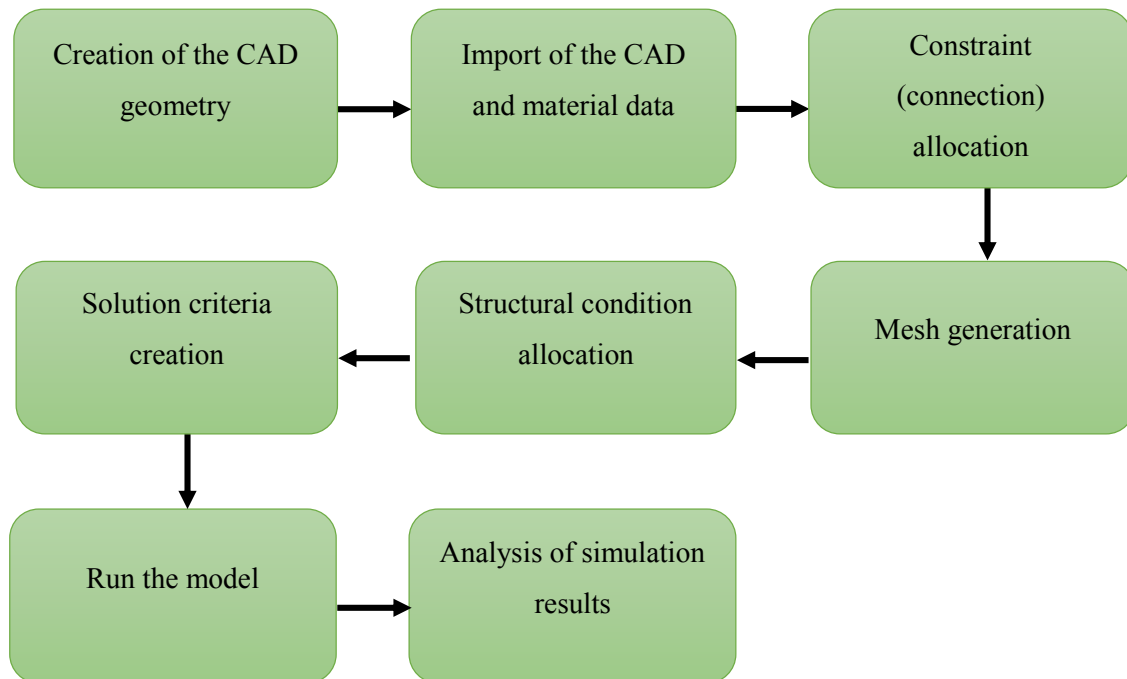
Figure 8-10. Computational analysis procedure.

8.4.3   CAD generation

The first and most important step of creating the finite element analysis simulation was creating an accurate interpretation of the geometry. This was done in a way that considered all future simulation procedures in order to create a model that meshed, applied constraints and applied structural conditions seamlessly. The way in which the stated finite element analysis method required the CAD to be generated makes use of the Ansys Design Modeler which is an integrated Ansys CAD generation package. This method eliminates the need to export and import CAD files from an external CAD package into the Ansys workbench, keeping the entire process in one individual software package. This decreased the overall solve time by aiding in the creation of a good mesh with few mesh impurities.

In order to create an accurate CAD model, it was important to study the components that make up the assembly being analysed. The MMSW is made up of a series of composite panels and support frames. There are three drift panels and two readout panels, each with a thickness of 11.4 mm, arranged in an alternating pattern, with 5 mm thick aluminium gas frames in between each layer, as observed in Figure 8-11. These panels are all made up of two 0.5 mm PCBs bonded with 0.2 mm of araldite glue to a 10 mm thick aluminium honeycomb core. The read out panels are slightly larger in the x-direction when compared to the drift panels. The outer edge of each of these panels is reinforced by a hollow aluminium cross section that essentially replaces the aluminium honeycomb structure in the area, acting as the core of the composite panel. These hollow sections have outer cross sectional dimensions of 30 mm x 10 mm and a wall thickness of 1.5 mm. In between each composite panel, along the perimeters of each, are aluminium gas frames, keeping the pressurised gas in the cavity that is created. These gas frames add a major contribution to the overall structural rigidity of the assembly. These gas frames are composed of solid aluminium beams of cross section 12 mm x 5 mm. There are also aluminium beams inside this gas region called mesh frames. These mesh frames hold the MMSW mesh in place and again add a significant contribution to the structure of the MMSW and consequently the Micromegas structures. The mesh frames are mounted to only the drift panels and have cross sectional dimensions of 12 mm and a height value of slightly lower than 5 mm. This value can be assumed to be equal to 5 mm for most calculations.

In the computational, Ansys model, all 9 layers of the MMSW were created separately on a series of offset planes that lie parallel to one another. These components were then linked together at a later stage using the Ansys static structural tool. The order of occurrence of these layers can be

seen in Figure 8-11. The gas regions are clearly represented by the white areas in between the green structure.

Drift Panel	
Gas drift region	
Readout panel	
Gas drift region	
Drift Panel	
Gas drift region	
Readout panel	
Gas drift region	
Drift Panel	
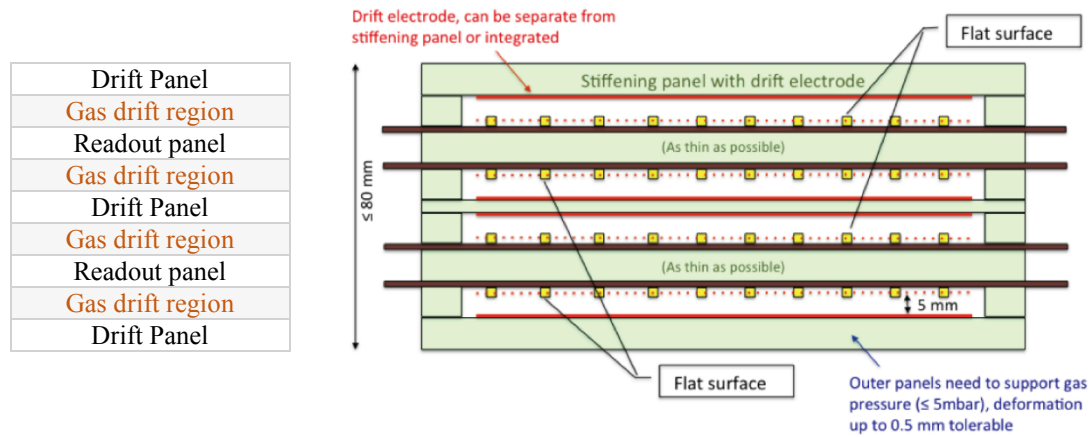
Figure 8-11. MMSW cross section.

The types of elements used for each of the components are listed below. A description of the reasoning for the use of each of the elements used will be explained later in this chapter.

1. Drift panel – Shell element – Two dimensional
2. Readout panel – Shell element – Two dimensional
3. Mesh frame – Beam element – One dimensional
4. Gas frame – Solid element – Three dimensional
5. Reinforcement frame – Beam element – One dimensional

These simplifications allow for a much quicker solving time as well as allowing quick changes to be made to the cross sections of the beams and the thickness and composite design of the planes.

The first component of the geometry created was the outer most panel of the structure which is one of the three drift panels. A labelled final sketch of the drift panel along with an enlarged image of one of its corners can be seen in Figure 8-12. Using the local co-ordinate system of a plane created specifically for this panel, the outer shape was defined in a sketch. The outer shape follows the trapezoidal shape of the drift panel of the MMSW precisely. Following the creation of the outer shape of this panel came a significant part of this construction method. This step involved using a sketch to imprint the outside geometry of all the geometry components that were to be linked to this panel. This was done to allow the panel to be split along these lines so that when meshed, the elements making up the solids and beams of each component lined up perfectly,

creating a faultlessly linked mesh. It also created the geometry areas necessary to apply the connections between the layered components. In the case of this drift panel; the gas frame, the mesh frame and the reinforcement frame all have connections that needed to be included in the geometry of the panel. For one dimensional beam elements, the exact line of the beam element should simply be followed on the panel to perform this operation. The reinforcement frame and the mesh frame are both beam elements and were therefore represented by lines running through the centre of the bar on the sketch. The gas frame is, however, a solid element and its imprint on the panel, therefore followed the outside edges of the area of the bar that is in contact with the panel. These lines can all be observed in the labelled image in Figure 8-12.

Once all of these lines were created, more lines were added to the geometry of the panel to help create regular shapes on the panel in order to enable the creation of a well arranged mesh. This can be observed in the represented corner of the drift panel in Figure 8-12.

At this stage the two points where the MMSW was to be constrained in the thermal simulation were added to the geometry. This constraint is done to avoid rigid-body motion and to create a point of reference for the thermal expansion. The creation of this geometry at this stage, allowed for a quick constraint to be made during the model processing.
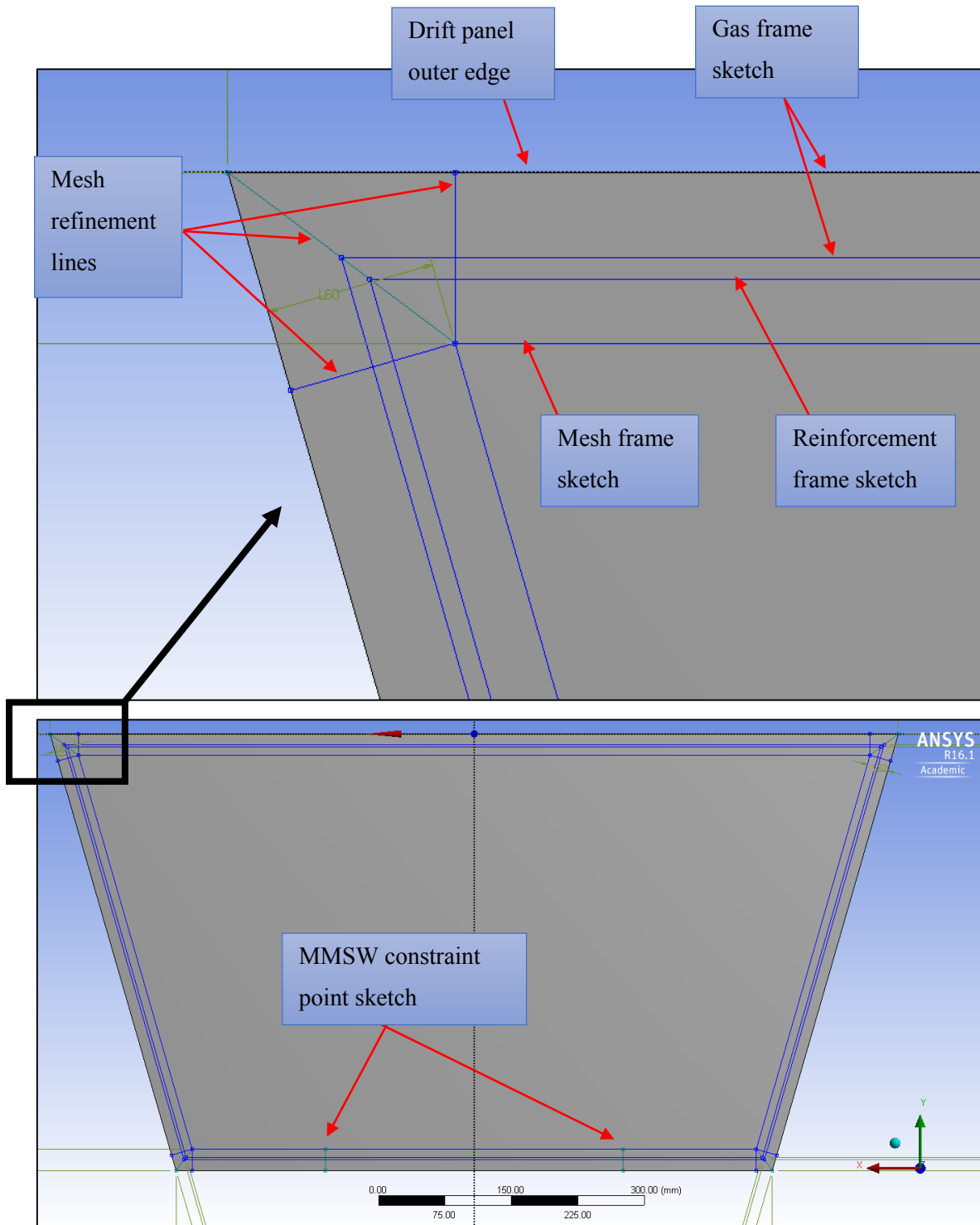
Figure 8-12. Drift panel sketch.

The next step was to create the plane required for the gas frame and the mesh frame to be created on. This plane runs directly through the middle of these frames and was created by offsetting a plane from the drift panel plane. The offset plane was positioned to lie at the midpoint of these frames in the z-direction.

Once the plane was created, the geometry of each of these frames was included. A copy of the outside geometry of the drift panel was projected onto this plane to use as a base geometry for these two components. The geometry for the mesh frame was created by generating a line through the centre of where the frame was expected to go. This is done because the frame is created using beam elements. The gas frame, however, is not made from beam elements and consequently, is not as simple as this. At this stage, the outside edges of the gas frame were added to the sketch. At this stage, the plane had one continuous line to create the mesh frame and two continuous lines to create the gas frame. A labelled sketch of the mesh frame and the gas frame can be observed in Figure 8-13.
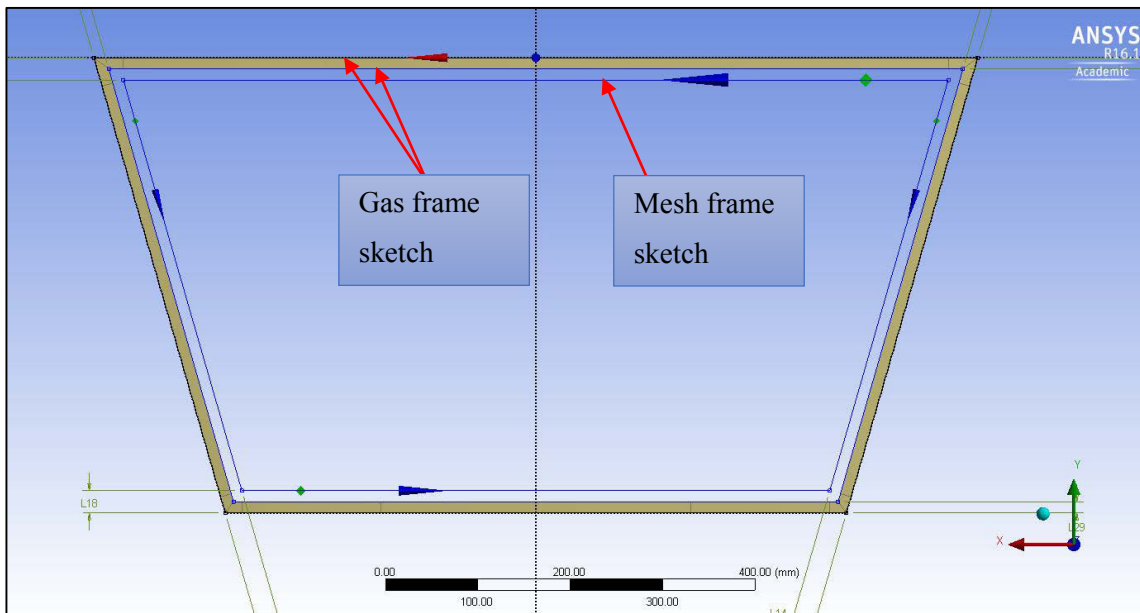
Figure 8-13. Mesh frame and Gas frame sketch.

Next, the readout panel plane was created. This plane was also created by offsetting a plane by a set amount from the drift plane in order to run directly through the centre of the readout panel. Once the plane was created, an image of the outside perimeter of the drift panel was once again projected off the drift panel sketch to create a base sketch for the readout panel. The readout panel

is larger than the drift panel in the x-direction. The bigger sketch was therefore created according to the new dimensions by offsetting lines from the projected plane. The geometry for the gas frame, reinforcement frame and mesh frame were all included in the same way as it was done for the drift plane. A sketch of this readout plane can be observed in Figure 8-14.
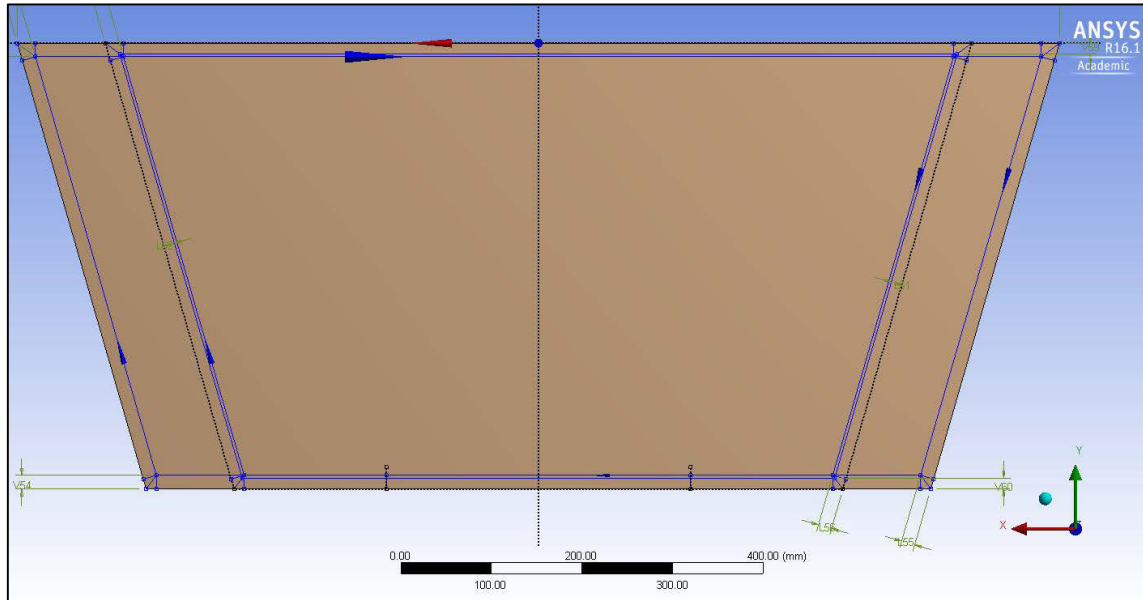
Figure 8-14. Readout panel sketch.

The sketches for the three different layers found in the MMSW were now created, namely the drift plane containing the drift panel and the drift reinforcement bar, the gas plane containing the mesh frame and the gas frame, and the readout plane containing the readout panel and the readout reinforcement bar.

It was now possible to create the geometry of the drift panel and the readout panels using shell elements called surfaces in Ansys Design Modeler. These surfaces were created on the outside edges of each of the panel sketches and given a thickness of 11.4 mm which is equal to their total thickness in reality. By doing this, two parts, called bodies, were created.

The next step was creating the geometry of the panel reinforcement frames and the mesh frame. This was done using beam elements called lines in Ansys Design Modeler. The sketches created previously for each of these frames were used. Once the lines were created, cross sections of the two beams were drawn and applied to the lines to create parts for the assembly. The cross sections

for the panel reinforcement frame and the mesh frame can be found in Figure 8-15 and Figure 8-16 respectively.
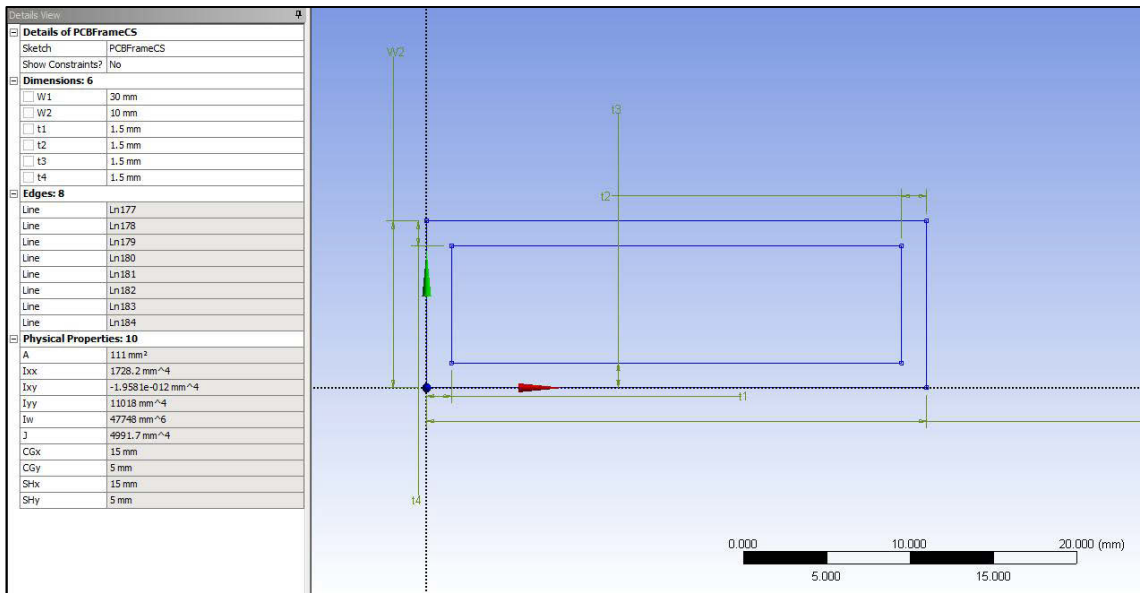
Figure 8-15. Panel reinforcement frame cross section.
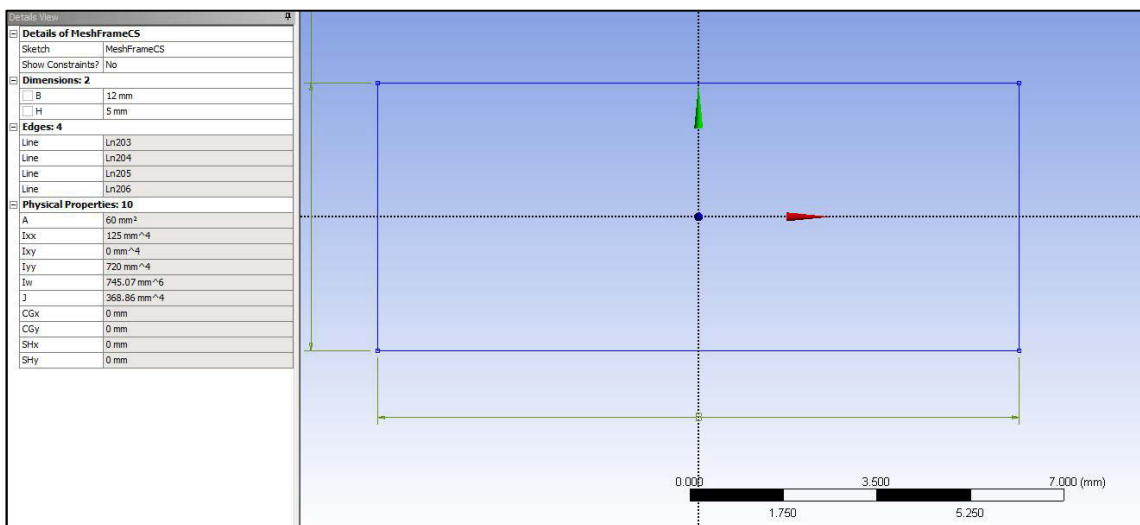
Figure 8-16. Mesh frame cross section.

The gas frame was now created by extruding the sketch previously specially constructed, into a solid part. The gas frame was generated using this method in order to create three dimensional elements in its area. This is the only part which both panels need to be constrained to. If this part was a one dimensional beam element, by constraining the two shell elements that surround it to

the beam element, the three layers would all have nodes connected directly to each other. This would result in all shear effects between the layers being lost. The three dimensional solid part negates this effect resulting in the necessity of its use.

At this stage, the geometry created was split up into smaller parts in order to create a better mesh. A function called 'face split' broke up the drift panel and the readout panel into many different surfaces along their sketch lines. The solid gas frame was also split in the same places using an extruded perpendicular surface from the sketches. The effects of these part splits will be observed when the mesh of the assembly is created, as discussed in Chapter 8.4.5.

Using the Ansys Design Modeler, it is possible to create a pattern, copying the geometry from one plane and creating it in another. The second plane containing the copied geometry can be offset to a desired specification. This function means that to create the MMSW, only one drift plane, one gas plane and one readout plane needed to be created. Using this function, the drift plane was replicated and offset to its correct locations twice, the readout plane was replicated and offset once and the gas plane was replicated and offset three times. Once all three planes had been replicated, all the required parts had been created successfully and the image in Figure 8-17 could be observed.
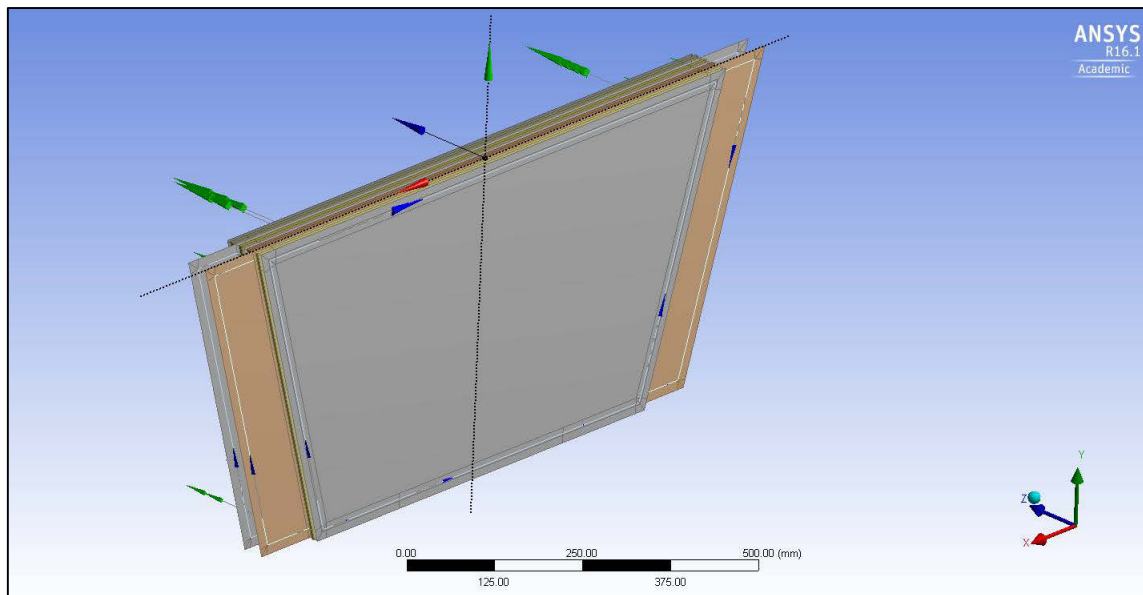
Figure 8-17. Ansys Design Modeler geometry of MMSW.

The final step that had to be completed using the Ansys Design Modeler was creating links between all bonded components existing on the same plane. The Design Modeler allows the user to create a link called a joint between two parts on the same plane that are to act together in the simulation. The panel reinforcement frames and each of their corresponding panels are an example of this form of geometry and are linked together using this function.

The material properties were now applied to the components of the MMSW. Aluminium was applied to the mesh frame, gas frame and panel reinforcement frame. The panels were allocated a composite layup represented in Figure 8-18. The material properties of these components can be observed in Appendices H.1, H.2, H.3, and H.4.

Layer	Material	Thickness (mm)	Angle (°)
(+Z)			
5	FR4	0.5	0
4	Araldite	0.2	0
3	Honeycomb Alu	10	0
2	Araldite	0.2	0
1	FR4	0.5	0
(-Z)			

Figure 8-18. Composite lay-up.

8.4.4 Model Constraints

The creation of a constraint between two parts is called a connection in the Ansys Static Structural analysis system. In the case of the model of the MMSW, connections needed to be made between the mesh frames and the drift panels in the form of a bonded contact pairs. This linked the beam elements of the gas frame to the shell elements of the drift panels.

Another connection that needed to be made was between the gas frames and the panels that exist on either side of them. Each gas frame has one readout panel on one side of it and one drift panel on the other side of it. Using the bonded contact tool in the Ansys Static Structural analysis system, the faces on the panels that were previously split to follow the geometry of the gas frames were bonded to the surfaces of the gas frames that came into contact with them. On completion of these connections, the entire MMSW model was fully assembled and ready to be processed.

8.4.5 Discretisation

Discretisation of a model is the process of reducing it into a series of elements to create a mesh. The method of the creation of a mesh of a finite element model has a great deal of importance. The accuracy of the results and the run time of the simulation greatly rely on the density and the quality of the mesh. For this reason, it is essential that a good mesh is created.

The mesh for the MMSW model was created with the addition of a mapped face meshing tool. This tool ensured that quadrilaterals were used in the mesh for improved mesh accuracy. The advantage gained from the act of splitting the panels and the solid gas frames in the Ansys Design Modeler can now be observed. Because these parts, were split into separate parts, the mesh used the edges of these splits as a location for the creation of nodes. This can be seen in the example image in Figure 8-19. In this image, one can clearly see how the mesh has been created, following the lines of the split geometry. The split geometry helped ensure that the mesh, for all layers of the MMSW, were perfectly aligned and simplified the geometry into regular shapes which helped create a more regular mesh.
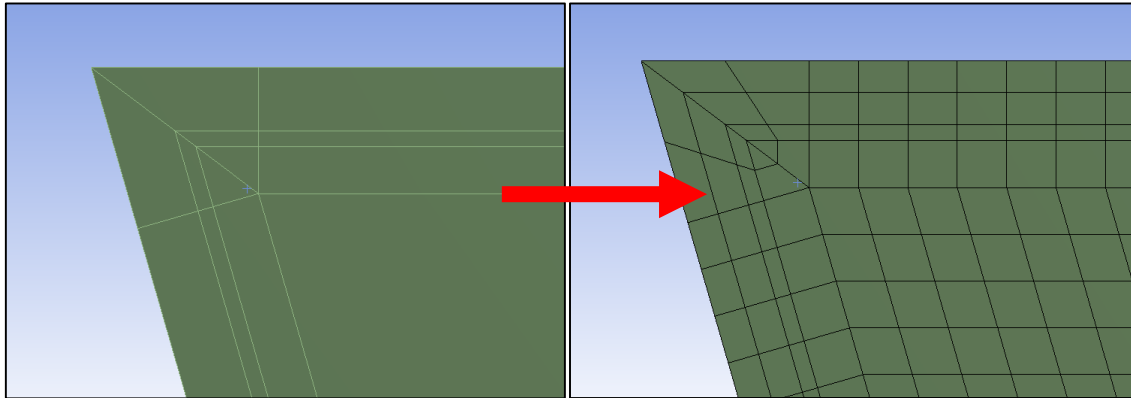
Figure 8-19. Geometry controlled mesh.

The image represented in Figure 8-20 shows the completely meshed MMSW model. A quick and easy check that can be used to examine the quality of the mesh is a visual inspection. If regular and evenly spaced quadrilaterals, making up a large portion of the meshed geometry are observed, then the user can be confident that the mesh is reliable (Javidinejad, 2012). This regularly meshed surface can be clearly observed in Figure 8-20.
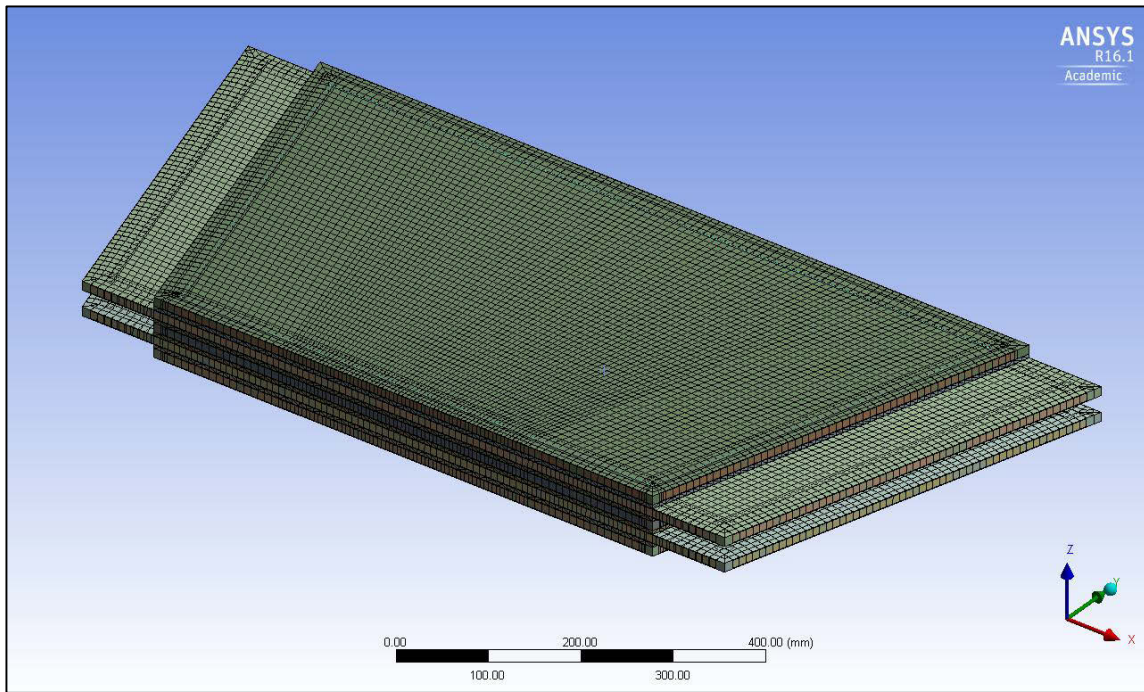
Figure 8-20. Meshed MMSW.

Another indication of the mesh quality can come from the mesh element shape quality checks provided by the Ansys Workbench. The quality check defined as, element metrics, analyses the element shapes of the mesh. If the data is skewed to the right then one can confirm that a good mesh has been created and few errors will result due to the shape of the mesh (ANSYS, 2013). Figure 8-21 is the element shape analysis completed for the mesh of the MMSW simulation. It can be observed that the data is skewed to the right indicating that the quality of the element shapes produced are good.
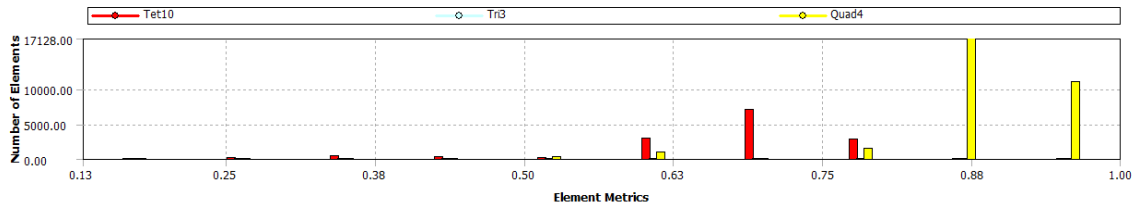
Figure 8-21. Mesh element shape quality.

8.4.6   Model Conditions

In order to create a repeatable simulation in the experiment, the creation of the model conditions in the finite element model met all the requirements described in the methodology of the overall analysis.

In finite element models, the model must be constrained in all of its degrees of freedom to prevent rigid body motion. Rigid body motion occurs when the model is free to be accelerated when a force is applied to it. To prevent this, the constraints in the model need to collectively restrict all six degrees of freedom. A fixed point constraint was applied to Point 1 in Figure 8-22. The second point, however, could not also be a fixed constraint. A fixed constraint at this point would restrict movement in the x-direction in the area labelled X in Figure 8-22. For this reason, only a constraint in the y-direction was applied at point 2, only restricting motion in the y-direction as specified in the model requirements.

Ansys Static Structural is primarily a tool used for physical force loads on objects. For this reason, it is impossible to change the initial temperature of a model from 22°C, while the final temperature can easily be changed to a required value. This made it impossible to change the temperature of the model to suit the required 23°C and 24°C initial conditions. This was overcome due to the fact that thermal expansion of a material is a linear function when calculated over such a small temperature range and therefore does not rely on the initial and final temperatures but instead the difference between the two. In order to achieve a temperature change from 23°C to 50°C, instead of changing the initial temperature, the final temperature is changed to 49°C.
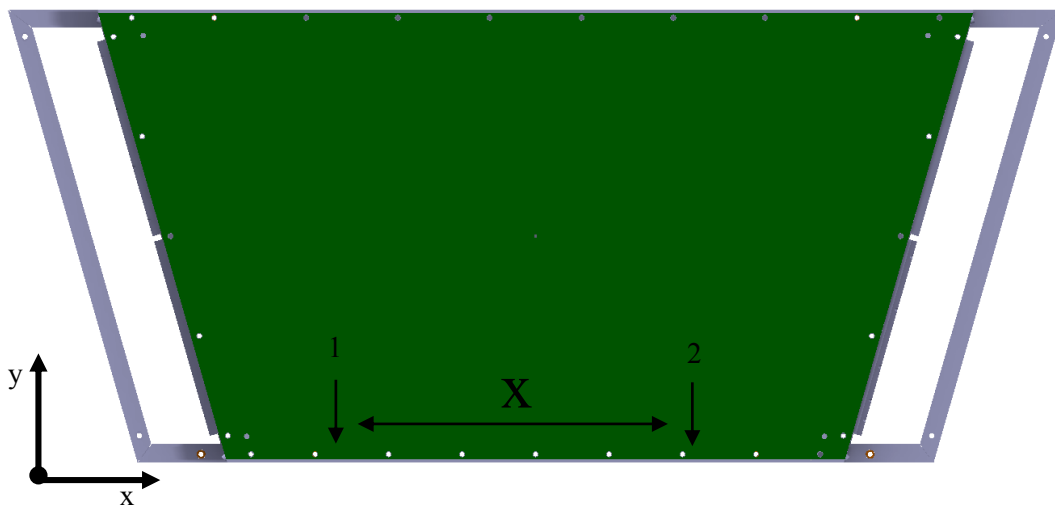
Figure 8-22. FEA constraints.

8.4.7 Results

The finite element model was run three times, each time with a small change in the model conditions. The change in condition for each of the simulations was a change in temperature that was set to a 28°C, a 27°C and a 26°C change resulting in a varying displacement measurement due to thermal expansion.

A displacement in the y-direction, solution criterion was specified. This solution representation best describes a thermal expansion in the y-direction as specified by the overall analysis constraints. A y-directional probe was placed at the central x-value at the maximum y value of the MMSW model and thereafter, every 50 mm in the positive and negative x-directions. These probes gave exact values of the deformation of the material in the y-direction at each of the points they were positioned at.

The simulation was first conducted for a change in temperature of 28°C. Figure 8-23 is a graphical representation of the overall deformation of the MMSW in the y-direction. From this image, one can see that the maximum positive y-directional expansion when referenced to the fixed point is 259 μm. An expansion in the negative y-direction of 40 μm can be observed. It can also be seen that the maximum deformation occurs at the x-direction extremities of the MMSW while the lowest y-directional expansion occurs at the centre location of the MMSW, when referring to its x-coordinate.
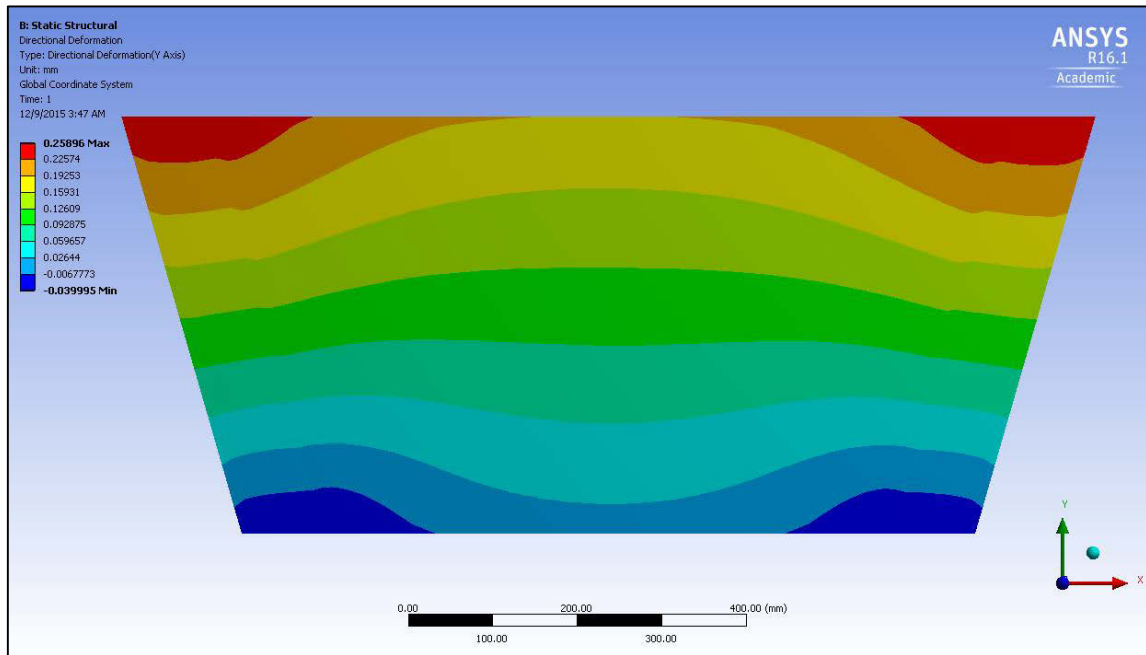
Figure 8-23. MMSW 28°C total thermal expansion in the y-direction.

Table 8-1 is a representation of the probe numbers, their distance from the centre line of the MMSW and the y-directional expansion value that each of them experienced. Figure 8-24 is a graphical representation of these values on a scatterplot. The lowest y-directional thermal expansion that the top of the MMSW experienced was 192 µm.

Table 8-1. MMSW 28°C thermal expansion y-direction probe results.

Probe number	Distance from centre (mm)	y-direction expansion (μm)
1	0	192
2	50	192
3	100	194
4	150	196
5	200	200
6	250	206
7	300	215
8	350	226
9	400	241
10	450	255
11	478	256
12	500	252
13	550	251
14	575	247
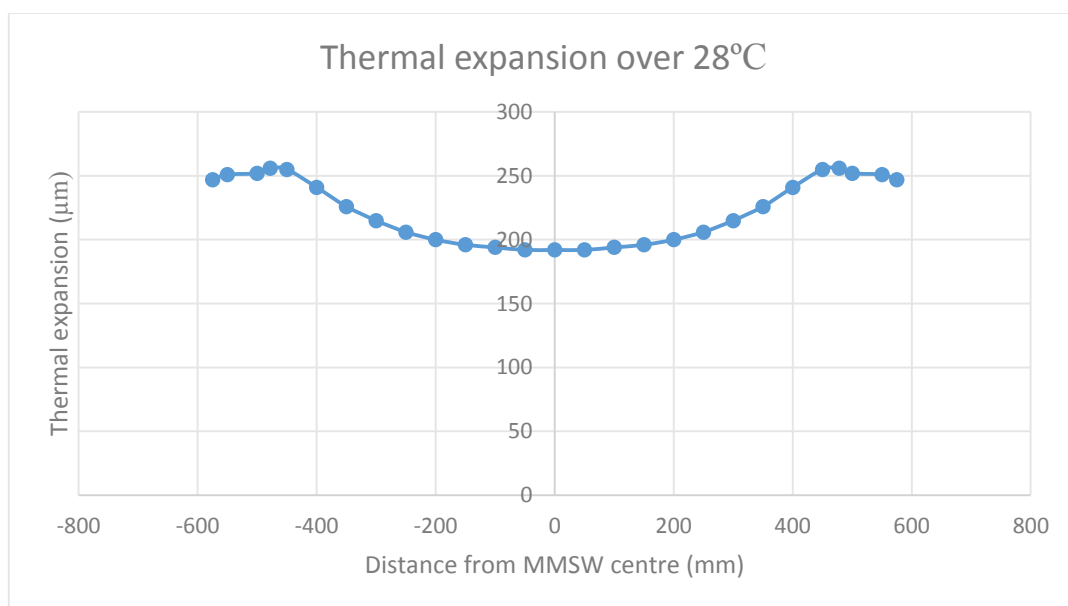
Figure 8-24. Scatterplot representing the MMSW 28°C thermal expansion y-direction probe results.

The simulation was then conducted for a change in temperature of 27°C. Figure 8-25 is a graphical representation of the overall deformation of the MMSW in the y-direction. From this image, one can see that the maximum positive y-directional expansion when referenced to the fixed point is 250 µm. An expansion in the negative y-direction of 39 µm can also be observed. It can also be seen that the maximum deformation occurs at the x-direction extremities of the MMSW while the lowest y-directional expansion occurs at the centre location of the MMSW, when referring to its x-coordinate.
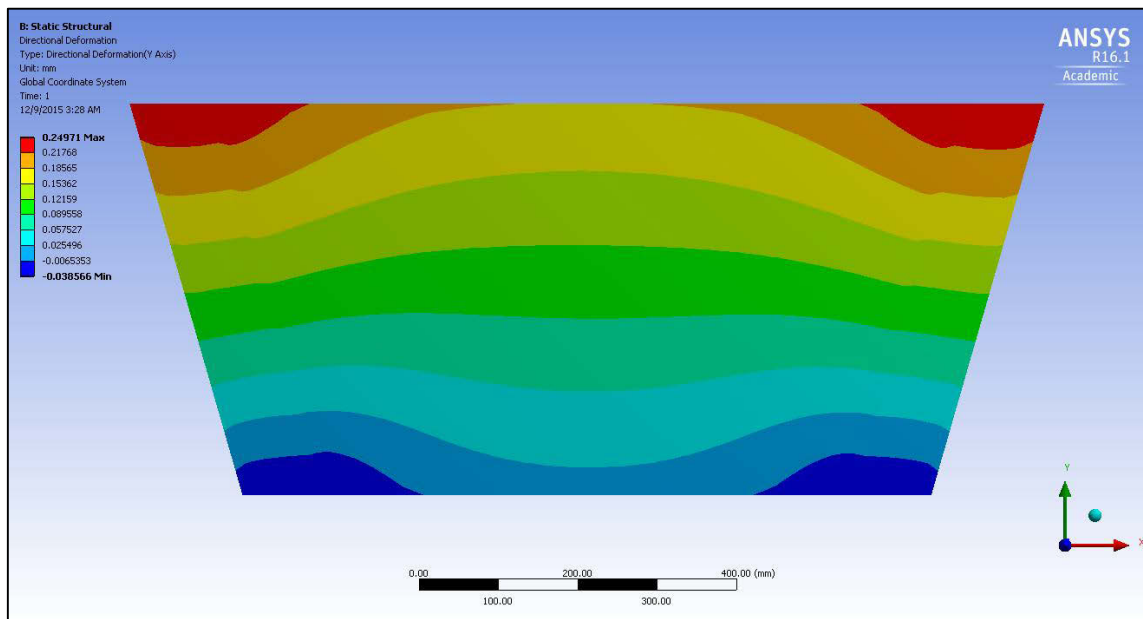
Figure 8-25. MMSW 27°C total thermal expansion in the y-direction.

Table 8-2 is a representation of the probe numbers, their distance from the centre line of the MMSW and the y-directional expansion value that each of them experienced. Figure 8-26 is a graphical representation of these values on a scatterplot. The lowest y-directional thermal expansion that the top of the MMSW experienced was 185 µm.

Table 8-2. MMSW 27°C thermal expansion in y-direction probe results.

Probe number	Distance from centre (mm)	y-direction expansion (µm)
1	0	185
2	50	185
3	100	187
4	150	189
5	200	193
6	250	199
7	300	207
8	350	218
9	400	232
10	450	246
11	478	247
12	500	243
13	550	242
14	575	238
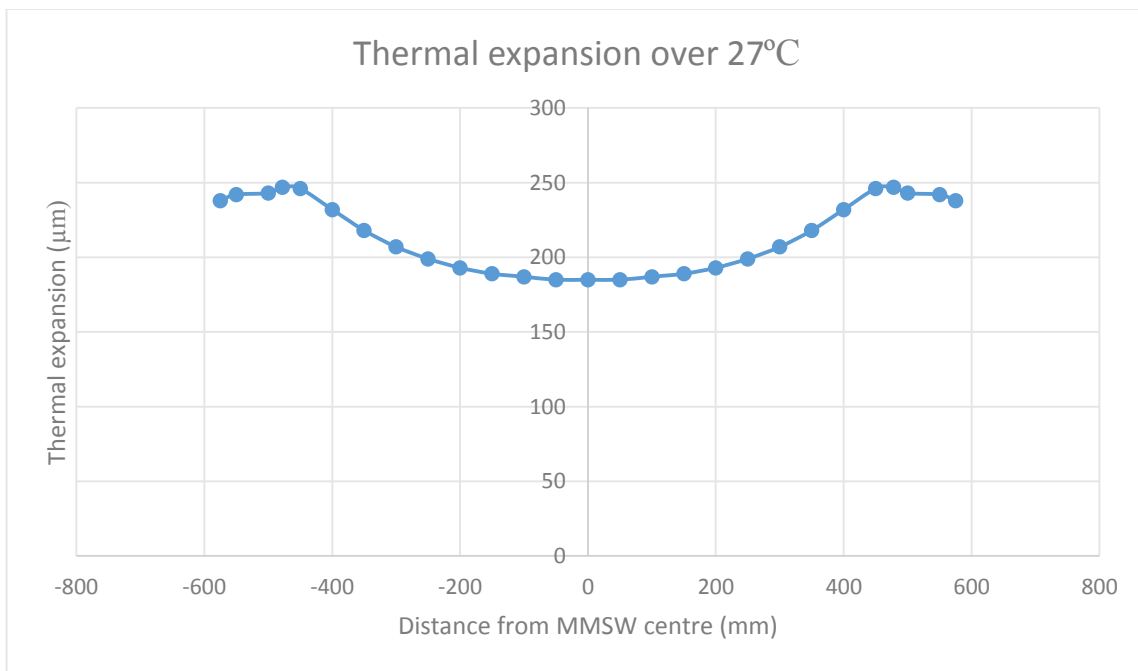
Figure 8-26. Graph representing the MMSW 27°C thermal expansion y-direction probe results.

Finally, the simulation was conducted for a change in temperature of 26°C. Figure 8-27 is a graphical representation of the overall deformation of the MMSW in the y-direction. From this image, one can see that the maximum positive y-directional expansion when referenced to the fixed point is 240 µm. An expansion in the negative y-direction of 37 µm can also be observed. It can also be seen that the maximum deformation occurs at the x-direction extremities of the MMSW while the lowest y-directional expansion occurs at the centre location of the MMSW, when referring to its x-coordinate.
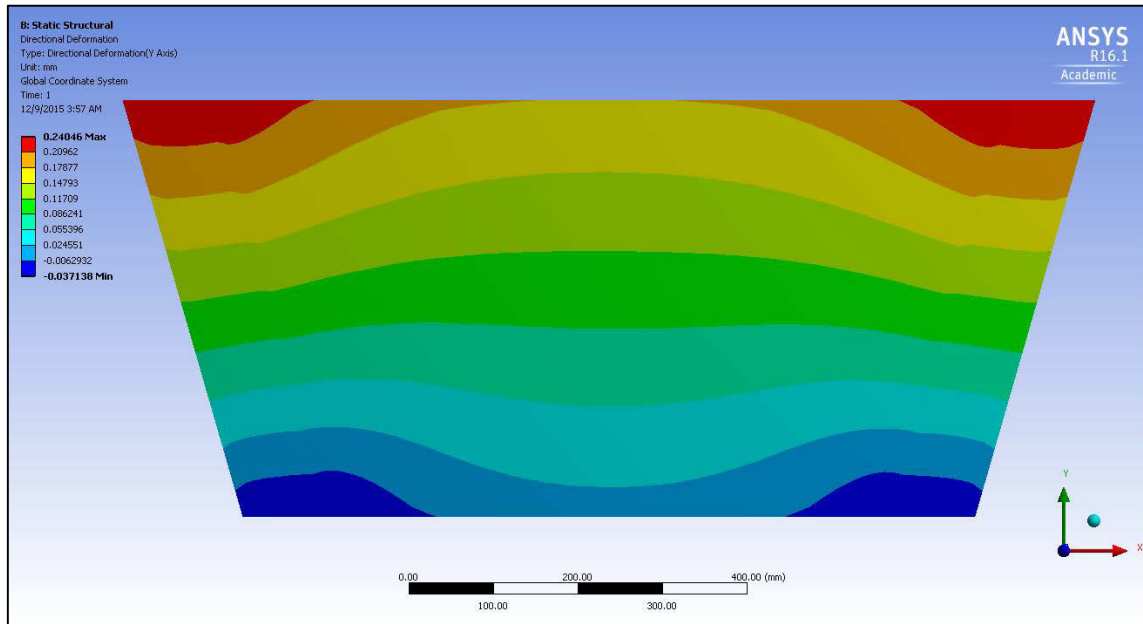
Figure 8-27. MMSW 26°C total thermal expansion in the y-direction.

Table 8-3 is a representation of the probe numbers, their distance from the centre line of the MMSW and the y-directional expansion value that each of them experienced. Figure 8-28 is a graphical representation of these values on a scatterplot. The lowest y-directional thermal expansion that the top of the MMSW experienced was 178 µm.

Table 8-3. MMSW 26°C thermal expansion in y-direction probe results.

Probe number	Distance from centre (mm)	y-direction expansion (µm)
1	0	178
2	50	178
3	100	180
4	150	182
5	200	186
6	250	192
7	300	200
8	350	210
9	400	224
10	450	236
11	478	238
12	500	234
13	550	233
14	575	229
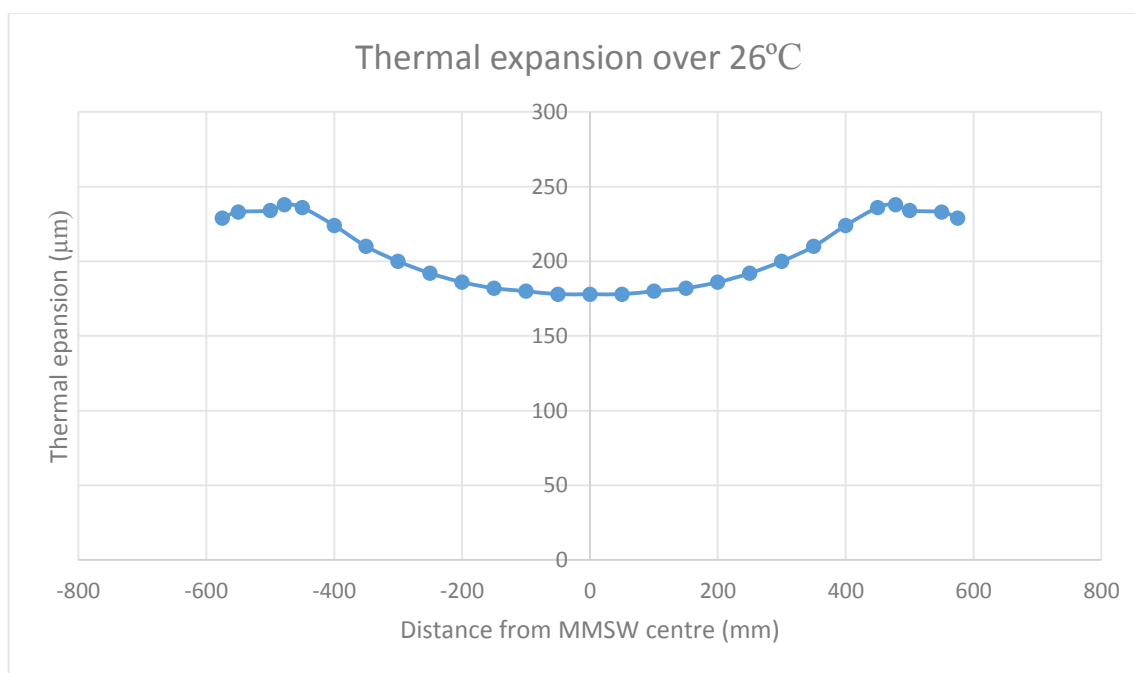
Figure 8-28. Graph representing the MMSW 26°C thermal expansion y-direction probe results.

8.4.8   Discussion – Computation Analysis

A thermal analysis of the MMSW was completed using a finite element analysis. Simplified analytical calculations performed at the extremities and center of the MMSW estimated that a maximum thermal expansion of about 270 μm was expected at the extremities and 173 μm at the center, in the y-direction for an increase of 27°C of the MMSW. The results obtained from the simulations at this change of temperature, showed that the maximum expansion in the positive y-direction from the fixed point at the MMSW extremity was 250 μm and the maximum thermal expansion in the negative y-direction from the fixed point was 39 μm. When adding these two values together, one can observe that the maximum thermal expansion experienced at the extremities was 289 μm. This value has a difference of only 19 μm from the estimated analytical calculation. The maximum expansion in the positive y-direction from the fixed point at the MMSW center was 186 μm and the maximum thermal expansion in the positive y-direction from the fixed point was 12 μm. When subtracting the second value from the first, the expansion at the center of the MMSW can be found. The maximum thermal expansion experienced at the center is therefore, 174 μm. This value has a difference of only 1 μm from the estimated analytical calculation of 173 μm.

This confirms that the results achieved from the finite element analysis are in the correct range and are therefore realistic results. The relevant results achieved from this simulation, however, do not take the thermal expansion in the negative y-direction into account, and instead, only the expansion in the positive y-direction are measured and analysed. This measurement procedure is adopted because a great deal of complexity is added when trying to measure the thermal expansion of the MMSW in both y-directions in the experimental analysis.

In future simulations of the MMSW and the Micromegas wedges, alike, it will be possible to create an axis of symmetry in the y-direction at the central point along its x-coordinates, halving the model and thus reducing the solve time substantially. A constraint in the x-direction should be applied to all geometry that touches this plane of symmetry in order to ensure that the model still acts in the same way as experienced before. This simplification is possible because the MMSW geometry and the way it thermally expands in the y-direction is symmetrical about this point. This was not done in the simulation of the MMSW because it has not done for the models of the Micromegas wedges.

8.5 Experimental Testing

8.5.1 Introduction

In order to recreate the conditions experienced by the MMSW in the computational analysis, many specific experimental constraints need to be applied. This experiment should only measure the y-direction thermal expansion and apply the correct constraints similar to those used in the finite element simulation process.

8.5.2 Apparatus

In order to complete the experimental analysis accurately and efficiently, a composites lab in Room 209, of Building 153 of the Meyrin CERN site, was available for use. The following equipment was used:

1. One Votsch composites oven, complete with thermocouple plugs.
2. Four micrometre dial gauges with a resolution of 10 μm.
3. One MMSW experimental test stand (Figure 8-29). Made exclusively from steel.
4. Teflon strips

Tests on the following two components were conducted:

5. Aluminium test bars
6. Micromegas portion mock-up – MMSW
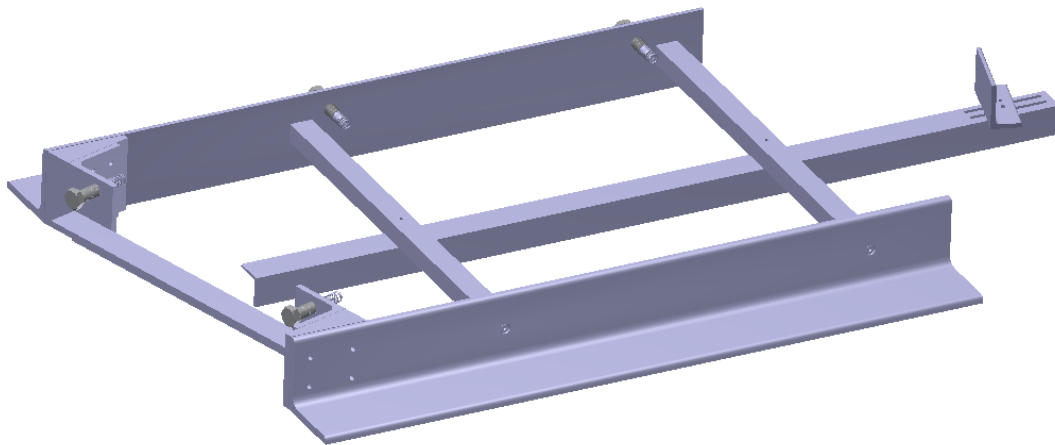
Figure 8-29. Micromegas test stand.

8.5.3 Equipment Testing

A series of test experiments were conducted in order to assess whether the equipment used, in particular the dial gauges, would behave reliably under the intended conditions, in particular, the temperature range. These testing experiments were also used to determine which of two different experimental methods would act most reliably. In order to make the testing relevant, the exact predicted MMSW experiment conditions were mimicked, the only difference being that the MMSW was not tested and instead, a uniform material was used as the test piece. The use of a uniform material negated the chance of any material or geometrical irregularities and allowed for an easy and reliable analytical calculation to compare to the experimental results obtained.

The tests involved the measurement of the thermal expansion of uniform aluminium bars. The thermal expansion of these aluminium bars can be easily calculated analytically and compared to the results obtained from the test experiments. Each of the aluminium bars were measured to get an accurate initial measurement to use in the analytical calculations. The bars were all measured to be 494 mm long when measured to the nearest millimetre.

The bars were placed on the steel MMSW experiment stand in a row, pushed up against the stand's edge. The dial gauges were placed in the same positions that they are to be placed in the MMSW experiment. The bars were placed on Teflon strips in order to reduce the friction, allowing easy expansion movement of the bars during heating. This arrangement can be observed in Figure 8-30.

Figure 8-30. Aluminium bar test experiment.

This experiment was carried out using two different methods – the same two methods proposed to be used for the MMSW experimental analysis. Testing both of the proposed methods enabled an understanding of the reliability of each of them to be gained in order to see which results are more accurate for the MMSW experimental analysis.

The first of these methods involves placing the room temperature aluminium bars on the steel MMSW experiment stand previously heated to 50ºC. This method negates the effect of thermal expansion of the steel frame and removes the need to subtract the value of the theoretical expansion of the steel. It does, however, create an element of inaccuracy due to the fact that the frame cools when it is exposed to the cool air during opening of the oven door. Room temperature aluminium bars were placed on the hot frame and the dial gauges were zeroed. It is very difficult to determine how much and how evenly the frame cools during this operation. This experiment was completed three times using four aluminium bars each time.

The second methods involves placing the room temperature aluminium bars on a room temperature steel MMSW experiment stand. This method allowed both the steel frame and the aluminium bars to thermally expand at the same time as the temperature was increased. The two materials, however, have a varying coefficient of thermal expansion. The reading on the dial gauges is therefore a result of a combination of the two varying thermal expansions. The true thermal expansion of the aluminium bars can easily be calculated by subtracting the theoretical thermal expansion of the steel frame from the reading observed by the dial gauges, negating the effects of the steel expansion. It must be noted that the dial gauges, along with their stands are determined to be entirely made from steel. By fixing these gauges to the steel MMSW experiment stand, they can be assumed to be part of the stand. The length of the steel used in the theoretical calculation for the thermal expansion of steel is therefore exactly the same as the length of the aluminium bars used. This experiment was completed three times using four aluminium bars each time.

Once placed in the vented oven, the apparatus was heated for four hours for both methods of experimentation to allow a consistent temperature reading throughout the oven to be reached. This ensured that the entire experiment was at a constant temperature and accurate readings could be taken.

Once temperature was reached the oven was opened and the values on the dial gauges were quickly read. Each bar was pushed up against the steel frame before reading the dial gauges to check for movement away from this end constraint during heating.

The initial readings when the aluminium bars were at room temperature and the final dial gauge readings when the aluminium bars were at 50°C were taken from each of the experiments. In each experiment, four aluminium bars were used along with a single dial gauge for each bar. These results are represented in the tables found in Appendix I.1 and Appendix I.3. A final summary of the expansion observed by the dial gauges can be seen in Table 8-4 and Table 8-6. The errors of each experimental analysis along with an average error across each of two experimental methods can be observed in Table 8-5 and Table 8-7. Example calculations showing the method of calculating the analytical values of measured thermal expansion as well as the error percentage can be observed in Appendix I.2 and Appendix I.4. The three experiments where cold aluminium bars are placed on the hot MMSW frame are labelled Experiment 1A, Experiment 1B and Experiment 1C. The experiments where cold aluminium bars are placed on the cold MMSW frame are labelled Experiment 2A, Experiment 2B and Experiment 2C.

Table 8-4. Experiment 1 change in dial gauges.

Dial Gauge Number	Experiment 1A Change in dial gauge reading (µm)	Experiment 1B Change in dial gauge reading (µm)	Experiment 1C Change in dial gauge reading (µm)
1	300	300	310
2	230	300	290
3	270	270	300
4	240	290	300
Average	260	290	300
Analytical Value	300.550	312.109	312.109

Table 8-5. Experiment 1 error percentages.

Dial Gauge Number	Experiment 1A Error (%)	Experiment 1B Error (%)	Experiment 1C Error (%)	Average (%)
1	-0.18	-3.88	-0.68	-1.58
2	-23.47	-3.88	-7.08	-11.48
3	-10.16	-13.49	-3.88	-9.18
4	-20.15	-7.08	-3.88	-10.37
Absolute Average	13.49	7.08	3.88	8.15

Table 8-6. Experiment 2 change in dial gauges.

Dial Gauge Number	Experiment 2A Change in dial gauge reading (μm)	Experiment 2B Change in dial gauge reading (μm)	Experiment 2C Change in dial gauge reading (μm)
1	160	130	150
2	150	140	160
3	150	130	140
4	150	120	150
Average	152.5	130	150
Analytical Value	146.422	129.527	157.684

Table 8-7. Experiment 2 error percentages.

Dial Gauge Number	Experiment 2A Error (%)	Experiment 2B Error (%)	Experiment 2C Error (%)	Average (%)
1	9.27	0.37	-4.87	1.59
2	2.44	8.09	1.47	4.00
3	2.44	0.37	-11.21	-4.20
4	2.44	-7.36	-4.87	-3.26
Absolute Average	4.15	4.05	5.61	4.60

On inspection of these obtained results, it is clear that Experiment 2, where the cold aluminium bars were placed on a cold MMSW experiment stand produced more accurate results with an

absolute average error of 4.6 while Experiment 1 gave an absolute average error of 8.15. Experiment 2 is therefore determined to be the more accurate method. It should also be noted that all of Experiment 1's results were lower than the expected analytical solution. This is a result of cooling of the MMSW experiment stand when the oven was opened to place the aluminium bars on the stand.

It has also been observed that no dial gauge showed a repeatedly high error and they can all be used for the MMSW analysis.

8.5.4   Procedure

The procedure for the MMSW thermal expansion experiments followed a very similar procedure that was followed for the aluminium bar thermal expansion experiments. This was done in an attempt to allow the reliability of the aluminium bar experiment to support the results found during the MMSW thermal experiments.

The MMSW was placed on its test stand and pushed against two support bars. It was important to note the positioning of these support bars. The positioning of these support bars followed the constraints indicated in the methodology in Chapter 8.2.

Figure **8-31** shows the setup of this experiment.
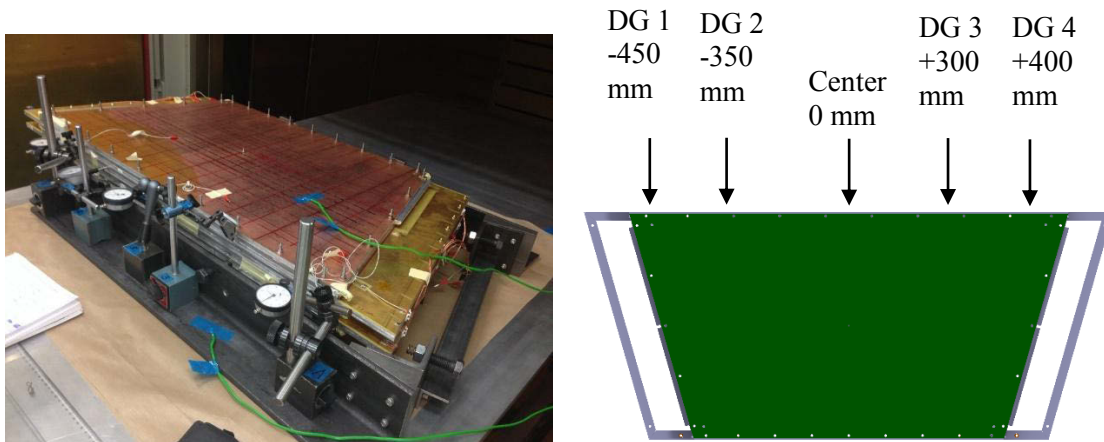
Figure 8-31. MMSW experiment setup.

Once the MMSW was placed on its stand, the micrometre dial gauges were placed as observed in

Figure **8-31**. These dial gauges were placed to measure the expansion across the entire length of the MMSW.

Once the dial gauges were in position, all initial conditions were recorded. This involved the initial readings on all of the dial gauges as well as the initial temperature in the oven. The oven was then closed, set to reach a temperature 50°C and turned on. The oven was left at the set temperature of 50°C for four hours before being turned off. Once the oven was turned off, the doors were opened and the readings on each of the dial gauges were read and recorded. The apparatus was now left to cool before starting the next experiment.

The MMSW thermal experiment was conducted using two different methods, the same two methods that were used for the thermal experiments conducted on the aluminium bars. The first experiment involved the heating of the MMSW experimental frame to an initial temperature of 50°C. Once this temperature was reached, the room temperature MMSW was placed on the hot frame and left in the oven at a set temperature of 50°C to allow the MMSW to heat up to this temperature, thermally expanding on a preheated, constant temperature MMSW stand. This negated the effects of expansion of the stand and allowed the dial gauges to give true thermal expansion values, requiring no further theoretical calculations. This experiment was completed three times. The experiments are labelled, Experiment 3A, Experiment 3B and Experiment 3C.

The second experiment involved the heating of the MMSW and the MMSW stand at the same time. The two components were placed in the oven together at room temperature and heated simultaneously to a temperature of 50°C. This resulted in the dial gauge readings being a combination of the thermal expansion of the MMSW and the thermal expansion of the MMSW experiment stand. As done in the aluminium bar experiment, the analytical value of the thermal expansion of the steel MMSW stand could now be added to the dial gauge readings. The value achieved from this simple calculation represents the true values of the expansion of the MMSW. This experiment was completed four times. The experiments are labelled, Experiment 4A, Experiment 4B, Experiment 4C and Experiment 4D.

8.5.5 Results

The experiment in which the room temperature MMSW was placed on an already hot frame, Experiment 3, was completed three times while the experiment in which the two components were heated up together, Experiment 4, was completed four times. The results for each of the dial gauges for each of these experiments can be observed in Appendix J.1 and Appendix J.2 while a summary of the results of each of the experiments can be seen in Table 8-8 and Table 8-9.

Table 8-8. Experiment 3 results summary.

Dial Gauge No.	Position (cm)	Thermal Expansion (µm)		
		Experiment 3A	Experiment 3B	Experiment 3C
1	-45	220	230	220
2	-35	180	220	200
3	30	200	220	200
4	40	250	250	220

Table 8-9. Experiment 4 results summary.

Dial Gauge No.	Position (cm)	Thermal Expansion (µm)			
		Experiment 4A	Experiment 4B	Experiment 4C	Experiment 4D
1	-45	256	240	244	256
2	-35	256	230	214	236
3	30	246	240	214	246
4	40	266	260	204	216

8.5.6   Discussion – Experimental Analysis

A thermal analysis of the MMSW was completed using an experimental analysis approach. The expected results from the experimental analysis are to be about 39 µm less than the 270 µm expansion predicted by the analytical solution. This 39 µm is the amount in which the MMSW expanded in the negative y-direction in the computational simulation. The experimental analysis did not measure the expansion in the negative y-direction and therefore a significantly smaller expansion is observed. By subtracting the 39 µm negative direction expansion from the 270 µm analytical expansion, one would expect the experimental expansion to be about 231 µm. The data obtained from the experimental analysis lies in the range of 200 µm to 266 µm, a maximum value of 35 µm deviation from the results expected from the analytical calculation. Using this information, one can deduce that the experimental results are in the correct range of values and are therefore realistic results.

When conducting the experimental analysis, the initial temperature was not controlled and therefore ranged between 22°C, 23°C and 24°C for the experiments. For this reason, the results of the experiments cannot be directly compared to each other, and neither can a direct average of the experiments be calculated. Because the expansion of the MMSW is approximately linear with a change in temperature, however, approximated values can be calculated by dividing the thermal expansion of an experiment by that particular experiment's temperature change and then multiplying the result by the standard temperature change of 27°C. This will create results that approximates all the experiments to have a common temperature change. This method is not used for the final error evaluation for the analysis because by using this simplification, the results lose a small amount of accuracy. The way the MMSW is constrained and measured, allowing expansion in all directions and only measuring at the maximum positive y-values, results in the measured results deviating slightly from linearity with the change in temperature.

Table 8-10 and Table 8-11 are the equivalent results at a temperature change of 27°C, achieved using the method described above.

Table 8-10. Experiment 3 at only 27°C expansion results summary.

Dial Gauge No.	Position (cm)	Thermal Expansion (µm)		
		Experiment 3A	Experiment 3B	Experiment 3C
1	-45	220	230	220
2	-35	180	220	200
3	30	200	220	200
4	40	250	250	220

Table 8-11. Experiment 4 at only 27°C expansion results summary.

Dial Gauge No.	Position (cm)	Thermal Expansion (µm)			
		Experiment 4A	Experiment 4B	Experiment 4C	Experiment 4D
1	-45	268	240	234	268
2	-35	268	230	205	247
3	30	257	240	205	257
4	40	278	260	196	226

The equivalent results of the seven conducted experiments observed in the two tables above are portrayed in the scatter plot in Figure 8-32. The thermal expansion in the positive y-direction can be observed in the y-axis of the graph while the x-directional distance from the centre of the MMSW can be observed on the x-axis of the graph. The three red curves represent the experiments when the cold MMSW was placed on an already heated experiment stand, Experiment 3. The four blue curves represent the experiment when the MMSW and its stand were heated up in the oven together, Experiment 4.
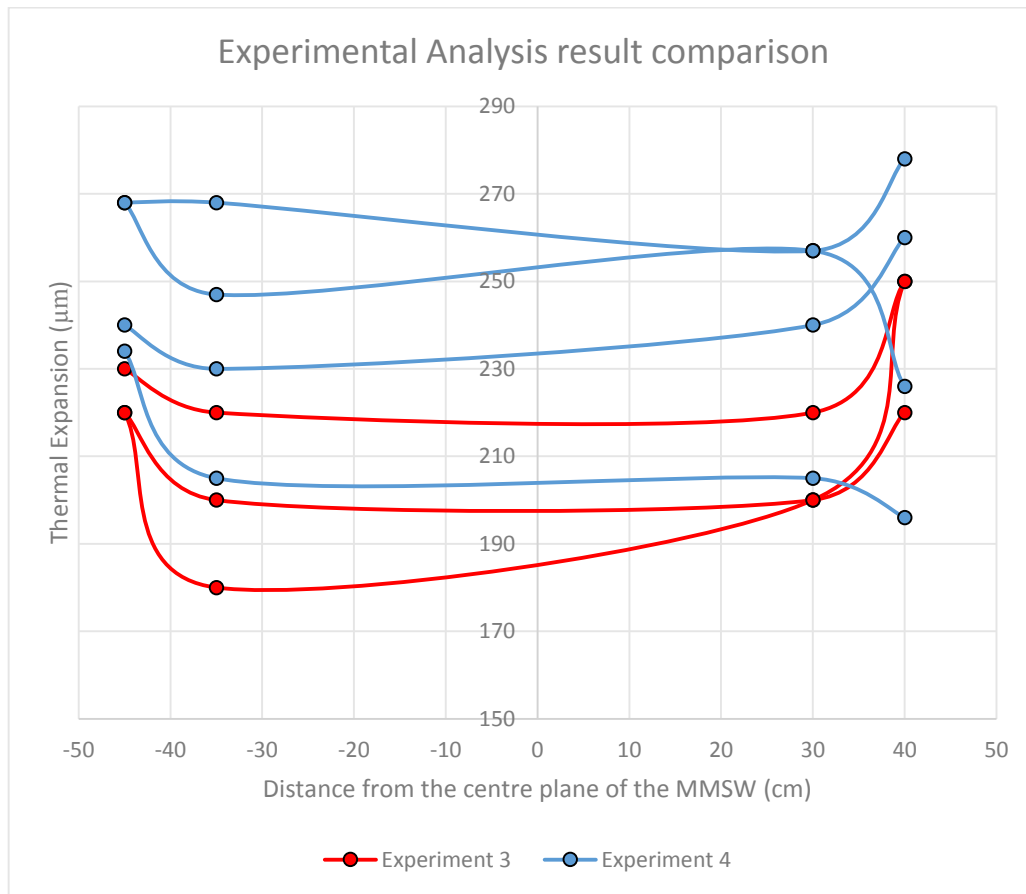
Figure 8-32. Experimental analysis results.

It is clear from the scatterplot that the experiment when the cold MMSW was placed on an already heated MMSW stand, represented by the three red lines, produced lower expansion values than the experiment when the two components were heated up together. These results mimic the error shown for the experiments of the aluminium bars. The likely reason for this difference is the possibility that the stand cooled down when the oven door was opened allowing cool air to enter and when the cold MMSW was placed on the stand. This means that the dial gauges' initial positions were read with the MMSW stand somewhat below 50°C. The result of this is the ignored small amount of expansion of the MMSW stand while heating back up to the 50°C, resulting in slightly reduced results.

8.6 Computational and Experimental Results Compared

The aim of this MMSW thermal analysis was to perform an investigation as to whether or not the computational analysis techniques used were reliable and accurate so as to verify previous results and lend validity to future models using the same techniques and simplifications. In order to achieve this, the results of the analysis had to be compared to other results believed to be accurate. An analytical calculation of this complex geometry is very difficult to achieve, with varying geometry in all directions, for this reason, the experimental analysis had to be conducted and the results used as a baseline to test the computational analysis results.

The error percentage found in the computational analysis is calculated using the following formula:

$$Percentage\ Error = \frac{Approximate\ computational\ value - Measured\ value}{Measured\ value} \times 100$$

The experimental analysis results obtained were used as the measured values while the approximate values used were the values obtained from the computational analysis. Using varying experimental data as the measured solution may not be common practice, however, in this case, it is necessary.

The data processing followed a strict procedure to ensure that the results were analysed appropriately. The procedure followed for the processing of this data can be observed in the flow diagram found in Figure 8-33.
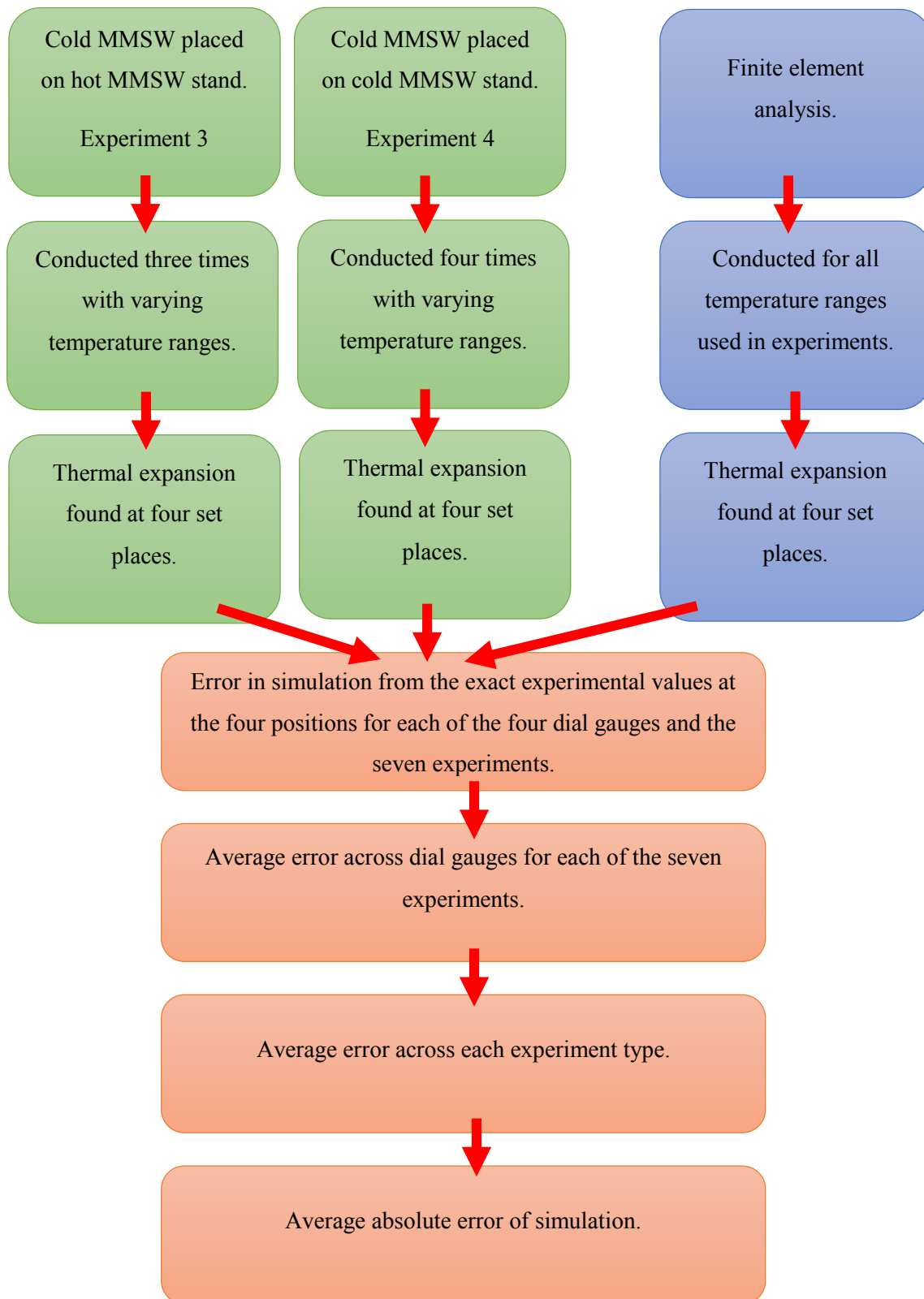
Figure 8-33. MMSW simulation comparative analysis.

The error values of the simulations when compared to the experimental values for each of the four points for each of the experiments can be found in the tables in Appendix J.1 and Appendix J.2. A summary of all the errors for each of the simulations can be found in Table 8-12 and Table 8-13. The average error for each experiment and the average error for each experiment type is shown.

Table 8-12. Experiment 3 average computation error.

Dial Gauge Number	Experiment 3A Error (%)	Experiment 3B Error (%)	Experiment 3C Error (%)
1	11.8	7.0	11.8
2	21.1	-0.9	9.0
3	3.5	-5.9	3.5
4	-7.2	-7.2	5.5
Absolute Average	10.9	5.3	7.5
Averaged Averages	7.9		

Table 8-13. Experiment 4 average computation error.

Dial Gauge Number	Experiment 4A Error (%)	Experiment 4B Error (%)	Experiment 4C Error (%)	Experiment 4D Error (%)
1	-0.4	2.5	-3.3	-0.4
2	-11.7	-5.2	-1.9	-4.2
3	-12.6	-13.8	-6.5	-12.6
4	-9.4	-10.7	9.8	11.6
Absolute Average	8.5	8.1	5.4	7.2
Averaged Averages	7.3			

Using the information in tables Table 8-12 and Table 8-13 one can conclude that the error in the simulations when compared to Experiment 3 is 7.9 % while the error of the simulations when compared to experiment 4 is 7.3 %. When finding an average error, treating all seven individual experiments equally, the error percentage of 7.6 % is achieved.

CHAPTER 9 - MICROMEGAS ANALYSIS DISCUSSION

It is important to note that the results for thermal expansion are not the true values for the total thermal expansion in the y-direction. The results neglect thermal expansion in the negative y-direction.

A major difference between the results provided and the true values for the thermal expansion is that for a true value for thermal expansion, the Micromegas should be constrained in the y-direction fully at an edge, perpendicular to the direction of measured expansion. This will avoid expansion occurring in both y-directions which makes measurement of the true directional expansion very difficult. Figure 9-1 shows an exaggerated expansion analysis, showing clearly how expansion occurs in both y-directions. In reality, it is not possible to constrain this edge in the y-direction perfectly without creating undesired stresses in the MMSW. For this reason this method was not used in the computational analyses.
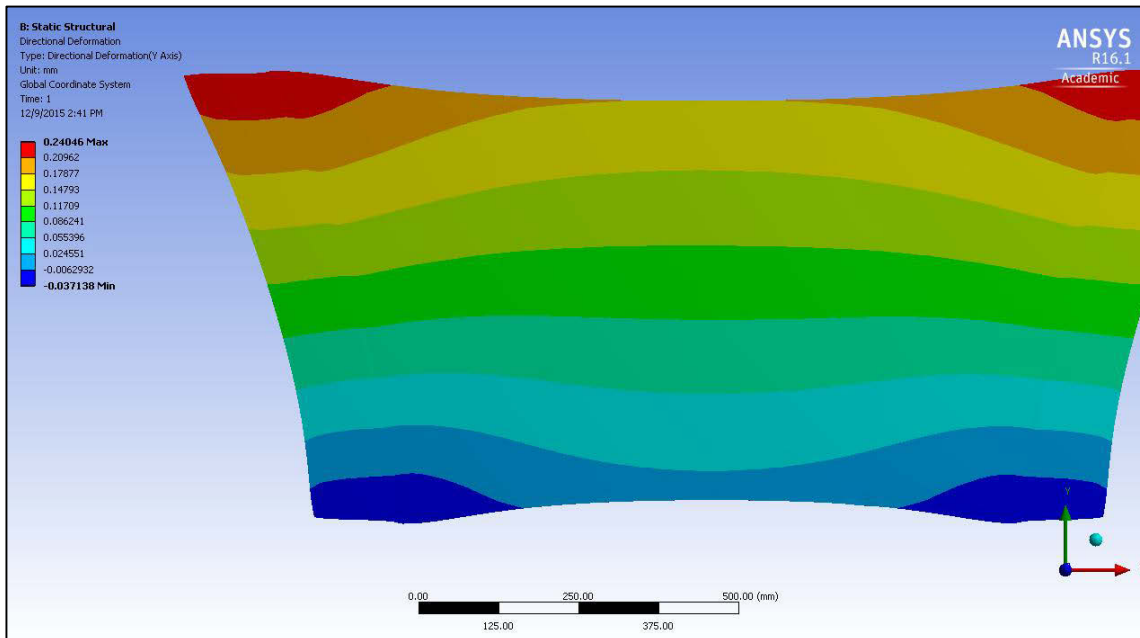
Figure 9-1. 780 times exaggeration of y-direction thermal expansion.

The two materials that have the largest effect on the thermal expansion of the Micromegas mock-up are aluminium and fibreglass. The aluminium has a coefficient of expansion of 23 ppm/K while the fibreglass has a much lower coefficient of thermal expansion of 13 ppm/K. It is known that the aluminium in the structure is concentrated to the outer frame and therefore the thermal

expansion due to aluminium is more significant in this area. It is evident that the Micromegas will expand to a greater extent on its outer walls and less as you near the centre. This can be observed in all the experimental and computational data acquired.

As done when analysing the experimental results in Chapter 8.5.6, the experimental results have been linearly changed to all be a representation of the thermal expansion due to a 27°C change in temperature. The average thermal expansion values of the seven experiments conducted were averaged again and compared to the results obtained from the equivalent finite element analysis simulation. The results of this simplification and averaging process can be observed in Table 9-1 and again graphically on the graph in Figure 9-2. The experimental results are represented in blue, the computational results represented in red and the analytical results represented in orange. Analysing the graph in Figure 9-2, it is observed that the results obtained from all three techniques are very similar.

Table 9-1. Experimental vs. Computational data.

		Thermal Expansion (μm)	
Dial Gauge No.	Position (cm)	Experimental Data Average at 27°C change	Computational Data at 27°C change
1	-45	240	246
2	-35	221	218
3	30	226	207
4	40	240	232
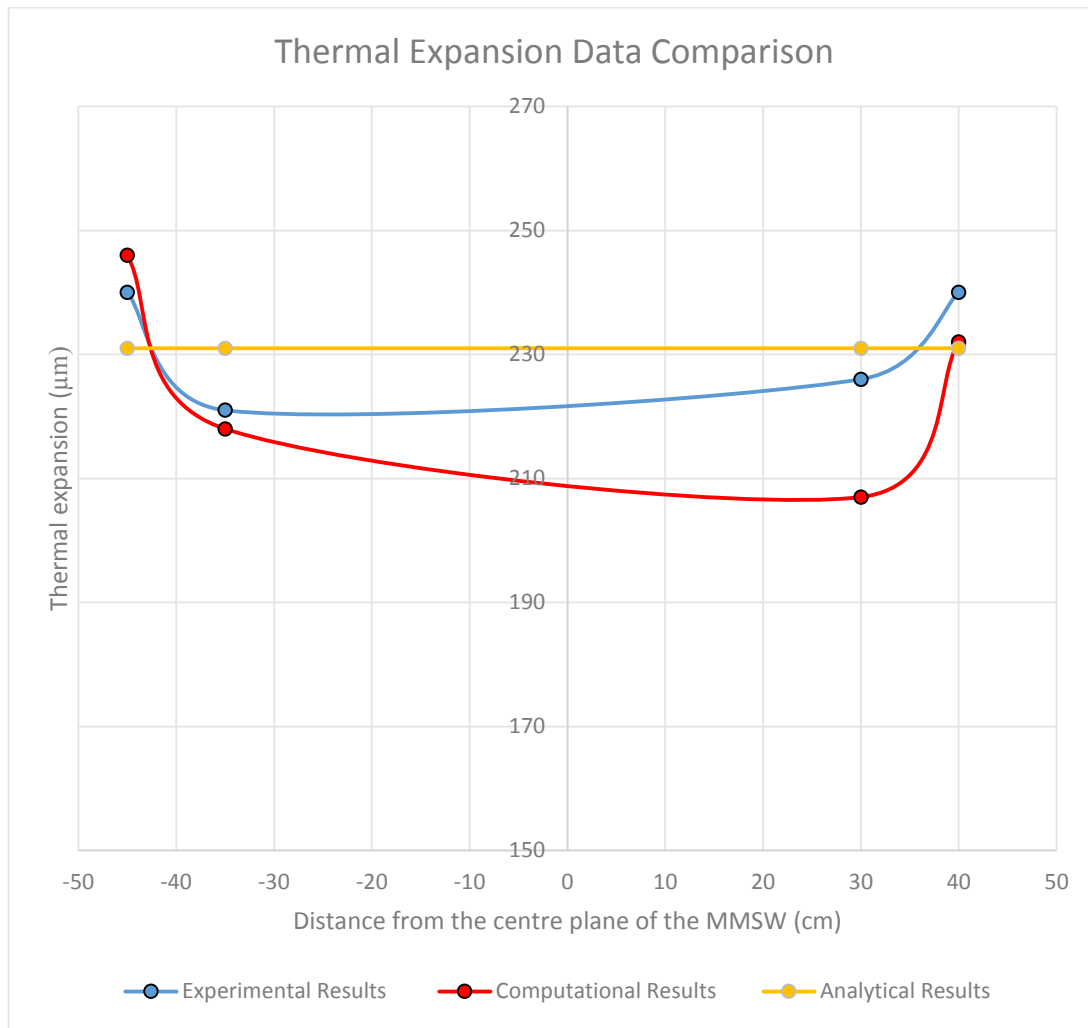
Figure 9-2. Experimental vs. computational vs. analytical data scatterplot.

CHAPTER 10 - CONCLUSION

The planned upgrade of the ATLAS Experiment during Long Shutdown 2 includes the necessity of the production of the New Small Wheel for installation into the experiment's assembly. The NSW is comprised of a structural skeleton and numerous muon tracking and triggering sectors. With the creation of these sectors, originated the requirement of a variety of component transport, storage and assembly procedures and tools. The handling of the delicate Micromegas chambers and NSW sectors, using these tools, is to be done in a way that minimises the stresses induced on the structure at all times, which was of primary concern in this work.

The NSW sector's spacer frame mounts were to be designed, creating a mounting point on the sectors, enabling the manipulation of the Micromegas chambers and the NSW sectors during all procedures and operations until they are assembled to the NSW. A series of tools were also to be designed that are to be used for all transport, storage and assembly procedures. The designs of these tools are to consider ergonomics, time efficiency, cost efficiency and structural safety. A storage area for these Micromegas chambers and NSW sectors as well as a floor plan arranging the storage, assembly and transport tools in Building 191 was to be provided. A final task, investigating the computational method used to analyse the stresses in the Micromegas wedges was to be achieved.

The stresses, space constraints and ergonomics involved with the design of the spacer frame mounts were considered when completing their design. A different mount was designed for each of the two support points for the large sector while one mount of uniform design was adequately designed for the two support points of the small sector. These sector mounts have been combined with the mounts used to support the NSW sectors during NSW assembly and include all restrictions that occur due to this procedure.

A tool was designed, capable of transporting the Micromegas chambers and NSW sectors to the various points that they needed to reach on the Meyrin, CERN site. This tool is an adaption of the tool, previously used for the transport of the EO muon chambers, using many of the tool's original components. Four of these tools are to be manufactured. A safety report confirms the safety of the old and new components of the tool under the loads exerted when transporting four Micromegas chambers or two NSW sectors. Stability during lifting operations of this tool and its components is studied and confirmed. The tool is designed with all components experiencing a safety factor above 2, as specified for all lifting equipment by the Euro-code.

The creation of a tool used to assemble the sTGCs to the Micromegas chambers to produce NSW sectors, while conforming to the complete set of requirements, was realised. The alignment precision required for the assembly of the NSW sectors is achieved by the use of adjustment mechanisms in the sector support slings. This tool reuses sector support components previously used for the Micromegas chamber and NSW sector transport tool. This reuse of components reduces the manufacture requirements of the tool and reduces the amount of handling of the delicate NSW sectors. The tool is designed with all components experiencing a safety factor above 2, as specified for all lifting equipment by the Standard BS EN 13155:2003. The plan of the storage and building layout of Building 191 was realised. This plan incorporates time efficiency, space efficiency and ergonomics to achieve a capable, yet adaptable layout. The storage area is able to store a total of eight Micromegas chambers or NSW sectors while the four transport tools are able to store a further sixteen Micromegas chambers or eight NSW sectors.

An experiment was successfully completed, analysing the techniques and simplifications associated with the finite element analysis used to analyse the stresses and deformations that occur in the Micromegas wedges due to normal operation and transport, storage and assembly procedures. Analytical, experimental and computational analyses were all conducted on the MMSW, a mock-up of a multiplet of the Micromegas wedge. A detailed understanding of the Micromegas wedge's thermal expansion properties was thereby achieved. A thermal expansion analysis with constant constraints and conditions across all of the three analysis platforms was conducted and the results were compared. It was discovered that the results obtained from the computational analysis had an average error of 7.6 % when compared to the obtained experimental results. This confirms that the Micromegas wedges can be analysed using the tested computational analysis procedures with an acceptable error.

REFERENCES

Aalco, 2015. *Aluminium Alloy 6082 - T6 Extrusions.* [Online]
Available at: http://www.aalco.co.uk/datasheets/Aluminium-Alloy-6082-T6-Extrusions_338.ashx

ANSYS, 2013. *ANSYS Mechanical APDL Element reference,* Canonsburg, Pennsylvania: ANSYS INC.

ATLAS, C., 2007. *ATLAS EXPERIMENT.* [Online]
Available at: http://www.atlas.ch/photos/full-detector-photos.html
[Accessed 26 July 2015].

ATLAS, C., 2008. The ATLAS Experiment. *Journal of Instrumentation 3.*

ATLAS, C., 2013. *ATLAS New Small Whell Technical Design Report,* Athens: Scientific Text Book Publishers.

ATLAS, C., 2015. *ATLAS Experiment.* [Online]
Available at: http://atlas.ch/
[Accessed 4 August 2015].

Beringer, J., 2012. Review of particle Physics. *Physical review D,* 86(1).

Bianco, M., 2014. *Micromegas for the ATLAS Muon System Upgrade,* Geneva: s.n.

CERN, 2009. *LHC The Guide,* Geneva: Communication Group.

CERN, 2015. *MAPCERN.* [Online]
Available at: https://maps.cern.ch/
[Accessed 12 April 2015].

Delpero, T., Lepoittevin, G. & Sanchez, A., 2010. *Finite Element Modeling with ANSYS,* Zurich: s.n.

Groppi, D., Konicek, . J., Vorres, . C. & Yuhas, D., 1995. *A system of electronic laminates with improved registration properties*. s.l. Patent No. PCT/US1993/010770.

Haba, 2008. *http://www.haba.ch/up/ktml/files/produkte/aluminium/de/Alu6082infode.pdf.* [Online]
Available at: http://www.haba.ch/up/ktml/files/produkte/aluminium/en/Alu6082infoen.pdf

Jacob, M., 1984. *Large Hadron Collider in the LEP Tunnel,* s.l.: s.n.

Javidinejad, A., 2012. FEA Practical Illustration of Mesh Quality results differences between structured mesh and unstructured mesh. *International Scholarly research Notices,* Volume 2012.

Kaps, H., 2013. *stability of Cargo suspension Arrangements,* Bremen: Transport Information Service.

La Rocca, P. & Riggi, F., 2014. The upgrade programme of the major experiments at the Large Hadron Collider. *Journal of Physics: Conference Series,* 515(1).

Lazic, Z., 2004. *Design of Experiments in Chemical Engineering.* Weinheim: WILEY-VCH.

Manutan, 2015. *Manutan.* [Online]
Available at: https://www.manutan.fr/fr/maf
[Accessed 13 July 2015].

Mikenberg, G., 2015. *NSW Assembly meeting* [Interview] (July 2015).

Montgomery, D. C., 2013. *Design and Analysis of Experiments.* Danvers: John Wiley & Sons, Inc.

Pitot, J., 2014. *Engineering Computational Methods,* Durban, South Africa: University of KwaZulu-Natal.

Ponsot, P., 2015. *ATLAS Experiment - New Small Wheel Engineering Activities Update,* Geneva: s.n.

Ravikumar, B., Krishna, S. & Rajashekhar, S., 2007. Evaluation of Mechanical Properties of AA6082-T6 Aluminium Alloy using pulse and non-pulse current GTAW Process. *International Journal of Innovation Research in Science Engineering and Technology,* 3(12).

Rogers, C., 2015. *Rogers Corporation.* [Online]
Available at: http://www.rogerscorp.com/acs/products/55/RO4350B-Laminates.aspx
[Accessed 3 June 2015].

Rossi, F., 2015. *Thermo-Mechanical Modelling of New Small Wheel Micromegas Quadruplets,* s.l.: s.n.

Sinclair, P. & ATLAS, C., 2015. *NSW CAD,* s.l.: s.n.

SkyCiv, 2015. *SkyCiv online engineering software.* [Online]
Available at: https://skyciv.com/beam-calculator-features/
[Accessed 10 12 2015].

Spigo, G., 1989. *Shear stresses on the insulation between coil and wedge due to thermal contraction,* s.l.: s.n.

Weil, E. & Levchik, S., 2004. A Review of Current Flame Retardant Systems for Epoxy Resins. *Journal of Fire Sciences,* 22(1).

Zimmermann, s., 2014. *The ATLAS Experiment New Small Wheel Upgrade Project,* Geneva, Switzerland: s.n.

APPENDIX A - Sector Analysis

A.1 Centroids of sectors

In order to accurately calculate the stresses induced in all of the lifting tools and mounts, the centre of mass of the sectors needs to be defined. An assumption is made that the centre of mass is equal to the centre of area which can easily be calculated using the sector geometry. The final locations of these centroids can be observed in Figure A-1 and Figure A-2 in Appendix A.2.

Due to symmetry of the sectors along their width, the x-value of the centroid can easily be shown to be:

$$\bar{x} = 1110 \ mm$$

The y-value for the centre of area of the large sector can be calculated by splitting the shape into two trapeziums as follows:

The area of a trapezium can be calculated using Equation 8 as follows:

$$A = \left(\frac{a + b}{2}\right) h$$

Equation 8

The area of the red trapezium in Figure A-1 is:

$$A_{RED} = \left(\frac{1892.49 + 2089.68}{2}\right) 1410$$

$$A_{RED} = 2807429.85 \ mm^2$$

The area of the green trapezium in Figure A-2 is:

$$A_{GREEN} = \left(\frac{504.42 + 1872.92}{2}\right) 2310$$

$$A_{GREEN} = 2745827.7 \ mm^2$$

The centre of area of a trapezium is calculated using Equation 9 as follows:

$$\bar{y} = \frac{h(2a+b)}{3(a+b)}$$

Equation 9

The centroid of the red trapezium is:

$$\overline{y_{RED}} = \frac{1410((2 \times 1892.49) + 2089.68)}{3(1892.49 + 2089.68)}$$

$$\overline{y_{RED}} = 693.36 \ mm$$

The centroid for the green trapezium is:

$$\overline{y_{GREEN}} = \frac{2310((2 \times 504.42) + 1872.92)}{3(504.42 + 1872.92)} + 1410$$

$$\overline{y_{GREEN}} = 2343.38 \ mm$$

Once the centroid and area of each trapezium is calculated, the centroid of the full sector can be calculated using Equation 10 as follows:

$$\bar{y} = \frac{\sum \bar{y}A}{\sum A}$$

Equation 10

$$\bar{y} = \frac{(693.36 \times 2807429.85) + (2343.38 \times 2745827.70)}{2807429.85 + 2745827.70}$$

$$\underline{\bar{y} = 1509.2 \ mm}$$

The centroid for the small sector is calculated in the same way giving values equal to:

$$\underline{\bar{x} = 910.75 \ mm}$$

$$\underline{\bar{y} = 1400.8 \ mm}$$

A.2 Tension in slings due to hanging the NSW sectors and Micromegas chambers

In order to calculate the tension in the sector slings and hence, the forces applied to the sector support beam and spacer frame mounts, the mass of the sector can be assumed to be a point load located at the centroid of the sector (Point C in Figure A-1) as shown in Appendix A.1.

To calculate the tension in these slings for the large sector, the moments about point A can be calculated to find the tension in the sling at point B.

Figure A-1. Large sector with mounts.

The moments about point A are equal to zero. The tension in sling B can therefore be calculated using Equation 11 as follows:

$$\sum M = \sum (Distance \times Force) = 0$$

Equation 11

$$\sum M_A = (Dac_x \times Fc_y) + (Dab_x \times Fb_y)$$

$$0 = (286.6 \times 14225) + ((286.6 + 663.1) \times Fb_y)$$

$$\underline{Fb_y = 4293\ N}$$

The force in sling A can therefore be calculated using the balance of vertical forces as:

$$Fa_y = Fc_y - Fb_y$$

$$Fa_y = 14225 - 4293$$

$$\underline{Fa_y = 9932\ N}$$

The tension in the slings and the force applied to the support beam when the large Micromegas chamber is hung can be calculated in the same way as that of the large NSW sector. The mass of the large Micromegas chamber can be assumed to be a point load located at the centroid of the sector (Point C in Figure A-1). The moments about point A can be calculated to find the tension in the sling at point B.

The moments about point A are equal to zero. The tension in sling B can therefore be calculated using Equation 11:

$$\sum M = \sum (Distance \times Force) = 0$$

Equation 11

$$\sum M_A = (Dac_x \times Fc_y) + (Dab_x \times Fb_y)$$

$$0 = (286.6 \times 6671) + ((286.6 + 663.1) \times Fb_y)$$

$$\underline{Fb_y = 2013\ N}$$

The force in sling A can therefore be calculated using the balance of vertical forces as:

$$Fa_y = Fc_y - Fb_y$$

$$Fa_y = 6671 - 2013$$

$$\underline{Fa_y = 4658\ N}$$

The tension in the slings and the force applied to the support beam when the small sector is hung can be calculated in the same way as that of the large sector. The mass of the sector can be assumed to be a point load located at the centroid of the sector (Point C in Figure A-2). The moments about point A can be calculated to find the tension in the sling at point B.
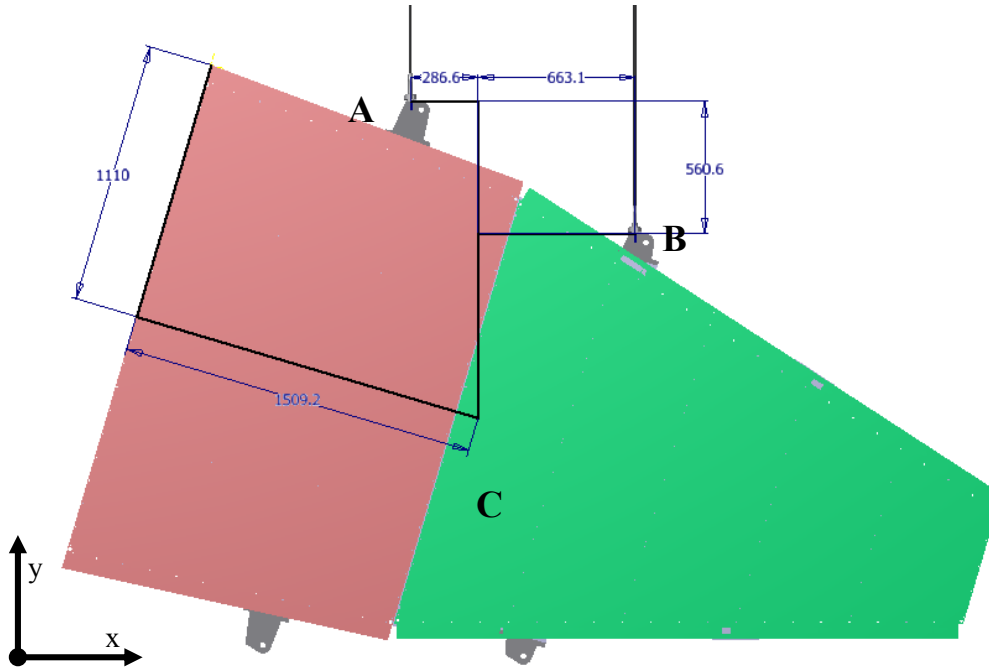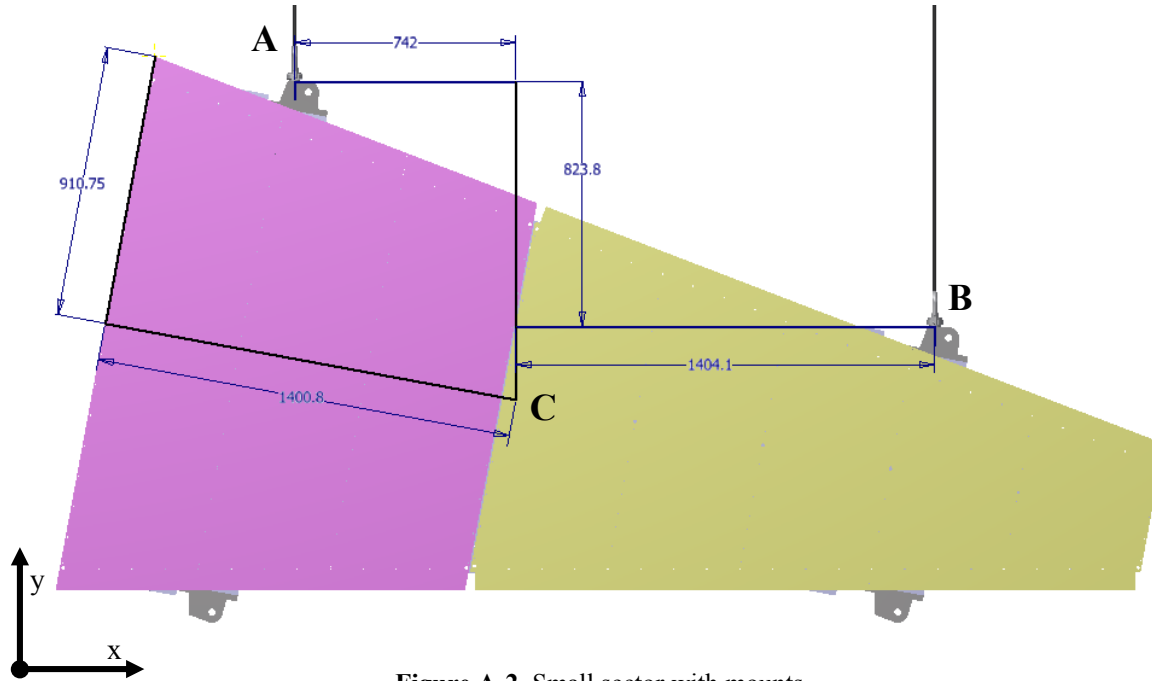

Figure A-2. Small sector with mounts.

The moments about point A are equal to zero. The tension in sling B can therefore be calculated using Equation 11:

$$\sum M = \sum (Distance \times Force) = 0$$

Equation 11

$$\sum M_A = (Dac_x \times Fc_y) + (Dab_x \times Fb_y)$$

$$0 = (742 \times 10791) + ((742 + 1404.1) \times Fb_y)$$

$$\underline{Fb_y = 3731\ N}$$

The force in sling A can therefore be calculated using the balance of vertical forces as:

$$Fa_y = Fc_y - Fb_y$$

$$Fa_y = 10791 - 3731$$

$$\underline{Fa_y = 7060\ N}$$

The tension in the slings and the force applied to the support beam when the small Micromegas chamber is hung can be calculated in the same way as that of the small NSW sector. The mass of the small Micromegas chamber can be assumed to be a point load located at the centroid of the sector (Point C in Figure A-2). The moments about point A can be calculated to find the tension in the sling at point B.

The moments about point A are equal to zero. The tension in sling B can therefore be calculated using Equation 11:

$$\sum M = \sum (Distance \times Force) = 0$$

Equation 11

$$\sum M_A = (Dac_x \times Fc_y) + (Dab_x \times Fb_y)$$

$$0 = (742 \times 5425) + ((742 + 1404.1) \times Fb_y)$$

$$\underline{Fb_y = 1876\ N}$$

The force in sling A can therefore be calculated using the balance of vertical forces as:

$$Fa_y = Fc_y - Fb_y$$

$$Fa_y = 5425 - 1876$$

$$\underline{Fa_y = 3549\ N}$$

APPENDIX B - Spacer Frame Mount Analysis

B.1 Third angle orthographic projection – Spacer frame mount
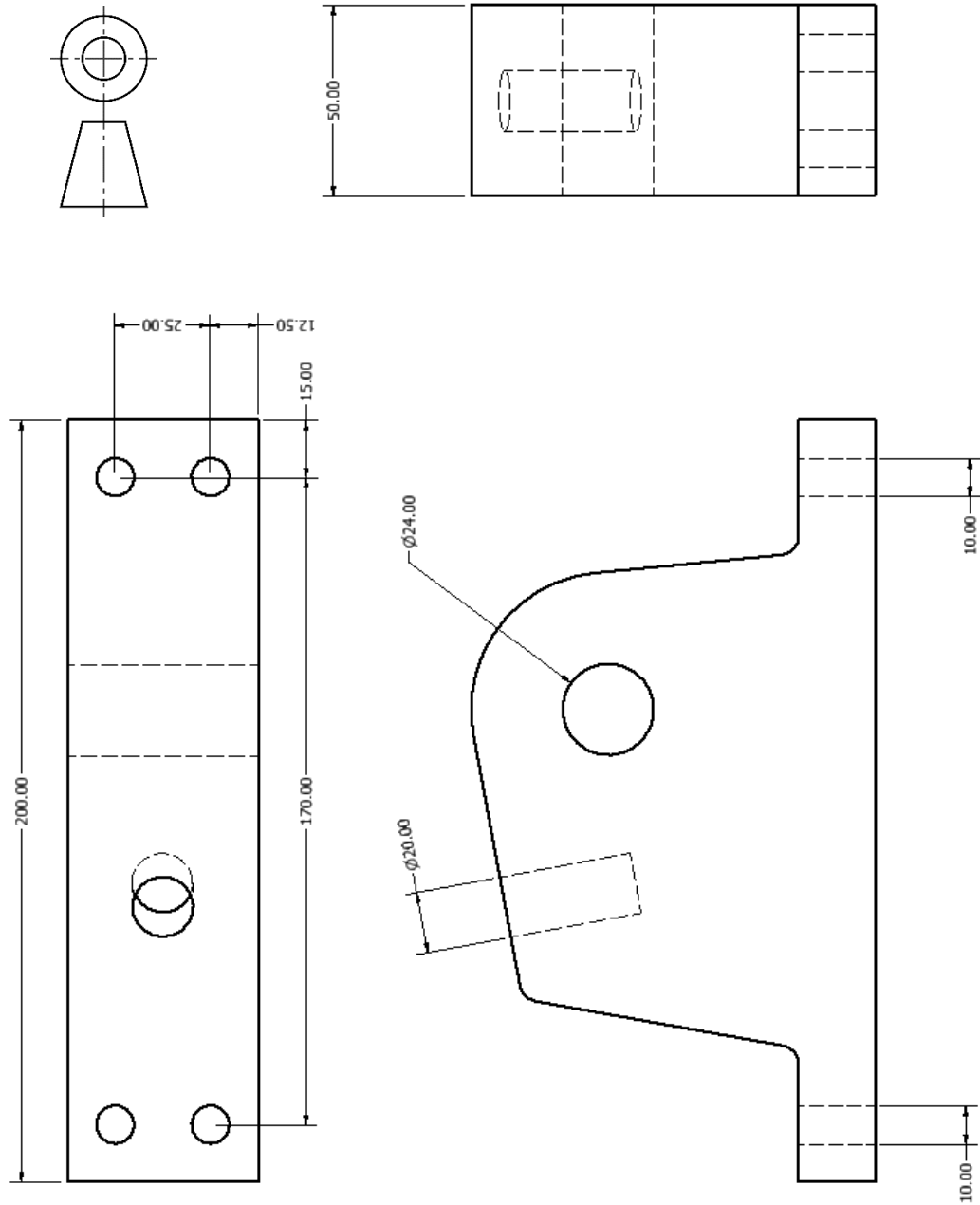
B.2 Spacer frame mount FEA conditions

Vertical load applied to the internal surface of this hole – Simulating force applied to the thread.

Infinitely rough surface connection applied to this surface – Assumption made that no horizontal movement will occur.

Fixed connection between the lower face of the bolt head and its contact surface – Assumption that no movement or separation will occur.

Fixed connection between the outer face of the bolt and this tapped hole of the spacer frame connection – Assumption that no movement will occur.

Fixed supports applied to the internal surfaces of these holes – Simulating fixed spacer frame pins

Figure B-1. Spacer frame mount FEA geometry and conditions.

B.3 Spacer frame mount FEA results

The von mises stresses concluded from the Ansys FEA simulations for the spacer frame mounts can be observed in Figure B-2, Figure B-3 and Figure B-4.
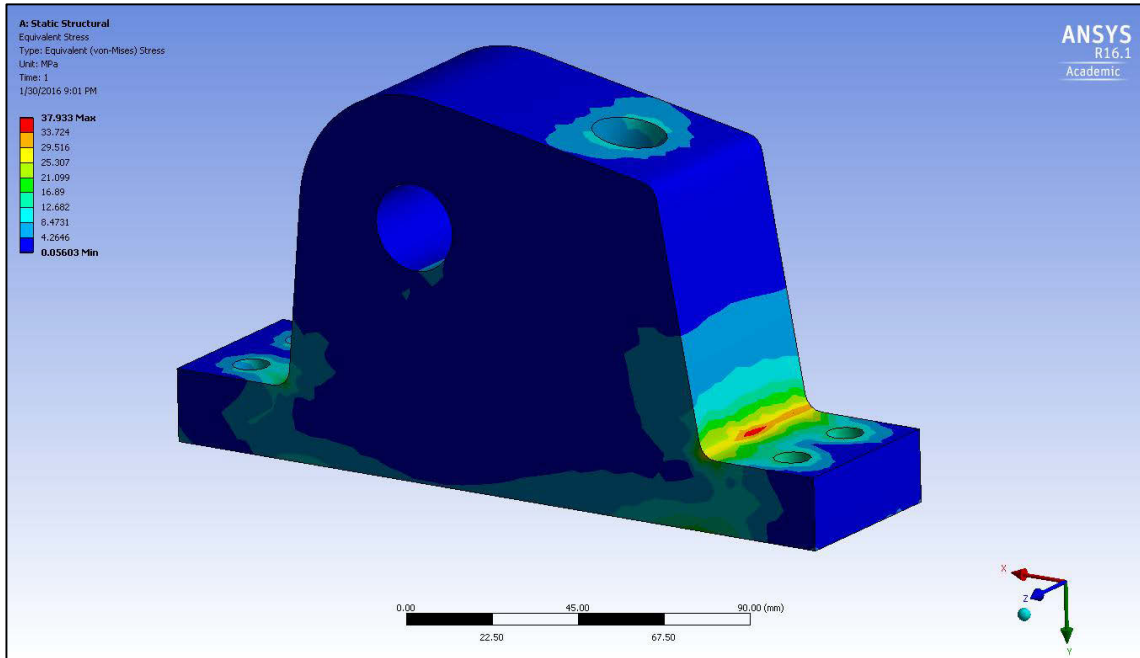
Figure B-2. Small sector spacer frame mount.
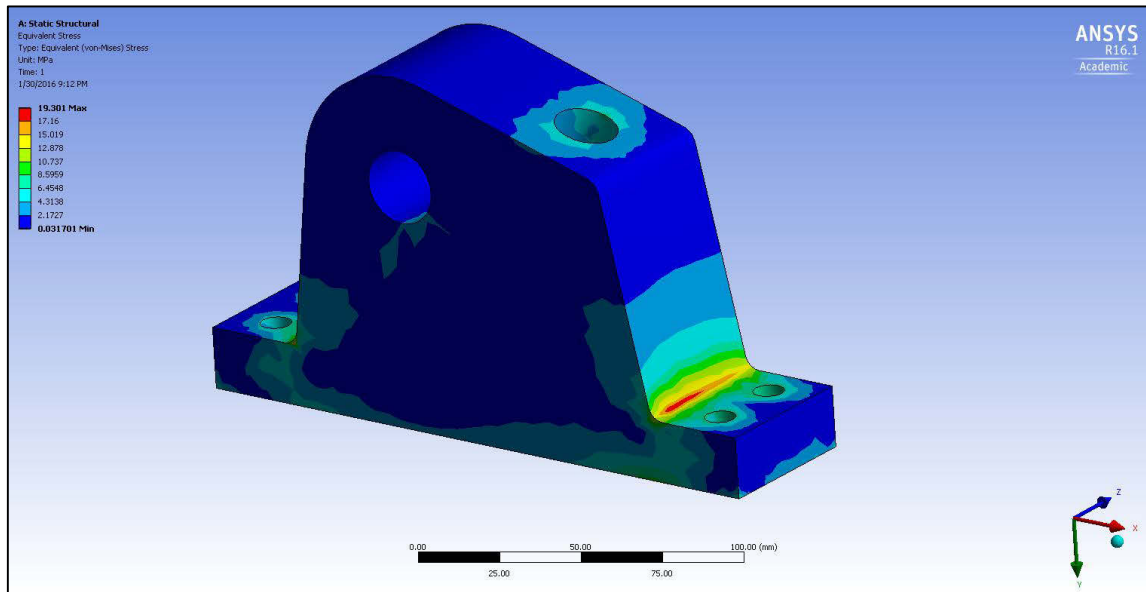
Figure B-3. Large sector spacer frame mount light side.
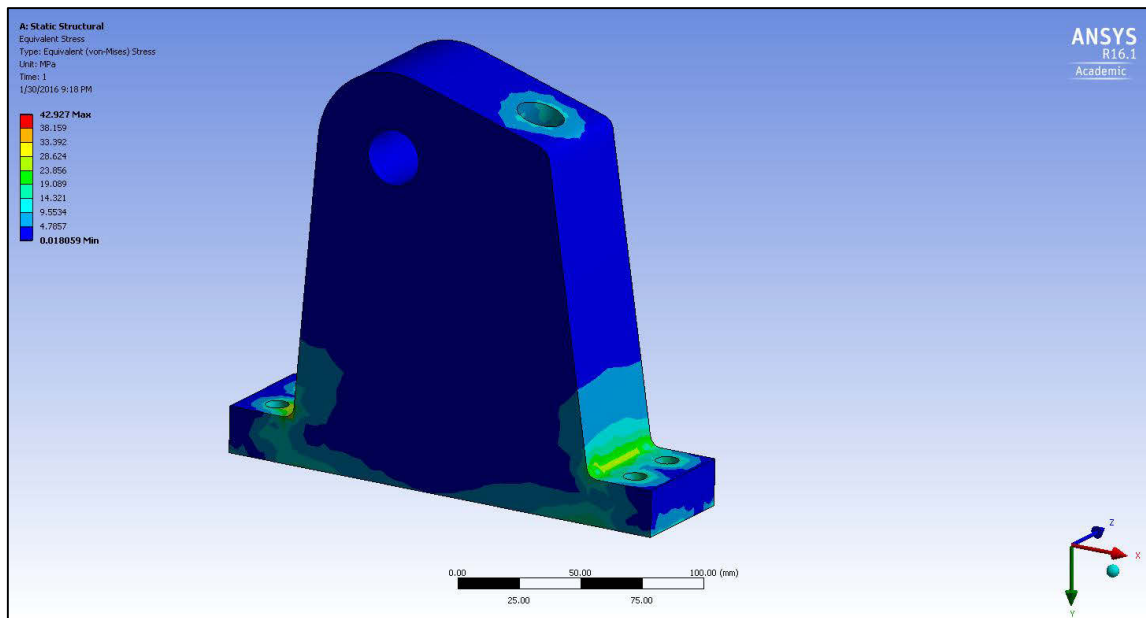
Figure B-4. Large sector spacer frame mount heavy side.

B.4 Calculation of safety factors of spacer frame mounts

The largest stress applied to the spacer frame mounts is equal to 42.93 MPa.

Using S235JRG2 steel with a yield strength of 235 MPa the following safety factor is calculated using Equation 3.

$$SF = \frac{\sigma_y}{\sigma_b}$$

Equation 3

$$SF = \frac{235}{42.93}$$

$$SF = 5.47$$

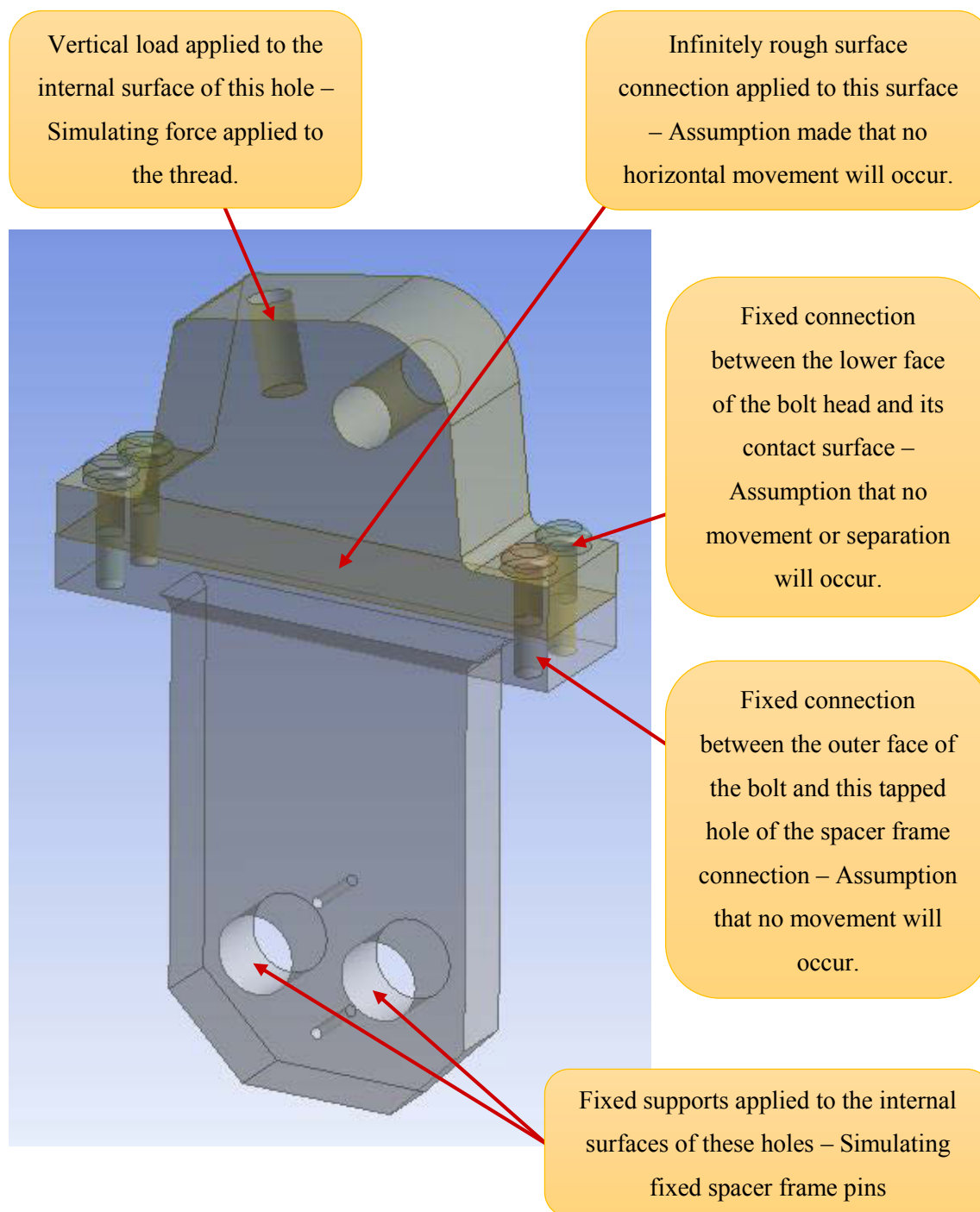Using Aluminimum 6082 – T6 with a yield strength of 250 MPa the following safety factor is calculated using Equation 3.

$$SF = \frac{\sigma_y}{\sigma_b}$$

Equation 3

$$SF = \frac{250}{42.93}$$

$$SF = 5.82$$

Using Aluminimum 5083 – H112 with a yield strength of 190 MPa the following safety factor is calculated using Equation 3.

$$SF = \frac{\sigma_y}{\sigma_b}$$

Equation 3

$$SF = \frac{190}{42.93}$$

$$SF = 4.43$$

APPENDIX C - Free Body, Shear and Bending Moment Diagrams for the Transport Tool

C.1 Force diagrams for the sector support beams due to a large sector

An online bending moment calculator was used to calculate the bending moment in the sector support beam. The online calculations were checked and the results are confirmed to be accurate for all represented diagrams. The software used is called 'Beam Calculator' and designed by 'SkyCiv'.

The free body diagram represented in Figure C-1 is a representation of the forces applied to the sector support beam by the large sector. The two red forces are the two loads applied to the support beam by the tension in the slings produced by the weight of the large sector. The green distributed load is a result of the weight of the beam at a total mass of 230 kg. The two supports on the outer edges of the beam are the reaction forces resulting due to the sector support beam resting on the cross beams.

Figure C-1. Free body diagram for the large sector support beam.

Figure C-2 represents the shear forces applied to the beam while Figure C-3 shows the bending moments applied to the beam. It can be observed that the maximum applied bending moment in the sector support beam due to the hanging of the large sector is equal to 17192 Nm.

Figure C-2. Shear force diagram for the large sector support beam.

Figure C-3. Bending moment diagram for the large sector support beam.

C.2 Force diagrams for the sector support beams due to a small sector

The free body diagram represented in Figure C-4 is a representation of the forces applied to the sector support beam by the small sector. The two red forces are the two loads applied to the support beam by the tension in the slings produced by the weight of the small sector. The green distributed load is a result of the weight of the beam at a total mass of 230 kg. The two supports on the outer edges of the beam are the reaction forces resulting due to the sector support beam resting on the cross beams.
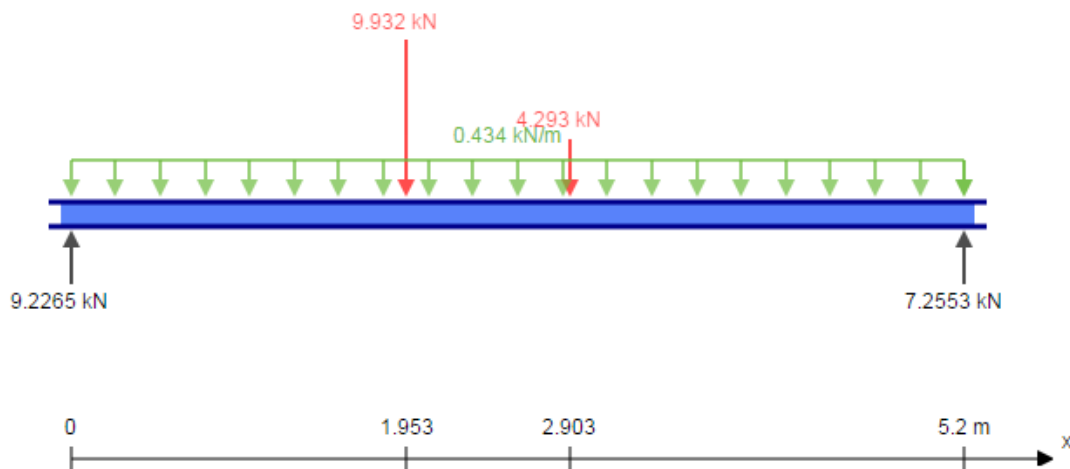
Figure C-4. Free body diagram for the small sector support beam.

Figure C-5 represents the shear forces applied to the beam while Figure C-6 shows the bending moments applied to the beam. It can be observed that the maximum applied bending moment in the sector support beam due to the hanging of the small sector is equal to 11372 Nm.
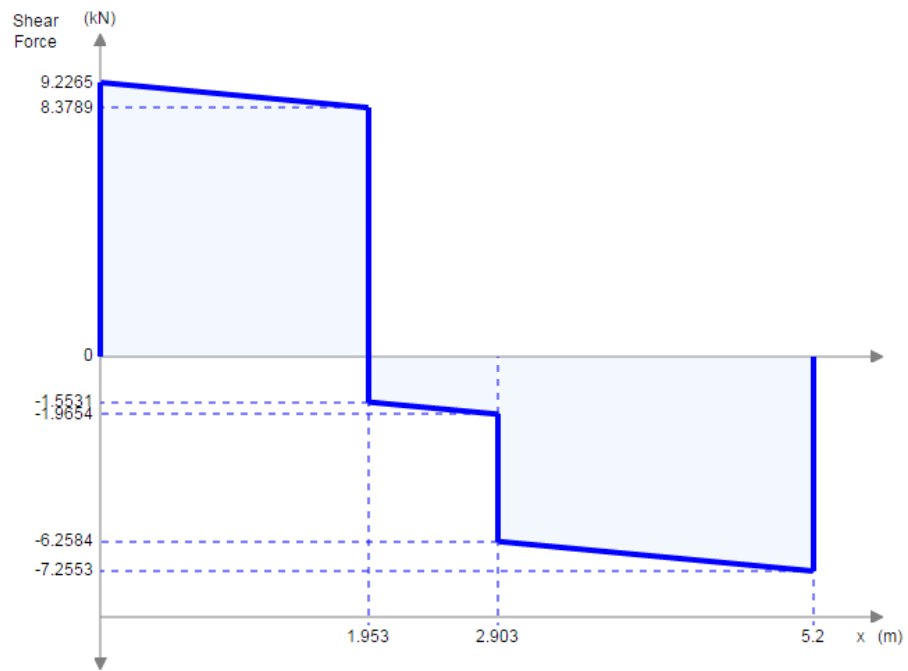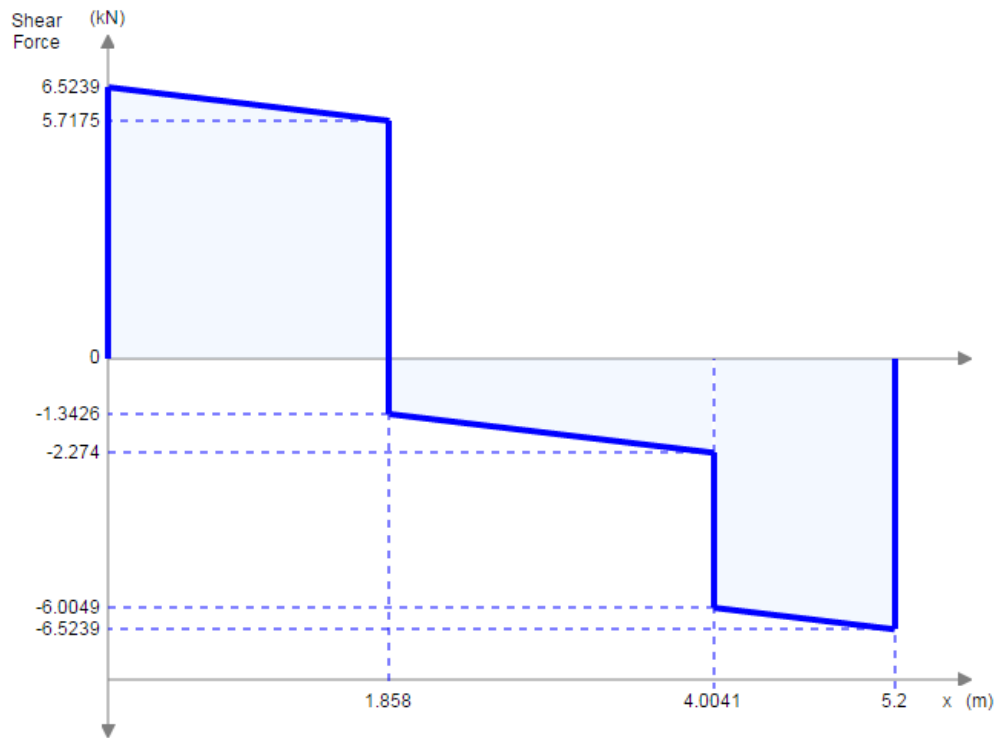
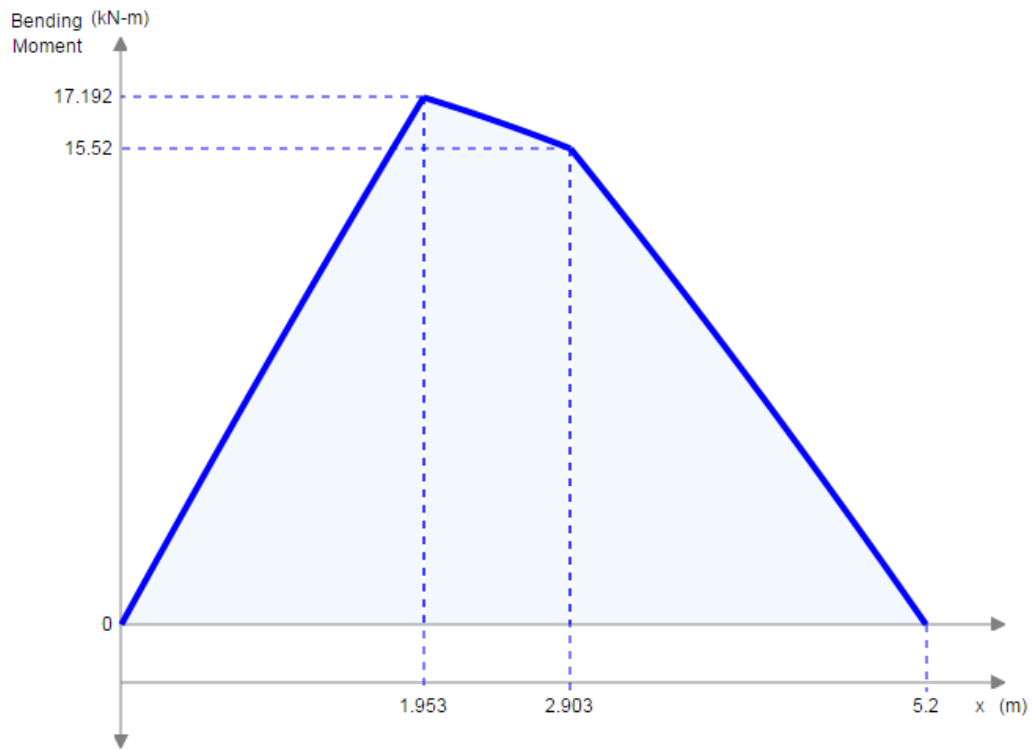**Figure C-5.** Shear force diagram for the small sector support beam.
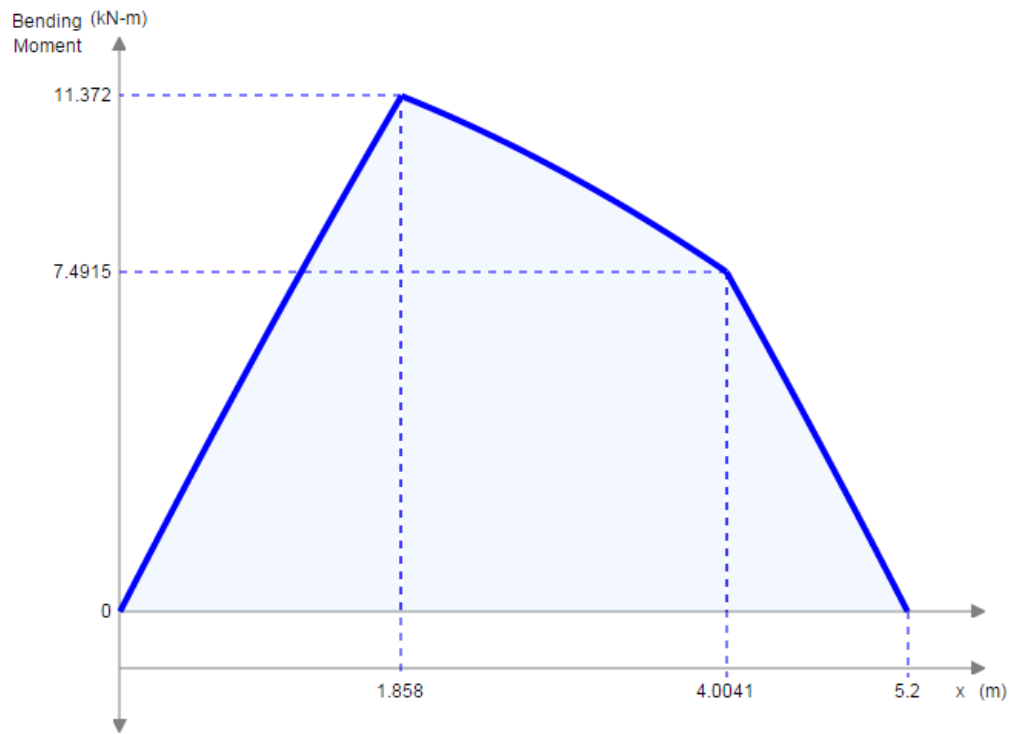
Figure C-6. Bending moment diagram for the small sector support beam.

C.3 Force diagrams for the sector support beams due to a large Micromegas chamber

The free body diagram represented in Figure C-7 is a representation of the forces applied to the sector support beam by the large Micromegas chamber. The two red forces are the two loads applied to the support beam by the tension in the slings produced by the weight of the large Micromegas chamber. The green distributed load is a result of the weight of the beam at a total mass of 230 kg. The two supports on the outer edges of the beam are the reaction forces resulting due to the sector support beam resting on the cross beams.
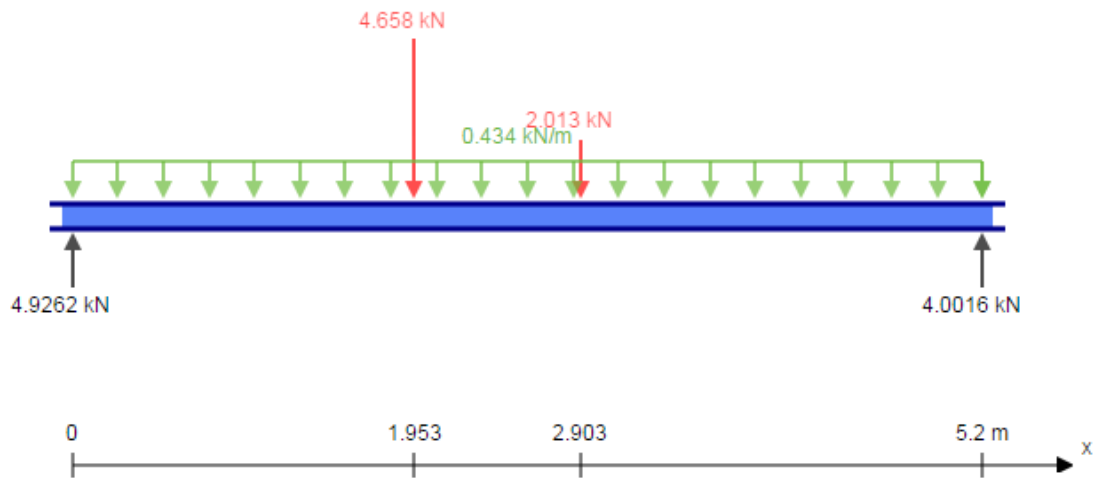
Figure C-7. Free body diagram for the large Micromegas chamber support beam.

Figure C-8 represents the shear forces applied to the beam while Figure C-9 shows the bending moments applied to the sector support beam. It can be observed that the maximum applied bending moment due to the hanging of the large Micromegas chamber is equal to 8793 Nm.
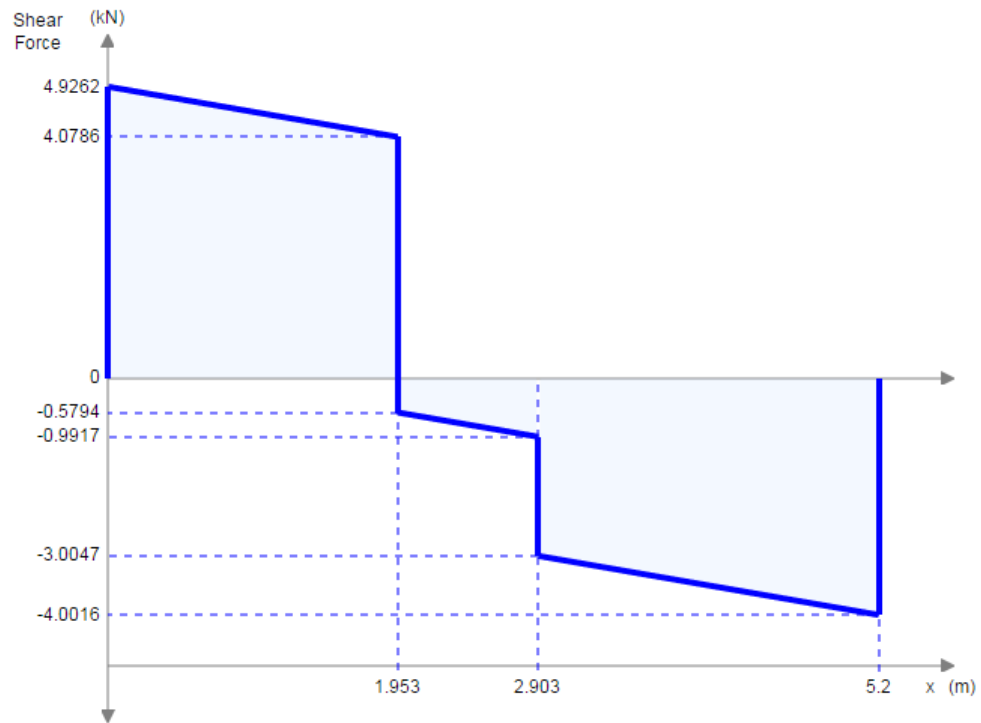
Figure C-8. Shear force diagram for the large Micromegas chamber support beam.
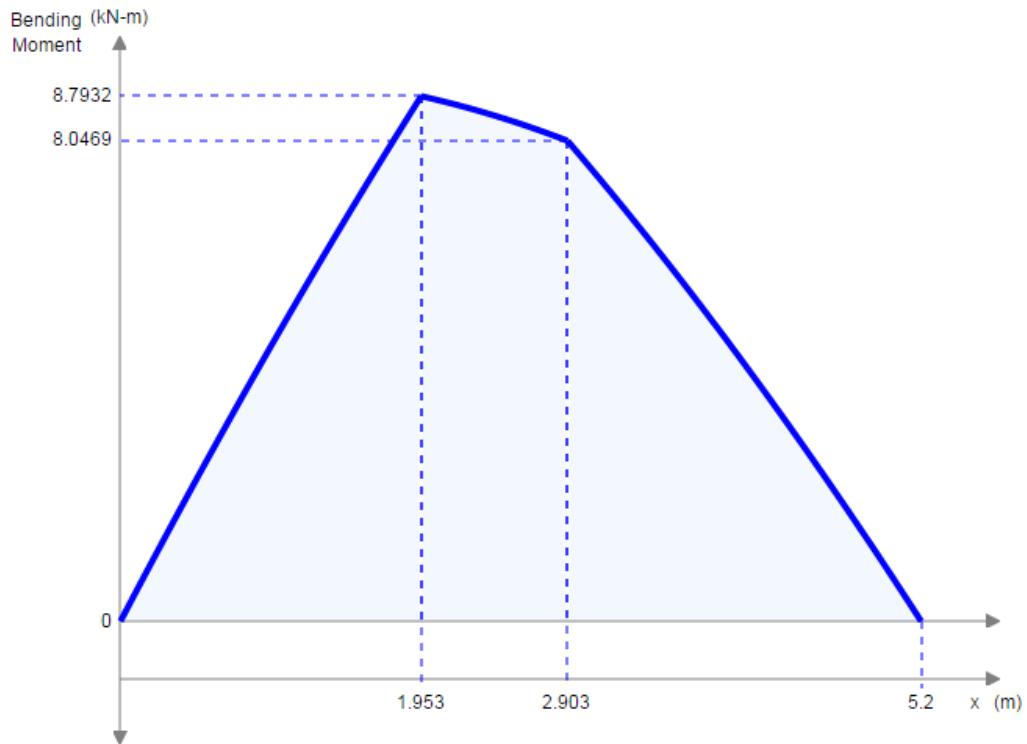
Figure C-9. Bending moment diagram for the large Micromegas chamber support beam.

C.4 Force diagrams for the sector support beams due to a small Micromegas chamber

The free body diagram represented in Figure C-10 is a representation of the forces applied to the sector support beam by the small Micromegas chamber. The two red forces are the two loads applied to the support beam by the tension in the slings produced by the weight of the small Micromegas chamber. The green distributed load is a result of the weight of the beam at a total mass of 230 kg. The two supports on the outer edges of the beam are the reaction forces resulting due to the sector support beam resting on the cross beams.
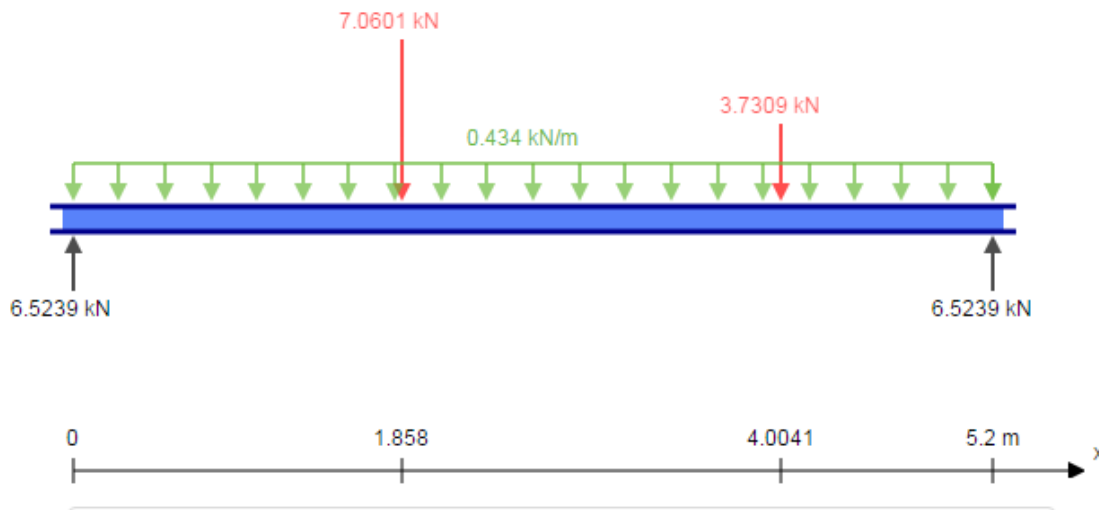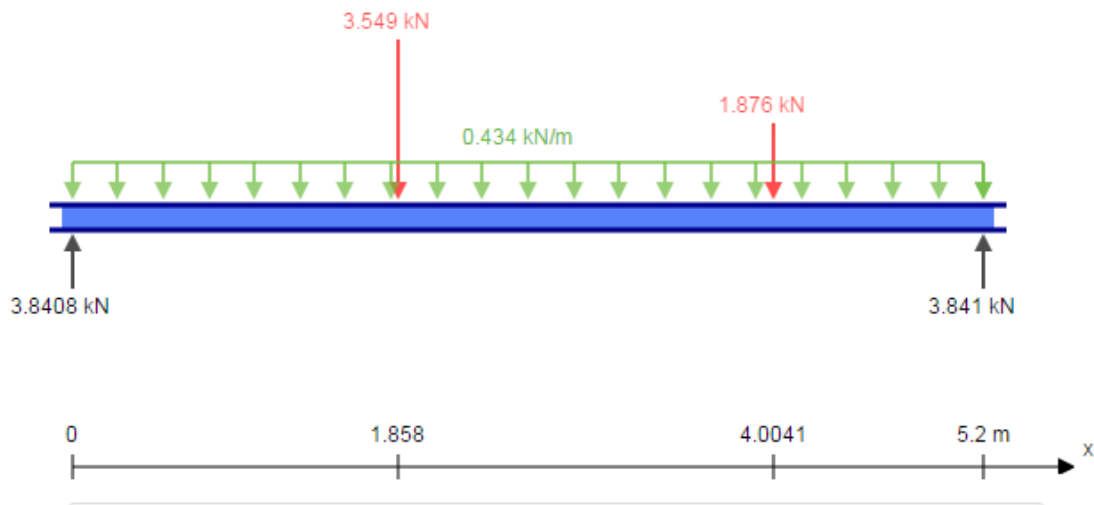

Figure C-10. Free body diagram for the small Micromegas chamber support beam.

Figure C-11 represents the shear forces applied to the beam while Figure C-12 shows the bending moments applied to the sector support beam. It can be observed that the maximum applied bending moment due to the hanging of the small Micromegas chamber is equal to 6387 Nm.
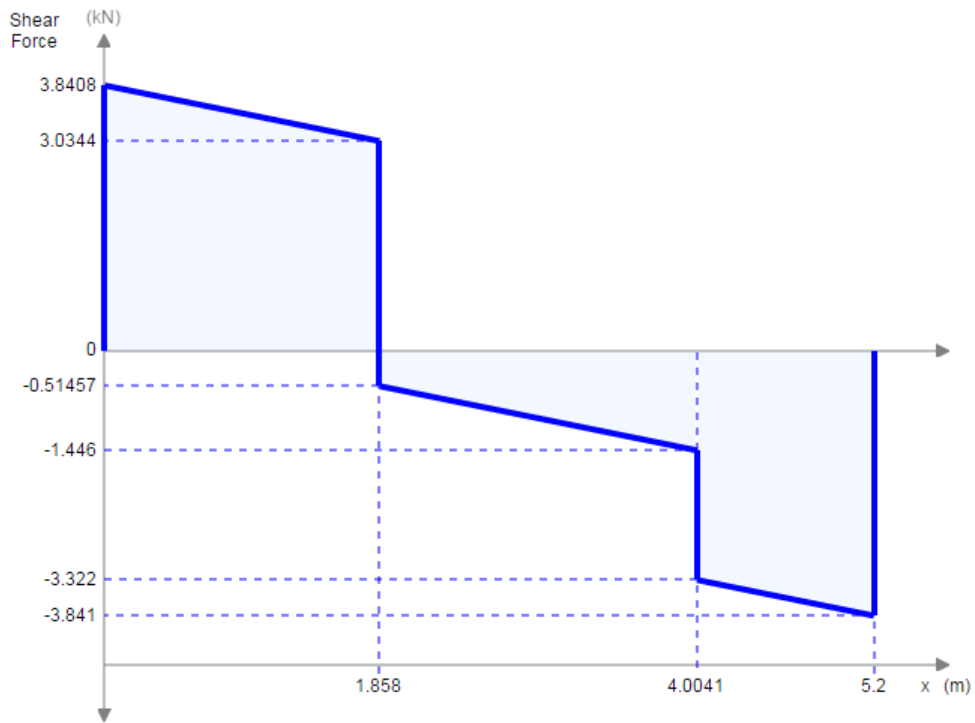
Figure C-11. Shear force diagram for the small Micromegas chamber support beam.
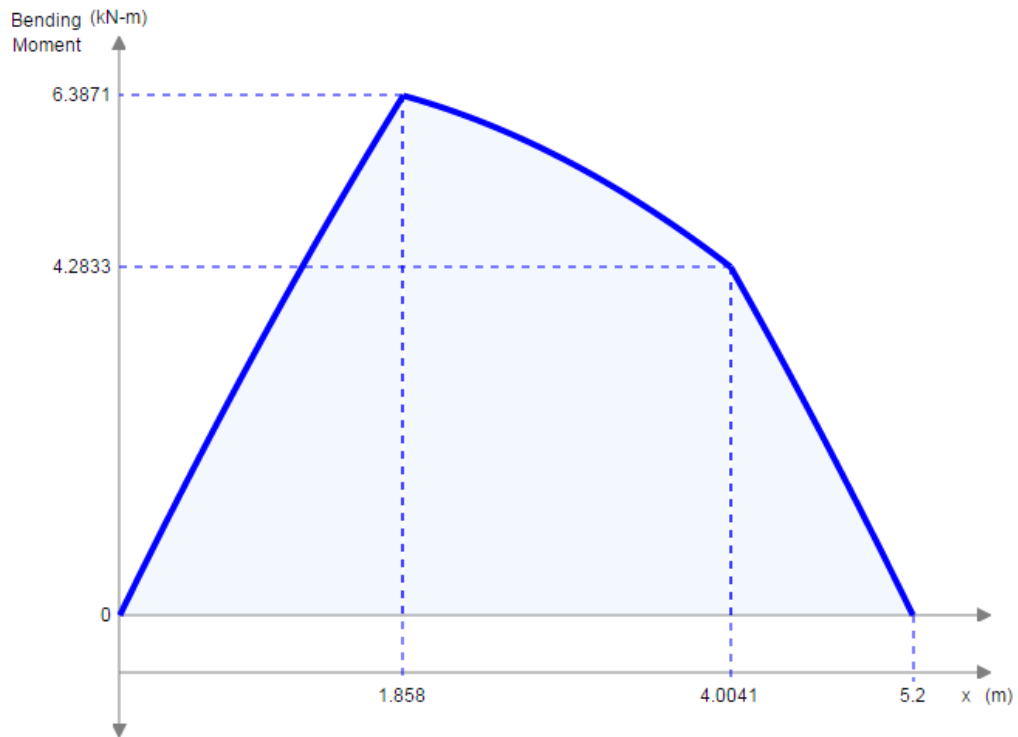
Figure C-12. Bending moment diagram for the small Micromegas chamber support beam.

C.5 Force diagrams for the cross beam by the large sector support beam – Heavy side

In order to calculate the reaction forces and bending moment applied to the cross beam, a simplification was made to its geometry. Because the loads act symmetrically about the beams centre axis, the simplification represented in the geometry in Figure C-13 was made.
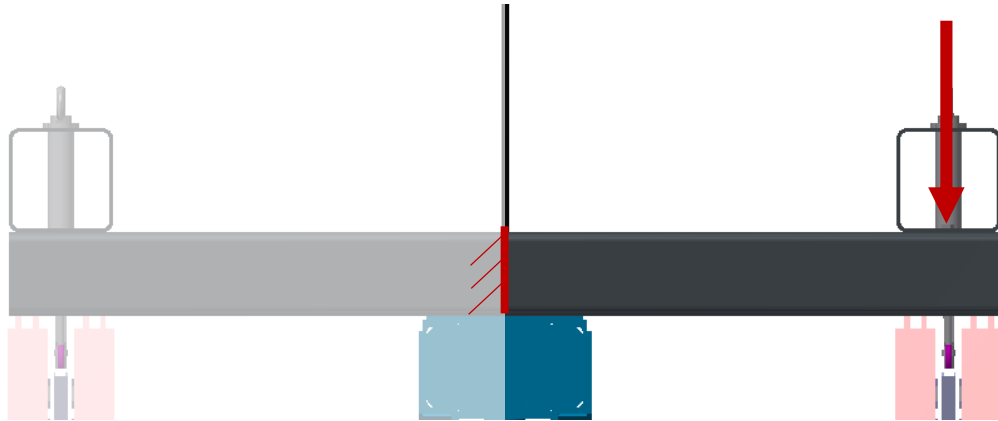
Figure C-13. Cross beam symmetry simplification.

The free body diagram represented in Figure C-14 is a representation of the forces applied to the cross beam when experiencing a maximum load applied by the heavier side of the sector support beam. The red force is the load applied to the cross beam by the sector support beam. The green distributed load is a result of the weight of the beam at a total mass of 63 kg. Due to the simplification made to the geometry, the reaction force represented is half of its true value. To get the true reaction force on the beam, the value shown must be doubled to get a value of 19.0716 kN.

Figure C-14. Free body diagram for cross beams – Heavy side.

Figure C-15 represents the shear forces applied to the beam while Figure C-16 shows the bending moments applied to the beam. It can be observed that the maximum applied bending moment in the cross beam occurs at its support and is equal to 8912.3 Nm.

Figure C-15. Shear force diagram for the cross beams – Heavy side.

Figure C-16. Bending moment diagram for the cross beams – Heavy side.

C.6 Force diagrams for the cross beam due to the large sector support beam – Light side

In order to calculate the reaction forces and bending moments applied to the cross beam due to the hanging of a large sector on the light side of the transport tool, the same simplification due to symmetry can be applied to the geometry as found in the analysis of the cross beam due to the support of the heavy side of a large sector.

The free body diagram represented in Figure C-17 is a representation of the forces applied to the cross beam when experiencing a load due to the sector support beam's light side. The red force is the load applied to the cross beam by the sector support beam. The green distributed load is a result of the weight of the beam at a total mass of 63 kg. To get a true reaction force on the beam, the value shown must be doubled to get a value of 15.1282 kN.

Figure C-17. Free body diagram for cross beams – Light side.

Figure C-18 represents the shear forces applied to the beam while Figure C-19 shows the bending moments applied to the cross beam. It can be observed that the maximum applied bending moment in the cross beam occurs at its support and is equal to 7039.2 Nm.

Figure C-18. Shear force diagram for the cross beams – Light side.

Figure C-19. Bending moment diagram for the cross beams – Light side.

C.7 Force diagrams for the cross beam due to four large Micromegas chamber support beams – Heavy side

In order to calculate the reaction forces and bending moments applied to the cross beam due to the hanging of four large Micromegas chambers on the heavy side of the transport tool, the same simplification due to symmetry can be applied to the geometry as found in the analysis of the cross beam due to the support of the heavy side of a large sector.

The free body diagram represented in Figure C-20 is a representation of the forces applied to the cross beam when experiencing a load due to the sector support beam's heavy side when carrying four large Micromegas chambers. The red force is the load applied to the cross beam by the sector support beam. The green distributed load is a result of the weight of the beam at a total mass of 63 kg. To get a true reaction force on the beam, the value shown must be doubled to get a value of 20.530 kN.
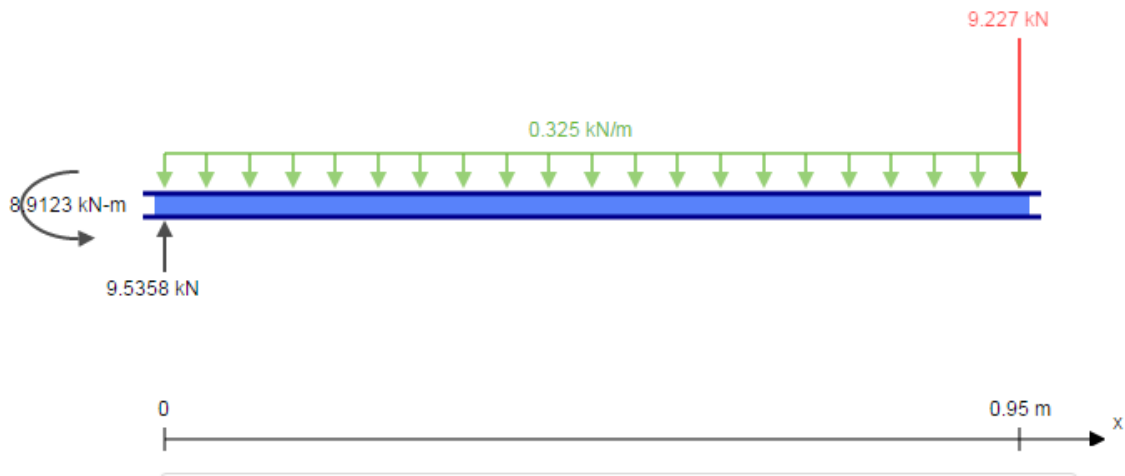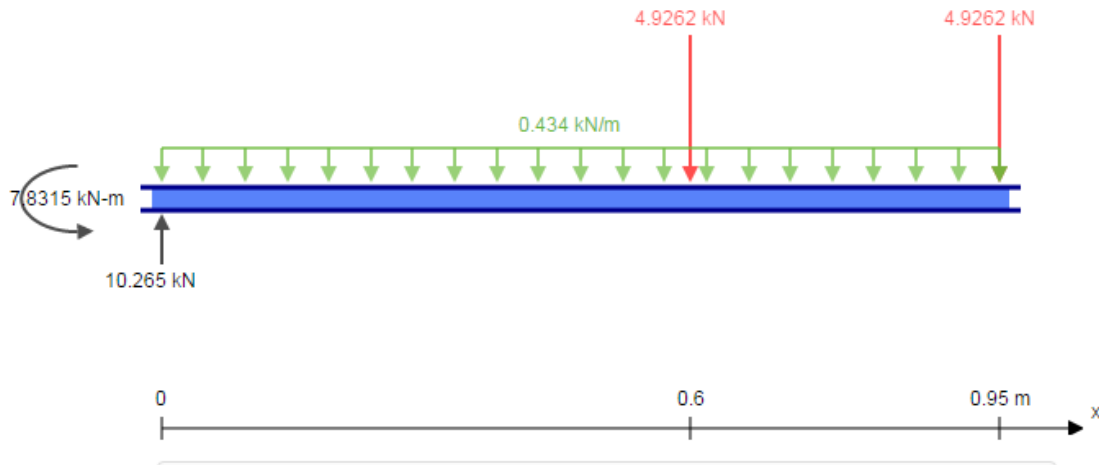

Figure C-20. Free body diagram for cross beams – Heavy side.

Figure C-21 represents the shear forces applied to the cross beam while Figure C-22 shows the bending moments applied to the cross beam. It can be observed that the maximum applied bending moment in the cross beam occurs at its support and is equal to 7831.5 Nm.
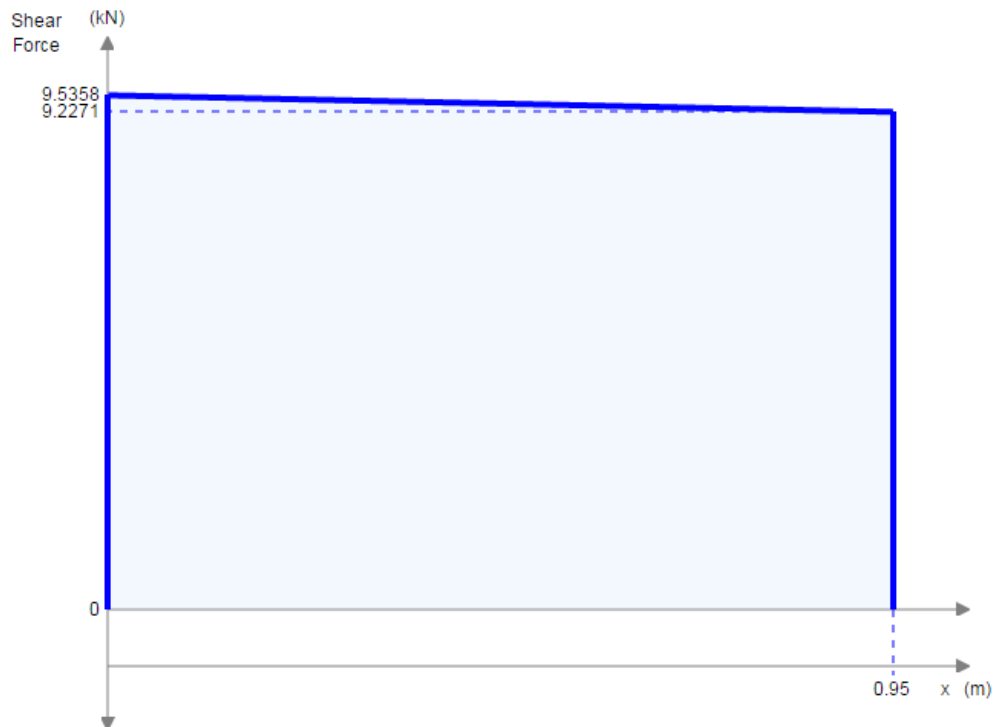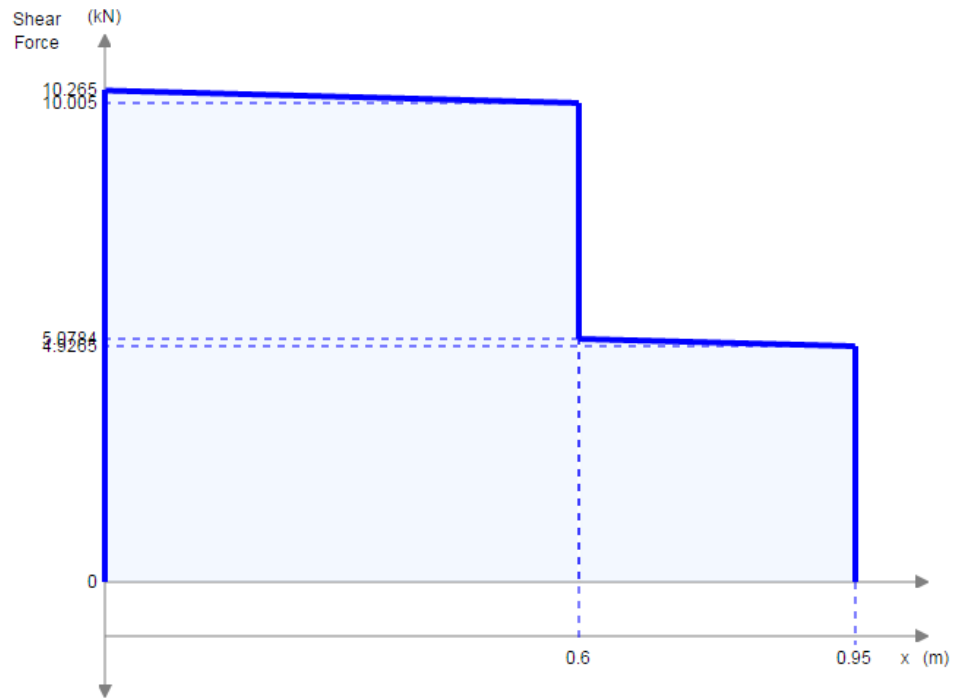
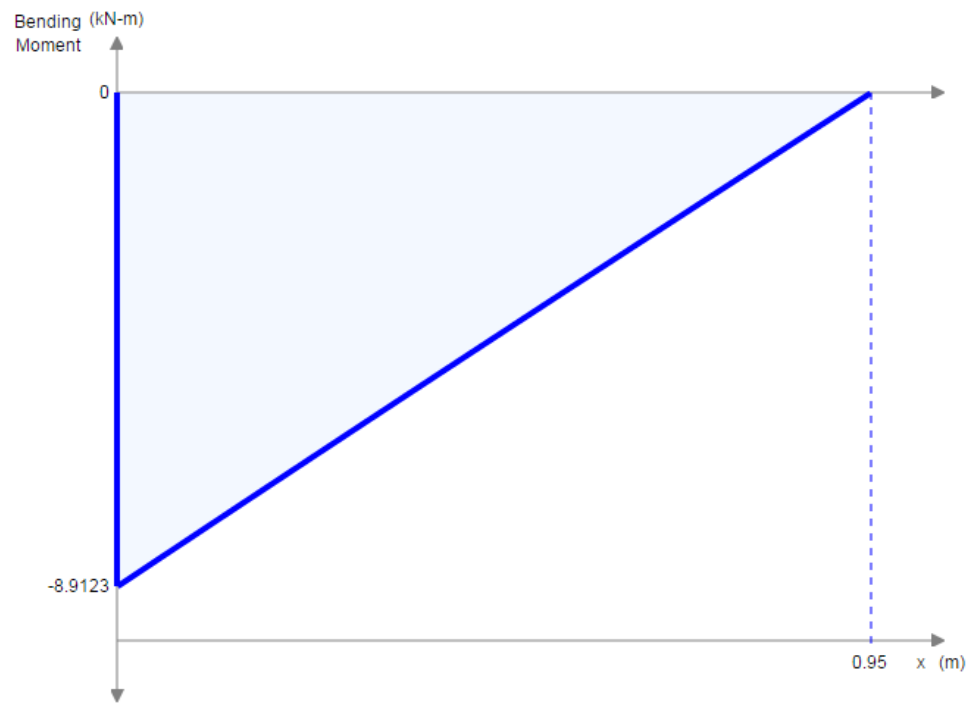**Figure C-21.** Shear force diagram for the cross beams – Heavy side.
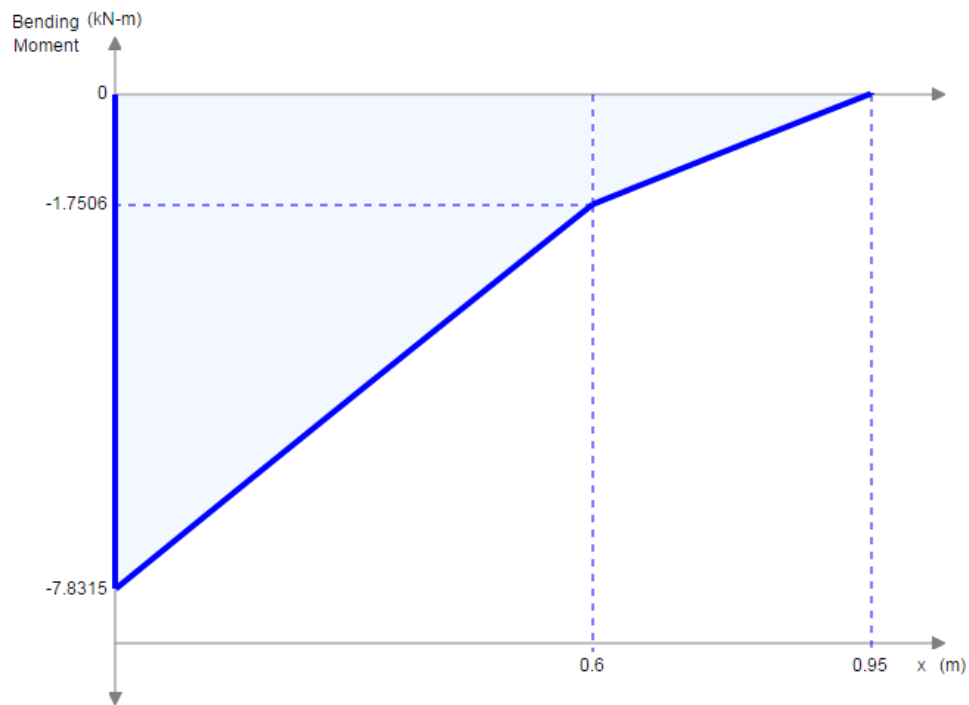
Figure C-22. Bending moment diagram for the cross beams – Heavy side.

C.8 Force diagrams for the cross beam due to four large Micromegas chamber support beam – Light side

In order to calculate the reaction forces and bending moments applied to the cross beam due to the hanging of four large Micromegas chambers on the light side of the transport tool, the same simplification due to symmetry can be applied to the geometry as found in the analysis of the cross beam due to the support of the heavy side of a large sector.

The free body diagram represented in Figure C-23 is a representation of the forces applied to the cross beam when experiencing a load due to the sector support beam's light side when carrying four large Micromegas chambers. The red force is the load applied to the cross beam by the sector support beam. The green distributed load is a result of the weight of the beam at a total mass of 63 kg. To get a true reaction force on the beam, the value shown must be doubled to get a value of 16.831 kN.
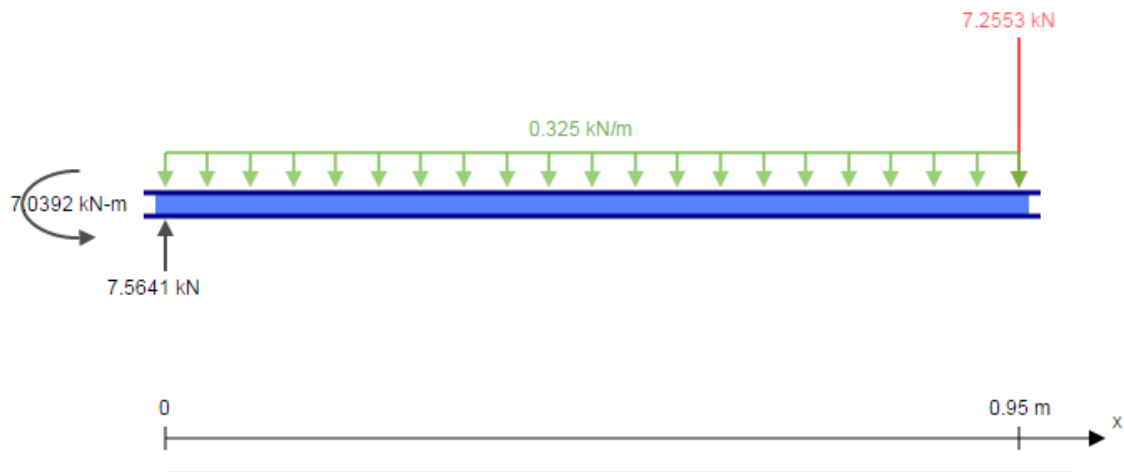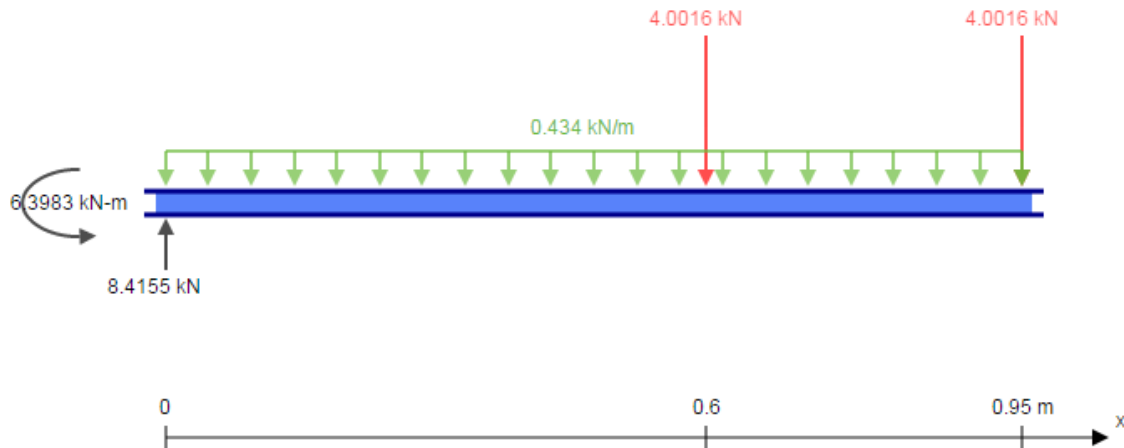

Figure C-23. Free body diagram for cross beams – Light side.

Figure C-24 represents the shear forces applied to the cross beam while Figure C-25 shows the bending moments applied to the cross beam. It can be observed that the maximum applied bending moment in the cross beam occurs at its support and is equal to 6398.3 Nm.
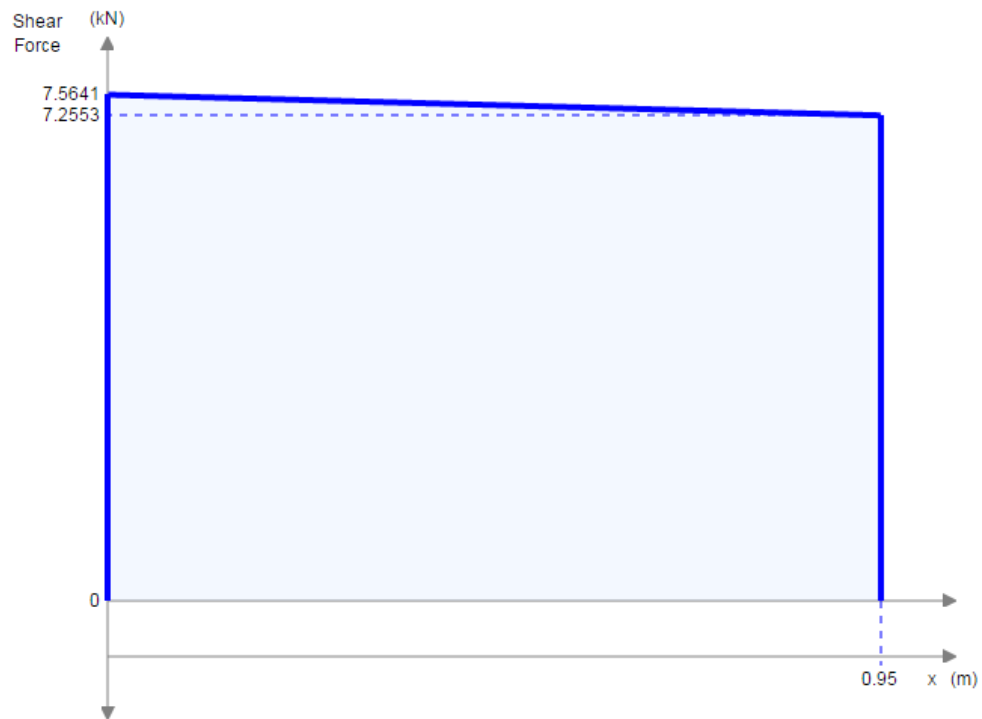
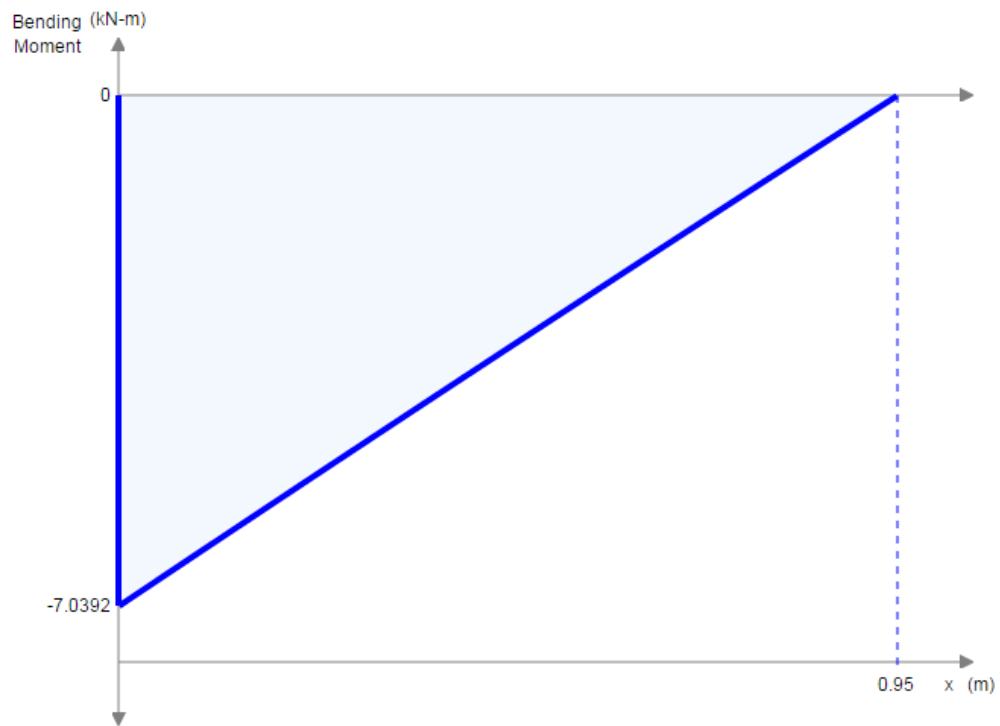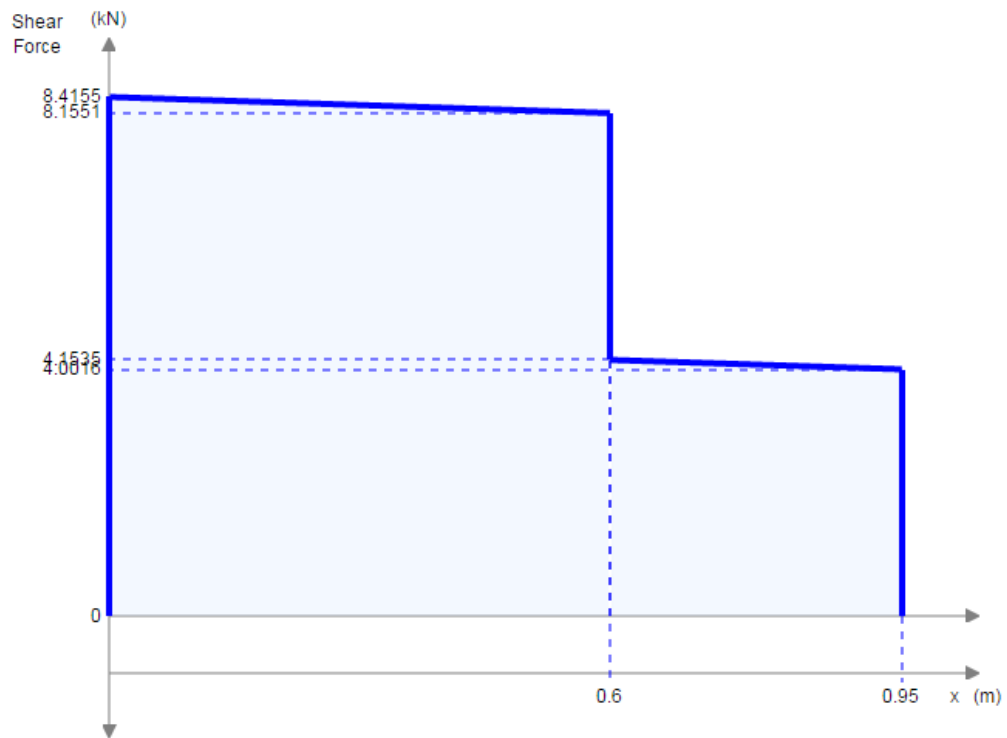**Figure C-24.** Shear force diagram for the cross beams – Light side.
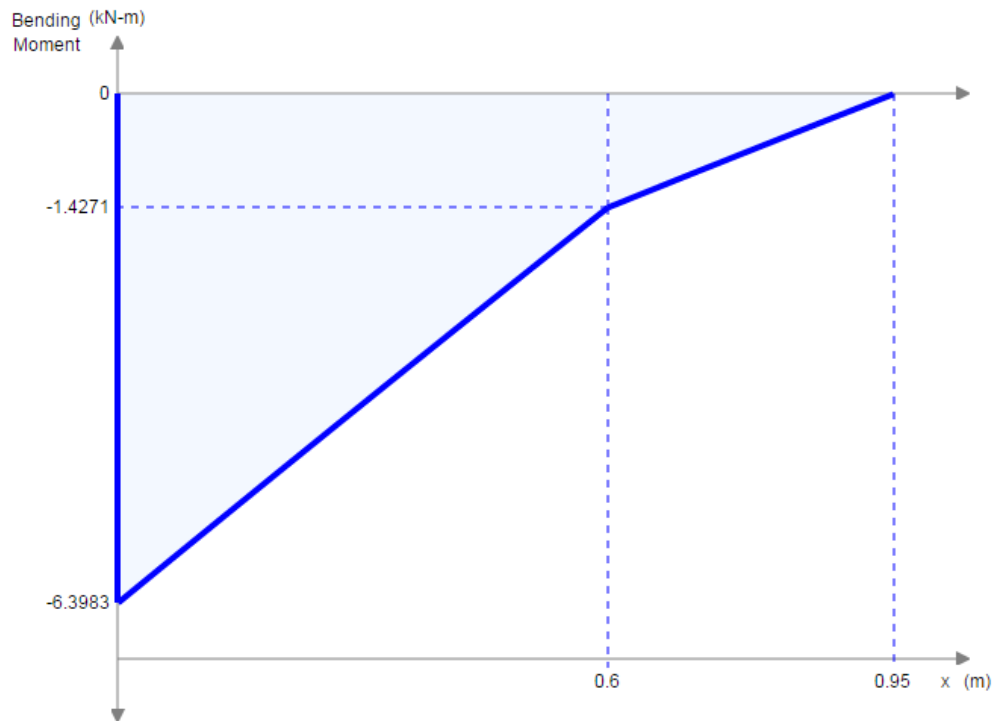
Figure C-25. Bending moment diagram for the cross beams – Light side.

C.9 Force diagrams for the long beam when transporting four large Micromegas chambers

The free body diagram represented in Figure C-26 is a representation of the forces applied to the long beam when experiencing a load due to the support of four large Micromegas chambers. The red forces are the loads applied to the long beam by the cross beams. The green distributed load is a result of the weight of the long beam at a total mass of 430 kg.
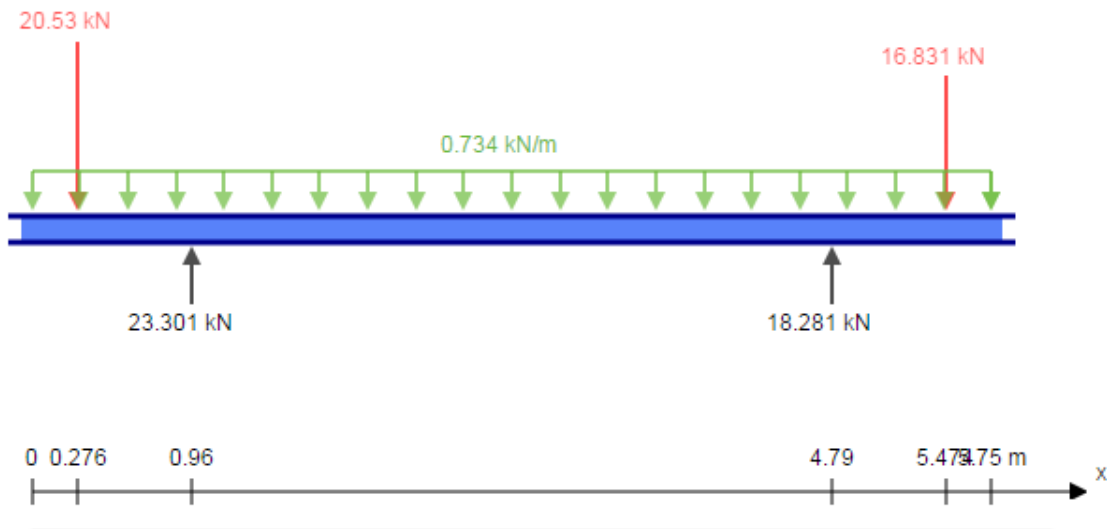
Figure C-26. Free body diagram for the long beam.

Figure C-27 represents the shear forces applied to the long beam while Figure C-28 shows the bending moments applied to the long beam. It can be observed that the maximum applied bending moment in the long beam is equal to 14381 Nm.

Shear (kN)
Force

17.536
17.034

2.0664
0
-0.74486

-20.733
-21.236

0.276   0.96   3.7752   4.79   5.4745.75   x (m)

Figure C-27. Shear force diagram for the long beam.

Bending (kN-m)
Moment

0

-11.472
-11.85

-14.381

0.276   0.96   3.7752   4.79   5.4745.75   x (m)
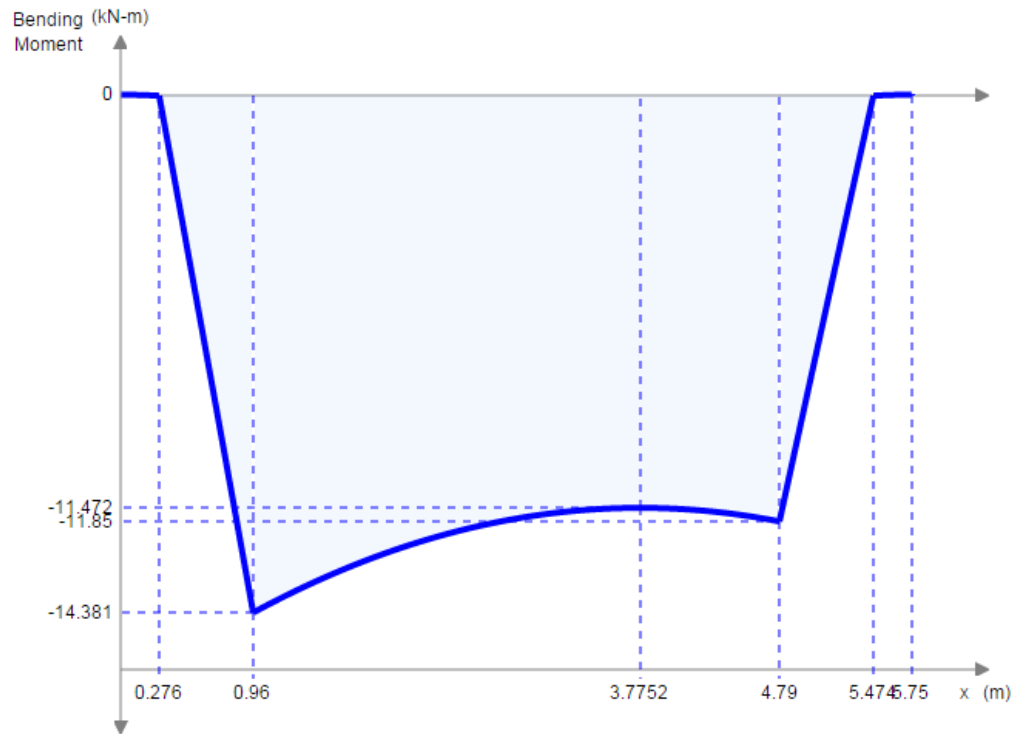
Figure C-28. Bending moment diagram for the long beam.

C.10 Force diagrams for the sector support beam due to the large sector when lifted by the crane

The free body diagram represented in Figure C-29 is a representation of the forces applied to the sector support beam by a large sector when it is being lifted off the transport tool. The red forces are the loads applied to the sector support beam by the sector sling mounts. The green distributed load is a result of the weight of the beam at a total mass of 230 kg. The two reaction forces shown are the sling mounts for the lifting operation.
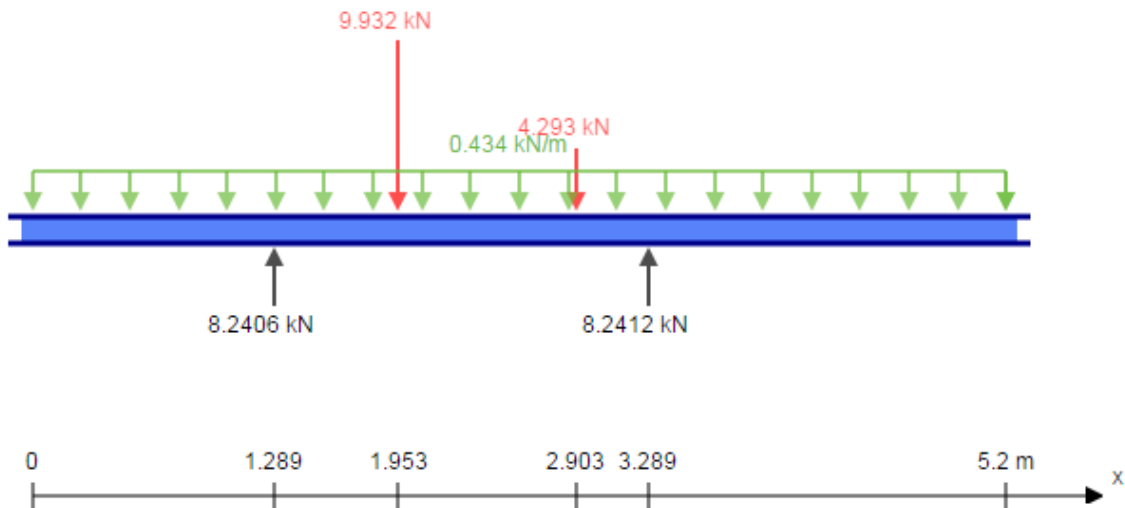
Figure C-29. Free body diagram for the large sector support beam when lifted.

Figure C-30 represents the shear forces applied to the beam while Figure C-31 shows the bending moments applied to the beam. It can be observed that the maximum applied bending moment in the sector support beam occurs at one of the sector sling mounts and is equal to 4644.1 Nm.
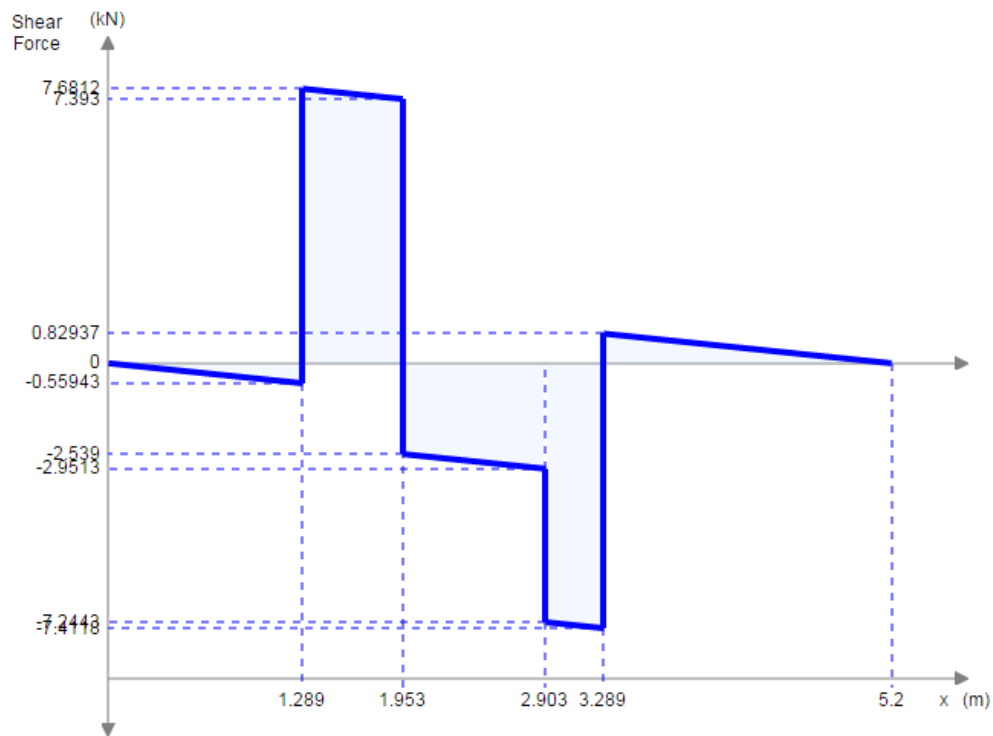
Figure C-30. Shear force diagram for the large sector support beam when lifted.
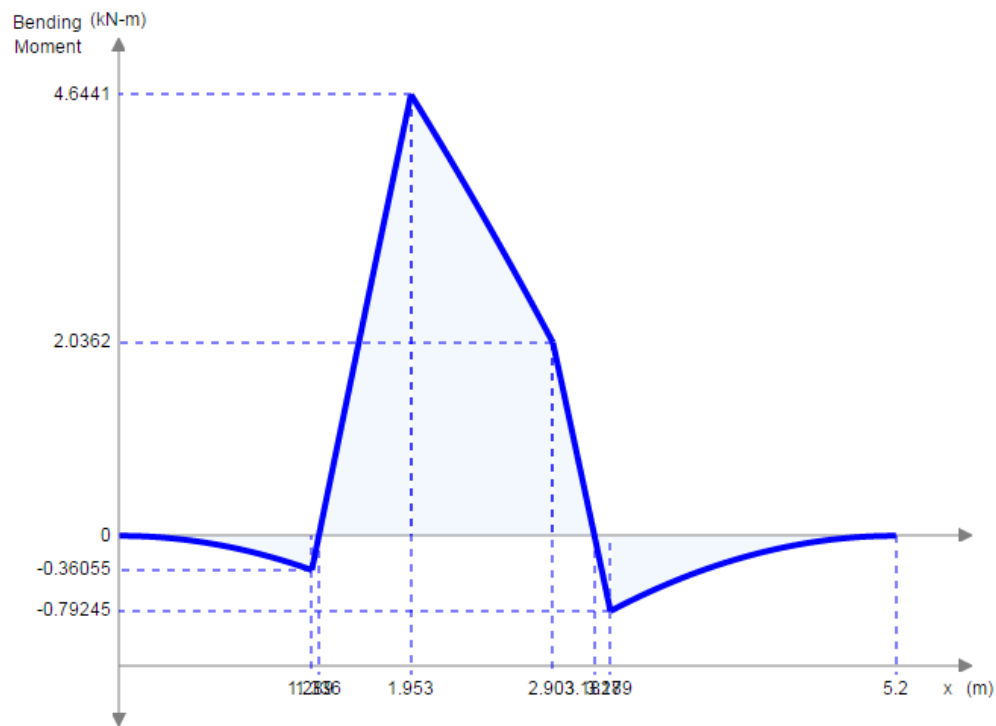
Figure C-31. Bending moment diagram for the large sector support beam when lifted.

C.11 Force diagrams for the sector support beam due to the small sector when lifted by the crane

The free body diagram represented in Figure C-32 is a representation of the forces applied to the sector support beam by a small sector when it is being lifted off the transport tool. The red forces are the loads applied to the sector support beam by the sector sling mounts. The green distributed load is a result of the weight of the beam at a total mass of 230 kg. The two reaction forces shown are the sling mounts for the lifting operation.
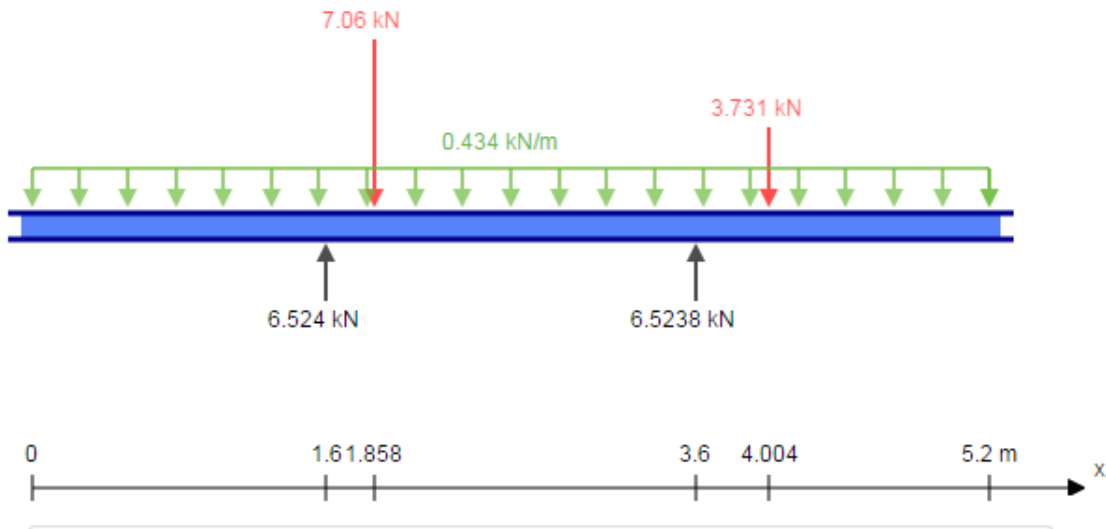
Figure C-32. Free body diagram for the small sector support beam when lifted.

Figure C-33 represents the shear forces applied to the beam while Figure C-34 shows the bending moments applied to the beam. It can be observed that the maximum applied bending moment in the sector support beam occurs at one of the sector support beam sling mounts and is equal to 2062.8 Nm.
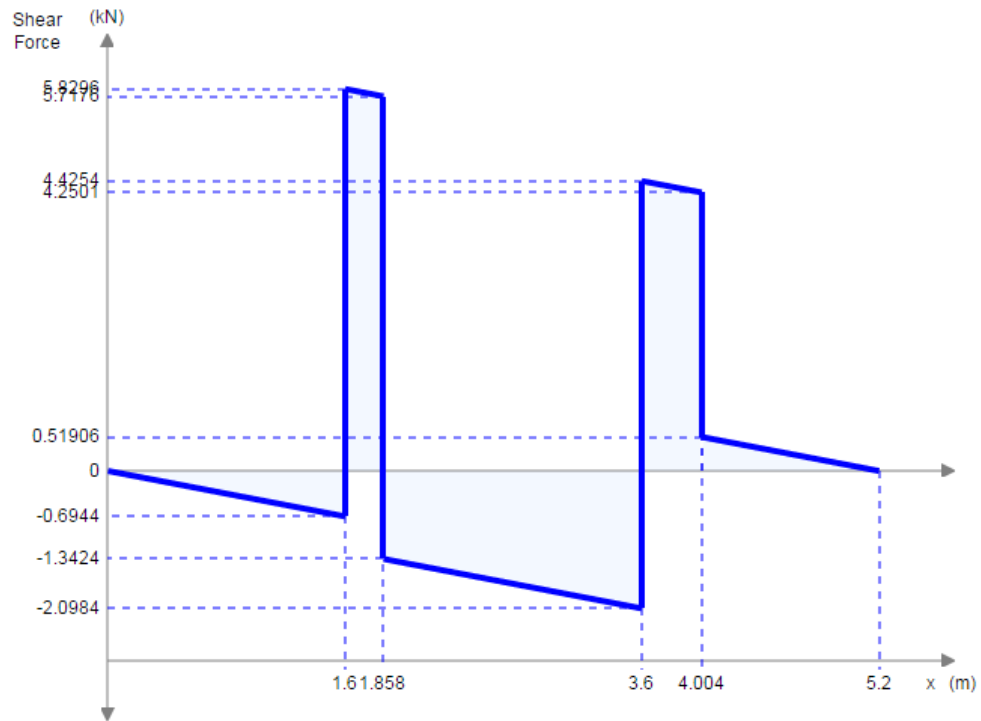
Figure C-33. Shear force diagram for the small sector support beam when lifted.
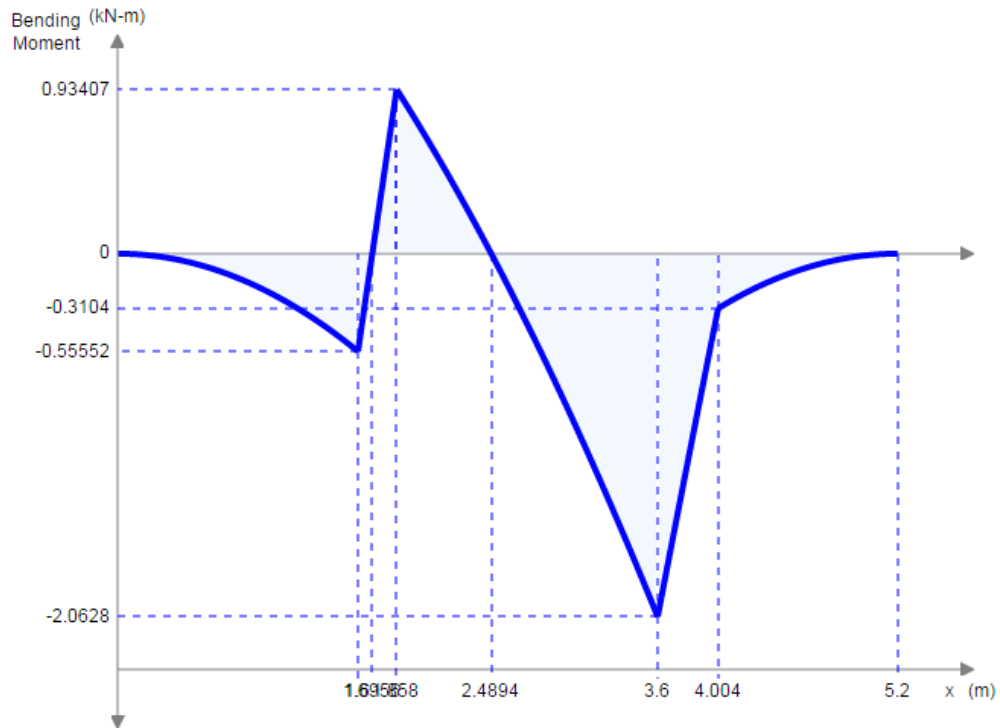
Figure C-34. Bending moment diagram for the small sector support beam when lifted.

C.12 Force diagrams for the long beam when the loaded tool is lifted by the crane

The free body diagram represented in Figure C-35 is a representation of the forces applied to the long beam when the loaded tool, with four large Micromegas chambers, is being lifted by the crane. The red forces are the loads applied to the long beam by the cross beams. The green distributed load is a result of the weight of the beam at a total mass of 1062 kg if the weight of the posts are included. The two reaction forces shown are the sling mounts for the lifting operation.
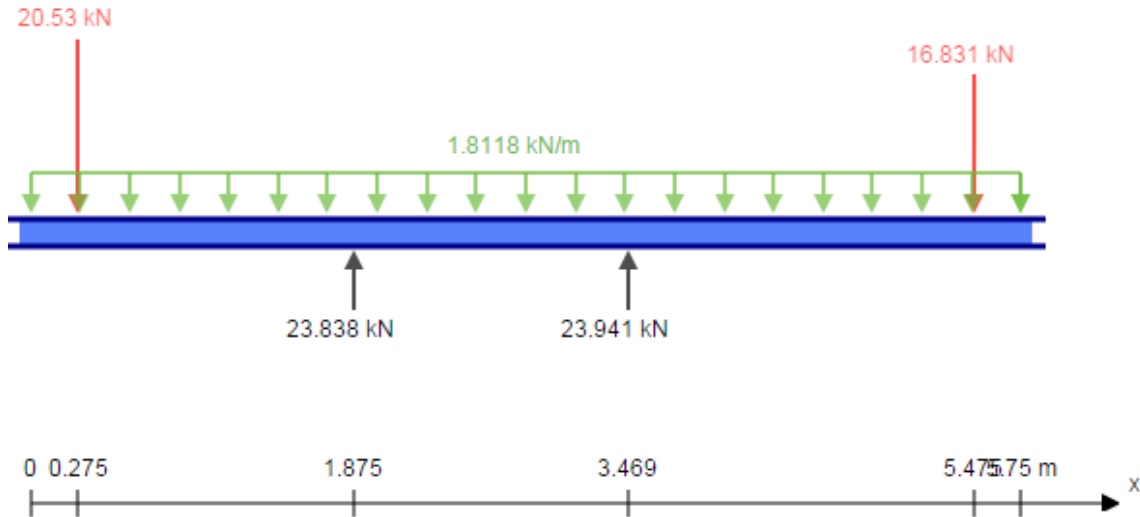
Figure C-35. Free body diagram for the long beam when the loaded tool is being lifted.

Figure C-36 represents the shear forces applied to the beam while Figure C-37 shows the bending moments applied to the beam. It can be observed that the maximum applied bending moment in the long beam occurs at one of the sling mounts and is equal to 38477 Nm.

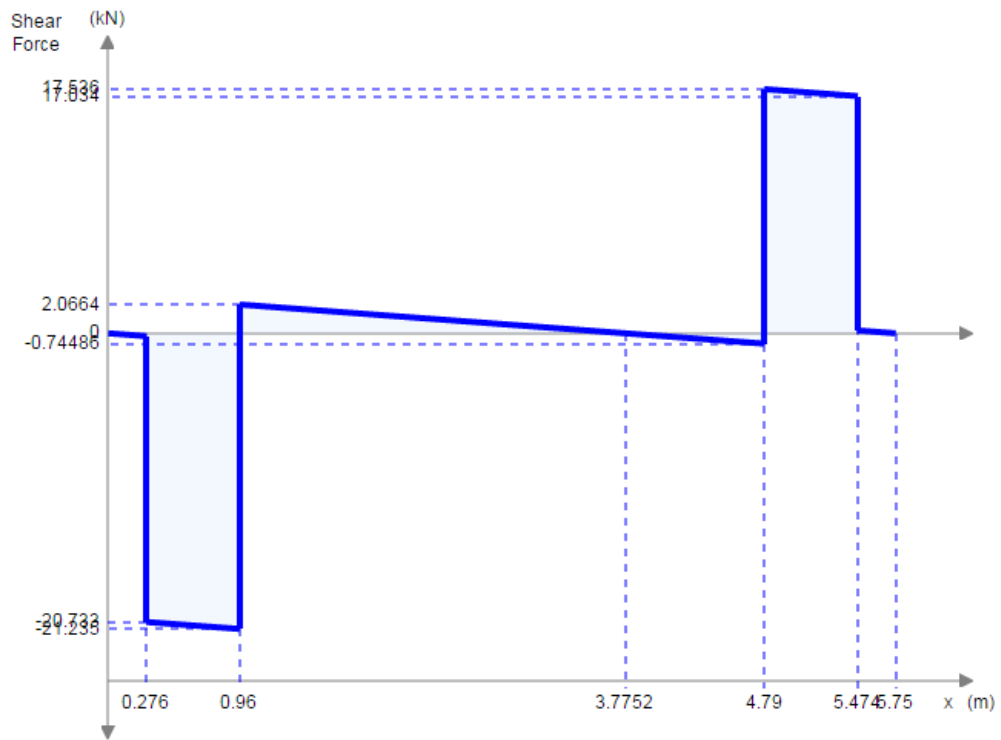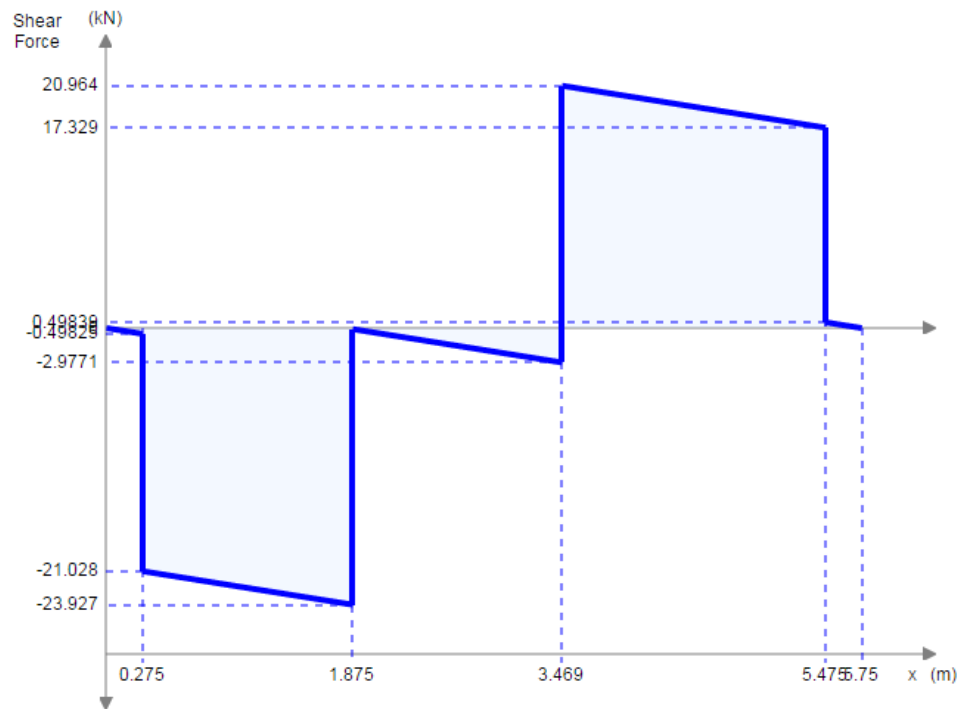**Figure C-36.** Shear force diagram for the long beam when the loaded tool is being lifted.
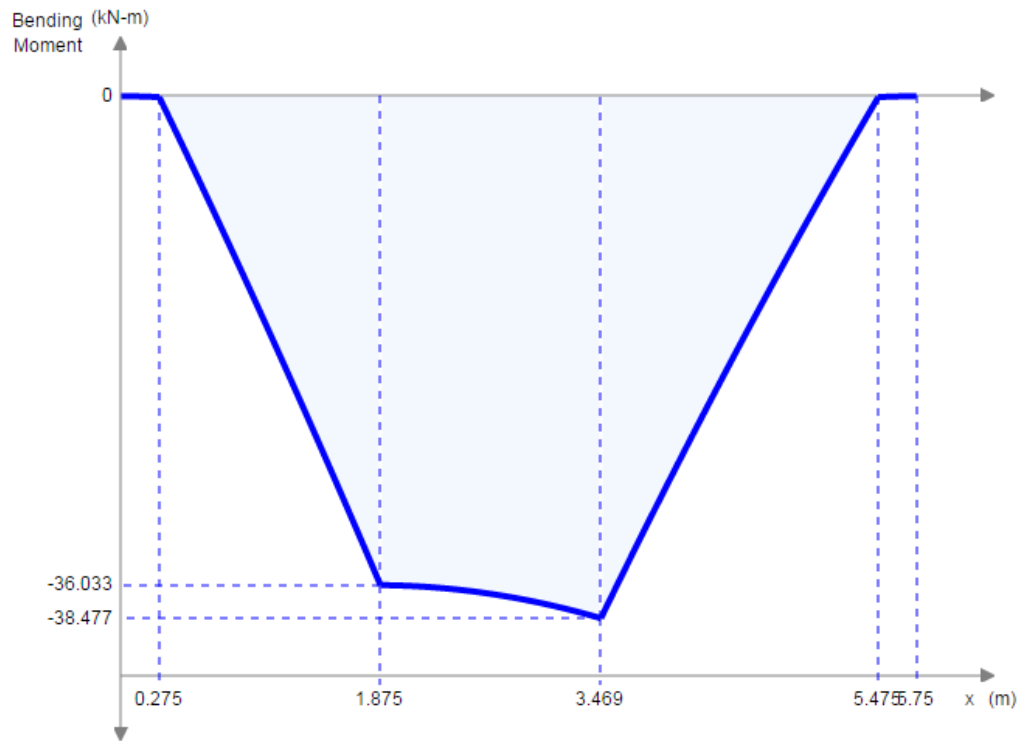
Figure C-37. Bending moment diagram for the long beam when the loaded tool is being lifted.

APPENDIX D - Complex Geometry Moments of Inertia

D.1 Moment of inertia of the long beam – Outer region

In order to calculate the moment of inertia of the long beam the parallel axis theorem represented in Equation 12 is to be used due to the geometry not being uniform as seen in by the representation of the long beams cross section in Figure D-1:

$$I_{gg} = I_{cm} + AH^2$$

Equation 12
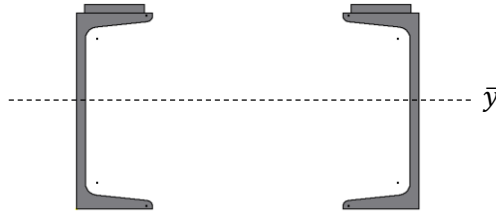
Figure D-1. Long beam cross section.

A centroid $\bar{y}$ needs to be found for the cross-section of the composite shape using Equation 10:

$$\bar{y} = \frac{\sum \bar{y}A}{\sum A}$$

Equation 10

$$\bar{y} = \frac{(90 \times 2800) + (184 \times 440)}{2800 + 440}$$

$$\bar{y} = 102.765 \; mm$$

$$I_{gg} = I_{cm} + AH^2$$

Equation 12

$$H = \bar{y} - \frac{y}{2}$$

$$H_{C-Channel} = 102.765 - \frac{180}{2}$$

$$H_{C-Channel} = 12.765$$

$$H_{Top \; plate} = 184 - 102.235$$

$$H_{Top \; plate} = 81.735 \; mm$$

Using the parallel axis theorem, Equation 12, for the C-Channel:

$$I_{gg} = I_{cm} + AH^2$$

Equation 12

$$I_{gg} = 13540000 + (2800 \times 12.765^2)$$

$$I_{gg} = 13.996 \times 10^6 \ mm^4$$

Using the parallel axis theorem for the Top Plate and the moment of inertia of a rectangle using Equation 13:

$$I = \frac{BD^3}{12}$$

Equation 13

$$I = \frac{55 \times 8^3}{12}$$

$$I = 2345.\dot{6} \ mm^4$$

$$I_{gg} = I_{cm} + AH^2$$

Equation 12

$$I_{gg} = 2345.\dot{6} + (440 \times 81.235^2)$$

$$I_{gg} = 2.906 \times 10^6 \ mm^4$$

∴ Adding the moments of inertia together and doubling the result, the moment of inertia of the outer region of the long beam will be given as:

$$I_{gg \ Total} = (I_{gg \ C-Channel} + I_{gg \ Top \ Plate}) \times 2$$

$$I_{gg \ Total} = (13.996 \times 10^6 + 2.906 \times 10^6) \times 2$$

$$I_{gg \ Total} = 33.804 \times 10^6 \ mm^4$$

The relative section modulus is given by Equation 14:

$$w_x = \frac{I_x}{y}$$

Equation 14

$$w_x = \frac{33.804 \times 10^6}{102.765}$$

$$w_x = 328944.68 \ mm^3$$

D.2 Moment of inertia of the post

In order to calculate the moment of inertia of the post, Equation 12 is to be used due to the geometry not being standard as seen in by the representation of the post cross section in Figure D-2:

$$I_{gg} = I_{cm} + AH^2$$
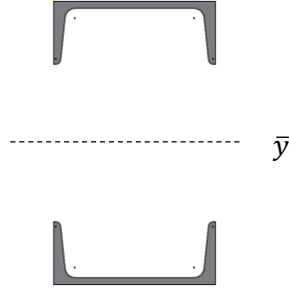
Figure D-2. Post cross section.

Using Parallel Axis Theorem, Equation 12, for a C-Channel:

$$I_{gg} = I_{cm} + AH^2$$

Equation 12

$$I_{gg} = 1140000 + (2800 \times 138.4^2)$$

$$I_{gg} = 54.77 \times 10^6 \ mm^4$$

∴ Adding the moments of inertia of the C-Channels, the moment of inertia of the post is:

$$I_{gg\ Total} = I_{gg\ C-Channel} \times 2$$

$$I_{gg\ Total} = 54.77 \times 10^6 \times 2$$

$$I_{gg\ Total} = 109.55 \times 10^6 \ mm^4$$

Now, the section modulus can be found using Equation 14:

$$w_x = \frac{I_x}{y}$$

$$w_x = \frac{109.55 \times 10^6}{157.5}$$

$$w_x = 695555.56 \; mm^3$$

D.3 Moment of inertia of the post extension

In order to calculate the moment of inertia of the post, the Equation 12 is to be used due to the geometry not being standard as seen in by the representation of the post cross section in Figure D-3:

$$I_{gg} = I_{cm} + AH^2$$

Equation 12
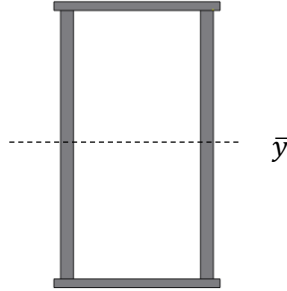
Figure D-3. Post cross section.

Finding the moment of inertia of the top and bottom plate using Equation 13:

$$I = \frac{BD^3}{12}$$

Equation 13

$$I = \frac{196 \times 10^3}{12}$$

$$I = 16333.33 \ mm^4$$

Using parallel axis theorem, Equation 12:

$$I_{gg} = I_{cm} + AH^2$$

Equation 12

$$I_{gg} = 16333.33 + (1960 \times 163.5^2)$$

$$I_{gg} = 52.41 \times 10^6 \ mm^4$$

Finding the moment of inertia of the upright plates:

$$I = \frac{BD^3}{12}$$

$$I = \frac{15 \times 317^3}{12}$$

$$I = 39.82 \times 10^6 \ mm^4$$

∴ Adding all the moments of inertia together, the total moment of inertia of the post extension is:

$$I_{gg\ Total} = (I_{top-plate} \times 2) + (I_{web} \times 2)$$

$$I_{gg\ Total} = (52.41 \times 10^6 \times 2) + (39.82 \times 10^6 \times 2)$$

$$I_{gg\ Total} = 184.46 \times 10^6 \ mm^4$$

Now, using Equation 14 for the section modulus:

$$w_x = \frac{I_x}{y}$$

Equation 14

$$w_x = \frac{184.46 \times 10^6}{168.5}$$

$$w_x = 1094718.1 \ mm^3$$

D.4 Moment of inertia of the long beam – Inner

In order to calculate the moment of inertia of the long beam, Equation 12 is to be used due to the geometry not being standard as seen in by the representation of the post cross section in Figure D-4:

$$I_{gg} = I_{cm} + AH^2$$

Equation 12
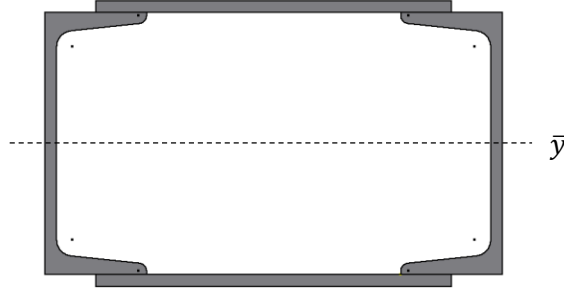
Figure D-4. Long beam cross section – Inner

Finding the moment of inertia of the top and bottom plate using Equation 13:

$$I = \frac{BD^3}{12}$$

Equation 13

$$I = \frac{245 \times 8^3}{12}$$

$$I = 10453.3 \ mm^4$$

Using parallel axis theorem, Equation 12:

$$I_{gg} = I_{cm} + AH^2$$

Equation 12

$$I_{gg} = 10453.3 + (1960 \times 94^2)$$

$$I_{gg} = 17.33 \times 10^6 \ mm^4$$

The moments of inertia of the C-Channels are equal to:

$$I_{gg} = 13540000$$

∴ adding all the moments of inertia together, the total moment of inertia of the long beam is:

$$I_{gg\ Total} = \left(I_{top-plate} \times 2\right) + \left(I_{C-Channel} \times 2\right)$$

$$I_{gg\ Total} = (17.33 \times 10^6 \times 2) + (13.54 \times 10^6 \times 2)$$

$$I_{gg\ Total} = 61.74 \times 10^6\ mm^4$$

Now, using Equation 14 to find the section modulus:

$$w_x = \frac{I_x}{y}$$

Equation 14

$$w_x = \frac{61.74 \times 10^6}{98}$$

$$w_x = 630 \times 10^3\ mm^3$$

APPENDIX E - Safety Report

E.1 Transport tool safety report

Micromegas Chamber NSW Sector Transport Tool Analysis

Peter James Sinclair

This technical note concerns the mechanical calculations for the tooling that will be used to transport Micromegas chambers and fully assembled sectors for the New Small Wheel (NSW) project of the ATLAS Experiment, for Long Shutdown 2. The applied loads to the tooling considered are of the worst possible cases.

1. Introduction

The transport of Micromegas chambers and fully assembled sectors has become necessary in the manufacture of the NSW due to the availability of floor space being dispersed around the CERN premises. In order to save manufacturing time, resources and money the old transport tool used to transport the EO muon chambers for The ATLAS Experiment is to be modified to accommodate the new Micromegas chambers and fully assembled NSW sectors. The stress analysis of the transport tool should therefore be revised in order to ensure that the modifications and the new loads meet safety requirements.
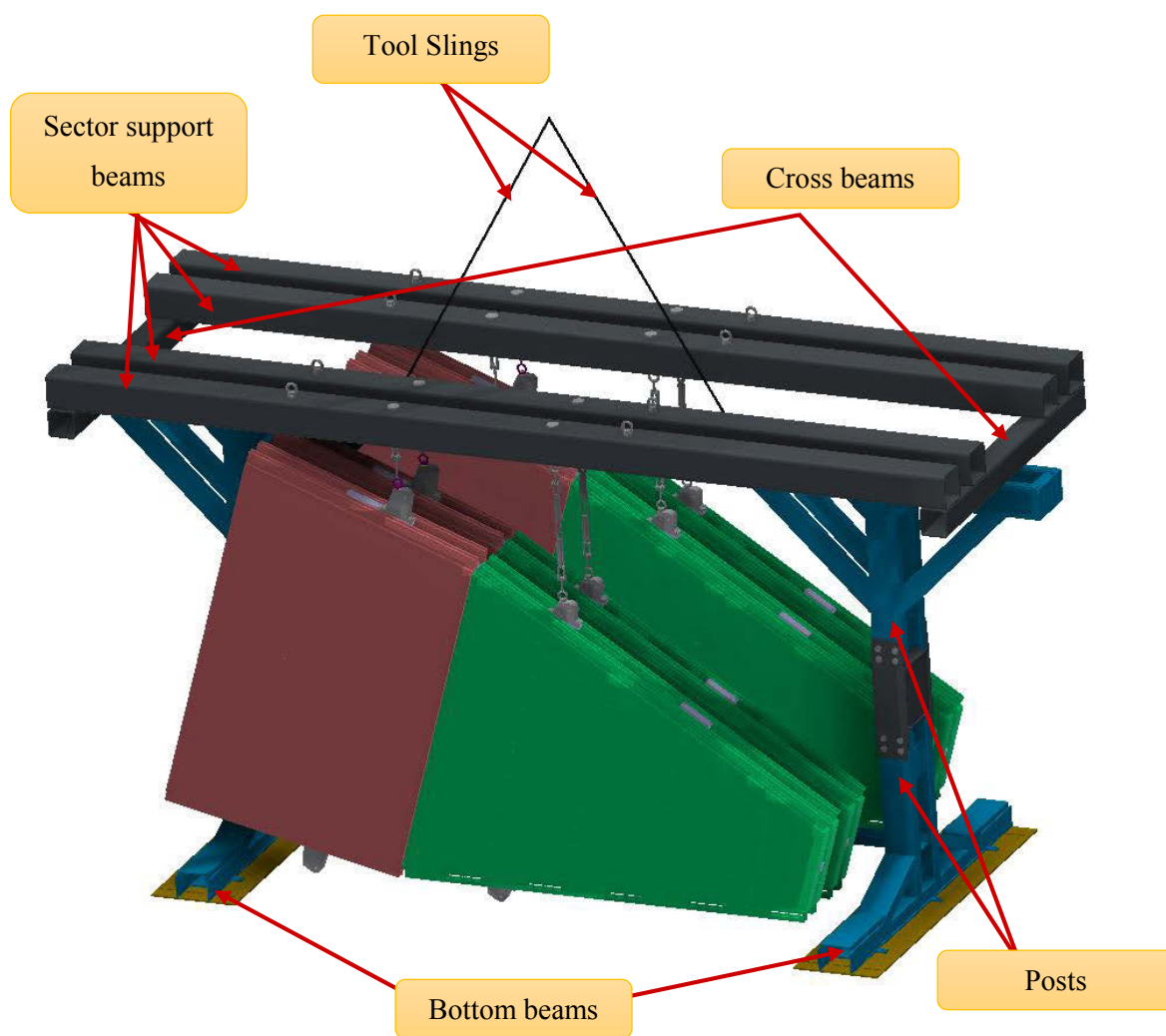
Figure E-1. Transport tool.
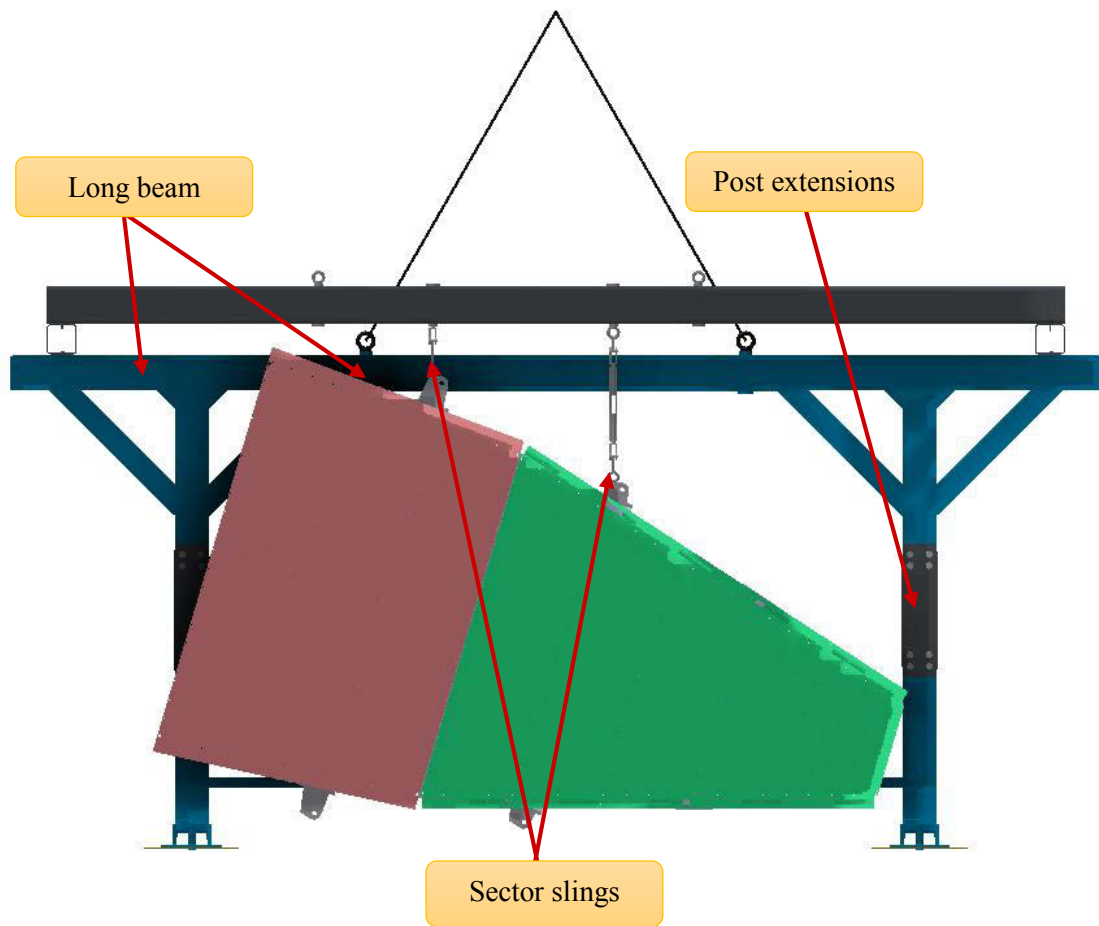
Figure E-2. Transport tool - Front view.

2. Design requirements

1. Ensure that four Micromegas chambers or two fully assembled sectors of the NSW can be transported.

2. All lifting components must have a safety factor of at least 2 as per the Standard ES EN 13155:2003.

3. The tool must be stable when at rest and when being lifted.

3. Design Description

The old EO muon chamber transport tool has been modified in the following ways to ensure that it is suitable to carry the Micromegas chambers and NSW sectors.

1. The posts have been extended by 368 mm to gain the height needed for the sectors to hang comfortably from the tool.
2. The support beams and the cross beams have been changed.
3. Two of the hoist points have been removed
4. An extra hoist point has been added

4. Stress analysis

The total masses and accompanying weights of all the components that are relevant to the stress analysis calculations can be seen in Table E-1. Acceleration due to gravity is assumed to be $g = 9.81 \frac{m}{s}$.

Table E-1. Relevant components with their masses and weights.

Component	Mass (kg)	Weight (N)
Large Sector	1450 x 2	14225 x 2
Small Sector	1100 x 2	10791 x 2
Large double Micromegas chamber	680 x 4	6671 x 2
Small double Micromegas chamber	553 x 4	5425 x 4
Sector Support Beam	230 x 4	2256 x 4
Cross Beam	63 x 2	618 x 2
Long Beam	430	4218.3
Post original x 2	260 x 2	2551 x 2
Post extension x 2	56 x 2	549 x 2
Post and post extension x 2	316 x 2	3100 x 2
Unloaded Tool	1188	11654
Loaded Tool (2 large Sectors)	4548	44616
Loaded Tool (2 small Sectors)	3848	37749
Loaded Tool (4 large MMs)	4828	47363
Loaded Tool (4 small MMs)	4320	42379

Stress analysis of the sector support beam

The highest load applied to the sector support beams is the applied bending stress when they are being used to manipulate fully assembled NSW sectors.

When the support beam is resting on the transport tool, the maximum stress can be calculated using Equation 2: The stress due to bending is used while the stress due to shear forces are negligibly small and have been omitted from the calculations.

$$\sigma_b = \frac{M}{W}$$

Equation 2

The sector sling mount points are not positioned symmetrically in between its two support points and therefore the bending moments are not symmetrical through the beam. The largest bending moment is a result of the hanging of the large sector. this moment is calculated to be:

$$M = 17192 \; Nm$$

The maximum bending stress can therefore be calculated using Equation 2 as:

$$\sigma_b = \frac{M}{W}$$

Equation 2

$$\sigma_b = \frac{17192}{0.000357}$$

$$\sigma_b = 48.16 \; MPa$$

The yield strength of the steel used for the support beams can be divided by this maximum bending stress to calculate a safety factor using Equation 3:

$$SF = \frac{\sigma_y}{\sigma_b}$$

Equation 3

$$SF = \frac{235}{48.16}$$

$$SF = 4.9$$

The sector support beam can therefore survive the applied stresses with a safety factor of 4.9 when supporting a fully assembled large NSW sector. The bending moments when the cross beam is

supporting a small sector or a large or small Micromegas chamber are all calculated to be lower than the moment created by the large sector. This means that a higher safety factor will result and the design is OK for all these scenarios.

Stress analysis of the cross beams

The highest load applied to the cross beams is when the transport tool is used to transport two fully assembled NSW sectors from their assembly station/storage area to the NSW assembly station. The beam on the side where the weight of the sector is biased towards experiences the greater force of 9227 N.

The forces applied to the cross beam are due to the weight of the two sectors and their two support beams. The forces applied on either side of the cross beam are equivalent. For this reason, the calculation can be simplified using symmetry.

The maximum moment can be calculated as:

$$M = 8912.3 \ Nm$$

This calculated moment is the worst case in the uniform cross beam used. The maximum bending stress can therefore be calculated using Equation 2 as:

$$\sigma_b = \frac{M}{W}$$

Equation 2

$$\sigma_b = \frac{8912.3}{218 \times 10^{-6}}$$

$$\sigma_b = 40.9 \ MPa$$

The yield strength of the S235JRG2 steel used for the cross beams can be divided by this maximum bending stress to calculate a safety factor using Equation 3:

$$SF = \frac{\sigma_y}{\sigma_b}$$

Equation 3

$$SF = \frac{235}{40.9}$$

$$SF = 5.7$$

The cross beam can therefore survive the applied stresses when they are at a maximum value with a safety factor of 5.7.The bending moments when the cross beam is supporting two small sectors or four large or small Micromegas chambers are all calculated to be lower than the moment created by the two large sectors. This means that a higher safety factor will result and the design is OK for all these scenarios.

Stress analysis of the long beam

The highest load applied to the long beam is when the transport tool is used to transport four large Micromegas chambers from Building 899 to the assembly station in Building 191. The load applied to the long beam is a result of the chambers, the support beams and the cross beams.

The maximum moment is found directly above the left post and is equal to:

$$M = 14381 \; Nm$$

This calculated moment is the worst case in the long beam. The maximum bending stress can therefore be calculated using Equation 2 as:

$$\sigma_b = \frac{M}{W}$$

Equation 2

$$\sigma_b = \frac{14381}{3.2894 \times 10^{-4}}$$

$$\sigma_b = 43.72 \; MPa$$

The yield strength of the S235JRG2 steel used for the long beam can be divided by this maximum bending stress to calculate a safety factor using Equation 3:

$$SF = \frac{\sigma_y}{\sigma_b}$$

Equation 3

$$SF = \frac{235}{43.72}$$

$$SF = 5.38$$

The long beam can therefore survive the applied stresses when they are at a maximum value with a safety factor of 5.38, meaning that the design is OK. The bending moments when the long beam is supporting two small sectors or four large or small Micromegas chamber are all calculated to

be lower than the moment created by the large sectors. This means that a higher safety factor will result and the design is OK for all these scenarios.

Stress analysis of the post and post extension

The highest load applied to the post and the post extension of the transport tool is when only one large NSW sector is loaded on the tool. The load applied is a result of a bending moment created by the sector, the sector support beam and the cross beam.

The moment created in the post is calculated to be:

$$M = 8912.3 \ Nm$$

This calculated moment is the worst case bending moment in the post. The maximum bending stress can therefore be calculated using the Equation 2:

$$\sigma_b = \frac{M}{w}$$

Equation 2

The bending stress applied to the original post is equal to:

$$\sigma_b = \frac{8912.3}{695555.56 \times 10^{-9}}$$

$$\sigma_b = 12.81 \ MPa$$

The yield strength of the S235JRG2 steel used for the post can be divided by this maximum bending stress to calculate a safety factor using Equation 3:

$$SF = \frac{\sigma_y}{\sigma_b}$$

Equation 3

$$SF = \frac{235}{12.81}$$

$$SF = 18.35$$

The post can therefore survive the applied stresses when they are at a maximum value with a safety factor of 18.35, meaning that the design is OK.

Using Equation 2, the bending stress applied to the post extension can be calculated to be:

$$\sigma_b = \frac{8912.3}{1094718.1 \times 10^{-9}}$$

$$\sigma_b = 8.14 \, MPa$$

The yield strength of the S235JRG2 steel used for the post extension can be divided by this maximum bending stress to calculate a safety factor using Equation 3:

$$SF = \frac{\sigma_y}{\sigma_b}$$

Equation 3

$$SF = \frac{235}{8.14}$$

$$SF = 28.87$$

The post extension can therefore survive the applied stresses when they are at a maximum value with a safety factor of 28.87, meaning that the design is OK.

Stress analysis of the large sector support beam during lifting

The highest load applied to the sector support beam of the transport tool during lifting is when a large NSW sector is loaded on it. The load applied is a result of a bending moment created by the sector and the top sling mounts. The maximum moment created in the beam is calculated to be:

$$M = 4644.1 \, Nm$$

This calculated moment is the worst case bending moment in the sector support beam. The maximum bending stress can therefore be calculated using the Equation 2:

$$\sigma_b = \frac{M}{W}$$

Equation 2

The bending stress applied to the beam is equal to:

$$\sigma_b = \frac{4644.1}{0.000357}$$

$$\sigma_b = 13.0 \, MPa$$

The yield strength of the S235JRG2 steel used for the beam can be divided by this maximum bending stress to calculate a safety factor using Equation 3:

$$SF = \frac{\sigma_y}{\sigma_b}$$

<div style="text-align: right;">**Equation 3**</div>

$$SF = \frac{235}{13.0}$$

$$SF = 18.1$$

The sector support beam can therefore survive the applied stresses when they are at a maximum value with a safety factor of 18.1, meaning that the design is OK.

<div style="text-align: center;">**Stress analysis of the long beam during transport tool lifting**</div>

The highest load applied to the long beam of the transport tool during lifting is when four large Micromegas chambers are loaded on it. The load applied is a result of a bending moment created. The maximum moment created in the beam is calculated to be:

$$M = 38477 \; Nm$$

This calculated moment is the worst case bending moment in the sector support beam. The maximum bending stress can therefore be calculated using the Equation 2:

$$\sigma_b = \frac{M}{w}$$

<div style="text-align: right;">**Equation 2**</div>

The bending stress applied to the beam is equal to:

$$\sigma_b = \frac{38477}{0.00063}$$

$$\sigma_b = 61.07 \; MPa$$

The yield strength of the S235JRG2 steel used for the beam can be divided by this maximum bending stress to calculate a safety factor using Equation 3:

$$SF = \frac{\sigma_y}{\sigma_b}$$

<div align="right">**Equation 3**</div>

$$SF = \frac{235}{61.07}$$

$$SF = 3.85$$

The sector support beam can therefore survive the applied stresses when they are at a maximum value with a safety factor of 3.85, meaning that the design is OK.

Stress analysis of the sling attachment

Equation 3 is used to calculate the safety factors for all the components used to attach the Micromegas to the sector support beam

$$SF = \frac{Max\ Allowable\ Force}{Max\ Applied\ Force}$$

<div align="right">**Equation 3**</div>

<div align="center">Large Sector – light side</div>

Turnbuckle:

Rated load	= 1800 kg
	= 17658 N
Actual load	= 4293 N
Safety Factor	= 4.1

Eye Bolts:

Rated load	= 1500 kg
	= 14715 N
Actual load	= 4293 N
Safety Factor	= 3.4

<div align="center">Large Sector – heavy side</div>

Shackle:

Rated load	= 2500 kg
	= 24525 N
Actual load	= 9932 N
Safety Factor	= 2.5

Eye Bolt:

Rated load	= 2300 kg
	= 22563 N
Actual load	= 9932 N
Safety Factor	= 2.3

Small Sector

Turnbuckle:

Rated load	= 1800 kg
	= 17658 N
Actual load	= 7060 N
Safety Factor	= 2.5

Eye Bolts:

Rated load	= 1500 kg
	= 14715 N
Actual load	= 7060 N
Safety Factor	= 2.1

5. **Stability Analyses**

Stability analysis of the sector support beam

In order to achieve stability of the tool during lifting operations, the point where the overhead crane meets the lifting slings needs to be directly above the objects centre of gravity. This stability analysis has been completed in accordance with each components predicted mass, this however, may not be their true masses after manufacture. The components should all be weighed to confirm their final mass and the slinging operation should be adjusted accordingly.

The stability of large sector support beam slings can be calculated using Equation 11:

$$\sum M_c = \sum (M \times d) = 0$$

Equation 11

$$(-1450 \times 0.360) + (1680 \times d) = 0$$

$$d = 0.311 \ mm$$

When lifting the large sector, the centre of the slings should therefore lie directly above the point that is 311 mm left of the centre point of the sector support beam. Equal length slings connected to the sling mounts will achieve this because the sling mounts are positioned symmetrically about this point.

The stability of the large Micromegas chamber support beam slings can be calculated using Equation 11:

$$\sum M_c = \sum (M \times d) = 0$$

Equation 11

$$(-680 \times 0.360) + (910 \times d) = 0$$

$$d = 0.269 \ mm$$

When lifting the large Micromegas chambers, the centre of the slings should therefore lie directly above the point that is 269 mm left of the centre point of the sector support beam. This is 42 mm to the right of the position for the large sector hoists. In order to achieve this change without moving the sling mounting points, the left sling should have a length of 2084 mm while the right sling should have a length of 2043.3 mm. This change in length can be achieved by the use of turnbuckles incorporated into the slings.

The centroids of the small sector and the small Micromegas chamber both lie directly in line with the centroid of the lifting beam. As a result of this, the sling hoist points for these beams can lie at 1 m, symmetrically about either side of the centre of the lifting beam.

Stability analysis of the transport tool

The total mass of an unloaded transport tool is equal to 1188 kg. This mass is applied symmetrically about the centre axis of the transport tool. When lifting an unloaded transport tool, the original hoisting points located symmetrically about this point can therefore be used. When lifting the tool with small Micromegas chambers or small NSW sectors loaded, the tool again has a symmetrical mass and the original hoisting points can be used.

The centre of mass of the large Micromegas chambers are at a position 360 mm to the left of the centre of mass of the unloaded transport tool. The total mass of the transport tool, including the symmetric mass of the sector support beams is calculated to be:

$$Total\ symmetrical\ mass = Transport\ tool + (sector\ support\ beam \times 4)$$

$$Total\ symmetrical\ mass = 1188 + (230 \times 4)$$

$$Total\ symmetrical\ mass = 2108\ kg$$

The mass of the four perfectly aligned double Micromegas chambers are calculated to be:

$$Total\ offset\ mass = Micromegas\ wedge \times 4$$

$$Total\ offset\ mass = 680 \times 4$$

$$Total\ offset\ mass = 2720\ kg$$

The moments about the centre of mass of the transport tool are equal to zero. Equation 11 can now be used to find the relative position of the new centre of the hoist points.

$$\sum M_c = 0$$

$$(M \times d) + (M \times d) = 0$$

$$(-2720 \times 0.360) + (4828 \times d) = 0$$

$$d = 0.203\ mm$$

The new center of hoist point should therefore be positioned 203 mm to the left of the old one. To achieve this, a new hoist point has been positioned 406 mm to the left of the original right hoist point.

When the transport tool is used to transport two large NSW sectors, the centre of mass of the assembly again changes. Using equation 11, the new centre of mass is shown to be:

$$\sum M_c = 0$$

$$(M \times d) + (M \times d) = 0$$

$$(-2900 \times 0.360) + (5008 \times d) = 0$$

$$d = 0.208 \, mm$$

This is only 5 mm to the left of the hoist position for the four Micromegas chambers and can therefore be ignored.

APPENDIX F - Free Body, Shear and Bending Moment Diagrams for the Assembly Tool

F.1 Force diagrams for the cross beam of the NSW sector assembly station

An online bending moment calculator was used to calculate the bending moment in cross beam. The online calculations were checked and the results are confirmed to be accurate. The software used is called *Beam Calculator* and designed by *SkyCiv*.

The free body diagram represented in Figure F-1 is a representation of the forces applied to the sector support beam by the heavy side of the large sector. The red force is the load applied to the support beam by the sector support beam supporting a large sector. The green distributed load is a result of the weight of the beam at a total mass of 51 kg. The two supports on the beam are the reaction forces resulting due to the upright supports of the assembly station.
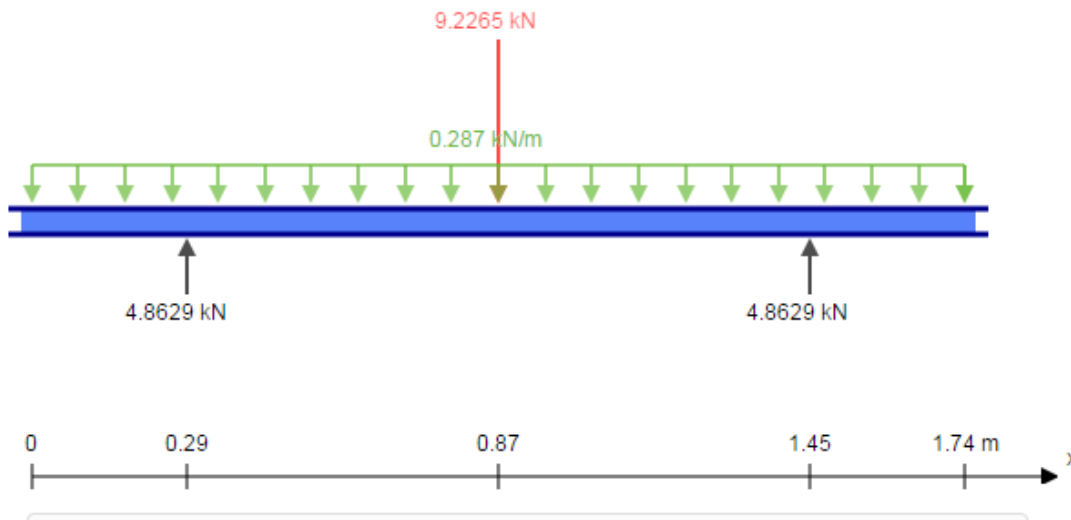
Figure F-1. Free body diagram for the NSW sector assembly stand cross beam.

Figure F-2 represents the shear forces applied to the beam while Figure F-3 shows the bending moments applied to the beam. It can be observed that the maximum applied bending moment in the NSW sector assembly station cross beam due to the hanging of the large sector is equal to 2711.9 Nm.
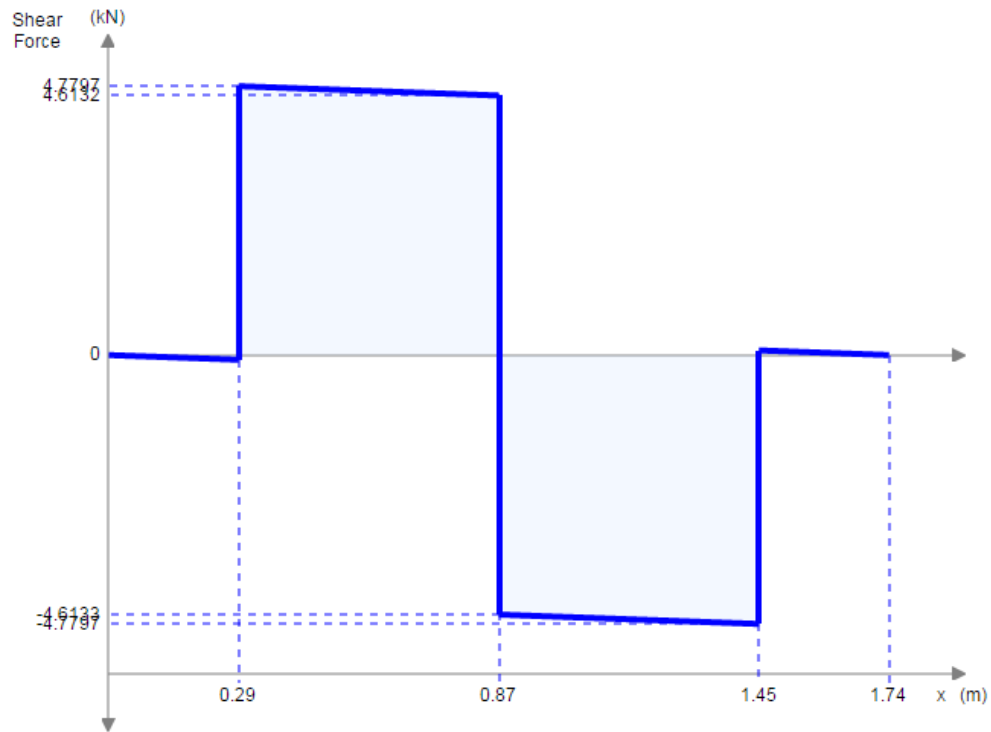
Figure F-2. Shear force diagram for the large sector assembly station cross beam.
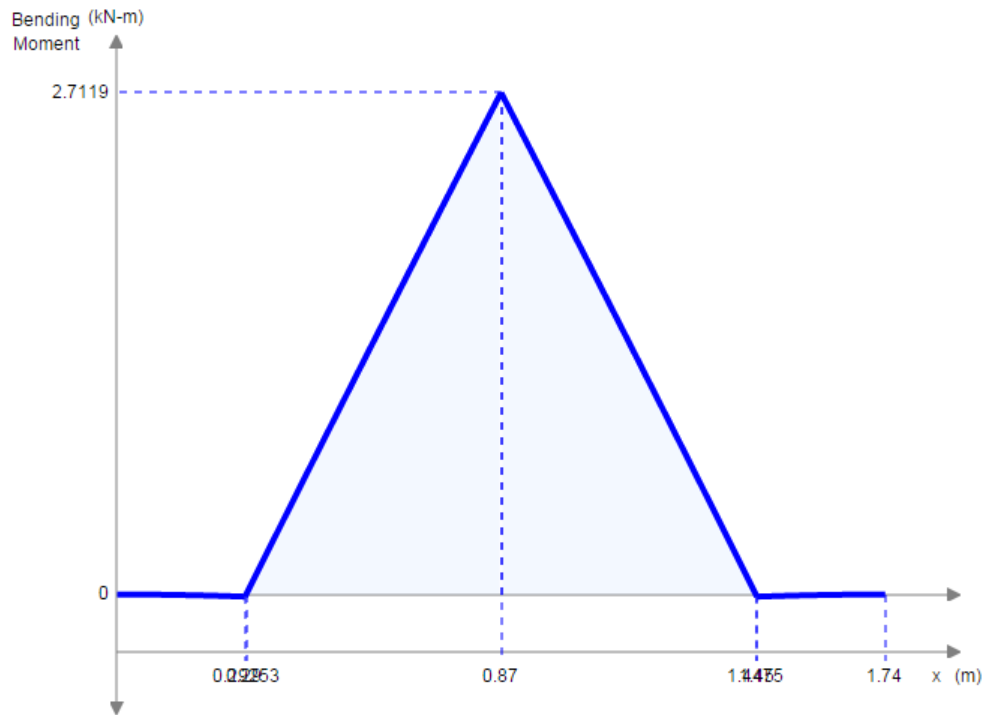
Figure F-3. Bending moment diagram for the large sector assembly station cross beam.

F.2 Stress analysis of the cross beam of the NSW sector assembly stand

The highest load applied to the NSW sector assembly stand cross beams is the applied bending stress when they are being used to assemble a large sector on its heavy side. The largest bending moment due to this load is shown in Appendix X to be:

$$M = 2711.9 \ Nm$$

When the sector support beam is resting on the cross beam, the maximum stress can be calculated using Equation 2. The stress due to bending is used while the stress due to shear forces are negligibly small and have been omitted from the calculation.

$$\sigma_b = \frac{M}{W}$$

Equation 2

$$\sigma_b = \frac{2711.9}{218 \times 10^{-6}}$$

$$\sigma_b = 12.44 \ MPa$$

The yield strength of the steel used for the cross beams can be divided by this maximum bending stress to calculate a safety factor using Equation 3:

$$SF = \frac{\sigma_y}{\sigma_b}$$

Equation 3

$$SF = \frac{235}{12.44}$$

$$SF = 18.89$$

The NSW sector assembly station cross beam can therefore survive the applied stresses with a safety factor of 18.89 when supporting a fully assembled large NSW sector.

APPENDIX G - MMSW Analysis

G.1 Approximated analytical calculation of the thermal expansion of the MMSW

This analytical calculation aims at investigating an approximation of the expected thermal expansion achieved at the extremities of the MMSW for the experimental and computational analyses when the MMSW is exposed to a temperature change of 27°C.

Assumptions:

1. Primary and only materials are FR4 (PCB) and Aluminium (frames)
2. Thermal expansion in the measured, y-direction is constant along the MMSW's perpendicular x-directional width.
3. Change in temperature is 27 degrees Celsius.
4. No shear strain occurs in the materials, indicating that the two materials experience the exact same amount of thermal expansion.
5. The coefficient of linear thermal expansion of FR4 is constant in the temperature range and is equal to the coefficient of thermal expansion used in the Micromegas computational analysis:

$$\alpha_{FR4} = 13 \times 10^{-6} \ ppm/k$$

6. The coefficient of linear thermal expansion of aluminium is constant in the temperature range and is equal to the coefficient of thermal expansion used in the Micromegas computational analyses:

$$\alpha_{Aluminium} = 23 \times 10^{-6} \ ppm/k$$

7. The modulus of elasticity of each of the two materials is:

$$E_{FR4} = 14700 \times 10^6 \ Pa$$

$$E_{Aluminium} = 70000 \times 10^6 \ Pa$$

Using Equation 4 and Equation 5:
$$\delta = \frac{FL}{EA}$$

Equation 4

$$\delta = \Delta T \times L \times \alpha$$

<div align="right">**Equation 5**</div>

It is important to note that the area used in this equation is not the cross sectional areas of each of the profiles of aluminium and FR4 but instead the area perpendicular to the expansion of the composite.

Equation 6 can be derived from Equation 4 and Equation 5 to calculate the shear forces experienced by each of the materials during the linear thermal expansion of a composite material. The aluminium experiences a compressive force giving it a negative value in the equation while the FR4 experiences an expansion force giving it a positive value.

$$(\Delta T \times L \times \alpha_{al}) - \left(\frac{FL}{E_{al}A_{al}}\right) = (\Delta T \times L \times \alpha_{FR4}) + \left(\frac{FL}{E_{FR4}A_{FR4}}\right)$$

<div align="right">**Equation 6**</div>

$$\left(27 \times (493 \times 10^{-3}) \times (23 \times 10^{-6})\right) - \left(\frac{F \times (493 \times 10^{-3})}{(70000 \times 10^6) \times (2615 \times 10^{-6})}\right)$$

$$= \left(27 \times (493 \times 10^{-3}) \times (13 \times 10^{-6})\right)$$

$$+ \left(\frac{F \times (493 \times 10^{-3})}{(14700 \times 10^6) \times (460 \times 10^{-6} \times 10)}\right)$$

$$F = 13332.34 \, N$$

Using this force, the total deflection can be calculated as:

$$\delta_{al} = \delta_{FR4} = (\Delta T \times L \times \alpha_{al}) + \left(\frac{FL}{E_{al}A_{al}}\right)$$

$$\delta = (27 \times (493 \times 10^{-3}) \times (23 \times 10^{-6})) - \left(\frac{13332.34 \times (493 \times 10^{-3})}{(70000 \times 10^6) \times (2615 \times 10^{-6})}\right)$$

$$\delta = 0.270 \times 10^{-3} mm = 270 \mu m$$

Using this total deflection, an equivalent coefficient of thermal expansion for the composite material can be calculated using Equation 5 as:

$$\delta = \Delta T \times L \times \alpha_{eq}$$

<div align="right">**Equation 5**</div>

$$270 \times 10^{-6} = 27 \times (493 \times 10^{-3}) \times \alpha_{eq}$$

$$\alpha_{eq} = 20.28 \, \frac{\mu m}{m \cdot °C}$$

This analytical calculation aims at investigating an approximation of the expected thermal expansion achieved at the center of the MMSW for the experimental and computational analyses when the MMSW is exposed to a temperature change of 27°C. The presence of aluminium is neglected for this calculation because it has a minimal effect on the expansion in this area.

$$\delta = \Delta T \times L \times \alpha_{eq}$$

Equation 5

$$\delta = 27 \times 493 \times (13 \times 10^{-6})$$

$$\delta = 173 \, \mu m$$

APPENDIX H - FEA Material Data

H.1 Aluminium FEA material data

1	Property	Value	Unit
2	Density	1.85E-09	tonne mm^-3
3	⊟ Orthotropic Instantaneous Coefficient of Thermal Expansion		
4	Coefficient of Thermal Expansion X direction	1.3E-05	C^-1
5	Coefficient of Thermal Expansion Y direction	1.3E-05	C^-1
6	Coefficient of Thermal Expansion Z direction	1.3E-05	C^-1
7	⊟ Orthotropic Elasticity		
8	Young's Modulus X direction	16800	MPa
9	Young's Modulus Y direction	14700	MPa
10	Young's Modulus Z direction	14700	MPa
11	Poisson's Ratio XY	0.14	
12	Poisson's Ratio YZ	0.12	
13	Poisson's Ratio XZ	0.12	
14	Shear Modulus XY	8400	MPa
15	Shear Modulus YZ	8400	MPa
16	Shear Modulus XZ	9100	MPa
17	⊟ Field Variables		
18	Temperature	Yes	
19	Shear Angle	No	
20	Degradation Factor	No	
21	⊟ Orthotropic Thermal Conductivity		
22	Thermal Conductivity X direction	0.00081	W mm^-1 C^-1
23	Thermal Conductivity Y direction	0.00081	W mm^-1 C^-1
24	Thermal Conductivity Z direction	0.00029	W mm^-1 C^-1
25	Specific Heat	6E+08	mJ tonne^-1 C^-1

H.2 Honeycomb FEA material data

1	Property	Value	Unit
2	Density	8.33E-11	tonne mm^-3
3	Isotropic Instantaneous Coefficient of Thermal Expansion	2.3E-05	C^-1
4	⊟ Orthotropic Elasticity		
5	Young's Modulus X direction	10	MPa
6	Young's Modulus Y direction	10	MPa
7	Young's Modulus Z direction	1000	MPa
8	Poisson's Ratio XY	1E-05	
9	Poisson's Ratio YZ	1E-05	
10	Poisson's Ratio XZ	1E-05	
11	Shear Modulus XY	10	MPa
12	Shear Modulus YZ	400	MPa
13	Shear Modulus XZ	200	MPa
14	⊟ Field Variables		
15	Temperature	Yes	
16	Shear Angle	No	
17	Degradation Factor	No	
18	Isotropic Thermal Conductivity	0.002	W mm^-1 C^-1
19	Specific Heat	8.75E+08	mJ tonne^-1 C^-1

H.3 Araldite FEA material data

1	Property	Value	Unit
2	Density	1E-09	tonne mm^-3
3	Isotropic Instantaneous Coefficient of Thermal Expansion	1.5E-05	C^-1
4	⊟ Isotropic Elasticity		
5	Derive from	Young's Modulus and Poisson's Ratio	
6	Young's Modulus	1904	MPa
7	Poisson's Ratio	0.35	
8	Bulk Modulus	2115.6	MPa
9	Shear Modulus	705.19	MPa
10	⊟ Field Variables		
11	Temperature	Yes	
12	Shear Angle	No	
13	Degradation Factor	No	
14	Isotropic Thermal Conductivity	0.00013	W mm^-1 C^-1
15	Specific Heat	1E+09	mJ tonne^-1 C^-1

H.4 FR4 FEA material data

	A	B	C
1	Property	Value	Unit
2	Density	1.85E-09	tonne mm^-3
3	⊟ Orthotropic Instantaneous Coefficient of Thermal Expansion		
4	Coefficient of Thermal Expansion X direction	1.3E-05	C^-1
5	Coefficient of Thermal Expansion Y direction	1.3E-05	C^-1
6	Coefficient of Thermal Expansion Z direction	1.3E-05	C^-1
7	⊟ Orthotropic Elasticity		
8	Young's Modulus X direction	16800	MPa
9	Young's Modulus Y direction	14700	MPa
10	Young's Modulus Z direction	14700	MPa
11	Poisson's Ratio XY	0.14	
12	Poisson's Ratio YZ	0.12	
13	Poisson's Ratio XZ	0.12	
14	Shear Modulus XY	8400	MPa
15	Shear Modulus YZ	8400	MPa
16	Shear Modulus XZ	9100	MPa
17	⊟ Field Variables		
18	Temperature	Yes	
19	Shear Angle	No	
20	Degradation Factor	No	
21	⊟ Orthotropic Thermal Conductivity		
22	Thermal Conductivity X direction	0.00081	W mm^-1 C^-1
23	Thermal Conductivity Y direction	0.00081	W mm^-1 C^-1
24	Thermal Conductivity Z direction	0.00029	W mm^-1 C^-1
25	Specific Heat	6E+08	mJ tonne^-1 C^-1

APPENDIX I - Aluminium Bar Test Experiment Results

I.1 Cold aluminium bar on hot MMSW experiment frame – Experiment 1

Table I-1. Experiment 1A results.

Dial Gauge Number	Initial dial gauge reading @ 24°C (μm)	Final dial gauge reading @ 50°C (μm)	Change in dial gauge reading (μm)	Error (%)
1	1000	1300	300	-0.18
2	500	730	230	-23.47
3	210	480	270	-10.16
4	2000	2240	240	-20.15
Average			260	-13.49
Analytical Value			300.550	0

.

Table I-2. Experiment 1B results.

Dial Gauge Number	Initial dial gauge reading @ 23°C (μm)	Final dial gauge reading @ 50°C (μm)	Change in dial gauge reading (μm)	Error (%)
1	500	800	300	-3.88
2	500	800	300	-3.88
3	430	700	270	-13.49
4	1000	1290	290	-7.08
Average			290	-7.08
Analytical Value			312.109	0

Table I-3. Experiment 1C results.

Dial Gauge Number	Initial dial gauge reading @ 23°C (μm)	Final dial gauge reading @ 50°C (μm)	Change in dial gauge reading (μm)	Error (%)
1	1890	2200	310	-0.68
2	940	1230	290	-7.08
3	1180	1480	300	-3.88
4	1860	2160	300	-3.88
Average			300	-3.88
Analytical Value			312.109	0

I.2 Cold aluminium bar on hot MMSW experiment frame – Experiment 1 – Sample calculations

Example calculation to find the 'Analytical value' for Experiment 1A

$$\alpha_{Aluminium} = 23.4 \times 10^{-6}$$

The thermal expansion of the aluminium bar of length 494 mm when heated from 24°C to 50°C can be determined to be:

$$\delta_{Al} = \Delta T \times L \times \alpha_{Al}$$

Equation 5

$$\delta_{Al} = (50 - 24) \times \frac{494}{1000} \times 23.4$$

$$\delta_{Al} = 295.412 \ \mu m$$

Example calculation of the error percentage for dial gauge 1 of Experiment 1A

$$Error \ Percentage = \frac{|Theoretical \ value - Experimental \ value|}{Theoretical \ value} \times 100$$

Equation 7

$$Error \ Percentage = \frac{|300.550 - 240|}{300.550} \times 100$$

$$Error \ Percentage = 20.15 \ \%$$

I.3 Cold aluminium bar on cold MMSW experiment frame – Experiment 2

Table I-4. Experiment 2A results.

Dial Gauge Number	Initial dial gauge reading. Al. bar @ 24°C (μm)	Final dial gauge reading. Al. bar @ 50°C (μm)	Change in dial gauge reading (μm)	Error (%)
1	2000	2160	160	9.27
2	910	1060	150	2.44
3	300	450	150	2.44
4	3000	3150	150	2.44
Average			152.5	4.15
Analytical Value			146.422	0

Table I-5. Experiment 2B results.

Dial Gauge Number	Initial dial gauge reading. Al. bar @ 27°C (μm)	Final dial gauge reading. Al. bar @ 50°C (μm)	Change in dial gauge reading (μm)	Error (%)
1	2030	2160	130	0.37
2	920	1060	140	8.09
3	320	450	130	0.37
4	3030	3150	120	-7.36
Average			130	0.37
Analytical Value			129.527	0

Table I-6. Experiment 2C results.

Dial Gauge Number	Initial dial gauge reading. Al. bar @ 22°C (μm)	Final dial gauge reading. Al. bar @ 50°C (μm)	Change in dial gauge reading (μm)	Error (%)
1	2000	2150	150	-4.87
2	890	1050	160	1.47
3	300	440	140	-11.21
4	3000	3150	150	-4.87
Average			150	-4.87
Analytical Value			157.684	0

I.4 Cold aluminium bar on cold MMSW experiment frame – Experiment 2 – Sample calculations

Example calculation to find the Analytical value for Experiment 2A:

$$\alpha_{Aluminium} = 23.4 \times 10^{-6}$$

$$\alpha_{Steel} = 12 \times 10^{-6}$$

The thermal expansion of the aluminium bar of length 494 mm when heated from 24°C to 50°C on a cold steel frame can be determined to be:

$$\delta = \Delta T \times L \times \alpha$$

Equation 6

$$\delta_{Gauge} = (\Delta T \times L \times \alpha_{Al}) - (\Delta T \times L \times \alpha_{St})$$

$$\delta_{Gauge} = \left((50 - 24) \times \frac{494}{1000} \times 23.4\right) - \left((50 - 24) \times \frac{494}{1000} \times 12\right)$$

$$\delta_{Gauge} = \left((50 - 24) \times \frac{494}{1000} \times (23.4 - 12)\right)$$

$$\delta_{Gauge} = 146.422$$

APPENDIX J - MMSW Test Experiment Results

J.1 Cold MMSW on hot MMSW experiment frame – Experiment 3

Table J-1. Experiment 3A results.

Dial Gauge Number	Initial dial gauge reading @ 23°C (μm)	Final dial gauge reading @ 50°C (μm)	Change in dial gauge reading (μm)
1	2000	2220	220
2	0	180	180
3	340	540	200
4	0	250	250

Table J-2. Experiment 3A error.

Dial Gauge Number	Change in dial gauge reading (μm)	Simulation Reading (μm)	Error (%)
1	220	246	11.8
2	180	218	21.1
3	200	207	3.5
4	250	232	-7.2

Table J-3. Experiment 3B results.

Dial Gauge Number	Initial dial gauge reading @ 23°C (μm)	Final dial gauge reading @ 50°C (μm)	Change in dial gauge reading (μm)
1	5000	5230	230
2	0	220	220
3	300	520	220
4	1000	1250	250

Table J-4. Experiment 3B error.

Dial Gauge Number	Change in dial gauge reading (μm)	Simulation Reading (μm)	Error (%)
1	230	246	7.0
2	220	218	-0.9
3	220	207	-5.9
4	250	232	-7.2

Table J-5. Experiment 3C results.

Dial Gauge Number	Initial dial gauge reading @ 23°C (μm)	Final dial gauge reading @ 50°C (μm)	Change in dial gauge reading (μm)
1	1000	1220	220
2	1000	1200	200
3	300	500	200
4	2000	2220	220

Table J-6. Experiment 3C error.

Dial Gauge Number	Change in dial gauge reading (μm)	Simulation Reading (μm)	Error (%)
1	220	246	11.8
2	200	218	9.0
3	200	207	3.5
4	220	232	5.5

J.2 Cold MMSW on cold MMSW experiment frame – Experiment 4

Table J-7. Experiment 4A results.

Dial Gauge Number	Initial dial gauge reading. MM @ 22°C (µm)	Final dial gauge reading. MM @ 50°C (µm)	Change in dial gauge reading (µm)	Actual MM thermal expansion (µm)
1	2000	2090	90	256
2	0	90	90	256
3	200	280	80	246
4	1000	1100	100	266

Table J-8. Experiment 4A error.

Dial Gauge Number	Change in dial gauge reading (µm)	Simulation Reading (µm)	Error (%)
1	256	255	-0.4
2	256	226	-11.7
3	246	215	-12.6
4	266	241	-9.4

Table J-9. Experiment 4B results.

Dial Gauge Number	Initial dial gauge reading. MM @ 23°C (μm)	Final dial gauge reading. MM @ 50°C (μm)	Change in dial gauge reading (μm)	Actual MM thermal expansion (μm)
1	2010	2090	80	240
2	30	100	70	230
3	210	290	80	240
4	1000	1100	100	260

Table J-10. Experiment 4B error.

Dial Gauge Number	Change in dial gauge reading (μm)	Simulation Reading (μm)	Error (%)
1	240	246	2.5
2	230	218	-5.2
3	240	207	-13.8
4	260	232	-10.7

Table J-11. Experiment 4C results.

Dial Gauge Number	Initial dial gauge reading. MM @ 24°C (μm)	Final dial gauge reading. MM @ 50°C (μm)	Change in dial gauge reading (μm)	Actual MM thermal expansion (μm)
1	4000	4090	90	244
2	1000	1060	60	214
3	400	460	60	214
4	1000	1050	50	204

Table J-12. Experiment 4C error.

Dial Gauge Number	Change in dial gauge reading (μm)	Simulation Reading (μm)	Error (%)
1	244	236	-3.3
2	214	210	-1.9
3	214	200	-6.5
4	204	224	9.8

Table J-13. Experiment 4D results.

Dial Gauge Number	Initial dial gauge reading. MM @ 22°C (μm)	Final dial gauge reading. MM @ 50°C (μm)	Change in dial gauge reading (μm)	Actual MM thermal expansion (μm)
1	4000	4090	90	256
2	1000	1070	70	236
3	380	460	80	246
4	1000	1050	50	216

Table J-14. Experiment 4D error.

Dial Gauge Number	Change in dial gauge reading (μm)	Simulation Reading (μm)	Error (%)
1	256	255	-0.4
2	236	226	-4.2
3	246	215	-12.6
4	216	241	11.6

In order to get an accurate reading of the thermal expansion of the MMSW in Experiment 4, the expansion of the steel frame should be added to the dial gauge reading. This will give an absolute thermal expansion value of the Micromegas similar to the values recorded in experiment three. Because the entire frame is steel and the dial gauges along with their stands are steel too, one can simply use the length of the aluminium when calculating the thermal expansion analytically.

$$\alpha_{Steel} = 12 \times 10^{-6}$$

$$\delta = \Delta T \times L \times \alpha$$

Equation 5

$$\delta_{Steel} = (\Delta T \times L \times \alpha_{St})$$

$$\delta_{Gauge} = \left((50 - 22) \times \frac{494}{1000} \times 12\right)$$

$$\delta_{Steel} = 166 \ \mu m$$

At:

$$T_i = 23$$

$$\delta_{Steel} = 160 \ \mu m$$

At:

$$T_i = 24$$

$$\delta_{Steel} = 154 \ \mu m$$